Technische Universität München
TUM School of Natural Sciences

Development of the first Human-scale Dark-field Computed Tomography System

Manuel Peter Viermetz

Vollständiger Abdruck der von der TUM School of Natural Sciences der Technischen Universität München zur Erlangung eines

Doktors der Naturwissenschaften (Dr. rer. nat.)

genehmigten Dissertation.

Vorsitz: Prof. Dr. David Egger

Prüfer*innen der Dissertation:

1. Prof. Dr. Franz Pfeiffer
2. Prof. Dr. Daniel Rückert

Die Dissertation wurde am 02.11.2022 bei der Technischen Universität München eingereicht und durch die TUM School of Natural Sciences am 30.11.2022 angenommen.

Chair of Biomedical Physics
Department of Physics
School of Natural Sciences
Technical University of Munich

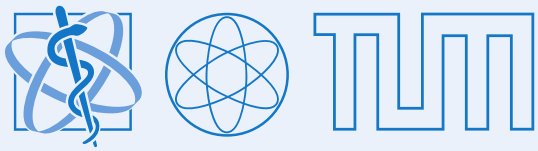

Development of the first Human-scale Dark-field Computed Tomography System

Manuel Peter Viermetz

PhD Thesis

Supervisor:
Prof. Dr. Franz Pfeiffer

Abstract

X-ray computed tomography (CT) is the most widely used 3D medical imaging modality today. It has been refined over several decades, with the most recent innovations including dual-energy and spectral photon-counting technologies. Going beyond the presently used X-ray attenuation, it has been discovered that wave-optical contrast mechanisms offer the potential of complementary information, particularly on otherwise unresolvable tissue microstructures [94], [7]. One such approach is dark-field imaging, which gained attention in medical imaging during the last decade. It has been shown to provide significant benefit in radiological applications, such as imaging of lung disease in small animals [107], [152]. Until now, however, dark-field CT could not be translated to the human scale, it has been restricted to bench top and small-animal systems, with scan times exceeding several minutes. This is mainly because the up-scaling and adaptation to the mechanical complexity, speed, and size of a human CT scanner so far remained an unsolved challenge.

The content of this thesis is to develop the first dark-field CT scanner for imaging human-sized objects. To retrieve the additional dark-field contrast a Talbot-Lau interferometer is implemented into a clinical CT system. Before such a system can be set up, several challenges related to clinical CT must be identified and overcome. Among these are for example the influence of the large X-ray source size, bent gratings, and the compact system dimensions. Additionally, the hostile environment of a clinical CT gantry, where system vibrations can easily degrade the interferometer performance, must be taken into account. For reconstruction of attenuation and dark-field contrast from the measured data a novel processing approach is required which simultaneously compensates for vibration-induced artifacts. The implementation is realized in cooperation with microfabrication experts from Karlsruhe Institute for Technology (KIT) and engineers from Philips GmbH for fabrication and system integration.

In the last part of the thesis, the dark-field CT prototype is characterized with regard to stability, dose, resolution, and imaging performance. The first dark-field CT images of a human-sized anthropomorphic body phantom are presented. These reconstructions from an axial single rotation scan at a measurement time of only one second are a major milestone in CT imaging. Besides the characterization of the setup performance, several case studies with test objects are evaluated using, e.g., ventilated ex-vivo porcine lungs. These experiments demonstrate promising results for imaging with dark-field contrast in clinical CT, particularly, for imaging of the lung. Eventually, based on these results an outlook towards first in-vivo application is possible.

Zusammenfassung

Die Röntgen-Computertomografie (CT) ist heute das am häufigsten verwendete medizinische 3D-Bildgebungsverfahren. Sie wurde über mehrere Jahrzehnte hinweg verfeinert, wobei zu den jüngsten Innovationen die Dual-Energy- und die spektrale Photonenzählung gehören. Neben der bisher genutzten Röntgenabschwächung gelten jedoch auch wellenoptische Kontrastmechanismen als vielversprechend. Diese haben das Potenzial zusätzliche Informationen über das untersuchte Material zu liefern, insbesondere über die ansonsten nicht auflösbare Mikrostruktur [94], [7]. Ein solcher Ansatz ist die Dunkelfeld-Bildgebung, die im letzten Jahrzehnt in der medizinischen Bildgebung an Aufmerksamkeit gewonnen hat. Sie zeigte in Kleintiermodellen einen deutlich verbesserten radiologischen Nutzen, speziell bei Lungenerkrankungen [107], [152]. Bislang konnte die Dunkelfeld-CT jedoch noch nicht auf den menschlichen Maßstab übertragen werden. Sie war daher auf Labor- und Kleintiersysteme mit einer Untersuchungsdauer von mehreren Minuten beschränkt. Dies liegt vor allem daran, dass die Skalierung und Anpassung an die mechanische Komplexität, Geschwindigkeit und Größe eines CT-Scanners für Menschen bisher eine ungelöste Herausforderung darstellte.

Der Inhalt dieser Arbeit ist es, den ersten Dunkelfeld-CT-Scanner für die Bildgebung von Objekten in menschlicher Größe zu entwickeln. Um den zusätzlichen Dunkelfeldkontrast zu gewinnen, wird ein Talbot-Lau-Interferometer in ein klinisches CT-System integriert. Bevor ein solches System eingerichtet werden kann, müssen mehrere Herausforderungen identifiziert und überwunden werden. Zu diesen gehören unter anderem der Einfluss der großen Röntgenquelle, gebogener Gitter und die kompakte Systemgröße. Außerdem muss die anspruchsvolle Umgebung in einer klinischen CT Gantry berücksichtigt werden, in welcher Systemvibrationen die Leistung des Interferometers leicht gefährden können. Für die Rekonstruktion der Messdaten ist eine neuartige Verarbeitung der Messdaten erforderlich, um vibrationsbedingte Artefakte zu kompensieren. Diese Prozessierung gibt schließlich die Rekonstruktionen der Röntgenabschwächung und des Dunkelfeldkontrastes im Objekt aus. Die Implementierung wird in Zusammenarbeit mit Mikrofabrikationsexperten des Karlsruher Instituts für Technologie (KIT) und Ingenieuren von Philips GmbH für die Herstellung und Systemintegration realisiert.

Im letzten Teil der Arbeit wird der Dunkelfeld-CT-Prototyp hinsichtlich Stabilität, Dosis, Auflösung und Bildqualität charakterisiert. Dort werden auch die ersten Dunkelfeld-CT-Bilder eines menschengroßen anthropomorphen Körperphantoms vorgestellt. Diese Rekonstruktionen aus axialen Einzelrotationsscan mit einer Messzeit von jeweils nur einer Sekunde sind ein wichtiger Meilenstein für die CT Bildgebung. Neben der Charakterisierung der Leistungsfähigkeit des Aufbaus werden mehrere Fallstudien mit Testobjekten ausgewertet, z.B. mit beatmeten ex-vivo Schweinelungen. Diese Experimente demonstrieren vielversprechende Ergebnisse für die Bildgebung mit Dunkelfeldkontrast in der klinischen CT, insbesondere für die Bildgebung der Lunge. Schließlich ist auf der Grundlage dieser Ergebnisse ein Ausblick auf erste in-vivo-Anwendungen möglich.

Dedicated to my parents.

Parts of the methods and results presented in this thesis have been published in the following articles:

Viermetz, M., Gustschin, N., Schmid, C., Haeusele, J., von Teuffenbach, M., Meyer, P., Bergner, F., Lasser, T., Proksa, R., Koehler, T., & Pfeiffer, F. (2022). "Dark-field computed tomography reaches the human scale," *Proceedings of the National Academy of Sciences*, 119(8), e2118799119. https://doi.org/10.1073/pnas.2118799119

Viermetz, M., Gustschin, N., Schmid, C., Haeusele, J., Noël, P., Proksa, R., Loescher, S., Koehler, T., & Pfeiffer, F. (2022). "Technical design considerations of a human-scale Talbot-Lau interferometer for Dark-field CT," *IEEE Transactions on Medical Imaging*. https://doi.org/10.1109/TMI.2022.3207579

Viermetz, M., Gustschin, N., Schmid, C., Haeusele, J., Proksa, R., Koehler, T., & Pfeiffer, F. (2022). "Dark-field imaging on a clinical CT system: Realization of Talbot-Lau interferometry in a gantry." *Proc. SPIE 12304, 7th International Conference on Image Formation in X-Ray Computed Tomography*. https://doi.org/10.1117/12.2646439

Viermetz, M., Gustschin, N., Schmid, C., Haeusele, J., Koehler, T., & Pfeiffer, F. (2022). "Initial Characterization of Dark-field CT on a clinical gantry." *IEEE Transactions on Medical Imaging*. https://doi.org/10.1109/TMI.2022.3222839

M. Viermetz developed and performed the wave-optical simulations, designed and implemented the interferometer, conducted the measurements, processed and analyzed all data, and wrote the manuscript. F. Pfeiffer, T. Koehler, and R. Proksa developed the research idea and supported the entire development process. M. von Teuffenbach and T. Koehler devised the basis for the data processing. M. Viermetz, C. Schmid, and J. Haeusele extended the data processing supported by T. Koehler, T. Lasser, F. Bergner, and F. Pfeiffer. P. Meyer manufactured the X-ray compatible gratings and N. Gustschin characterized them. M. Viermetz, N. Gustschin, T. Koehler, R. Proksa, and S. Loescher developed the interferometer design and realized the implementation into a clinical CT system. M. Viermetz, N. Gustschin, and J. Haeusele adjusted the interferometer.

Parts of this thesis are literal excerpts of the papers including paragraphs in Chapters 3 and 7.

Contents

1 Introduction to Dark-field CT

The first chapter is an introductory part which serves to motivate the reader about the background and work carried out in the context of this thesis. First, the state-of-the-art clinical computed tomography systems which are currently used in the clinics are explained. Then the concept of dark-field imaging and latest laboratory implementations are discussed. Finally, a brief outline is given on how a translation from laboratory table-top systems to a clinical CT can be achieved and what development steps are required.

1.1 State of the Art Clinical Computed Tomography

Image-based diagnostic systems have a particular importance in modern medicine. They allow insights into the patient in a non-invasive way by utilizing ultrasound, radio-frequencies, or X-rays. While *ultrasound imaging* is portable, fast, and cheap, it comes with the drawback of having only limited contrast and resolution. Contrary, *Magnet Resonance Imaging* (MRI) is a stationary, rather slow, and expensive imaging modality but comes with excellent contrast. It uses radio-frequencies in a strong magnetic field to resolve characteristic spin effects of hydrogen atoms in the patient. In MRI, the resolution, magnetic field strength, and acquisition time are strongly linked. Consequently, today, by maximizing the magnetic field strengths, high resolution at a reasonable acquisition time are achieved. The measurement time – during which the patient must not move – is still comparably long. Furthermore, while soft tissue contrast is outstanding, imaging of bones is difficult due to the low amount of hydrogen atoms in this material. *Computed tomography* (CT) completes the imaging portfolio as a technique with high resolution and a high acquisition speed. This allows fast and precise diagnostics and, different to MRI, it does not require a magnetic field or radio-frequencies. Consequently, CT has no restrictions concerning metal implants, such as pacemakers, which are often problematic in MRI. However, as CT is based on X-ray attenuation, it comes with ionizing radiation dose for the patient. This must be kept low and requires a trade-off between indication for a CT scan and risk due to the ionizing radiation.
For the development of computer assisted tomography, Allan Cormack and Godfrey Hounsfield received the Nobel Prize in Physiology or Medicine in 1979 [128]. The fundamental concept of CT systems has not gone through major transformations since its first clinical application in 1972. Similar to the first CT machines also today's systems are essentially an X-ray source and a detector which are rotated around a stationary patient. Naturally, every component and concept has undergone many iterations of optimizations in the meanwhile. Combined with technical novelties, latest CT systems have now greatly increased the image quality, acquisition speed, and dose efficiency. For example, state-of-the-art CT systems have multi-row detectors which range from 16 lines up to 256 lines. This allows a maximum coverage exceeding 10 cm along the z-axis per rotation. Moreover, the bore radius, i.e., the cylindrical opening into which the patient is positioned, was extended. It is today about 70 cm in diameter, which provides

patient comfort and allows better accessibility during CT intervention. To allow sort acquisition times, the gantry rotation period has been decreased to below 0.3 s in modern CT machines. A consequence of these advances are high centrifugal forces on the imaging components, such as the detector and the X-ray tube.
To lower the radiation dose for the patient, pre-filtering and flux variation depending on the body part and size have been introduced. In addition, contrast agents are used to solve problems with low contrast-to-noise ratio in soft tissues and further decrease the dose. These agents are liquids containing strongly attenuating elements which are injected into the patient's blood vessels. They then enhance the contrast between soft tissue, the vessels, or soft tissues resorbing the agent. Most recently, innovations towards energy-discriminating X-ray imaging pushed new CT systems with special sources or detectors to the clinics. These systems utilize the energy dependency of the attenuation coefficient to extract even more information from a CT scan. For example, this new technology allows to better differentiate soft tissues or contrast agents. However, still only the attenuation of X-ray photons in the patient is considered in these systems.

1.2 Dark-field Imaging

With dark-field imaging the restriction to attenuation contrast can be overcome. It adds another contrast modality representing the small-angle scattering power of the material to X-ray imaging systems. In pre-clinical studies, this new contrast has been identified as a promising imaging channel for lung-related diseases. The porous structure of the lung tissue with many air-to-soft-tissue interfaces causes strong small-angle scattering of the X-rays. This signal can be correlated to various disease models [107], [75], [49], [106], [51], [50].
To resolve refraction and small-angle scattering of X-rays, a wave-optical measurement approach is required. There are several concepts available to measure the small deviations in the wave-front, particularly when working with synchrotron sources. For example, analyzer-based, propagation-based phase-contrast, or speckle imaging, which rely on highly coherent radiation, can be used to retrieve this image information [4], [159], [38]. This thesis, however, focuses on grating-based imaging solutions implemented as Talbot-Lau interferometers. These come with the advantage that they can be made compatible with in-coherent radiation sources. This is important because clinical X-ray sources come with large focal spots and a poly-chromatic X-ray spectrum. Both these characteristics lead to highly in-coherent radiation, but cannot be avoided when high X-ray flux is required. Consequently, Talbot-Lau interferometers currently have the highest feasibility for making dark-field contrast accessible in a clinical setting.
Talbot-Lau interferometry allows simultaneous imaging of attenuation, diffraction, and small-angle scattering. Originally being a synchrotron-only technology, the method was extended to conventional X-ray tubes in 2006 [94]. Further milestones on the path to clinical application were the availability of high-aspect-ratio gratings [77] and powerful processing and reconstruction approaches [158], [125].
Early, dark-field radiography and tomography, i.e., imaging in two and three dimensions, respectively, have been available at laboratory systems for quite some time [95], [92], [91]. These commonly focus on high sensitivity and high spatial resolution for small biological specimen [32], [54], [148], [149], [13], [16], [85], [53], [138]. For the development of clinical dark-field CT, the up-scaling to large sample sizes was soon identified to be a major challenge.
In 2013, an important milestone was achieved when the first grating-based Talbot-Lau interferometer in a small-animal gantry was demonstrated [121], [122], [154]. The *skyscan* was developed in collaboration with Bruker GmbH and can perform phase-contrast and dark-field

sensitive tomographic scans of mice within an acquisition time of several minutes. This system has been commercialized and is part of active research in the field of small-animal studies. With the results from this system, initial in-vivo studies demonstrated that clinical application of dark-field imaging can solve the low contrast issue, e.g., in imaging of the lung [154], [75], [76], [49], [135], [152], [51].
This first small-animal dark-field CT system, however, also revealed that scan time and stability are main concerns for future larger implementations. In 2017, the implementation of a Talbot-Lau interferometer into a clinical C-arm system struggled with stability issues. This made clear that a stable gantry solution is favorable as it provides better mechanical stability [55]. To work around stability issues and the complex acquisition of CT, recently several clinical grating-based radiography prototypes have been published. These systems are usually specialized for a particular purpose, such as mammography, extremity, or chest radiography [119], [67], [37], [147], [146]. Here, mostly a quasi-stationary interferometer and a scanning procedures are combined to produce high sensitivity and large field of view attenuation and dark-field radiography images. At these implementations, first clinical studies on diagnostic value of the clinical dark-field radiography for lung-disease are performed. They revealed that dark-field imaging can provide promising help for staging COPD and COVID-19 disease [146], [35], [34].

1.3 Roadmap from Laboratory to Clinical Dark-field CT

To bring dark-filed CT to clinical application a Talbot-Lau interferometer which can rotate around the patient is required. One option is to develop such a system as an entirely new clinical CT system, purpose built for such a Talbot-Lau interferometer. The complexity involved in such CT systems, however, makes their development a multi-year effort, even for specialized manufacturers. Therefore, it is reasonable to make use of existing CT systems which are already highly optimized and well-tested. The dark-field imaging technology then has to be implemented into such an existing clinical CT machine. This makes efficient use of the available clinical CT know-how which lies in the reliable gantry design together with the optimized detector and X-ray source. On the contrary, this requires adapting the Talbot-Lau interferometer to a predetermined system, which comes with a variety of challenges and limitations.
Even though dark-field CT has been demonstrated in a small-animal scanner [122], [135], [132] the feasibility of a clinical scale dark-field CT remained a controversial issue. The associated large field of view, the required compact and cylindrical interferometer geometry, and an acquisition with continuous gantry rotation accompanied by mechanical system instabilities are some of many potential problems [150]. While the first small-animal dark-field CT basically is a laboratory Talbot-Lau interferometer on a rotating gantry, the translation from clinical dark-field radiography systems to clinical dark-field CT is not as straightforward. Particularly, the change in geometry to a total length under one meter with a 70 cm bore radius for the patient is a major problem. This leaves only about 30 cm of space along the beam path to implement the three gratings of the interferometer. Such constraints render most existing concepts from dark-field radiography systems incompatible because these often rely on long propagation distances between the gratings.
In this thesis, the design of first dark-field CT prototype in a clinical CT is derived and its implementation into a state-of-the-art Brilliance iCT (Philips) is demonstrated. A wave-optical simulation framework has been developed and is used to analyze challenges in the design of the Talbot-Lau interferometer. Based on this simulation, the best performing geometry and grating configuration is identified. In this process, recently revealed issues, such as grating acceptance and deformation due to bending, are considered. For stable implementation into

the clinical CT gantry, custom mounts and adjustment mechanics have been developed and are presented here. Since intrinsic vibrations of the system persist and the gantry rotates during the scan, a novel data processing procedure is required. It is introduced here and then used to characterize the first clinical dark-field CT implementation in detail. Most important characterization aspects are the performance of the bent gratings, the impact of the vibrations, the sensitivity to beam hardening and its correction, the resolution of the reconstruction, and an analysis of the patient dose exposition. Based on several scans of test phantoms and biological samples, e.g., a ventilated ex-vivo lung, the performance of the system is demonstrated.
In Figure 1.1, the first dark-field CT prototype is shown. In the developed system, the changes to the original conventional CT are kept to a minimum. Consequently, this prototype demonstrates that dark-field CT can be integrated into existing CT infrastructure. The initial results show that this system produces novel dark-field and attenuation images of human sized objects from a single scan.

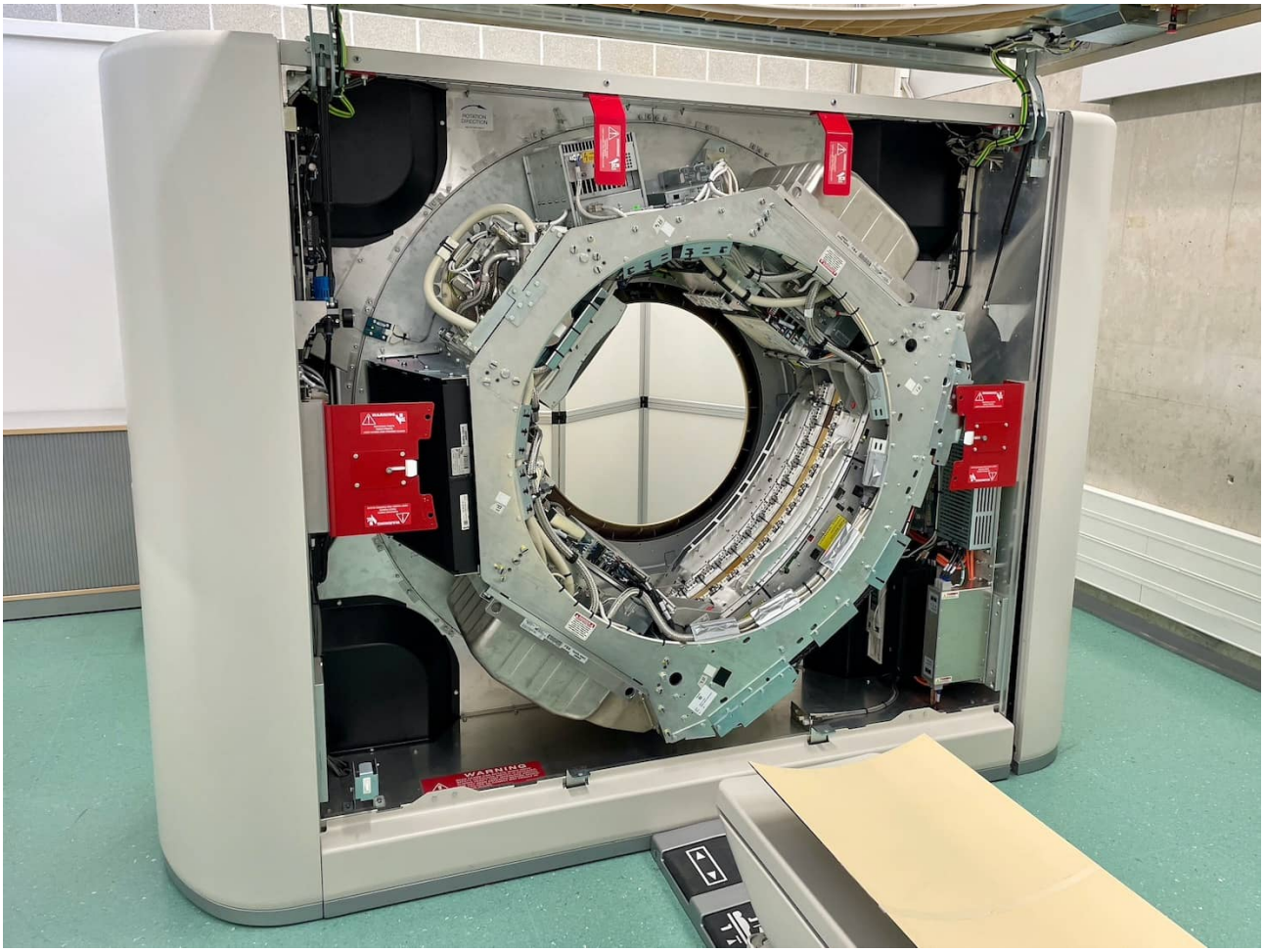

Figure 1.1: First dark-field computed tomography prototype set up at the Munich Institute of Biomedical Engineering (TUM). Designed and built in collaboration between the Technical University Munich, Karlsruhe Institute of Technology, and Philips GmbH.

Theoretical Background 2

In this chapter, the theoretical background of X-ray interaction, Talbot-Lau interferometry, and Computed Tomography is introduced in the context of this thesis. Before the focus drifts to dark-field imaging with a clinical CT system, here, the Talbot-Lau interferometry is introduced. For clarity, this introduction is based on the more ideal environment in a laboratory implementation. Thereafter, relevant mathematical frameworks for processing of Talbot-Lau interferometry data and filtered back projection for CT reconstruction is expanded.

2.1 X-ray Generation

X-rays are regularly produced from natural processes like radioactive decay, as part of cosmic radiation or from peeling adhesive tapes [69]. For X-ray imaging, however, dedicated X-ray sources are required which can produce a high amount of radiation from a rather small source spot on demand. There are a variety of source technologies available to fulfill these requirements, e.g., synchrotrons, free electron laser, X-ray tubes, or radio isotope sources.
Synchrotrons and free electron lasers are the most elaborate sources, which constantly push the limits of highest radiation forward. They combine high photon flux with high spatial and temporal coherence, and the produced spectrum can usually be tuned. A comprehensive description can be found in the book by Als-Nielsen and McMorrow [2]. Compared to synchrotrons the free electron laser facilities are relatively young with the first demonstration in 2009 [29]. Since these sources are massive and expensive facilities, recently, also more compact sources based on the inverse Compton-effect have been introduced [58], [9], [2], [28]. These sources are an interesting compromise to make imaging with highly brilliant X-rays more available.
In contrast to the large-scale facilities there are also more cost-efficient, less complex and more compact alternatives. Particularly, the X-ray tube, which actually initiated the discovery of X-rays, is still the most common X-ray generator. Only isotope-based gamma sources are more compact and less complex in operation; however, they come with serious safety concerns. In contrast to X-ray tubes the isotope sources actually contain radioactive material and cannot be turned off but only shielded. Therefore, isotope-based gamma sources are rarely used, e.g., for field inspection or military application.
The majority of X-ray sources for medical imaging, non-destructive testing and scientific experiments are X-ray tubes. Their concept remained similar to the original Coolidge X-ray tube, but many optimizations have been introduced. As illustrated in Figure 2.1, in a first step free electrons are generated through thermal emission at the cathode. This requires a heated filament wire which provides the electrons with excessive thermal energy to overcome their binding energy. The free electrons are then accelerated towards the anode by a high voltage applied between cathode and anode. This acceleration voltage is usually in the keV range and depends on the application. Electrostatic or electromagnetic focusing can be used to focus the electron beam into a small interaction area on the anode target.

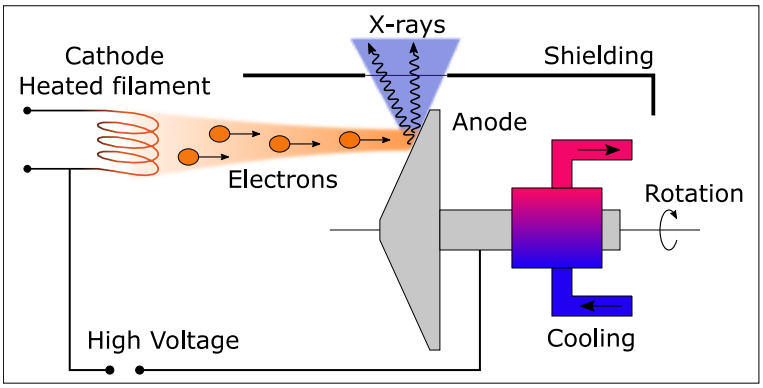

Figure 2.1: Schematic of a rotating X-ray tube. From an electrically heated filament electrons are emitted. A high voltage potential between the cathode and the anode accelerates the electrons onto the target. During collision and deceleration of the electrons in the target X-rays and heat are produced. The X-rays are emitted through an exit port and the heat is removed by a cooling system. To avoid melting of the target surface the anode is continuously rotated to spread the heat load.

When the electrons hit the anode, they are rapidly decelerated by interaction with the target material atoms. This process generates electromagnetic radiation equal to the energy loss. Consequently, if a 80 keV electron is stopped in a single interaction process a 80 keV photon is produced. However, the deceleration process usually takes several interactions generating multiple photons with different energies. This generates a continuous spectrum referred to as *bremsstrahlung*.

Besides the bremsstrahlung also characteristic X-ray emission lines can be found in X-ray tube spectra. The bombarding electrons have enough energy to kick out bound electrons from the innermost shells of the target atoms. This ionization of the target material, however, does not directly generate X-rays. Only the subsequent filling of the vacant hole in the shell from an outer shell produces X-rays at characteristic energies. The formation of K_α, K_β and K_γ lines depends on from where the filling electron originated from. This is illustrated in Figure 2.2. Similarly, there are also characteristic lines when a hole in another shell, e.g., in the L shell, is filled from a higher shell.

As an example, Figure 2.3 shows a simulated X-ray spectrum where tungsten is used as the target anode material. The continuous bremsstrahlung spectrum and the sharp characteristic peaks are clearly visible. It is important to note that the radiation from the characteristic X-ray emission is localized in very sharp peaks but contributes only a single digit percentage to the total flux. In this simulation, an acceleration voltage of 80 kVp has been applied, consequently the bremsstrahlung stops at 80 keV. The simulation also included a 3 mm thick aluminum filter

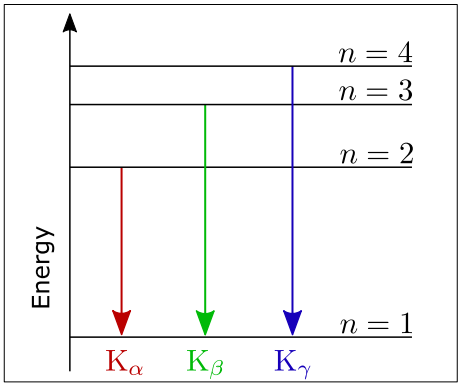

Figure 2.2: Transitions generating the characteristic X-ray lines in a spectrum. A hole in the inner shell, here the K shell, is filled by an electron from a higher shell. The energy difference is then emitted as a photon as a characteristic emission.

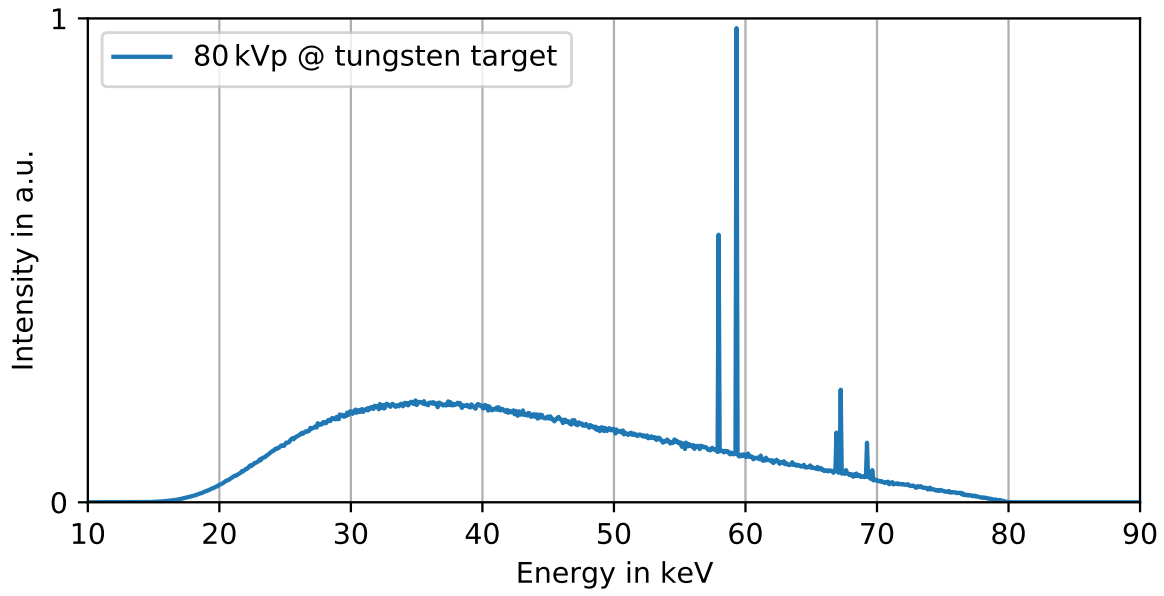

Figure 2.3: Spectrum of an X-ray tube with tungsten anode. The continuous bremsstrahlung spectrum is superimposed with sharp characteristic emission lines. This spectrum is filtered with 3 mm aluminum to remove the low energies. The data has been simulated with Penelope [104].

representing the X-ray tube exit port and common pre-filtering for clinical imaging. Such a filtration is very common in clinical application to optimize the wide poly-chromatic spectrum and narrow its band-with by removing low-energy photons. These soft X-rays are not useful for imaging purposes as they are too easily absorbed.
While this X-ray generation process is the most common approach, it is rather inefficient. Most of the energy put into acceleration of the electrons goes directly to heat and only about 1% is actually converted to X-ray radiation. Unfortunately, the X-ray emission from the electron bombardment is almost uniform in all directions. There is no focusing possible as there are no suitable mirrors or lenses for photons in the X-ray energy range. Consequently, only a small fraction of the generated X-ray radiation can leave the X-ray tube through the exit port. The rest of the radiation is lost as it is absorbed in the shielding which surrounds the entire X-ray tube. Depending on the exit port size this reduces the X-ray photon yield to about 0.03% of the invested energy [10].
For applications where a high X-ray flux is required the thermal conduction of the target material alone is then no longer sufficient. It cannot distribute the heat load fast enough and eventually the target material would melt at the focal spot. A solution is the concept of a rotating anode, which is illustrated in Figure 2.1. The electrons are accelerated onto a stationary focal spot on the target surface while the anode rotates continuously. This leads to a stable X-ray production at high X-ray flux and distributes the heat over the entire target. The available heat capacity of the target is better utilized and allows exposures at extremely increased X-ray flux. The drawback is, however, that a sophisticated construction and cooling process is required to remove the thermal energy from the rotating target.
More information on X-ray tubes, particularly in the scope of medical imaging, can be found in the book by Behling [10]. For simulations of X-ray tube spectra the software PENELOPE [104] has been used, e.g., in Figure 2.3. To avoid the rather time-consuming simulation process a convenient alternative is to use pre-generated clinical spectra as provided by [52], [63], [64].

2.2 X-ray Interaction with Matter

A fundamental characteristic why X-rays are regularly used for imaging purposes is their unique interaction with otherwise optically dense objects. In [2] a comprehensive discussion of X-ray related topics can be found. Here, only a brief introduction summarizes the most relevant points for this thesis.
Since X-rays are electromagnetic waves like visible light, but in another energy range, they underlie the same interaction processes. The energy range of X-ray photons is between five and several hundred keV which corresponds to wavelengths around 0.1 Å to 10 Å. Since low energy X-ray photons are easily absorbed, e.g., by air, hard X-rays, which means photons with more than 10 keV, are required for medical imaging [5]. Those high-energy photons have a sufficient penetration depth to be utilized in medical imaging and still provide enough contrast by the material dependent interaction processes.

2.2.1 Free Space Propagation

In the absence of matter an electromagnetic wave can be described as oscillating electric and magnetic fields which propagate through space. According to Maxwell's equations the components of the electric and magnetic field are decoupled and a monochromatic and linearly polarized wave is described by,

$$\Psi(\boldsymbol{x}, t) = E_0 \, e^{i(\boldsymbol{k}\boldsymbol{x} - \omega t)} \, , \tag{2.1}$$

where E_0 is the electric field amplitude. The propagation in space and time is handled in the exponent by $\boldsymbol{x}$ and t denoting the position and time, respectively. The wave vector $\boldsymbol{k}$ points along the direction of the propagation and includes the wavelength λ of the wave by,

$$|\boldsymbol{k}| = k = \frac{\omega}{c} = \frac{2\pi}{\lambda} \, , \tag{2.2}$$

with c being the speed of light. Alternatively, the oscillation frequency of the wave, represented by ω, can also be derived from the quantum-mechanical particle energy of the photon represented by the wave,

$$E = \hbar\omega \, , \tag{2.3}$$

with $\hbar = h/2\pi$ and h being the Plank constant ($h \approx 4.135667 \cdot 10^{-15}\,\mathrm{eV\,s}$).
As a simplification, we can write for a monochromatic plane wave propagating along the z-axis and extending along the x-axis,

$$\Psi(x, z) = E(x) \, e^{ikz} \, , \tag{2.4}$$

which is sufficient for the simulations in this thesis and the following description of the Fresnel propagation.
When such a wave front propagates along the z-axis within the near-field regime, i.e., the Fresnel regime, the wave front can be described by the Huygens-Fresnel principle. It states that at any moment the wave front can be described by a sum of spherical waves originating from the previous wave front. This can be used to propagate a known wave front $\Psi(x, z = 0)$ by a propagation distance Δ to its new state as $\Psi(x, z = \Delta)$. This is done by integrating the contributions of all spherical waves which originated from the wave front $\Psi(x, z = 0)$, i.e., along the x-axis. This is known as the Fresnel diffraction integral,

$$\Psi(x, z = \Delta) = \frac{e^{ikz}}{i\lambda z} \int \Psi(x_0, z_0 = 0) \, e^{\frac{ik}{2z}(x - x_0)^2} \mathrm{d}x_0 \, , \tag{2.5}$$

where the integral covers all positions along the x-axis in the starting position of the wave front, i.e., here at $z = 0$. This propagation step can also be interpreted as a convolution between the original wave front $\Psi(x, z = 0)$ and the Fresnel propagator,

$$P(x, z = \Delta) = \frac{e^{ikz}}{i\lambda z}\, e^{\frac{ik}{2z}x^2} \ . \tag{2.6}$$

Together with the convolution theorem,

$$\mathcal{F}\big\{f(a,b) * g(a,b)\big\} = \mathcal{F}\left\{f(a,b)\right\} \cdot \mathcal{F}\left\{g(a,b)\right\} \ , \tag{2.7}$$

the convolution between $\Psi(x, z = 0)$ and $P(x, z = \Delta)$ can be vastly simplified. It says that the propagated wave front can be calculated by multiplying the two functions in the Fourier space. Consequently,

$$\Psi(x, z = \Delta) = \mathcal{F}^{-1}\big\{\mathcal{F}\left\{\Psi(x, z = 0)\right\} \cdot \mathcal{F}\left\{P(x, z = \Delta)\right\}\big\} \ , \tag{2.8}$$

where $\mathcal{F}$ and $\mathcal{F}^{-1}$ represent the Fourier transform and its inverse, respectively. A comprehensive description of the Fresnel propagation and Fresnel propagator function can be found in [88][Chapter 1.4].

2.2.2 Complex Index of Refraction

In presence of matter the electromagnetic wave undergoes changes depending on the material properties described by the complex refractive index:

$$n = 1 - \delta + i\beta \ , \tag{2.9}$$

with δ and β representing phase-shifting and attenuating effects of the interaction. For a plane wave, the interaction with matter can be described as,

$$\Psi_{\text{interact}}(z, t) = E_0\, e^{i(nkz - \omega t)} = E_0\, e^{i(kz - \omega t)}\, e^{-k\beta z}\, e^{-ik\delta z} \ . \tag{2.10}$$

After the separation of the exponents we can identify two changes to the unperturbed free wave propagation. The amplitude becomes reduced by an exponential decay with $-k\beta z$ and the wave is shifted in phase with $k\delta z$. Consequently, the index of refraction contains information on the attenuation and in-elastic scattering processes in β. The refraction of the radiation is described by δ.
For X-rays, the refractive index n is close to 1 with δ in the order 10^{-5} and β is usually even smaller [2, p. 23]. The refractive index parameters δ and β can be directly related to the scattering processes based on the forward atomic scattering factor $f^0 = f_1^0 + if_2^0$,

$$\delta(E) = \frac{n_a r_e \lambda^2}{2\pi} \cdot f_1^0(E) \ , \tag{2.11}$$

$$\beta(E) = \frac{n_a r_e \lambda^2}{2\pi} \cdot f_2^0(E) \ . \tag{2.12}$$

Here, $r_e = e^2/(4\pi\epsilon_0 m_e c^2) \approx 2.82\,\text{fm}$ is the classical electron radius, $\lambda(E) = \frac{hc}{E}$ is the incident radiation wavelength, and n_a is the atomic number density. In [19] a comprehensive database for $f^0(E, Z)$ can be found and for simulation software integration a library is available [110].
Examples for attenuation and refraction are illustrated in Figure 2.4. There the interaction process of the plane wave with a purely attenuating and a purely phase-shifting material is shown.

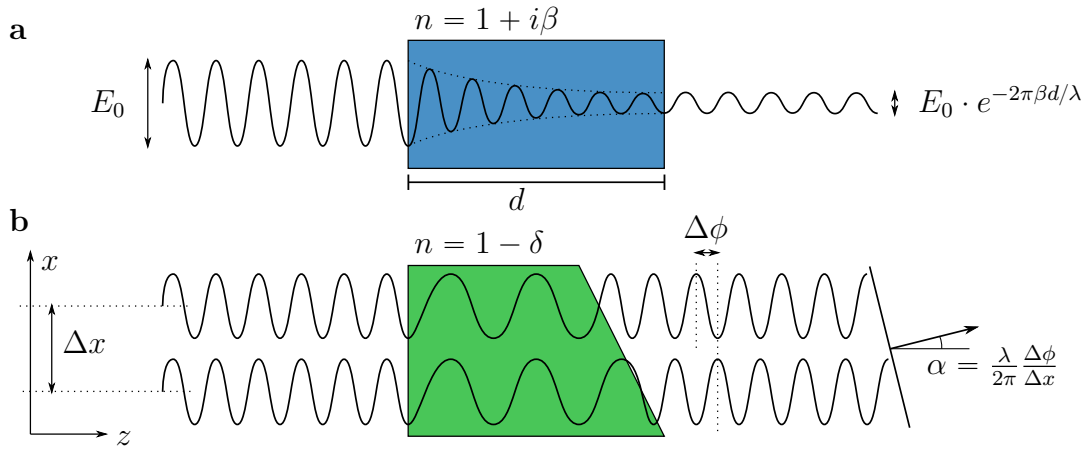

Figure 2.4: Illustration of the effects caused by the transmission and refraction of electromagnetic radiation in matter. **a,** Attenuation of the wave caused by the imaginary part of the refractive index β and no phase-shift is involved. **b,** As the real part δ causes a longer wave length within the matter ($\mathrm{Re}(n) < 1$ for X-rays) refraction occurs. Due to the wedge-shaped sample this leads to a phase-shift and refraction by the angle α.

Refraction and phase-shift The phase-shift caused by the material interaction over the distance d along the beam axis z is

$$\Delta\phi = k \int_0^d \delta(z)\mathrm{d}z = k\delta d = \frac{2\pi}{\lambda} \cdot \delta d \,. \tag{2.13}$$

This shift causes a refraction of the wave front, i.e., a change of direction, at edges or areas where the sample thickness changes.
The refraction angle indicated as α in Figure 2.4b can be calculated from ray optics to

$$\tan(\alpha) \approx \alpha = \frac{\lambda}{2\pi}\frac{\partial\phi}{\partial x} \,, \tag{2.14}$$

with x being the direction of refraction perpendicular to the propagation axis [8].
As previously mentioned, δ is in the magnitude of 10^{-5} for X-rays. Consequently, typical refraction angles are in the nanoradian range and allows the use of the small angle approximation in Equation (2.14).

Attenuation In Equation (2.10) an exponential decay of the wave front amplitude was found. In Figure 2.4a this effect is illustrated and with,

$$I(z) = |\Psi(z)|^2 = \Psi_0^2 \cdot e^{-4\pi\beta z/\lambda} \,, \tag{2.15}$$

the intensity behind the object can be calculated. For an unperturbed wave, i.e., without any sample, the intensity simplifies to $I(z) = I(z = 0) = \Psi_0^2 = I_0$, consequently we can write,

$$I(z) = I_0 \cdot e^{-4\pi\beta z/\lambda} \,, \tag{2.16}$$

which can be reshaped introducing the *linear attenuation coefficient* $\mu = 4\pi\beta/\lambda$ to,

$$I(z) = I_0 \cdot e^{-\mu z} \,. \tag{2.17}$$

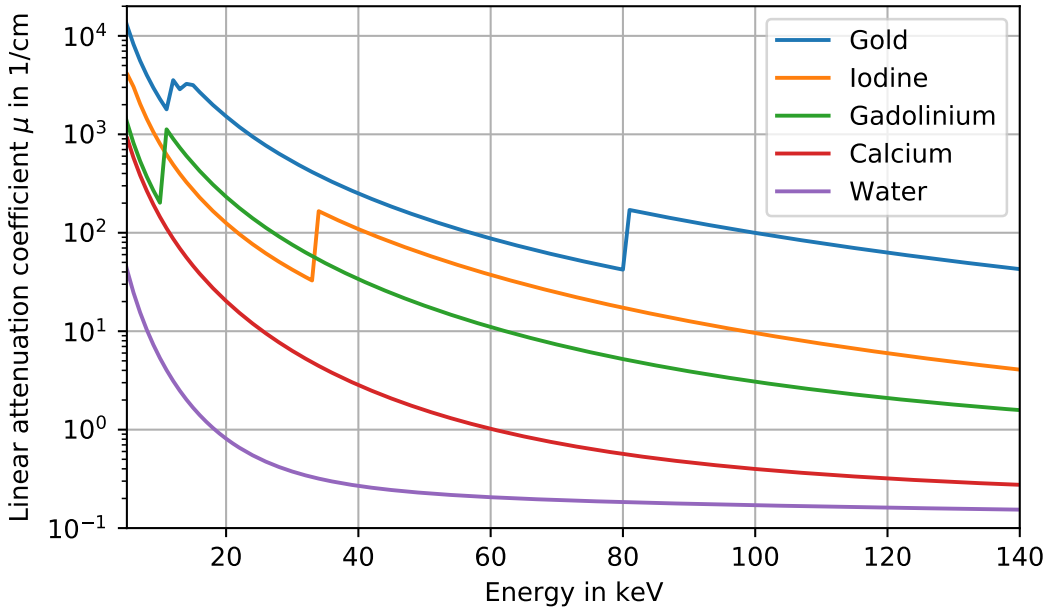

Figure 2.5: Linear attenuation coefficient for various materials. The attenuation generally decreases towards higher photon energies and lower Z materials. From the characteristic shell structures of the materials different absorption edges can be seen, e.g., for gold and iodine. This plot has been generated based on the xraylib database [110].

This coefficient μ is used in most X-ray imaging applications and mostly is sufficient because the different attenuation processes cannot be differentiated. It summarizes the various processes which lead to intensity losses:

$$\mu = \mu_{\text{photo}} + \mu_{\text{elastic}} + \mu_{\text{inelastic}} \tag{2.18}$$

It is important to note that the linear attenuation coefficient is energy-dependent, as can be seen in Equations (2.11) and (2.12). In Figure 2.5, this energy dependence is illustrated for different materials. The characteristic edges here arise from the shell structure of the atoms where the photoelectric absorption rapidly increases.

2.2.3 Photoelectric Absorption

In this process, a bound electron of the material interacts with an incoming X-ray photon. The photon is absorbed, and its energy is transferred to the bound electron. This added energy allows the electron to overcome the binding energy and leads to ionization of the atom. Another path would be an atomic transition to a higher shell (atomic excitation) which is rather rare when working with X-ray energies. The remaining energy goes into kinetic energy of the photoelectron and the ionized atom. The vacancy left behind by the electron is filled by an electron from an outer shell. Characteristic X-ray fluorescence radiation or an Auger electron can be emitted when the electron vacancy is filled.
Since only electrons on shells with lower binding energy than the incoming photon energy contribute to photoelectric absorption, characteristic edges occur which can be seen in Figure 2.5. If the photon energy exceeds the binding energy of the innermost electrons, the majority of photoelectric absorption occurs at the K-shell electrons [99, p. 337].

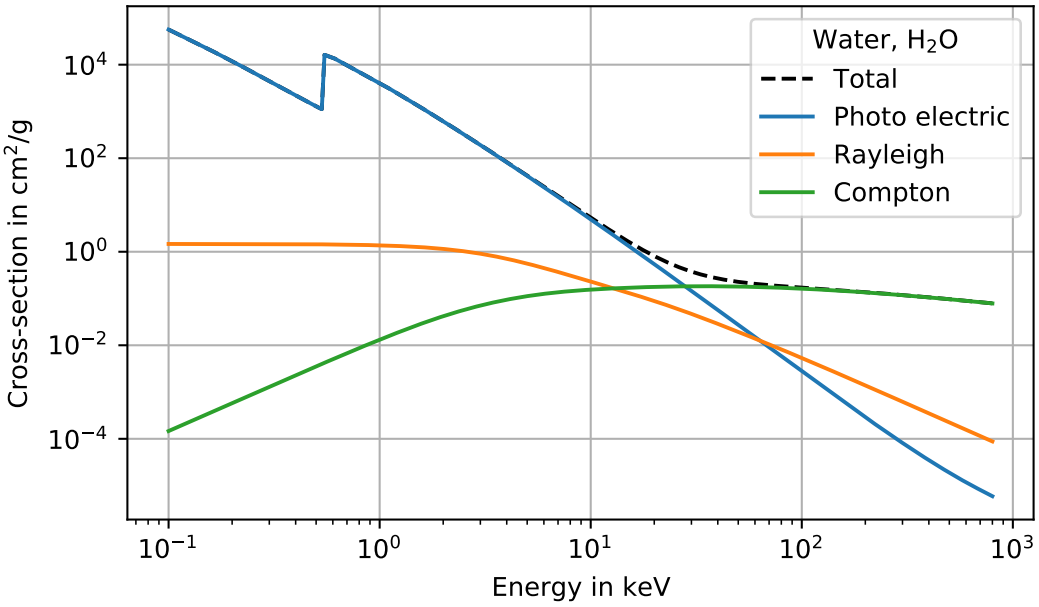

Figure 2.6: Cross-section of the different interaction coefficients for water. Photoelectric absorption dominates in the low-energy regime. For higher energies above 30 keV Compton scattering dominates. This plot has been generated based on the xraylib database [110].

As an approximation, the photoelectric absorption cross-section is,

$$\sigma_{\text{ph}} \propto E^{-3} Z^4 \,, \tag{2.19}$$

with photon energy E and atomic number Z of the interaction material [2, p. 23]. However, this approximation should exclusively be used for light elements and not around electronic transitions.

2.2.4 Compton Scattering

This process is an incoherent scattering process where, in the particle model, a photon interacts with a weakly bound electron, i.e., outer shell electron. A small portion of energy is transferred to the electron as kinetic energy to eject the electron from the atom. Consequently, the photon has less energy after the interaction, which means the outgoing wave has a longer wavelength. The energy of the X-ray photon after the interaction can be derived from conservation of momentum and energy as,

$$E_{\text{out}}(E_{\text{in}}, \theta) = \frac{E_{\text{in}}}{1 - \frac{E_{\text{in}}}{m_{\text{e}} c^2}(1 - \cos(\theta))} \,. \tag{2.20}$$

Here, θ is the scattering angle of the photon and m_{e} is the rest mass of the electron [99, p. 303]. An approximation of this process has been derived by Klein and Nishina [65] for a free electron interacting with the photon. In Figure 2.7 the angular dependence of the total Compton scattering cross-section and the Klein-Nishina approximation are shown. While the Klein-Nishina overestimates the scattering cross-section in forward direction it works well for larger scattering angles. For heavier atoms the assumption of interaction with free electrons no longer holds because the inner shell electrons are more tightly bound. Then correction terms must be included to improve the Klein-Nishina approximation.

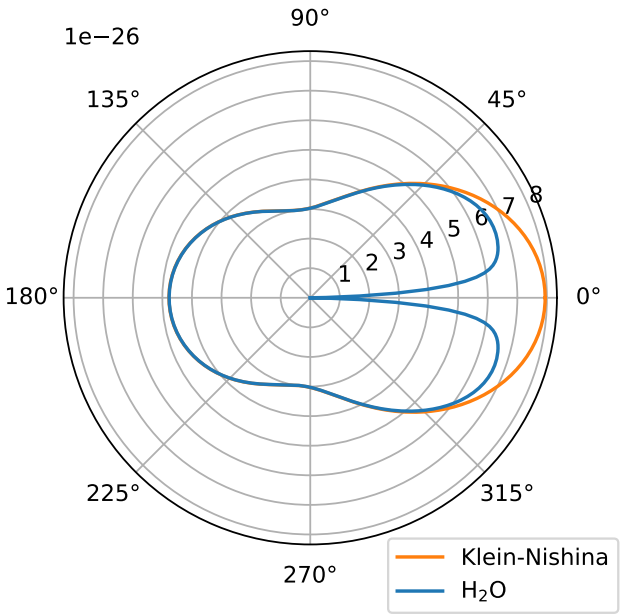

Figure 2.7: Compton scattering cross-section for a water molecule at a photon energy of 80 keV. The photon arrives from 180° and is emitted under an angle $\neq 0$ since there is no forward Compton scattering. The Klein-Nishina approximation works well for most directions, however, overestimates scattering in forward direction. The cross-section is given in cm^2 / electron / steradiant. This plot has been generated based on the xraylib database [110].

As can be seen in Figure 2.6, Compton scattering of X-rays with water becomes the dominant interaction process for energies above around 30 keV. For clinical X-ray imaging, where usually higher energies are used, this means that most of the image contrast is generated by Compton scattering. Since the energy transfer from the photon to the electron is rather small, the photon can still reach the detector, however, on the wrong pixel. Therefore, Compton scattering must be carefully considered in X-ray imaging machines as it can lead to blurred images.

2.2.5 Rayleigh Scattering

In an elastic scattering process the photon interacts either with bound electrons and is then called Rayleigh scattering or with free electrons, referred to as Thompson scattering. In the particle model, the interaction can be described by an induced oscillation of a charged particle by an incident photon. This oscillation then leads to an emission of a new particle with same energy and usually very similar direction. The energy transfer, e.g., to the electron, is comparably small and can be neglected. This also means, that via this process no ionization can take place since the electron does not gain energy to overcome the binding energy.
In Figure 2.8, the Rayleigh scattering cross-section is plotted for two different photon energies at a water molecule. Clearly a preference in forward direction can be seen and that lower energies tend to larger scattering angles.
The frequency of the electromagnetic wave of the scattering photon is much larger than the resonance frequency of the electron. As a consequence, the induced oscillation of the electron is not in phase with the incoming wave but shifted by 180°. When this is true for all electrons in the vicinity this means that the emitted waves from several electrons are coherent and can lead to interference of the scattered waves. This works best in the forward direction because for large scattering angles the individual scattering contributions interfere destructively.
In comparison to the other interaction processes the contribution of Rayleigh scattering to the total absorption cross-section is rather small. An example for water was previously presented in Figure 2.6. Each scattering event is strongly forward directed, hence, only little radiation is lost due to Rayleigh scattering. Further information on this topic can be found, e.g., in [48, Chapter 4.2].

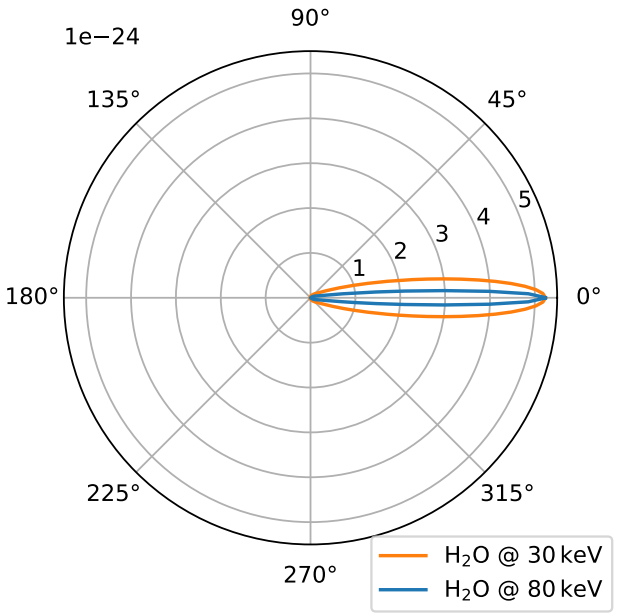

Figure 2.8: Rayleigh scattering cross-section for a water molecule at a photon energy of 30 and 80 keV. The incident photon arrives from 180° and is emitted mostly in forward direction. The cross-section is given in cm^2 / electron / steradiant. This plot has been generated based on the xraylib database [110].

2.3 Talbot-Lau Interferometer

As previously discussed the X-ray radiation undergoes several interactions when it passes matter and these can be used for imaging purposes. Naturally, attenuation effects, i.e., caused by photoelectric absorption, can easily be retrieved. This is done by measuring the intensity decrease in the transmitted wave in relation to a wave without a sample. The refraction or phase-shift of X-rays, however, cannot be measured directly and requires more sophisticated optical methods to retrieve it.
There are several methods which can directly resolve the phase-shift induced by the sample. Some examples are crystal-based X-ray interferometers [80], propagation-based phase-contrast [117], [21], [88], or speckle-based imaging [82], [18], [12], [141], [159]. These approaches require coherent X-rays and are therefore restricted to synchrotron facilities or special X-ray sources with sufficient coherence. Being limited to synchrotron X-ray sources also means that the maximum field of view is restricted to the available beam width. Consequently, the field of view is usually rather small and mostly samples are examined. While these methods are very sensitive and demonstrated well that phase-contrast can enhance X-ray imaging, they are impractical for most laboratory or clinical implementations.
An alternative approach is grating-based phase-contrast imaging which makes use of the slight change of direction induced by the refraction of the beam. While it initially was only available at synchrotron facilities it was successfully translated to conventional X-ray sources with low brilliance [94]. Consequently, this technique gained much attention during the last decade and has been significantly optimized [68], [93], [7], [79], [90], [102], [81]. It's compatibility with conventional X-ray sources allows phase-sensitive X-ray imaging for laboratory, industrial, and clinical implementations. In the following paragraphs the working principle and fundamental signal extraction of Talbot-Lau interferometry is presented.

2.3.1 Working Principle of Grating-Based Phase-Contrast

The fundamental idea is to retrieve the phase-shift from the refraction angle induced by the interaction with the sample. The angle, i.e., illustrated in Figure 2.4, which must be retrieved

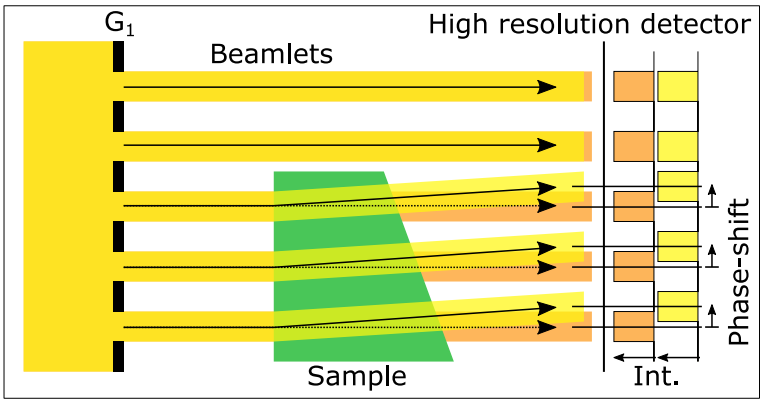

Figure 2.9: Resolving refraction with fine beamlets produced by a G_1. The incoming beam is converted to a fine pattern which is transmitted through the sample. Refraction distorts the pattern (yellow) and can be resolved by tracking the drifts of the individual beamlets on the detector. Reference beam path without sample is shown in orange.

lies in the micro to nanoradian range which makes this approach non-trivial.
For simplicity only refraction in one direction is considered, i.e., in Figure 2.4 only refraction along the x-axis but no refraction along the y-axis. This description matches most experimental implementations of grating-based imaging setups, but extensions of the sensitivity to two dimensions is possible as demonstrated in [14] or [39].
Instead of a homogeneous X-ray beam in grating-based phase-contrast imaging a structured beam is used. In Figure 2.9 a simplified sketch with only one grating illustrates the concept. An optical grating, called G_1, is placed in the beam path. It converts the homogeneous beam into a number of very fine parallel beams, referred to as beamlets. For now, in this discussion no interference effects between the individual slits is considered, which applies for coarse grating periods. These beamlets then pass the sample and interact with it individually. Attenuation in the sample obviously reduces the intensity, whereas a phase-shift induced by the sample leads to a small change of the propagation direction. Consequently, the beamlet hits the image plane not at the original position, but at a slightly shifted position. This spatial-shift is directly proportional to the phase-shift and can be measured with high resolution X-ray detectors.
The displacement of the beamlets is usually not more than a couple of micrometers but nevertheless the displacement can be directly retrieved with high-resolution cameras [145]. This comes at the typical cost for high-resolution measurements: Low availability of suitable detectors, small field of view, low count rate and efficiency, and not being compatible with hard X-rays. Since more common X-ray detectors have pixel sizes of 50 µm to 1.2 mm such a direct retrieval of the displacement is impractical. Therefore, a concept is required which is decoupled from the physical pixel size of the detector.
The solution is the introduction of an analyzer grating, referred to as G_2. It allows measuring the mean phase-shift of all beamlets which reach the same detector pixel. G_2 is positioned in front of the detector and has the same periodicity as the beamlet pattern. Consequently, depending on the detector pixel size and the G_2 period a couple or several hundred beamlets are averaged to one intensity measurement by the detector pixel.
The introduction of the analyzer grating also requires an adapted acquisition method. Instead of a single intensity measurement a phase-stepping or phase scanning must be performed. Thereby G_2 is moved perpendicular to its grating lines in multiple steps over the distance of one period. At each position, the intensity reaching the detector is measured. In theory (i.e., given a parallel X-ray beam and perfectly shaped gratings) this stepping-curve is a triangular intensity variation. Its maximum is at the G_2 position for which the grating gaps are aligned to the beamlet pattern, as in this configuration all the intensity reaches the detector. An example of obtaining a stepping-curve is illustrated in Figure 2.10. The two beamlets reaching pixel 1 are not refracted by the sample, consequently, the stepping curve is unchanged. If a phase-

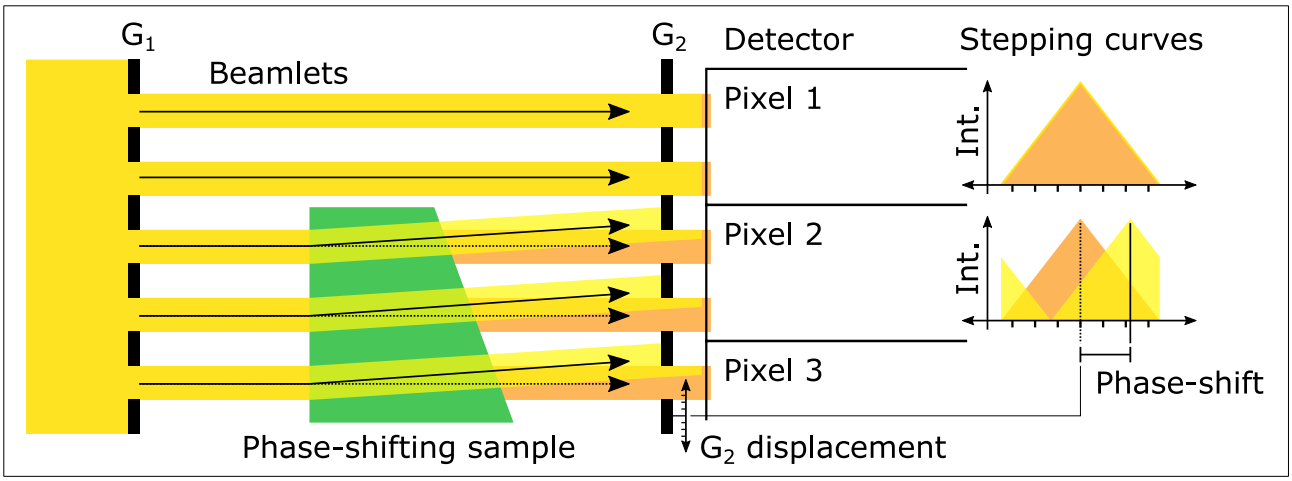

Figure 2.10: Resolving the phase-shift with stepping curves. G_2 is stepped over one grating period and several intensity measurements are preformed. This leads to one stepping curve for each pixel which plot the intensity falling through the G_2 slits onto the detector against the G_2 displacement. If the sample refracts the radiation the beamlets are slightly shifted and cause a shift of the measured stepping curve. Otherwise, the stepping curve remains unchanged. This concept allows the use of large detector pixels which average multiple beamlets to one stepping curve and can still retrieve the sub resolution shifts. Reference beam path without sample is shown in orange.

shifting sample is in the beam path, as for pixel 2, the beamlets are refracted and reach the G_2 plane at a slightly deflected position. The stepping-curve retrieves this as a shift relative to the previously acquired reference stepping-curve, i.e., sample free stepping-curve.
Obviously, this only works for samples which are homogeneous within the area of each detector pixel and refract all beamlets of the detector pixel identically. If the sample is not homogeneous over one pixel some beamlets are shifted more than others. Since only the mean phase-shift is retrieved the variance of the beamlet displacement leads to a change in contrast of the stepping curve. Consequently, not only the phase-shift but also the homogeneity or in-homogeneity of the sample can be retrieved. This is referred to as the dark-field or small-angle scattering

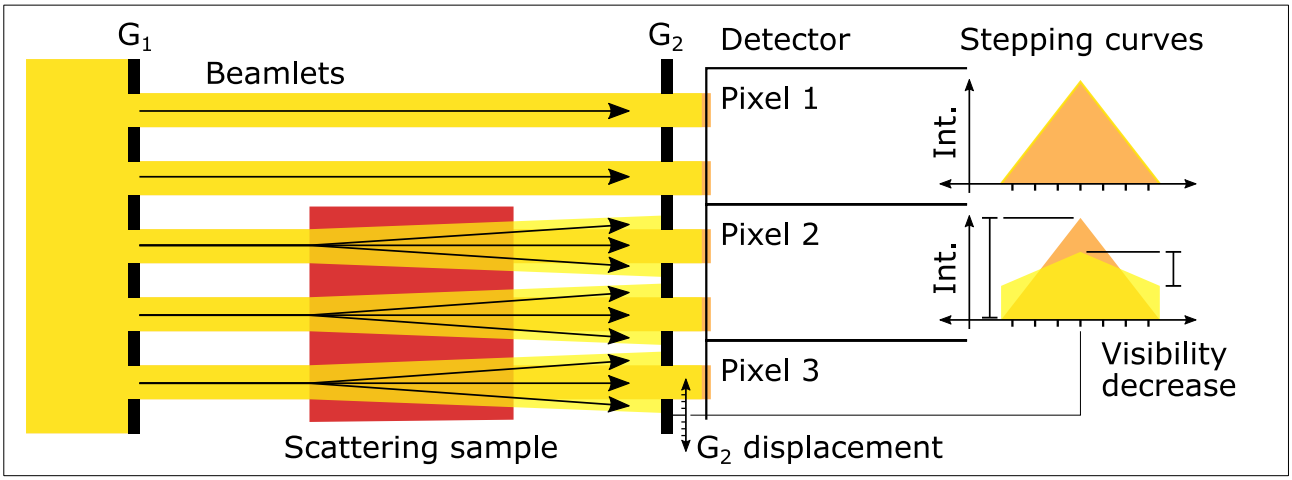

Figure 2.11: Resolving small-angle scattering with grating-based imaging. The beamlets are widened by the interaction with the sample and consequently the shape of the measured stepping curve is changed characteristically. From the loss of visibility between reference and sample scan the scattering power or dark-field signal can be derived.

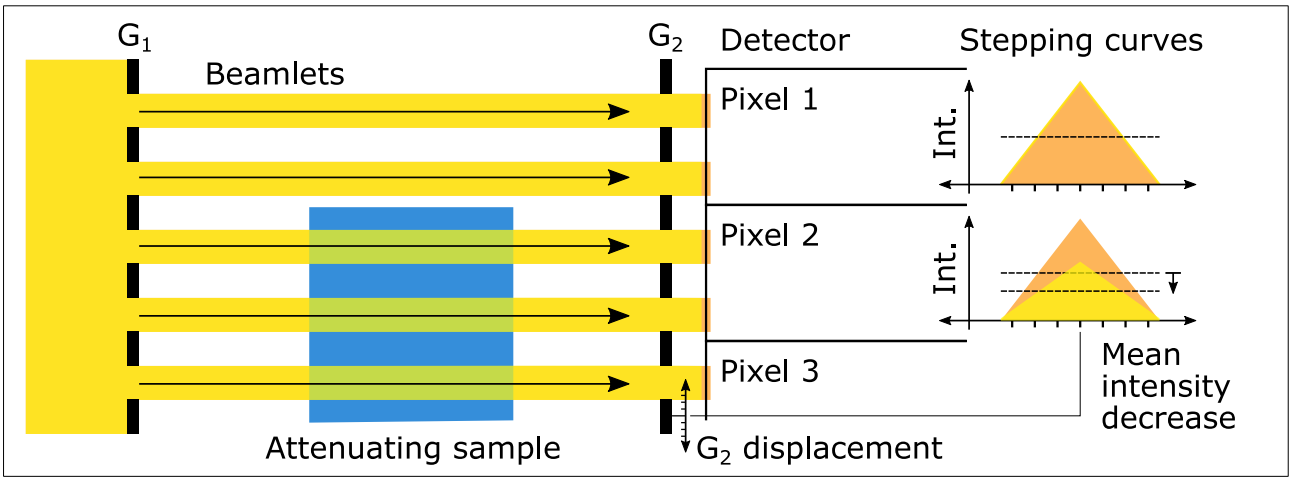

Figure 2.12: Resolving attenuation in grating-based imaging. This remains unaffected by the additional setup components and The beamlets are widened by the interaction with the sample and consequently the shape of the measured stepping curve is changed characteristically. From the loss of visibility between reference and sample scan the scattering power or dark-field signal can be derived.

signal. It is a valuable measure because it allows to resolve sample structures which are below the physical resolution of the detector by their scattering-power. This effect is illustrated in Figure 2.11 for a purely small-angle scattering sample.
Besides refraction and small-angle scattering, the attenuation in the sample can still be measured in a grating-based imaging setup. This is achieved by evaluating the mean intensity of the obtained stepping curves of each pixel. From its change between sample and reference measurement the sample's attenuation along the beam path can be derived as in conventional attenuation imaging. This is illustrated in Figure 2.12 for a purely attenuating sample.
Certainly, most objects induce multiple of these image-contrasts simultaneously as they attenuate, phase-shift, and perhaps also induce small-angle scatter. Since the distortions and changes to the stepping curve, however, are unique for each of the interaction effects they can be separated by analyzing the stepping curve. This decomposition of the stepping curve into the three contrast channels will be introduced in Section 2.3.4.

2.3.2 Designs and Effects

To resolve the small refraction of the radiation fine grating periods are required. The previous discussion and examples in Figures 2.9, 2.10, and 2.11, however, rely on gratings which produce perfectly sharp beamlets. With fine grating periods interference effects between the radiation from the individual grating slits arise and must be considered in the design. These interference can be exploited, e.g., as the Talbot effect. Furthermore, also the Lau effect which introduces an additional G_0 grating can be included. Discussion of these effects requires dropping the simplification of beamlets generating a simple binary intensity pattern in the G_2 plane. This allows us to now also include wavefront patterns which are generated based on interferometric effects alone. These patterns are equivalent to the pattern generated by the beamlets in the simplified model, but their formation might not be based purely on geometric relations. In the following sections different approaches are discussed how these fine *fringe patterns* can be generated in the G_2 plane.

Talbot Effect

The most important effect used in grating-based phase-contrast imaging systems is the Talbot effect. It requires coherent radiation and is based on interference effects behind a grating which structures to the incoming wavefront. The Talbot effect describes the phenomenon that this periodic pattern, here induced by G_1, reappears after certain distances as a so-called self-image. The periodic pattern can be in-printed into the beam either by attenuation or alternatively by a phase-shift. Here a brief description of the Talbot effect is presented, a comprehensive study of the Talbot effect can be found, e.g., in Paganin [88].
In Figure 2.13 the propagation of a monochromatic plane-wave through different phase-shifting gratings is illustrated. The phase-shifts are induced by a specific grating thickness which induces the desired phase-shift for the design energy of the system, e.g., a $\pi/2$ or a π phase-shift. As the structured wave-front propagates away from G_1 characteristic intensity variations are formed and after each integer multiple of the Talbot distance,

$$d_{\mathrm{T}} = \frac{2p_1^2}{\lambda} \,, \tag{2.21}$$

the original pattern re-occurs.
Of grater interest for grating-based imaging are, however, the fractional Talbot distances $d_{\mathrm{f\Gamma}}$. At these distances distinct periodic patterns of high and low intensity are generated, which can be utilized in imaging setups. In Figure 2.13a, at 1/4 d_{T} a box-like intensity pattern and at 3/4 d_{T} another but inverted one can be found. It is important to note that in this $\pi/2$ phase-shift case the occurring intensity patterns have the same periodicity as the G_1 phase-grating. Contrary, a π phase-shift in G_1 leads to a doubling of the pattern frequency and an entirely different arrangement of the intensity maxima. Such a π phase-shift case is for example shown in Figure 2.13b. Weitkamp et al. [144] conclude on a generalization of the various positions,

$$d_{\mathrm{f\Gamma}} = n\,\frac{2p_1^2}{\lambda} \,, \tag{2.22}$$

where n depends on the induced phase-shift in G_1:

$$n = \begin{cases} m/4 & m \in 2\mathbb{N}+1, \text{ for } \pi/2 \text{ shift grating} \\ m/16 & m \in 2\mathbb{N}+1, \text{ for } \pi \text{ shift grating} \end{cases} \tag{2.23}$$

The Talbot effect approach comes with several advantages. For example, it allows creating fine periodic intensity patterns without significant intensity loss due to attenuation in G_1. Furthermore, a frequency doubling of the pattern as observed for π phase-shifting gratings can be beneficial. It essentially leads to finer beamlets which can resolve finer refraction angles in a Talbot interferometer.
An important requirement for the Talbot effect is, however, sufficient spatial coherence of the X-rays. This is still an issue at laboratory X-ray tubes which produce poly-chromatic radiation from a rather large source spot and can be solved with the Lau effect.

Lau Effect

Similar to source blurring in microscopy an extended X-ray source also blurs the produced interference pattern produced by G_1 as the coherence is lost. By hypothetically reducing the size of the source to a spot the blurring can be eliminated. Since such a point-like source is usually not feasible or practical a compromise between blurring and small source size must be found.

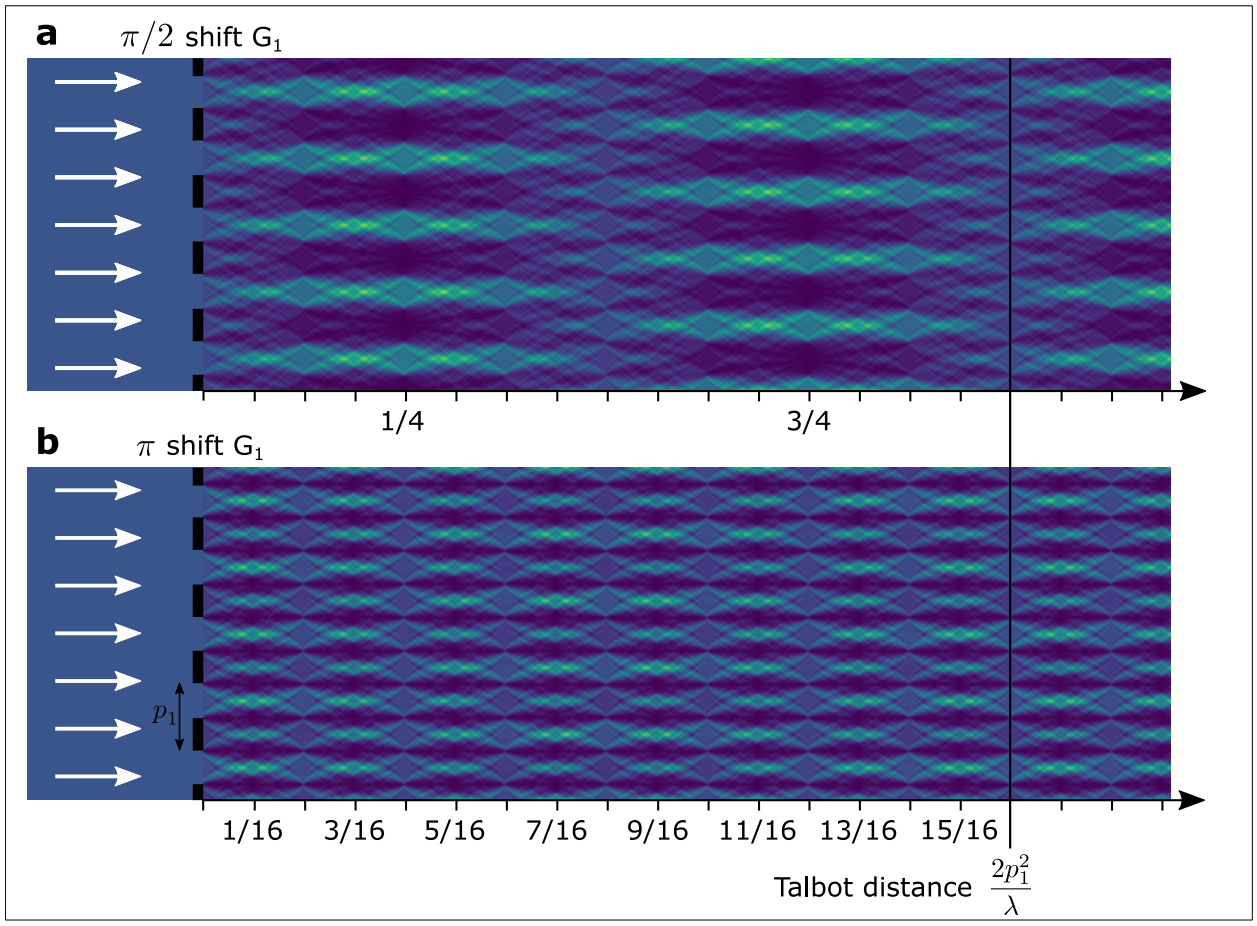

Figure 2.13: Monochromatic plane-wave simulations of the Talbot effect behind a $\pi/2$ and a π phase-shifting grating. The thickness of the gratings must be matched to the energy of the X-rays to precisely shift the phase by a quarter or half a wave-length, respectively. **a,** In a $\pi/2$ design the phase modulation leads to self-images of the G_1 in fractional Talbot distances $m/4, m \in 2\mathbb{N}+1$, with the same period of the G_1. The positions of maximum intensity alternate by half a period between the 1/4 and the 3/4 position. **b,** Behind a π shifting G_1 the induced phase modulation leads to binary intensity patterns in $m/16, m \in 2\mathbb{N}+1$, of the Talbot distance. The pattern is a factor two smaller than the G_1 period and does not alternate.

For a point source, the produced interference pattern would be a box-like intensity pattern. However, for the evaluation illustrated in Figure 2.10 based on an analyzer grating the box-shape is no requirement. It is only important that maxima and minima can be differentiated, and thus, we can allow blurring of the interference pattern as long as this constraint is met. We find that by projecting the feature size into the source plane the maximum allowed source size can be found as,

$$s' = \frac{L}{d}\frac{1}{2}\,p_2\,, \tag{2.24}$$

with L and d denoting the source to G_1 and G_1 to G_2 distance, respectively. Here, the feature size is the slit width of G_2, i.e., half the period of the interference pattern in the G_2 plane ($= 1/2\ p_2$).
There are X-ray source spots which fulfill this requirement as they are smaller than s'. However, most tubes and particularly the ones generating high X-ray flux operate with too large source spots. For those, a collimator slit with width s' would work but comes with the drawback that most of the flux is lost.

An extension uses the Lau effect which achieves a much better flux efficiency than a single collimator slit but still maintains the transverse coherence. Here, many of such collimator slits are positioned next to each other in a way that leads to constructive superposition of the resulting interference patterns in the G_2 plane. Since the aligned slits are essentially another grating which is placed upstream the other two gratings it is referred to as G_0. Similar to the previous equation the Lau effect is based on geometric optics, however, now instead of a single source it defines the period of the slit sources:

$$p_0 = \frac{L}{d}\, p_2 \ , \tag{2.25}$$

with L and d denoting the G_0 to G_1 and G_1 to G_2 distance, respectively.
This G_0 is also referred to as source grating because it creates the coherent X-ray sources required for the interferometer. Similar to G_2 also G_0 is an absorption grating which is designed to either stop the radiation or transmit it unaltered.
Based on these concepts and effects grating-based phase-contrast imaging can be performed at any X-ray source and X-ray detector. In 2006, the introduction of the source grating was a milestone as it unlocked first implementations at conventional X-ray sources [94], [144]. Grating-based imaging setups which are based on these two effects are hence referred to as a *Talbot-Lau interferometers*.

Absorption G_1 and Non-Interferometric Design

The Talbot effect is regularly used in gating-based phase-contrast imaging setups based on phase-shifting gratings as G_1. They are usually advantageous because their fabrication is easy, and they absorb only a small amount of the incident X-ray flux and thus are very efficient. However, the Talbot effect was originally discovered in optical experiments with absorption gratings and such an implementation is also feasible with an X-ray compatible absorption grating as G_1.
Contrary to the phase-shifting G_1 implementations the maximum intensity contrast is in such

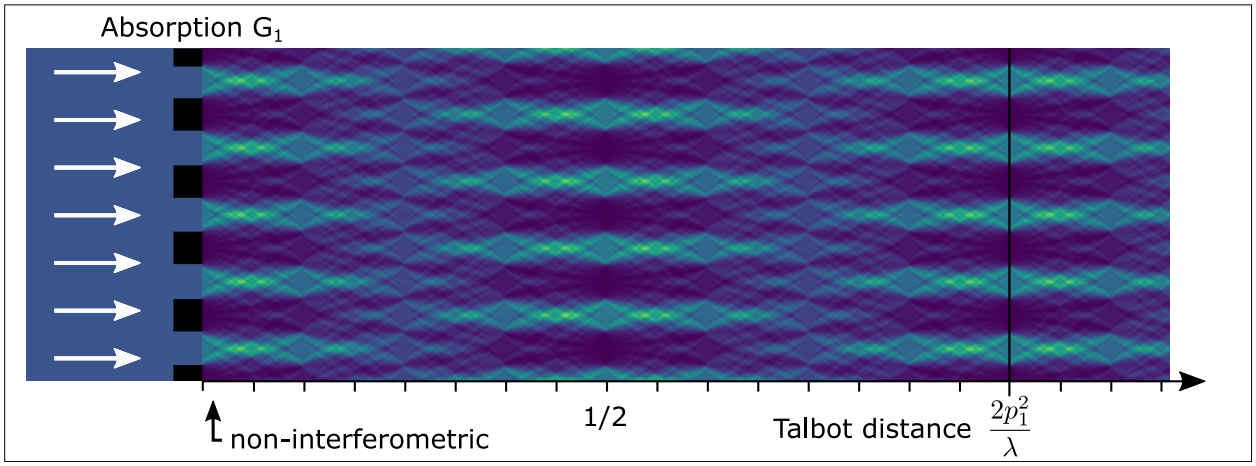

Figure 2.14: Monochromatic plane-wave simulation of a Talbot carpet behind an absorption grating. In odd multiples of 1/2 of the Talbot distances high contrast intensity patterns occur. Directly behind the grating, before any interference with neighboring slits takes place the shadow behind the grating bars dominates the pattern. This region is utilized in non-interferometric grating-based imaging implementations.

an absorption G_1 design found at

$$d_{\mathrm{fT}} = n \, \frac{2p_1^2}{\lambda} \, , \tag{2.26}$$

with,

$$n = m/2 \qquad m \in \mathbb{N}, \text{ for absorption grating} \, . \tag{2.27}$$

An example for a Talbot carpet generated by an absorption grating as G_1 is shown in Figure 2.14. Similar as in the $\pi/2$ phase shift design also in the absorption G_1 design the position of the pattern is shifted by half a period from one occurrence to the next.
Besides this interference-based intensity pattern the absorption G_1 design also provides a strong intensity pattern at extremely short propagation distances. In contrast to phase-shift G_1 based designs, directly behind the absorbing grating bars sharp shadows are cast. This can be observed in Figure 2.14 for propagation distances before $1/16 d_{\mathrm{T}}$. In this region, where not jet any interference between neighboring slits is constructive, the design is dominated by the shadow produced by G_1. There are actually several advantages in this situation, and it is regularly used in experiments where it is referred to as a *non-interferometric* design. These systems work similar to the previously discussed beamlets in Section 2.3.1. They come with the advantage that due to the absence of any interference the wavelength has no impact on the system performance (besides the performance of the absorption gratings, which usually varies with the X-ray energy). Particularly for setup geometries with large G_1 periods and strong divergence this design works well. Such a design has recently been demonstrated by Wu et al. [150].
A special variant of this implementation is referred to as *edge illumination* which projects only one beamlet on each detector pixel [86], [87], [30], [78]. It consequently works with a rather coarse grating and, by design, most of the radiation is stopped by G_1. This is caused by the large duty-cycle of G_1 which can be in the range of 75% depending on the detector pixel size [86]. This makes the method rather flux inefficient if used with the large pixels of standard X-ray detectors. In the edge illumination ecosystem such a G_1 is usually referred to as a set of pre-sample apertures.

Non-Binary Gratings

In the previous discussion only binary structures, as illustrated in Figure 2.15, were considered to produce these patterns. Simulations and experiments, however, showed that other grating profiles can also work well. A study by Yaroshenko et al. [153] evaluated trapezoidal and triangular grating profiles as illustrated in Figure 2.15. The evaluation revealed that such grating profiles for G_1 can shift the peak visibility closer to G_1 than with comparable binary profiles, i.e., requiring shorter propagation distances. These non-binary grating profiles can

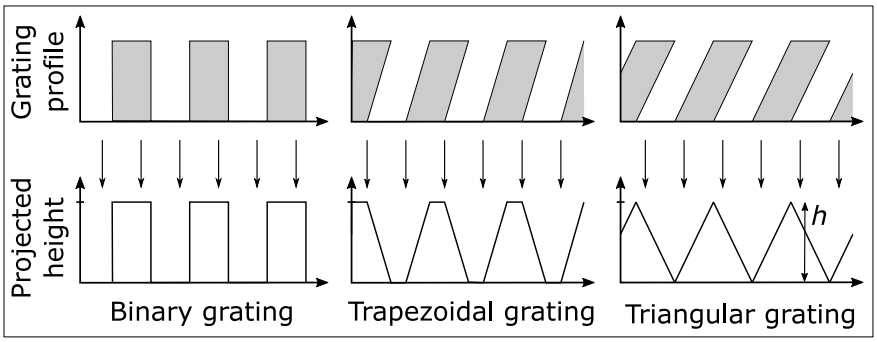

Figure 2.15: Binary and non-binary grating profiles. By fabrication of inclined rectangular profiles trapezoidal and triangular gratings can be produced. Grating heights h are measured from substrate to highest point.

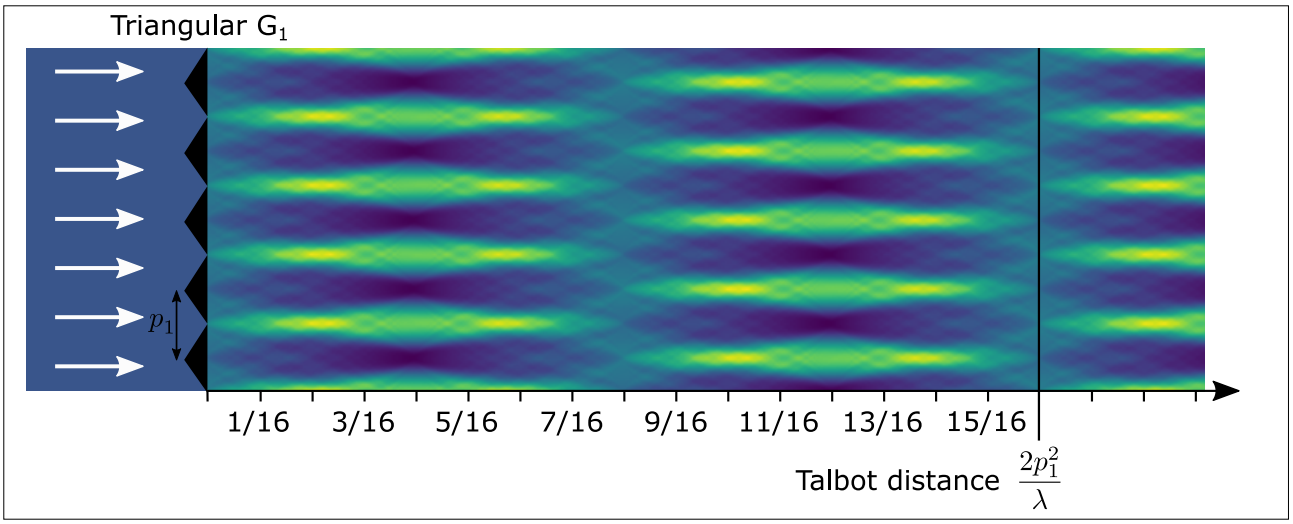

Figure 2.16: Monochromatic plane-wave simulation of a Talbot carpet behind a triangular grating. In odd multiples of 1/2 of the Talbot distances high contrast intensity pattern occur. Directly behind the grating, before any interferences with neighboring slits take place the shadow behind the grating bars dominates the pattern.

therefore be advantageous when working with compact system geometries. Furthermore, there is no frequency doubling as it has been found for π phase-shifting designs with binary grating profiles in Section 2.3.2.
In Figure 2.16, simulation results of a triangular phase grating as G_1 are shown. These demonstrate that the generated Talbot carpet consists of high contrast intensity patterns similar to a $\pi/2$ phase-shifting design. The most dominant contrast maxima are found at,

$$d_{\mathrm{fT}} = n\,\frac{2p_1^2}{\lambda}\,, \tag{2.28}$$

with,

$$n = m/4 \qquad m \in 2\mathbb{N}+1, \text{ for triangular grating}\,. \tag{2.29}$$

Compared to the results for a $\pi/2$ phase-shifting design, these maxima are more focused and extend over a wider range of propagation distances. This can be advantageous for implementations with a poly-chromatic spectrum. There no specific Talbot distances apply but the various contributions from the different wavelengths superimpose. Such spectral power weighted Talbot carpets of designs in a poly-chromatic spectrum will be presented in Figures 5.26 and 5.27.
It is important to note that the patterns behind these triangular or non-binary gratings are generated purely by the phase-shift induced by G_1. Consequently, relatively small grating heights are sufficient as long as they provide the required phase-shift. This is similar as for binary phase-shifting gratings and is advantageous as it simplifies fabrication of the gratings.

2.3.3 Geometric Constraints for Three Grating Interferometers

The previous discussion of the Talbot effect and the simulated Talbot carpets as shown in Figure 2.13 are based on plane waves. At synchrotron facilities the Talbot effect can be demonstrated in this ideal setting without any notable divergence of the beam [20]. At laboratory X-ray tubes, however, the divergence must be considered and can be described by spherical

instead of plane waves. A comprehensive analysis and evaluation of the associated geometrical effects has been published by Donath et al. [27] and is briefly summarized here.
For the following discussion it is important to precisely define what is meant by "source" throughout this section. At micro-focus X-ray tubes the focal spot is the source of the X-rays. At those sources, the small focal spot already achieves the required coherence and no G_0 is needed. For systems with a G_0, however, the created slit sources must be treated as individual source spots of the interferometer. By design, the superposition of all patterns from the individual sources overlap constructively.
Usually, the distance between source, i.e., micro-focus source spot or G_0 position, and G_1 is referred to as L. The distance between G_1 and G_2 is denoted as d and the sum $L + d = T$ gives the total interferometer length T. Obviously, at a setup with three gratings the distance between X-ray tube and X-ray detector must be larger than T.
Due to the divergence of the radiation from the source, i.e., the G_0 slit, the intensity pattern which forms behind the G_1 pattern must be re-scaled. This can be done by applying the Fresnel scaling theorem [88], which is essentially is the geometric projection of the G_1 plane into the G_2 plane. It can be described by the magnification factor M given by,

$$M = \frac{L + d}{L} \,. \tag{2.30}$$

The Talbot effect produces high-contrast intensity patterns at fractional Talbot distances. Depending on the induced phase-shift also causes doubling of the pattern frequency, as discussed in Section 2.3.2, can occur. Combining this with the magnification factor leads us to a definition of the grating period p_2 of G_2, based on the setup geometry and the G_1 period p_1:

$$p_2 = \begin{cases} M\ p_1 & \text{for } \pi/2 \text{ phase-shift } G_1 \text{ and absorption } G_1 \\ \frac{1}{2}\ M\ p_1 & \text{for } \pi \text{ phase-shift } G_1 \end{cases} \tag{2.31}$$

From this equation one can see that for reasonably large L the geometry approaches the plane wave scenario simulated in Figure 2.13.
Based on Equations (2.25) and (2.31) for every geometry defined by L and d the appropriate grating periods can be calculated. There are three categories, following the naming convention proposed by Donath et al. [27]:
In **Symmetric geometry** the inter-grating distances L and d are equal and thus G_0 and G_2 always have the same period. If a π phase-shift G_1 is used all three gratings have the same grating period. In case of a $\pi/2$ phase-shift G_1 the period of G_1 is reduced by a factor of two.
In **Asymmetric geometry** or **Conventional geometry** the G_0 to G_1 distance L is larger than d which is beneficial for imaging large samples at laboratory setups because the distance between sample (which is usually positioned close to G_1) and detector is small which limits magnification of the image.
The **Inverse geometry** is the reversed form of the asymmetric geometry, consequently, $L < d$. This design is suitable for high-resolution experiments which rely on geometric magnification of the sample.
One can summarize that in asymmetric and inverse designs the gratings with the finer periods are grouped closer together. Due to the divergence of the beam G_0 has smaller outer dimensions than G_2. Consequently, the inverse geometry comes with some practical advantages as here the finest grating is also the smallest one and the largest grating has a coarser and thus easier to fabricate period. These aspects will be discussed in more detail in Section 5.4.

2.3.4 Visibility and Conventional Data Model

An important performance measure of Talbot-Lau interferometers is the system visibility. It specifies the maximum interference pattern contrast which can be measured by the detector during a phase-stepping scan. In contrast to the ideal case illustrated in Figure 2.10 and 2.11 the stepping curves at a Talbot-Lau interferometer are not triangular shaped but blurred to a sinusoidal shape due to the extended slit sources of G_0.
In Figure 2.17, a sketch of two stepping curves measured by a detector pixel are shown. It illustrates how the visibility can be retrieved from a stepping curve of a reference scan. The visibility V is defined as,

$$V = \frac{a_1}{a_0} = \frac{I_{\max} - I_{\min}}{I_{\max} + I_{\min}} \,, \tag{2.32}$$

with a_0 and a_1 being the mean and amplitude of the stepping curve, respectively. Alternatively, one can calculate the visibility based on the minimum and maximum intensity measured in the stepping curve.
A model to describe the intensity measured by the detector pixel during a phase-stepping measurement has for example been derived by Bech [8, Chapter 2.4]. The author concludes that in general the measurement is described by,

$$I = \sum_{m=0}^{\infty} a_m \cos\left(\frac{2\pi m x}{p_2} + \Phi_m\right) \,, \tag{2.33}$$

where x is the grating displacement of, e.g., G_2, whose period is denoted by p_2. The parameters a_m and Φ_m describe the amplitude and interferometer phase coefficients of the mth order contributing to the interference pattern.

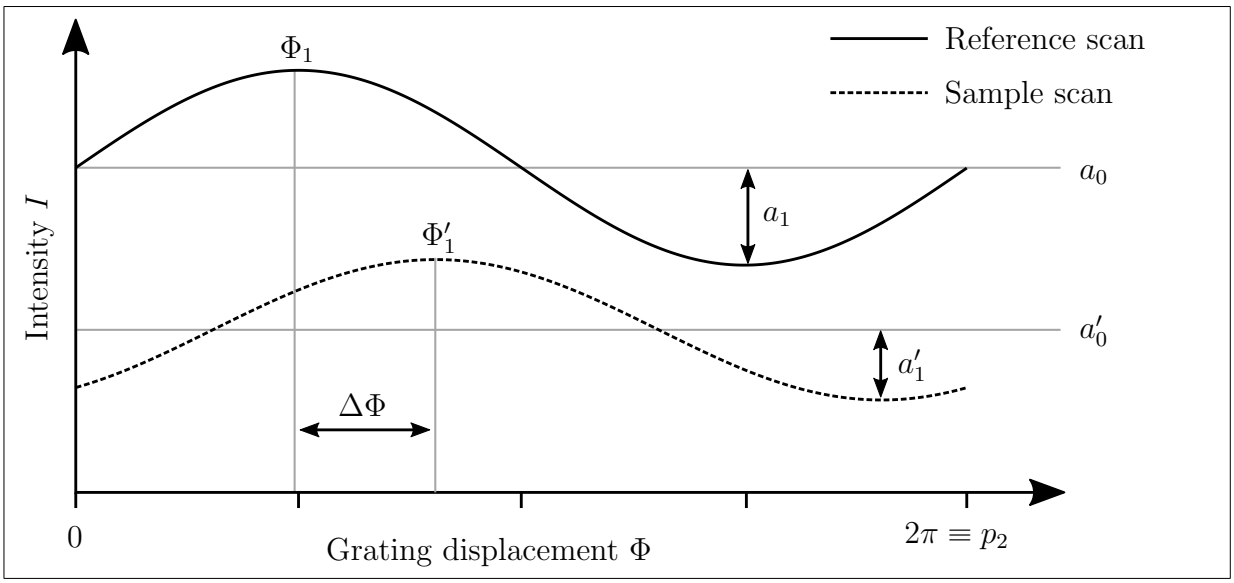

Figure 2.17: Phase-stepping curves of one detector pixel acquired without and with a sample in the beam path. The interferometer visibility is the ratio of curve amplitude to curve mean value in the reference case without any sample. Attenuation, refraction, and small-angle scattering induced by the sample lead to characteristic changes to the curve. As indicated, by calculating the mean signal, extracting the phase-shift of the curve, and estimating the loss in amplitude the sample properties can be retrieved.

In most cases where conventional X-ray tubes are used, i.e., coherence is moderate, radiation is poly-chromatic, and a G_0 is required, the higher orders can be neglected. An in-depth evaluation on this topic can be found in [8] where it is shown that higher orders $m > 1$ can be safely ignored. This reduces the conventional data model for Talbot-Lau interferometry to:

$$y_{\text{conventional}} := a_0 + a_1 \cos\Big(\underbrace{\frac{2\pi x}{p_2}}_{\phi} + \Phi_1 \Big) , \tag{2.34}$$

$$= a_0 \left(1 + V \cos(\phi + \Phi_1)\right) . \tag{2.35}$$

This data model will be used throughout this thesis and is extended in Chapter 7 to cover some special cases. The various coefficients are indicated in Figure 2.17. The interferometer phase ϕ is set by the displacement of a grating, here G_2 is moved, therefore the

$$\phi = 2\pi x / p_2 , \tag{2.36}$$

with G_2 displacement $x \in [0, p_2]$. In general also G_0 or G_1 could be displaced for this purpose. The sample scan is shown as a dashed line and the corresponding variables are marked with a prime.
When a sample is inserted into the beam path the interaction with the material causes attenuation, refraction, and small-angle scattering which leads to characteristic changes of the stepping curve. The attenuation decreases of the mean value of the curve and can be retrieved by,

$$T = \frac{a_0'}{a_0} . \tag{2.37}$$

Here, T denotes the transmission signal behind the sample which ranges from 1 to 0, for no attenuation to total absorption, respectively. The refraction leads to a relative shift of the curve indicated as $\Delta\Phi$,

$$\Delta\Phi = \Phi_1 - \Phi_1' . \tag{2.38}$$

When small-angle scattering occurs in the sample the visibility of the stepping curve gets reduced. This reduction is similar to the transmission signal, and we define the dark-field signal D as,

$$D = \frac{V'}{V} = \frac{a_1'/a_0'}{a_1/a_0} . \tag{2.39}$$

Analogue to the transmission signal the dark-field signal ranges from 1 to 0, for no scattering to strong scattering which eliminates the interferometer visibility, respectively.
Based on the conventional data model in Equation (2.35) the stepping curves in each detector pixel can be described and for each pixel a transmission T, differential phase-shift $\Delta\Phi$, and dark-field signal D can be retrieved. There are several methods to implement this processing step which are briefly discussed in the following section.

2.3.5 Standard Stepping Data Processing Methods

The most straightforward approach is to do a non-linear least-squares fit based on Equation (2.35) to the stepping curve. Essentially, a cosine function is fitted to the stepping curve which yields the required parameters to calculate the three signals. However, this approach is computationally expensive and there are more efficient signal extraction approaches.

Fourier Analysis A common processing method is the Fourier analysis which makes use of the observation that the stepping curve can be described by a Fourier series [91]. Since in general higher orders can be neglected at standard X-ray tube setups only the first order coefficients must be retrieved [8]. With the fast Fourier transform (FFT) an extremely fast data processing becomes possible, however, requires that the sampling points, i.e., the stepping positions, are perfectly equidistantly distributed over one oscillation of the curve. At most laboratory setups this can be achieved because the displacement of the grating during the phase-stepping is done with a high-precision actuator. This allows equidistant sampling over the interval of one grating period. Nevertheless, even high-precision actuators underlie positioning tolerances which can lead to artifacts in the processed data, which are difficult to suppress in the Fourier analysis.

Statistical Phase Retrieval (SPR) Another alternative is the statistical phase retrieval which uses a linearized form of the conventional model in Equation (2.34) applying the trigonometric identity,

$$\cos(\alpha+\beta) = \cos(\alpha)\cos(\beta) - \sin(\alpha)\sin(\beta)\ . \tag{2.40}$$

which leads to the linearized model of the conventional data model,

$$y_{\text{linear}} := \underbrace{a_0}_{b_0} + \underbrace{a_1\cos(\Phi_1)}_{b_1}\cos(\phi) - \underbrace{a_1\sin(\Phi_1)}_{b_2}\sin(\phi)\ , \tag{2.41}$$

with,

$$a_0 = b_0\ , \tag{2.42}$$

$$V = \frac{\sqrt{b_1^2+b_2^2}}{b_0}\ , \tag{2.43}$$

$$\Delta\Phi = \arctan 2(-b_2, b_1)\ . \tag{2.44}$$

Each stepping curve is a set of intensity measurements $\boldsymbol{y} = (y_0, y_1, ..., y_N)$ from the same detector pixel at the different interferometer phase positions $\boldsymbol{\phi} = (\phi_0, \phi_1, ..., \phi_N)$. This defines a set of linear equations, where N is the total number of steps:

$$\underbrace{\begin{pmatrix} 1 & \cos(\phi_0) & -\sin(\phi_0) \\ 1 & \cos(\phi_1) & -\sin(\phi_1) \\ \vdots & \vdots & \vdots \\ 1 & \cos(\phi_N) & -\sin(\phi_N) \end{pmatrix}}_{\boldsymbol{A}} \underbrace{\begin{pmatrix} b_0 \\ b_1 \\ b_2 \end{pmatrix}}_{\boldsymbol{b}} = \underbrace{\begin{pmatrix} y_0 \\ y_1 \\ \vdots \\ y_N \end{pmatrix}}_{\boldsymbol{y}} \tag{2.45}$$

We find $\hat{\boldsymbol{b}}$ by minimizing the L2 error,

$$\hat{\boldsymbol{b}} = \arg\min_{\boldsymbol{b}} ||\boldsymbol{y} - \boldsymbol{A}\,\boldsymbol{b}||^2\ . \tag{2.46}$$

This is the linear least-squares problem which can be re-arranged to,

$$\hat{\boldsymbol{b}} = (\boldsymbol{A}^T\boldsymbol{A})^{-1}\boldsymbol{A}^T\boldsymbol{y}\ . \tag{2.47}$$

For practical implementation a variety of optimized least-squares solution are already available in most common programming frameworks. These can usually avoid the explicit inversion in (2.47) and reduce the phase-stepping data processing to only two steps: Calculation of the $N \times 3$ matrix $\boldsymbol{A}$ as defined in Equation (2.45) and inserting it into a least-squares solver. For example, in Python [134] this can be realized with the numpy package [46]:

```
import numpy as np
b = np.linalg.lstsq(A, y)[0]
```

As a last step Equations (2.42), (2.43), and (2.44) are used to convert $\hat{\boldsymbol{b}}$ to intensity, visibility, and phase-shift.
This approach is essentially fitting a cosine function to the measured intensities, as suggested at the beginning of this section. The advantage is the efficiency due to linerization and in comparison to the Fourier analysis that the phase-sampling not necessarily must be equidistant. It is important to note that until this point only a **linearized phase-retrieval** without considering any statistical weights has been introduced. To extend the processing approach these weights can be added as suggested by Hahn [45, Chapter 3.2]. Based on the count rate of the individual measurements y_i its uncertainty σ_i is calculated as $\sigma_i = 1/y_i$. This allows to extend the minimization problem by introducing the statistical weights $w_i = 1/\sigma_i^2$, which yields:

$$\hat{\boldsymbol{b}} = \arg\min_{\boldsymbol{b}} ||\boldsymbol{w}(\boldsymbol{y} - \boldsymbol{A}\,\boldsymbol{b})||^2 \tag{2.48}$$

The weighted linear least-squares solution of this is then found by re-arranging to,

$$\hat{\boldsymbol{b}} = (\boldsymbol{A}^T\boldsymbol{w}\boldsymbol{A})^{-1}\boldsymbol{A}^T\boldsymbol{w}\boldsymbol{y}\ . \tag{2.49}$$

It is possible to simplify this expression to a linear least-squares form as the errors between the measurements are uncorrelated. This is achieved by defining,

$$A'_{i,j} = \sqrt{w_i}\cdot A_{i,j}\ \text{, and} \tag{2.50}$$
$$y'_i = \sqrt{w_i}\cdot y_i\ , \tag{2.51}$$

which can be inserted in (2.47) replacing $\boldsymbol{A}$ and $\boldsymbol{y}$, respectively. The linear least-squares solution then yields $\hat{\boldsymbol{b}}$.

Expectation Maximization (EM) A remaining problem in the previously introduced processing approaches is their trust into the stability and precision of the system. Positioning errors of the stepping actuator, variations in the photon flux, and changes of the visibility of the interferometer during the phase-stepping acquisition should not be excluded. As a solution we use an iterative algorithm to which we refer to expectation maximization or EM. It has similarity to the common expectation-maximization-algorithm as it uses an iterative two-step approach to find the best configuration of the model to the measured data. This allows to optimize the stepping positions $\boldsymbol{\phi}$ assuming that the step-to-step interferometer phase difference should be the same for all pixels.
Based on the conventional model from Equation (2.35) a slightly extended model is used, which allows fluctuations of the intensity ΔI, of the visibility ΔV, and of the interferometer phase Δs. The latter being particularly interesting as it allows us to identify deviations of the phase-stepping positions in $\boldsymbol{\phi}$. The slightly extended model is,

$$y_{\text{conventional, px}} := y^{\text{px}} = \Delta I\ a_0\left(1 + \Delta V\ V\cos\left(\phi + \Phi_1 + \Delta s\right)\right)\ , \tag{2.52}$$
$$= \Delta I\ a_0 + \Delta I\ \Delta V\ a_1\cos\left(\phi + \Phi_1 + \Delta s\right)\ , \tag{2.53}$$

which can again be linearized using the trigonometric identity in Equation (2.40),

$$\begin{aligned} y_{\text{linear, px}} := y^{\text{px}} = \underbrace{\Delta I}_{c_0}\; a_0 + \underbrace{\Delta I\; \Delta V\; \cos(\Delta s)}_{c_1}\; a_1 \cos(\Phi_1 + \phi) \\ - \underbrace{\Delta I\; \Delta V\; \sin(\Delta s)}_{c_2}\; a_1 \sin(\Phi_1 + \phi)\;, \end{aligned} \tag{2.54}$$

with,

$$\Delta I = c_0\;, \tag{2.55}$$

$$\Delta V = \frac{\sqrt{c_1^2 + c_2^2}}{c_0}\;, \tag{2.56}$$

$$\Delta s = \arctan 2(-c_2, c_1)\;. \tag{2.57}$$

Now, analogue to the SPR approach a set of linear equations is given, however, here not the entire phase-stepping of a single pixel in 'time-domain' is analyzed. Instead, one specific stepping position, e.g., step n where the interferometer phase due to the grating displacement is ϕ_n, is evaluated for all detector pixels. At this stepping position the intensity measured by the m detector pixels is given as $\boldsymbol{y}^{\text{px}} = (y_n^{\text{px}=0}, y_n^{\text{px}=1}, \dots y_n^{\text{px}=m})$. From prior pixel-wise SPR in 'time-domain' each pixel also has a corresponding $\boldsymbol{a_0}$, $\boldsymbol{a_1}$ and $\boldsymbol{\Phi_1}$. This can be used to write the following equation where only $\boldsymbol{c}$ is unknown:

$$\underbrace{\begin{pmatrix} a_0^{\text{px}=0} & a_1^{\text{px}=0}\cos(\Phi_1^{\text{px}=0} + \phi_n) & -\sin(\Phi_1^{\text{px}=0} + \phi) \\ a_0^{\text{px}=1} & a_1^{\text{px}=1}\cos(\Phi_1^{\text{px}=1} + \phi_n) & -\sin(\Phi_1^{\text{px}=1} + \phi) \\ \vdots & \vdots & \vdots \\ a_0^{\text{px}=m} & a_1^{\text{px}=m}\cos(\Phi_1^{\text{px}=m} + \phi_n) & -\sin(\Phi_1^{\text{px}=m} + \phi) \end{pmatrix}}_{\boldsymbol{A}} \underbrace{\begin{pmatrix} c_0 \\ c_1 \\ c_2 \end{pmatrix}}_{\boldsymbol{c}} = \underbrace{\begin{pmatrix} y_n^{\text{px}=0,0} \\ y_n^{\text{px}=1,0} \\ \vdots \\ y_n^{\text{px}=m} \end{pmatrix}}_{\boldsymbol{y}^{\text{px}}} \tag{2.58}$$

We now solve this again for a $\hat{\boldsymbol{c}}$ based on the L2 norm using linear least-squares,

$$\hat{\boldsymbol{c}} = \arg\min_{\boldsymbol{c}} ||\boldsymbol{y}^{\text{px}} - \boldsymbol{A}\,\hat{\boldsymbol{c}}||^2\;, \tag{2.59}$$

$$\hat{\boldsymbol{c}} = (\boldsymbol{A}^T\boldsymbol{A})^{-1}\boldsymbol{A}^T\boldsymbol{y}^{\text{px}}\;. \tag{2.60}$$

Obviously, also here statistical weights can be included to consider the variance of the individual measurements similar as introduced in the SPR. Inserting into Equations (2.55), (2.56), and (2.57) yields information on the fluctuations in the interferometer which appeared at the analyzed stepping position. This can for example be used to update the $\boldsymbol{\phi}$ by applying the identified phase-step position deviation Δs to the corresponding entry. Hence, we update,

$$\phi_n \rightarrow \phi_n + \Delta s\;. \tag{2.61}$$

As previously mentioned, the EM approach is an iterative procedure which requires several repetitions. First a pixel-wise SPR in time-domain is done as described in the previous paragraph and summarized in Equation (2.47). Here, each detector pixel is handled individually – hence pixel-wise – and the full stepping curve is evaluated. This is done based on an initial $\boldsymbol{\phi}$ which reasonably well describes the approximate stepping positions, e.g., equidistant stepping

over one grating period. As a result, we obtain a first guess on the coefficients of the stepping curve, i.e., a_0, a_1 and Φ_1. This obviously has to be repeated for each detector pixel.
Then in the second step a per-shot, i.e., per stepping position, SPR in spatial-domain is performed. This has been previously described in this paragraph and is summarized in Equation (2.47). It returns information on variations of the system and allows us to update the phase stepping positions in $\boldsymbol{\phi}$. This per-shot SPR has to be calculated for each stepping position individually to update the respective entry in $\boldsymbol{\phi}$. Afterwards, the pixel-wise SPR is repeated, however, now with an updated $\boldsymbol{\phi}$.
This procedure is iterated until a convergence criterion is reached, e.g., that the phase-stepping deviations are sufficiently small. Usually, only an optimization of the phase stepping positions is required at laboratory setups. The visibility is usually stable because the spectrum and source properties do not change. Variations in flux can more easily be corrected based on reference pixels measuring the intensity of the X-ray tube outside the interferometer and sample area.

2.4 Imaging with a Talbot-Lau Interferometer

The acquired image data is analyzed for changes of the obtained intensity, visibility, and phase of the interferometer in each pixel. This is done by comparing the measurement of the sample to a reference where no sample is in the beam path, as introduced in the previous section. This reveals information about the inner structure of the sample and even allows tomographic reconstructions of the material properties.

2.4.1 Radiography

Implementations which are designed for radiography imaging generate only a single 2D image of the X-rayed object. In most conventional X-ray imaging systems, which measure only the attenuation, this is done by measuring a single projection through the sample. For a Talbot-Lau interferometer, which might require some kind of phase-stepping, this usually means that several exposures of the same scene are measured. These are then combined to a single projection image, i.e., a radiography. The processing at a Talbot-Lau interferometer yields images of the three image channels: The transmission T, the differential phase-shift $\Delta\Phi$, and the induced drop of the visibility D as defined in Equations (2.37), (2.38), and (2.39).
The transmission image obtained from a Talbot-Lau interferometer is equivalent to the results measured at a conventional radiography machine. Only the noise level is increased when comparing the results measured at equal X-ray tube and detector settings. This originates from the additional interferometer gratings in the beam path which reduce the available X-ray flux and thus lower the statistics. Also, spectral effects can deviate because the gratings and their substrates might lead to some hardening of the X-ray spectrum.
The transmission image is particularly useful to analyze strongly attenuating objects inside a less attenuating object, e.g., bones in a patient. Each pixel relates to the line integral of the samples' attenuation coefficient along the beam path and therefore all depth information is lost. Based on Lambert-Beer's law in Equation (2.17) the relation is,

$$T = \frac{a_0'}{a_0} = e^{-\int \mu(z)\mathrm{d}z} \,, \tag{2.62}$$

where the sample's attenuation coefficient μ is integrated along the beam path z. For image evaluation and diagnostics of the attenuation information usually the negative logarithm of the

measured transmission image is used:

$$-\ln(T) = \int \mu(z)\mathrm{d}z \tag{2.63}$$

Besides the attenuation contrast also dark-field and differential phase-contrast can be retrieved when a Talbot-Lau interferometer is implemented into the imaging system. From the phase-shift induced by the sample a differential phase-contrast image is generated which can be related to the refractive index decrement δ. From Equations (2.13) and (2.14) the relation between δ and the resulting refraction angle α is known. During the measurement with a Talbot-Lau interferometer instead of α the displacement of the interference pattern is measured. We refer to this shift as $\Delta\Phi$ in rad as defined in Figure 2.17. It represents the shift of the phase of the periodic interference pattern, rather than a shift in micrometer. Then α can be set into relation to the measured displacement,

$$\alpha \approx \frac{p_2}{d} \cdot \frac{\Delta\Phi}{2\pi} \,, \tag{2.64}$$

and consequently,

$$\frac{\lambda}{2\pi}\frac{\partial\phi}{\partial x} = \frac{p_2}{d} \cdot \frac{\Delta\Phi}{2\pi} \,, \tag{2.65}$$

can be combined from Equation (2.14).
This allows us to link the measurements of differential phase-contrast image at a Talbot-Lau interferometer to refractive index decrement. It demonstrates that the measured phase shift represent the line integrals of the refractive index decrement δ. However, contrary to the attenuation coefficient, it is evaluated in its differential form along the direction perpendicular to the grating lines, i.e., here the x-axis:

$$\Delta\Phi = \frac{1}{k}\frac{2\pi\, d}{p_2}\frac{\partial\phi}{\partial x} = \frac{2\pi\, d}{p_2}\frac{\partial}{\partial x}\left(\int \delta(z)\mathrm{d}z\right) \tag{2.66}$$

One issue of this imaging method is the limitation that the shift of the interference pattern $\Delta\Phi$ can only be retrieved on the interval $[0...2\pi[$. Consequently, phase wrapping can occur in the differential phase-contrast image which can make the values ambiguous.
The second additional image channel is the dark-field signal, i.e., the information which can be retrieved from the visibility drop induced by small-angle scattering in the sample. Similar to the attenuation channel, also for the dark-field signal an exponential relation to a material property exists. The linear diffusion coefficient ϵ specifies the material's small-angle scattering power which leads to the reduction of the interferometer's visibility. The dark-field contrast image, i.e., the relative reduction of the system visibility, is described by,

$$D = \frac{V'}{V} = e^{\frac{-2\pi^2 d^2}{p_2^2}\int \epsilon(z)\mathrm{d}z} \,, \tag{2.67}$$

with a system-specific factor in the exponent. This formula, however, is only an approximation as it omits variation of the interferometer sensitivity along the beam path, i.e., small-angle scattering close to G_1 gives a stronger visibility-drop than when induced further away from G_1. Furthermore, effects such as visibility-hardening are not included. More information on this topic can be found in [8] and [23].

2.4.2 Computed Tomography

The spatial distribution of three material properties which are retrievable with a Talbot-Lau interferometer cannot be extracted from a single radiography. With a tomographic reconstruction, however, this is possible and 2D slices through the object, representing the respective coefficient, can be generated. This requires a set of several projections, which must be measured under different angles to the sample, and a tomographic reconstruction algorithm. Two common reconstruction methods are the filtered backprojection (FBP) and the statistical iterative reconstruction (SIR). They allow inverting the forward-projection step, i.e., solve for the coefficients along the line-integrals.
These computed tomography reconstructions then yield the attenuation coefficient μ, refractive index decrement δ, and linear diffusion coefficient ϵ for each voxel in the reconstructed volume which represents the mean material property within this area. Throughout this thesis only filtered backprojection with a standard ramp filter is used for the presented tomographic reconstructions. To compensate for the divergence in the geometry of the cone beam in a CT machine Feltkamp pre-weighting is applied. For further details concerning cone beam CT see the comprehensive work presented in the dissertation by Turbell [131].
While reconstruction of the attenuation and the linear diffusion coefficients is similar, an important difference is the variance of the sensitivity in the dark-field channel. Depending on the position along the beam path the small-angle scattering of the radiation leads to a larger or smaller visibility-drop. As described in [133] this behavior can be compensated by combining opposing rays during the reconstruction. This way the sensitivity gradient is efficiently removed.

2.4.3 Image Calibration in Clinical CT

In clinical CT machines and most laboratory X-ray imaging systems a poly-chromatic spectrum is used. The reconstructed attenuation coefficients from a computed tomography therefore represent the mean attenuation coefficient weighted with the power spectrum of the imaging setup. This can lead to discrepancies in the results when reconstructions from different machines, e.g., with different X-ray tubes, spectra, or detectors, are compared. The Hounsfield scale has been introduced to calibrate clinical CT machines to the attenuation properties of two reference materials and produce a dimensionless gray-scale image. Water and air are used to define the values 0 to -1000 of the scale, respectively. Throughout this thesis, the abbreviation HUa, for attenuation Hounsfield Units, is used which are defined as:

$$\mathrm{HUa}(\mu) = 1000 \cdot \frac{\mu - \mu_{\mathrm{water}}}{\mu_{\mathrm{water}} - \mu_{\mathrm{air}}} \tag{2.68}$$

Following from the definition, air and water are -1000 and 0 HUa. Bones have values around 250 to 2000 HUa, adipose tissue is found for HUa values between -120 and -90, and the lung parenchyma around -700 to -600 HUa [17].
In the dark-field channel the same problem arises, and a similar unit is introduced which has initially been proposed by [135] and has been adapted for clinical dark-field CT in [136] where the following section has recently been published. Since the linear diffusion coefficient depends not only on the feature size of the small-angle scattering structures but also on several system-specific parameters like the interferometer sensitivity or the used X-ray spectrum the reconstruction results can easily vary from system to system. To avoid these deviations, the reconstructed values can be calibrated to as dark-field Hounsfield units (HUd). Similar to the attenuation Hounsfield scale, this ensures a quantitative consistency between different dark-field

CT systems [135]. Different to the attenuation channel, neoprene foam and air are selected as reference calibration materials. Neoprene is a suitable material to model the microstructure of lung alveoli [124] featuring a weak attenuation but strong dark-field signal[1]. Nevertheless, further evaluation on long-term stability is required by future work. The HUd scale is defined by a value of 1000 for neoprene as a strongly scattering material and a value of 0 for air and every other non small-angle scattering material. A conversion from the reconstructed linear diffusion coefficient ϵ, i.e., the measure for the amount of small-angle scattering of the material, to dimensionless HUd is done by inserting,

$$\mathrm{HUd}(\epsilon) = 1000 \cdot \frac{\epsilon - \epsilon_{\mathrm{air}}}{\epsilon_{\mathrm{neoprene}} - \epsilon_{\mathrm{air}}} \,, \tag{2.69}$$

where $\epsilon_{\mathrm{neoprene}}$ and ϵ_{air} are the measured values obtained for a calibration neoprene material. This gives a similar image impression by attenuation images, since regions with lower small-angle scattering density are darker. Especially for imaging of the lung use of positive numbers for HUd ensures a clear differentiation to the attenuation HU, which are mostly negative for lung tissue.

2.5 Grating Fabrication

Talbot-Lau interferometry with X-rays, as used in this thesis, depends on X-ray compatible grating structures. The grating structures have been introduced in Section 2.3 as sets of parallel lines which imprint a periodic structure in the beam.
We differentiate between two types of gratings: The phase-shifting and the absorption gratings. The latter's purpose is to absorb all the radiation which hits the grating lines and lets the remaining radiation pass unhindered through the slits. Phase-shifting gratings, in contrast, are designed to only shift the phase of the radiation passing through the grating lines. Attenuation of the radiation in these gratings is an unwanted side effect which, however, is accepted as it is comparably small.
As has already been discussed in Section 2.2, X-ray attenuation in most materials is comparably weak. This is particularly problematic for absorption gratings, where all radiation hitting the grating structure should be absorbed. Naturally, a material with a high absorption coefficient in the X-ray energy range is selected. Mostly gold and sometimes tungsten is used as grating bar material in absorption gratings. However, the stopping power of those materials is still often not sufficient and the grating structures must have a significant extent along the beam axis. This increases the interaction path length in the grating bar material and these gratings can have a good performance as absorption gratings. In Figure 2.18, a rendering of such an absorption grating with a high-aspect-ratio grating structure is shown. For clarity, support structures are omitted in this illustration. The aspect ratio of the rendered grating is about 100, i.e., each absorber lamella is 100 times higher than it is wide.
For phase-shifting gratings, the height of the structures must be matched with the X-ray's phase-shift in the grating material. Depending on the material, the demanded phase-shift, and the X-ray energy a specific height can be calculated. These heights are usually significantly lower than for absorption gratings.
Besides the structure height, there is no difference in the fabrication process of phase-shifting and absorption gratings. However, due to the higher aspect ratios in absorption gratings, these

[1] Closed-cell plastic foam supplied by DRG GmbH (Austria) as ZK-CR-L is used throughout this thesis and referred to as neoprene.

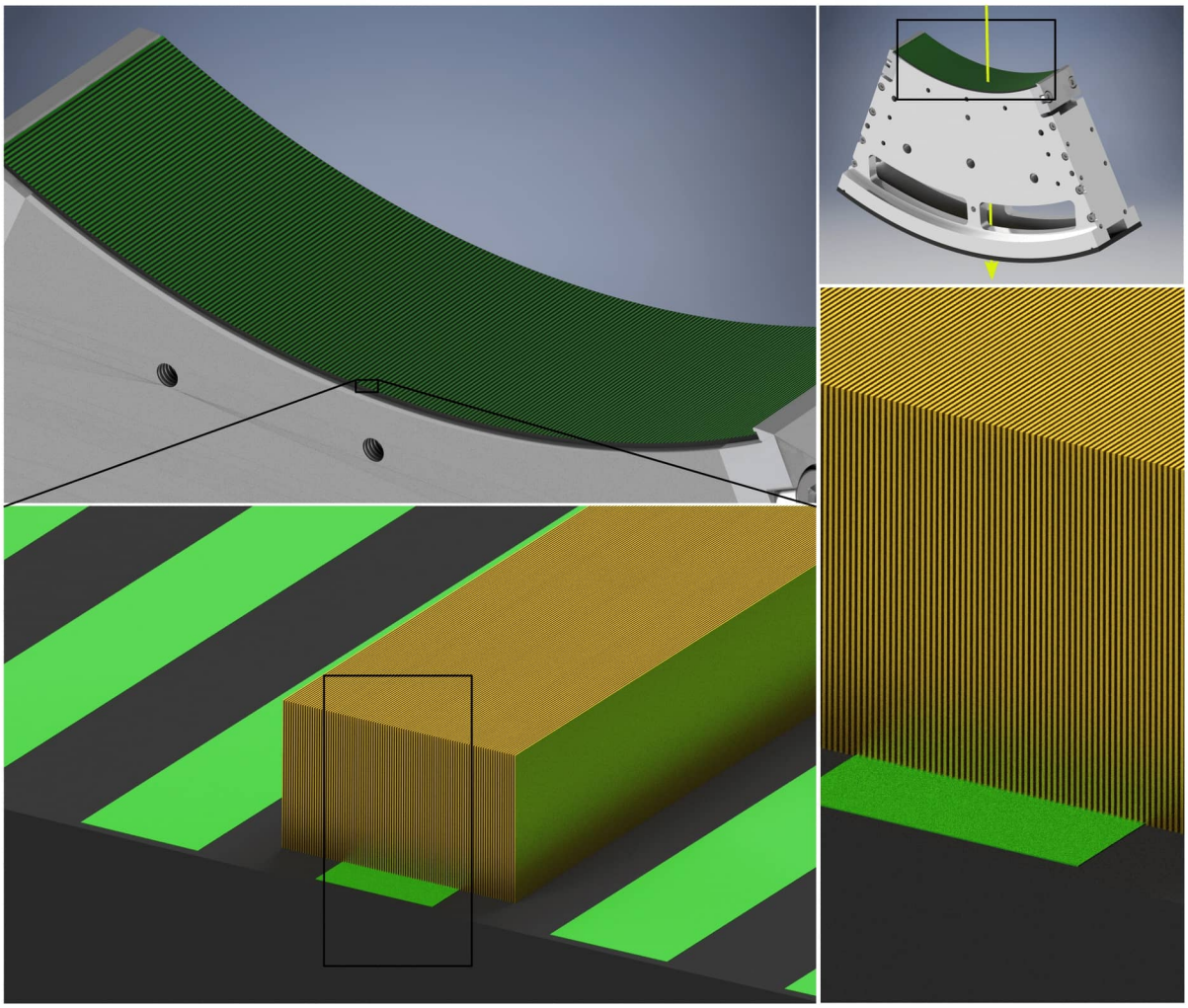

Figure 2.18: Renderings of a bent grating structure. The yellow arrow indicates the central X-ray beam traversing the grating under perpendicular incident. In the top panels, only a dummy line pattern representing the approximate grating layout is shown in green. In the lower two panels, renderings of several hundred grating lamellae in gold are included. They have a period of only a few micrometers, but a height–along the beam path–of several hundred micrometer. No support and stabilizing structures are included in this rendering. Image adapted from [136] CC BY.

are usually most difficult to be fabricated. There area various approaches and technologies to manufacture such X-ray compatible grating structures. Some are heavily based on etching processes in silicon crystals, another approach is LIGA process (germ. Lithographie, Galvanik, Abformung). In this thesis, all grating structures are fabricated based on the "direct" deep X-ray LIGA process. This process in described in the following paragraphs. Further information on this lithographic process can be found in [101], [79], [66], [77], [113].
The "direct" deep X-ray LIGA process involves X-ray lithography with synchrotron radiation and subsequent electroplating with gold. The process is illustrated in Figure 2.19 and uses X-ray lithography to imprint the grating layout from a mask into a thick polymer photo-resist. After development and removal of the unexposed resist, one is left with a grating-like polymer structure. Since this polymer is almost transparent to X-rays this structure is not yet suitable as an X-ray grating. Hence, the gaps are filled with an X-ray absorbing material such as, e.g., gold. For phase-shifting gratings also other materials such as nickle are suitable. For most gratings, the polymer resist can remain in the grating structure.

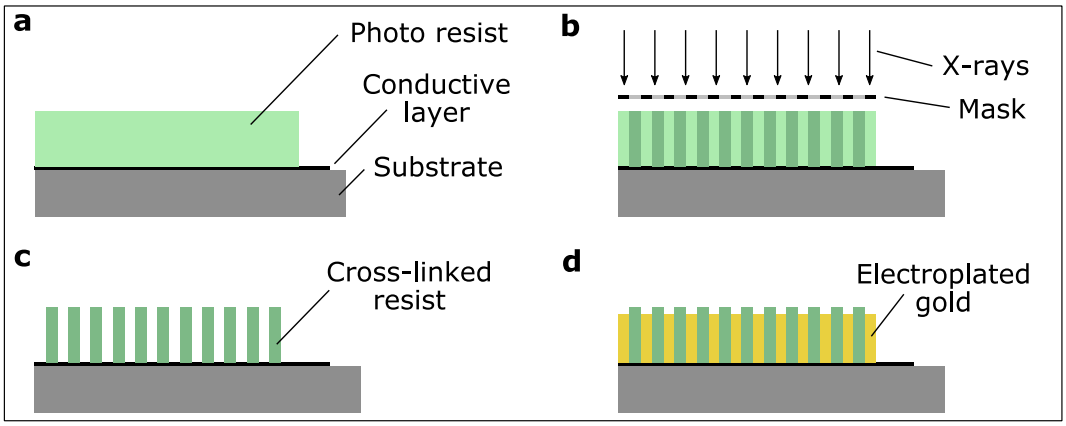

Figure 2.19: Simplified illustration of the LIGA grating fabrication process, here for example with an aspect-ratio of five. **a**, Photo resist is applied onto the substrate. **b**, The resist is exposed with high-energy photons or soft X-rays passing through an absorption mask that imprints the grating layout. **c**, During the development step the unexposed photo resist is washed away, leaving only the cross-linked resist. **d**, The gaps are filled via electroplating with an absorber material (e.g., gold) resulting in a lamella structure which can be used as an X-ray optical grating. Note, that the electroplated infill must be lower than the surrounding resist matrix. Image adapted from [140] CC BY.

This process comes with a remarkable scalability towards large resist thicknesses and high aspect-ratios. In the illustration in Figure 2.19 only an aspect-ratio (i.e., lamella height vs. width) of five is shown. However, the LIGA process currently achieves aspect-ratios exceeding 100 for grating periods of 4.8 µm with minimal defects [77]. Such an aspect ratio has been shown in the rendering in Figure 2.18.
For these high aspect-ratios, stabilization bridges between the resist lamella must be included in the layout. The polymer structures would otherwise easily distort or collapse between development and electroplating in Figure 2.19. A scanning electron microscopy (SEM) image of an absorption grating with many support structures is shown as an example in Figure 2.20. The view is almost vertical onto the grating surface, and the orientation of the grating lines are indicated by some gold-colored lines. In the inset, the gray colored polymer resist regularly has connecting bridges which discontinue the grating lines. The areas in between, black colored,

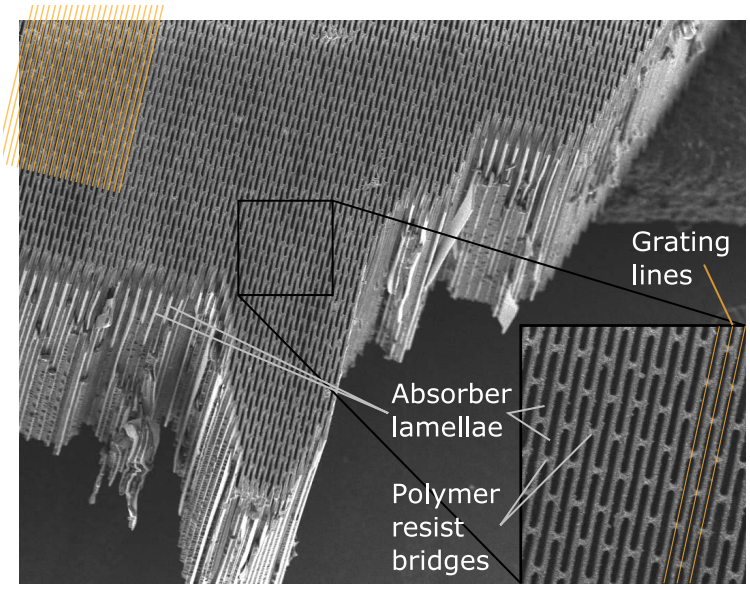

Figure 2.20: Scanning electron microscope (SEM) image of a broken absorption grating fabricated via the LIGA process. Gold colored lines illustrate how the grating lines are orientated. The polymer resist structure is colored in light gray. In the insert, the bridge structure of the resist can be observed. It discontinues the grating lines and thereby increases the stability of the resist during the fabrication when no yet any absorber material has been filled into the voids. The bridge fraction of this grating is about 10%.

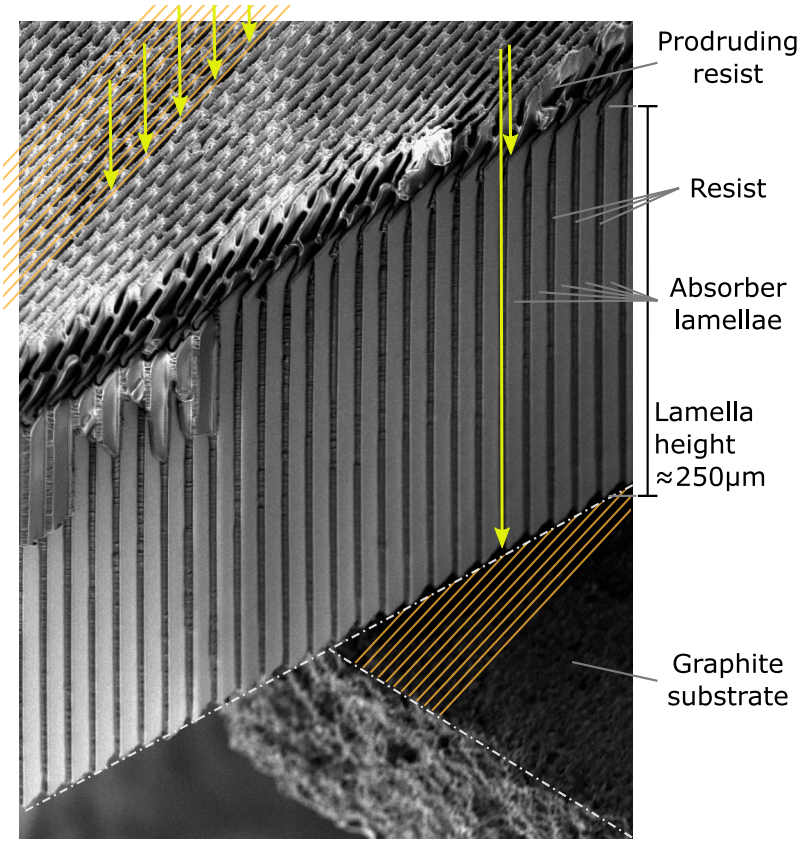

Figure 2.21: Scanning electron microscope (SEM) image of an absorption grating fabricated via the LIGA process. The graphite substrate and the grating structure were broken for the SEM evaluation and the break lines are indicated with white dash-dotted lines. The absorber lamellae are embedded between the resist, which is slightly higher and protrudes above the grating structure. The yellow arrows indicate the ideal vertical incidence of the X-ray beam. The two rays on the right illustrate a ray which passes through the gap between the absorber lamellae, while the other one is stopped. In two areas the line pattern of the grating structure is illustrated with gold colored lines.

are the areas where the absorber material forms a grating lamella. Obviously, only the surface of the grating is visible in a SEM image. Since the absorber lamellae are usually embedded in the polymer resist, the gold lamellae are not directly visible. In the inset, only shadows are visible, as the gold lamellae are too far inside the grating to be resolved by the SEM. Only at the boundaries, where the grating was broken, the inner structure including some absorber lamellae are revealed.

The drawback of this added stabilization structures is some loss of grating area and thus interferometer performance. The percentage of lost area is referred to as *bridge fraction* and usually lies between 1% and 10%. Consequently, a trade-off between few bridges, which can lead to defects and in-homogeneous grating quality, and too many bridges must be found to minimize the interferometer performance loss

To visualize the height of the grating structures, i.e., their aspect ratio, Figure 2.21 shows a more shallow angle onto the grating surface. Here also the polymer matrix which is slightly higher than the absorber lamellae can be clearly seen. With yellow arrows, the beam path of several X-rays area illustrated. They reach the grating surface under a perpendicular incidence and can pass through a slit between absorber lamellae, i.e., traverse the polymer. However, when an absorber lamella blocks the beam path, the ray will be absorbed.

The gratings presented in this thesis have been fabricated by the Karlsruhe Institute of Technology and microworks GmbH (Karlsruhe, Germany) based on this LIGA fabrication process. While in there a synchrotron is used as an X-ray source for the lithography step, the fabrication process can also be adapted to a laboratory X-ray source [97]. Bringing the LIGA process to more readily available X-ray sources is an important step to make X-ray compatible gratings more available.

Certainly, there are also other grating fabrication methods which, for example, are based on silicon etching. These, however, only reach aspect-ratios of up to 80 and are restricted to silicon

as the substrate material due to high purity requirements [116], [115]. Similar to the previous description also these silicon gratings are then filled with, e.g., gold via electroplating. Filling with tungsten has also been demonstrated, e.g., by Pinzek et al. [96], by pressing the infill via centrifugal force into the voids of the etched silicon substrate.
An advantage of the silicon etching-based fabrication approaches clearly is the lower cost and better availability. However, in contrast to the LIGA process there is no flexibility in choice of substrate material as only silicon is allowed. The LIGA process allows optimizing the substrate for its mechanical or X-ray transmission properties. For example, graphite or polyimide is regularly used as a substrate material. Both these materials combine good mechanical stability and excellent X-ray transmittance [66].

Grating Interferometer Simulation 3

For a comprehensive analysis and optimization of different Talbot-Lau interferometer designs a specialized simulation framework has been developed. It relies on Fresnel propagation of the wave field between the various interferometer components and is based on previous work by [73] or [103] and has recently been briefly described in [136] and [140].

3.1 Concept of the Framework

The simulation framework is designed to realistically model the various design aspects of Talbot-Lau interferometers in an X-ray imaging setup. Its primary purpose is to evaluate large sets of system parameters to identify the optimal setup geometry and grating specifications for a setup. Furthermore, it allows studying performance characteristics which are difficult to assess in an experimental setup.
The simulation framework must consider a large variety of realistic system properties to achieve correct performance results. This is important to be able to correlate experimental results with the simulation. Nevertheless, a slight overestimation of the system performance is common in simulation frameworks like this because not all defects and object properties can be incorporated into the simulation.
The framework does only include attenuation based interactions between X-rays and the sample which are implemented as filter materials in the beam path. These modify the applied X-ray spectrum and are sufficient for the evaluations presented throughout this thesis. Nevertheless, the framework can be extended to consider structured samples as demonstrated in [74] and [123]. There the same simulation framework has been used for spectral phase-contrast simulations of porous sample structures. This approach is similar to work by Malecki et al. [73].
Besides the grating parameters and the influence of spectral effects, the simulation must also handle the divergent geometry of a Talbot-Lau interferometer and the large source spot of clinical X-ray sources. Particularly, the latter becomes of great interest in the design process of a clinical dark-field CT as it leads to an increased sensitivity of the system performance to tolerances in the grating period.
The most important parameters of an interferometer design are the positions of the gratings and their periods, heights, duty-cycles, bridge fractions, bending radii, and profiles. Furthermore, the material and thickness of the substrates, the grating lamella, and the resist matrix can be selected. Additional parameter options can easily be added to the framework if required.
To include spectral effects, the X-ray spectrum of the source is used. This can either be measured with an energy resolving detector or simulated with, e.g., TASMIP [15] or the Penelope toolbox [104]. Additional filtration, e.g., representing a sample or the grating substrates can easily be applied to this spectrum. The required material interaction coefficients can be obtained from the xraylib library [110].
Since the underlying simulation approach relies on a mono-chromatic Fresnel propagation be-

tween the individual setup components, the spectrum of the X-ray tube must be separated in multiple energy bins. For each energy bin an individual mono-chromatic simulation is run. Eventually, the intensities reaching the detector plane are integrated according to the detector specifications. These then yield the result of the poly-chromatic grating interferometer simulation. These two parts of the framework are described in the following sections.

3.2 Mono-chromatic Simulation of the Interferometer

Each of the mono-energetic propagation simulations starts as a complex valued plane wave field (see Equation (2.1)) in front of G_1.

G_1 applied to a Plane Wave Based on the projection approximation, the structures of G_1 are applied to the wavefront inducing the characteristic attenuation and phase-shifts. Besides the obvious interaction with the grating bar material, which is usually gold or nickle, also, e.g., the material in the gaps of the grating can be considered. Furthermore, varying structure heights between neighboring lamella can be simulated by adding some noise to the height profile of the grating. In Figure 3.1, the structure of a G_1 is shown together with the complex wave field after being transmitted through this structure.

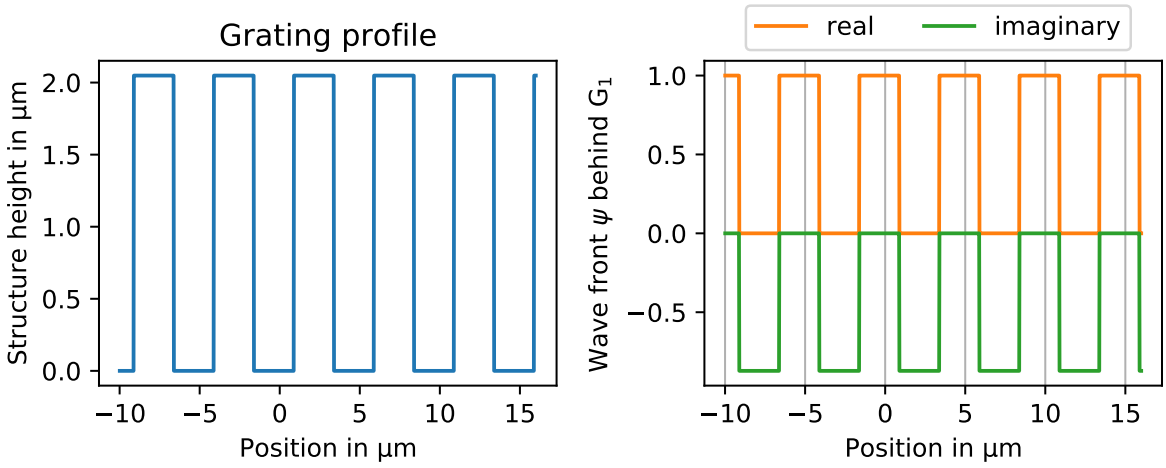

Figure 3.1: Mono-chromatic wave front after transmitted trough a G_1. A simple G_1 without an substrate, with 50% duty-cycle, 2 µm structure height, and no material between the grating lamella is used here. Consequently, the wave front remains unchanged at the positions where no material has been in the beam path. Gold has been used as the grating material.

Propagation from G_1 Plane to G_2 Plane This structured wave front is then propagated into the G_2 plane by applying Fresnel propagation as introduced in Section 2.2.1. To include the effects of a divergent beam the *Fourier scaling theorem* is applied. A comprehensive description and derivation of this theorem can be found in [88][Appendix B]. It allows to simulate a diverging wave front by combining a Fresnel propagation of the plane wave front and subsequent shifting and re-scaling as illustrated in Figure 3.2. The Fresnel propagation distance Δ and the actual

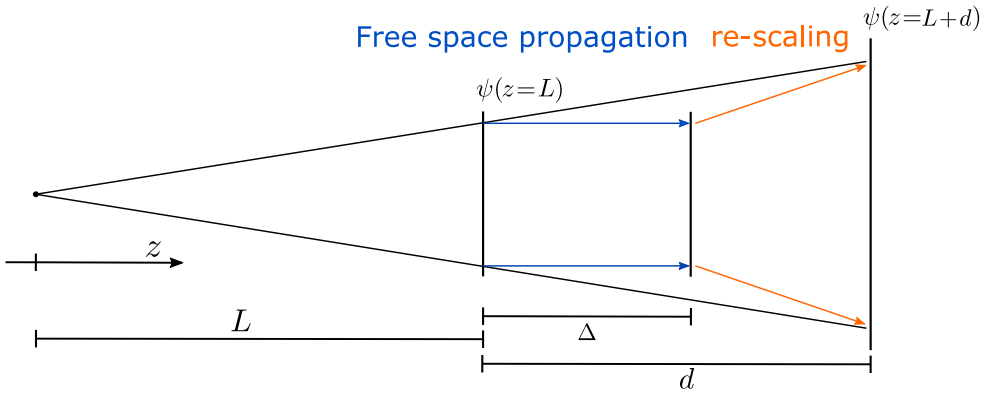

Figure 3.2: Fourier scaling theorem for propagation of a diverging wave front. The wave front Ψ is propagated as if in free space for a distance Δ and then shifted transversely and re-scaled to its diverged size in the target plane. The geometric magnification is $M = (L + d)/L$ and $\Delta = d/M$). For this approximation to apply, the divergence must be sufficiently small. More information can be found in [88][Appendix B].

distance in the divergent setup is related via the geometric magnification M,

$$M = \frac{L+d}{L}\,, \tag{3.1}$$

$$\Delta = \frac{d}{M}\,. \tag{3.2}$$

After the pane wave $\Psi(z = L)$ is Fresnel propagated for the distance Δ the resulting wave front must be shifted in transversal direction to the target position $L + d$. This is done without further propagation and its size must be re-scaled by the magnification factor M. Additionally, also the quadratic loss of intensity due to the spread of the wave as it diverges can be included in this last step.
During the propagation step also interactions with a sample can be included as it has for example been realized in [123]. To be able to consider the propagation effects, which are introduced by the sample's sub-structure, the object is first divided into sufficiently thin adjacent slices perpendicular to the propagation direction. Then the wave front is propagated from slice-to-slice and the object, i.e., respective slice, is applied to the wave front at each position. Since this simulation is restricted to a 2D plane this leads to a rather crude approximation depending on the structure of the sample and its orientation.
When the wave front reaches the G_2 plane the propagation effects have led to a notable change of the wave front as can be seen in Figure 3.3. This example simulation of a 21 keV wave front uses an interferometer setup with a design energy of 21 keV. A G_1 structure height of 2 µm gold is selected which induces a $\pi/2$ phase-shift for this energy. It is important to note that besides this phase-shift also some attenuation is caused by the gold. This leads to the intensity reduction in the blue curve in Figure 3.3.
For the example simulation G_2 is positioned at the position of the 3/4 Talbot order behind G_1. Consequently, a magnified intensity pattern similar to G_1 is generated in the G_2 plane with a significantly increased contrast compared to its state before the propagation, i.e., right behind G_1. While the blue curve in Figure 3.3 is dominated by attenuation induced features the orange curve is generated purely by interference effects.
Some fine overshoots are visible after the propagation in the orange curve in Figure 3.3. These are part of the mono-chromatic Fresnel propagation. As long as a sufficiently fine sampling is used these do not raise problems during the further simulation. It is important to clarify here

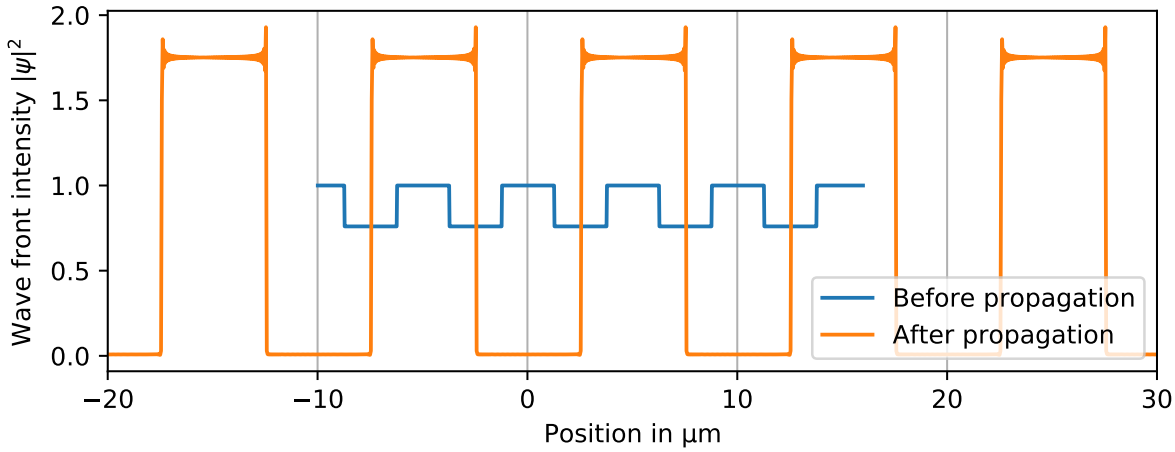

Figure 3.3: Wave front intensity before and after propagation from behind G_1 to the G_2 plane in a diverging beam ($L = d = 1270\,\text{mm}$). The G_2 position is here chosen to be in the 3/4 Talbot order for the simulated energy ($E = 21\,\text{keV}$). The re-scaling leads to a magnification by a factor of 2 and interference effects in the wave field cause high-intensity variations in the pattern. No quadratic loss in intensity due to the spread of the beam as it diverges is included here.

that such a rectangular pattern as shown in Figure 3.3 only occurs if energy, G_1 phase-shift, and propagation distance are precisely selected to lead to a fractional Talbot order with high contrast.

G_0 Blurring by Convolution The next step in the simulation framework is the conversion of the complex valued wave front to its intensity, as already plotted in Figure 3.3. This simplifies the following interaction processes with G_0 and G_2 which no longer induce any propagation effects.
Then G_0 is applied to the wave front by convolving the wavefront with a kernel representing the G_0 transmittance which has been projected into the G_2 plane over the G_1 plane. This simulates that the source spot is not a perfect point source in the G_0 plane, but an extended source as wide as a slit of G_0. As can be seen in Figure 3.4, this step leads to a triangular shape of the wave front because in these examples both patterns, the wave front and the G_0 transmittance, can be approximated as rect-functions of comparable dimensions.
In this step, the simulation can be extended to consider the influence of a large X-ray source spot which leads to multiple G_0 slits contributing to the kernel. This can furthermore be extended by including the source power profile to model, e.g., the Gaussian shape of the X-ray source spot. Consequently, every G_0 slit in the kernel has its unique intensity, depending on the source power profile in the G_0 plane. Ultimately, also the effects of the high aspect-ratio of the G_0 structures on its transmittance can be considered. This is achieved by generating a G_0 kernel based on the projected effective height, similar to the illustration in Figure 4.20. If a setup with bent gratings is simulated, the discussion in Section 4.5.5 must be considered as otherwise the effect is underestimated.
For simulations at small X-ray sources these additions are usually not required as only a few G_0 slits contribute to each sampling point in G_2. However, to accurately model effects of large X-ray source spots particularly the influence of the high-aspect-ratio grating structures must be considered. It leads to a worse transmission through the off-center G_0 slits which can lead to significant visibility degradation. In Section 4.5.5 this is introduced as grating's acceptance.

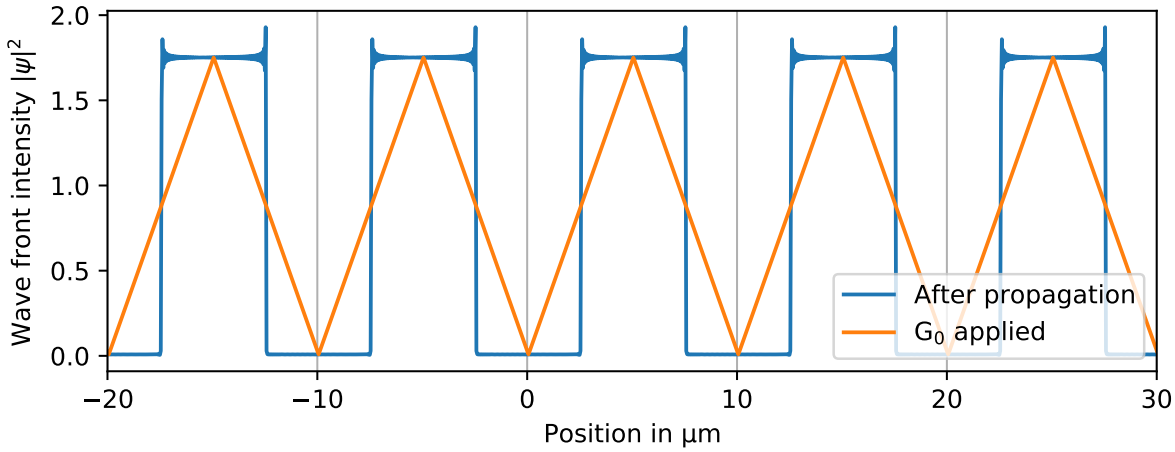

Figure 3.4: Wave front intensity before and after it has been convolved with the G_0 transmittance. The simplest G_0 transmittance is a single slit of G_0 projected into the G_2 plane through the G_1 plane. Then the convolution kernel is a rect-function whose width matches the pattern period in the wave front. The result of convolving two rect-functions with each other is a triangular pattern.

G_2 Stepping In the following step G_2 is applied to the wave front which acts as an analyzer of the periodic pattern of the wave front. Hence, it should have the same periodicity as the pattern of the wave front. Then it always absorbs the same part of the repetitive pattern and lets through for example only the peaks or only the minima of the wave front. To be able to evaluate the fine pattern with the analyzer grating a stepping curve must be acquired where G_2 is shifted in several steps over a total displacement of one grating period. The implementation is similar to the approach which is used at laboratory setups. The simulation applies the repositioned G_2 several times to the incoming wave front. The resulting intensity patterns are shown in Figure 3.5 for a stepping with five positions over one G_2 period. It is advantageous

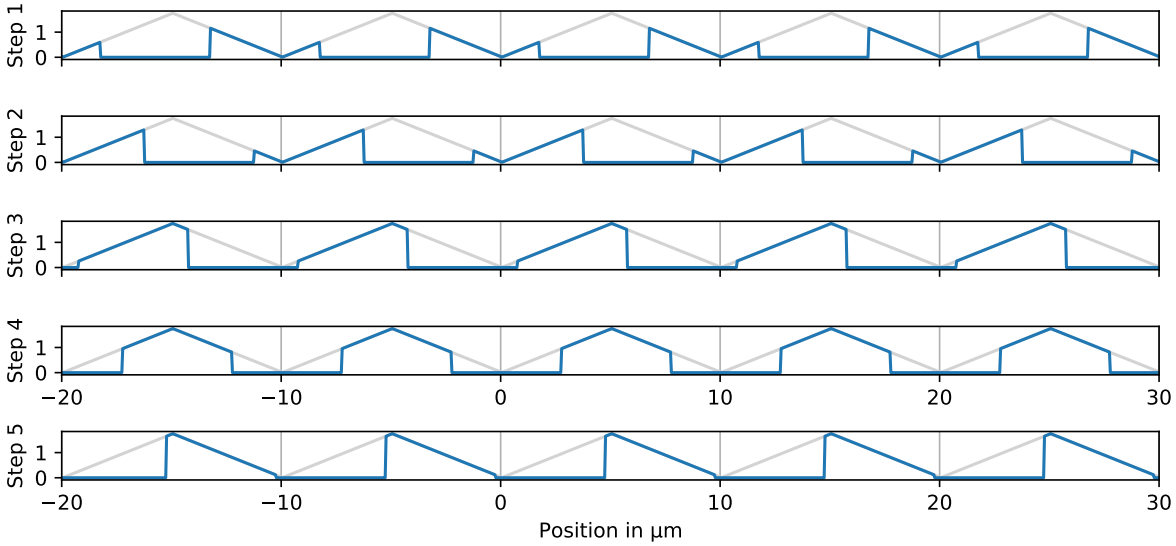

Figure 3.5: Wave front behind G_2 at five stepping positions over one G_2 period. G_2 is shifted equidistantly between the steps. The last step, which would be a full period from the start position, is omitted as it would give the same result as the first step.

to have an odd number of steps and make sure to not cover a full grating period. Otherwise, the last position would give the same result as the first one, i.e., having calculated redundant data. This way the stepping curve has best sampling and can later be processed by the Fourier processing approach as introduced in Section 2.3.5. This is a fast and robust method to extract the performance measures from the setup but requires a perfectly equidistant spacing between the individual stepping positions.

Binning to Physical Pixels As the last step of the simulation of a mono-chromatic wave-front through the interferometer the intensities are binned over the area of the physical pixel size. This yields a stepping curve as shown in Figure 3.6 for each simulated pixel. During this step, it is important to ensure that the pixel size is sufficiently large compared to the fine structure in the wave front to avoid aliasing artifacts between large box-like detector pixels and the fine periodic structure. As a solution, the detector point-spread-function can be included in this step which adds some blurring to the wave front and should eliminate any chance for aliasing artifacts.

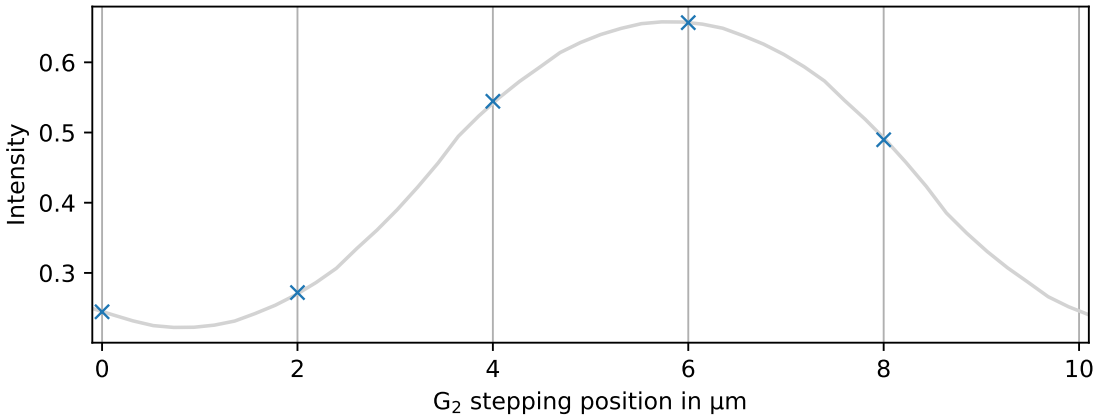

Figure 3.6: Stepping curve by binning the wave front intensity to the physical pixel size. As the pixels are much larger than the fine structure of the pattern only the mean intensity variations behind the analyzer grating, i.e., G_2, are measured. The gray line shows the stepping curve if more steps would be used.

3.3 Poly-chromatic Simulation of the Interferometer

After the mono-chromatic simulation for each energy bin in the X-ray spectrum has been generated a spectral visibility plot can be generated. Such a plot is shown in Figure 3.7. To generate such a plot, every obtained mono-chromatic stepping curve is evaluated separately. The results reveal that in this example the peak visibility is found as expected for 21 keV. This is in agreement with the design which uses a $\pi/2$ phase-shifting G_1 optimized for 21 keV.
To calculate the poly-chromatic performance of the interferometer in a specific X-ray spectrum a further step is required. For each stepping position and detector pixel the mono-chromatic results have to be weighted with the specific spectrum. They are then summed up following the detector integration characteristics. Here, photon counting and energy integrating detectors must be differentiated and also a separation for dual-energy systems is possible. An example

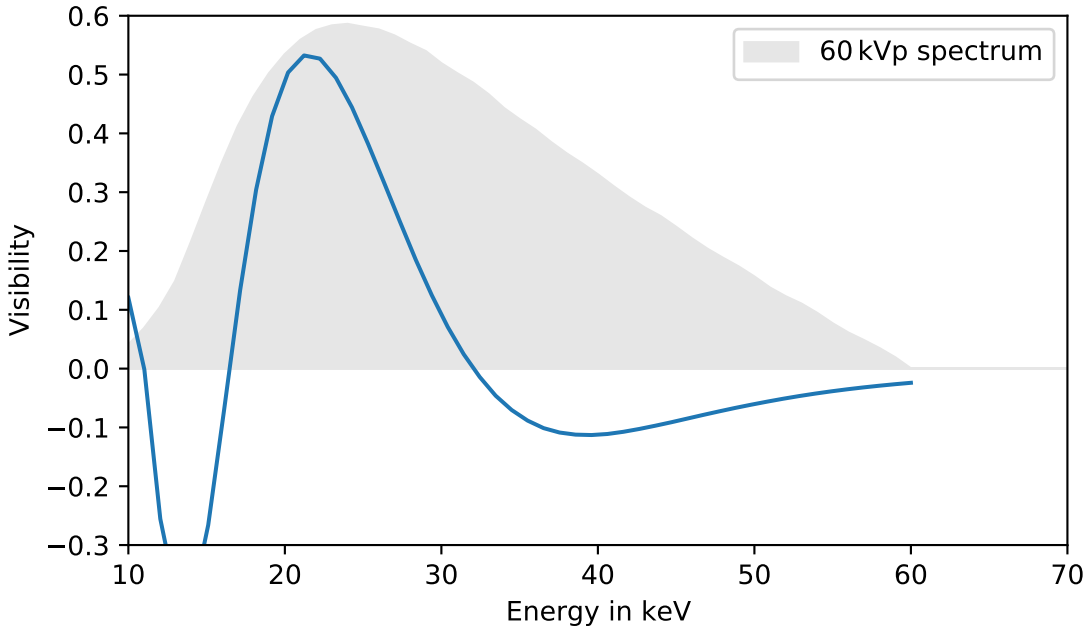

Figure 3.7: Spectral visibility plot for a simulation of a Talbot-Lau interferometer with a $\pi/2$ phase-shifting G_1 designed for 21 keV in a 3/4 fractional Talbot distance geometry. As expected, the peak visibility is found at 21 keV, however, for other energies significantly lower and even negative visibilities, i.e., where the Moiré fringe pattern is inverted, are found.

spectrum for a 40 kVp tungsten-anode X-ray source with a 0.8 mm aluminum filter is shown in Figure 3.7.
The resulting poly-chromatic stepping curves can then be processed with the Fourier processing approach. This returns the mean intensity of the stepping measurement, the interferometer visibility, and phase of the simulated system for the specific X-ray spectrum. For the example simulation presented throughout these sections the poly-chromatic mean visibility results to 22%.
By evaluating several adjacent detector pixels also the density of Moiré fringes on the detector can be estimated. This can be achieved by calculating the phase gradient between the stepping curves of neighboring pixels, which then can be converted to Moiré fringes per mm.

Shadowing in Grating Structures 4

In this chapter the shadowing artifact is closely evaluated. It is a common phenomenon in X-ray absorption grating structures and is one of the most important challenges for clinical dark-field CT. The origin of shadowing and several solutions and their realization are evaluated. First the focus is on the shadowing due to the divergence of the beam geometry, which can be compensated by bending the gratings. Afterwards, the grating acceptance is introduced which describes the shadowing caused by the size of the X-ray source spot. The latter is usually not troubling laboratory implementations, but can become highly critical for clinical dark-field systems.

4.1 Divergence-Induced Shadowing

At synchrotron facilities X-ray Talbot-Lau interferometers use an almost parallel beam and thus perform well with planar gratings. However, when this grating-based imaging method is used in a diverging beam performance limitations can arise. Such a diverging beam is commonly found in laboratory and clinical setups where the X-ray source is point-like. For this section, the source spot is approximated as a point from which spherically diverging radiation is emitted, a simplification which omits that the source spot is usually extended. This restriction will be lifted in Section 4.5 where consequently the effect of an extended X-ray source is discussed.

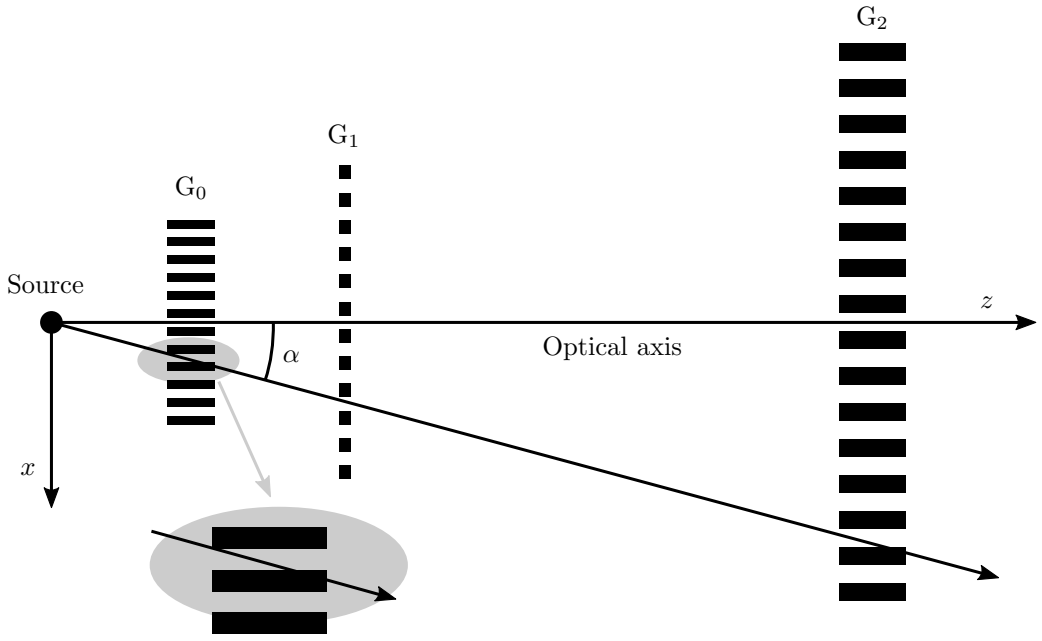

Figure 4.1: Illustration of a set of planar gratings in a divergent beam. The incident angle of the radiation onto the grating structure varies and depends on the distance from the optical axis.

In Figure 4.1, the illustration shows that the majority of rays intersects the gratings at a non-zero incident angle,

$$\alpha \quad = \quad \arctan(x/z) \; , \tag{4.1}$$

with z the distance from the source spot along the optical axis and x being the distance from the optical axis. Only a small fraction of the field of view around the optical axis intersects the grating setup under a perpendicular incident angle and thus performs similar as in a synchrotron implementation. Further away from the optical axis two problems arise which can significantly lower the performance of a Talbot-Lau interferometer.
As can be seen in the illustration in Figure 4.1 different ray paths have varying propagation lengths between the gratings. In designs which require specific propagation distances, e.g., into a certain fractional Talbot order, this effect can lead to performance issues due to the flat geometry of the gratings. In laboratory setups usually small detectors or X-ray tubes with limited opening angle are used, thus, the change in propagation length is negligible, particularly when poly-chromatic radiation is used. In a clinical CT gantry the opening angle, however, is roughly $\pm 25°$ which would lead to 10% longer propagation distance for the outer ray compared to the ray along the optical axis.
Another issue is referred to as shadowing and arises from the profile of the grating structures for X-ray Talbot-Lau interferometry. The fundamental problem is the increasing penetration power of harder X-rays which makes the design of compatible absorption gratings difficult. The gratings must have a non-negligible extension along the optical axis to be able to sufficiently attenuate the radiation. This structure height of the attenuating grating lamellae combined with a non-perpendicular angle of incidence leads to shadowing. An example illustration of the effect is shown in Figure 4.2. As a consequence of shadowing, the intensity profile behind the grating is no longer a binary line pattern. Instead, it degrades to a trapezoidal intensity pattern, depending on the angle of incidence. At an angle of incidence,

$$\alpha_\mathrm{m} \quad = \quad \arctan(p/h) \; , \tag{4.2}$$

with p and h denoting period and height as defined in Figure 4.2, the first contrast minimum is reached. In this case, the radiation traverses the grating structure in a way that all rays have the same interaction length with the attenuating material. Thus, the intensity profile behind the grating is only changed in absolute intensity but no line pattern is imprinted.

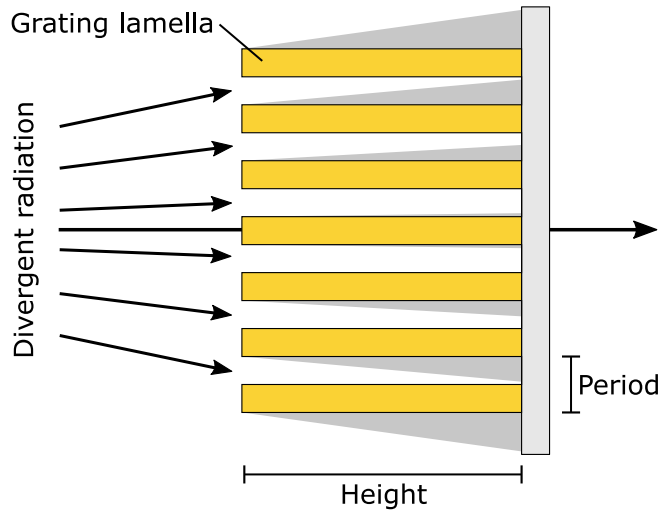

Figure 4.2: Illustration of shadowing at an absorption grating with high aspect-ratio. A cross-section perpendicular to the grating lines and the grating substrate is shown. There is no or only minor shadowing for rays with perpendicular angle of incidence. For off center rays shadowing increases perpendicular to the grating lines. Along the grating lines shadowing does not change, thus, the effect is direction dependent.
Image adapted from [140] CC BY.

Since in this work only one-dimensional gratings, i.e., line patterns, are used and no two-dimensional patterns as, e.g., demonstrated by Gustschin et al. [39], the shadowing effect only appears perpendicular to the grating lines. For each ray, the angle of incidence can be separated into components parallel and perpendicular to the grating lamellae. Only the component perpendicular to the grating lamellae leads to shadowing, while the remaining one leads to an increase of path-length through the grating. The later can actually be used to increase the effective height of the gratings by tilting the gratings in the direction of the beam-path but is negligible for the evaluation of shadowing. The strong direction dependency can be used for grating analysis as proposed by Schüttler et al. [114] and Gustschin et al. [41]. This recently developed grating characterization method can evaluate lamella inclination angle, height, and duty-cycle of gratings.
For Talbot-Lau interferometry the shadowing, i.e., unwanted attenuation and variance of effective grating profile, reduces the system performance. To reduce the effect gratings with a smaller aspect-ratio should generally be preferred for grating-based imaging with divergent radiation. For phase-gratings this usually can be realized by using a material with strong phase-shift, e.g., gold instead of nickel. However, for absorption gratings there are currently no alternatives to gold. This is because other materials with better radiation absorption properties, such as lead or tungsten are significantly more difficult to handle. For these materials often no electroplating at similar quality is possible or it is at least more difficult. Therefore, two approaches are discussed in the following sections which avoid shadowing by adapting the geometry of the grating profiles.

4.2 Focused Grating Lamellae

The parallel lamellae of conventional gratings, as shown in Figure 4.2, can be interpreted as collimator slits which are focused onto infinity. An obvious approach to avoid shadowing is to adapt this focusing distance to the actual X-ray source spot. This can be achieved by adapting the inclination grating structures to the divergence of the radiation. As illustrated in Figure 4.3, the inclination of every individual lamella must be set depending on its distance to the optical axis.
Besides the difficult fabrication of such a focused grating designs there are also two practical aspects which must be considered. A drawback is the reduced flexibility of the setup because already in the fabrication process the focal distance, i.e., distance between X-ray source spot and grating, is fixed. Installing the grating at another distance would lead to new shadowing. Furthermore, precise positioning of the grating is required to match the optical axis with the center of the grating. Only then all grating slits are correctly adjusted to the source spot and shadowing can be avoided.
Another challenge is the fabrication of such focused gratings. They can no longer be fabricated with the standard LIGA process because this process can only produce parallel lamellae. A solution are alternative processes which can produce divergent structures. Recently Shi et al. [115] demonstrated first fan-shaped or focused gratings based on a deep reactive ion etching process in silicon substrates. In this initial work the author achieved an aspect-ratio of 27 with a grating width of approximately 10 mm for a focus distance of 50 mm. The results clearly demonstrated an increase in X-ray flux as fewer photons are absorbed by shadowing in their G_0. It also improved the visibility of their interferometer as an improved homogeneity over the entire field of view was achieved.
An alternative fabrication method is a modified LIGA approach which uses a divergent X-ray source for lithography through a planar mask into a planar photo-resist. This can, for example,

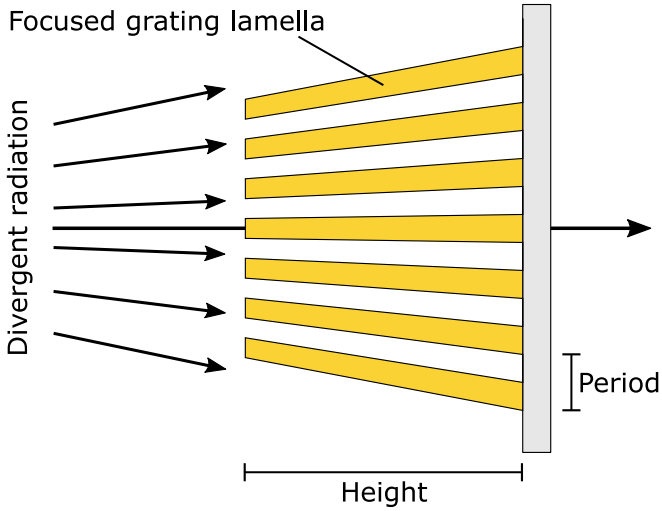

Figure 4.3: Illustration of a divergent grating which can efficiently compensate shadowing despite the large aspect-ratio. A cross-section perpendicular to the grating lines and the grating substrate is shown. Since the focal distance is set by the inclination of the lamellae these gratings can only be used at a certain distance from the X-ray source spot. The grating must also be precisely positioned to align the optical axis with the vertical lamella of the grating.
Image adapted from [140] CC BY.

use a laboratory X-ray tube as has recently been demonstrated by Pinzek et al. [97]. In this work, however, shadowing in the mask during the lithography exposure was identified as a problem. As a solution, the mask and substrate can be bent during the lithography exposure which strongly reduces the shadowing. Unfortunately this also removes the focusing in the resulting grating profile and thus is no solution for production of focused gratings. Currently the maximum demonstrated aspect-ratio of this fabrication approach is 17. This is significantly lower than the aspect-ratio of 100 which is commonly achieved in other LIGA applications (see Section 2.5). One advantage of this is laboratory X-ray tube based approach remains that already large grating areas $> 60\,\text{mm}$ have been demonstrated in the initial experiments.
For clinical CT, however, the hard X-ray spectrum and large coverage in fan direction require excessive up-scaling of both these fabrication methods.

4.3 Bent Gratings

An alternative approach to focus the grating slits into a focal spot is to bend the conventional flat grating to a cylindrical shape. In this process, the substrate and the grating structures are deformed together as one multi-layer object by applying mechanical force. The elegance of this approach is that as the grating substrates are elastic the focal distance can easily be changed by adapting the bending radius. This makes the design much more flexible than the focused grating design discussed in the previous section.
In Figure 4.4, an illustration of a bent grating shows how the deformation leads to a focusing of the grating slits. For better visualization a high aspect-ratio and strong curvature is chosen. In a real implementation, the deformation of the grating structure is relatively small, and the substrate is significantly thicker than shown in this sketch.
Precise positioning of the bent grating to focus into the X-ray source spot is an important requirement, similar as in the focused grating lamellae design. In contrast to the planar grating design with focused lamellae, the bending of the gratings to a cylinder surface leads to a radial symmetry of the entire setup. As a positive side effect this achieves constant propagation distances between the individual gratings for all rays. This requires obviously that all gratings of the interferometer are bent and focus into the X-ray source spot. Consequently, bent gratings cannot always be combined with flat gratings, including the planar grating design with focused lamellae. There are implementations where for example a planar G_0 is combined with bent G_1

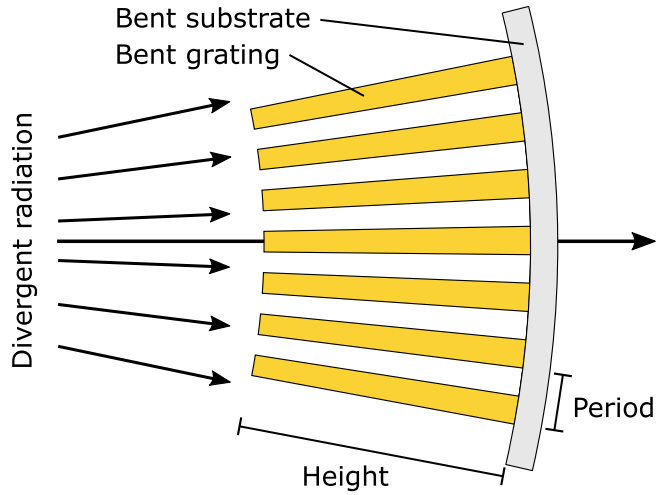

Figure 4.4: Illustration of a bent grating which can efficiently compensate shadowing despite the large aspect-ratio. A cross-section perpendicular to the grating lines and the grating substrate is shown. A planar grating is bent to a cylindrical shape by applying mechanical force to the substrate. The deformation leads to a focusing of the grating slits. Since the bending radius can be varied refocusing to another focal length is possible.
Image adapted from [140] CC BY.

and G_2 as demonstrated in [132]. In most cases these systems have rather small field of views. For larger field of views such a design must be carefully evaluated.

4.3.1 Substrate Materials

A standard substrate material for grating substrates is silicon because it is a well-understood material. Furthermore it is widely available in high quality, both these aspects are boosted by demands from the semiconductor industry. For grating fabrication by a silicon etching-based processes it is the only suitable material as this process relies on the material properties and the high purity. Silicon is also often used in the LIGA based grating fabrication process, but also a wide variety of other materials is possible.
A fundamental requirement for shadowing reduction by bending the gratings is mechanical flexibility of the grating. Unfortunately, silicon is a relatively brittle material which limits the ability to bend silicon-based gratings. Nevertheless, some bending is possible with the limitation to relatively large radii. Experiments demonstrated that 1 mm thick silicon wavers and etched absorption gratings in silicon can be bent to a radius around 1000 mm. An example of a bent silicon waver is shown in Figure 4.5. Experimental results of such 1 mm thick silicon wavers bent to a radius of about 1000 mm have recently been published by Pinzek et al. [96].

Figure 4.5: Photo of a 1 mm thick silicon waver bent to a radius of 995 mm. The substrate has been cut to a rectangular shape and is approximately 65 mm wide. In [96], recently silicon-based absorption gratings produced by a new fabrication process have been demonstrated. There a centrifugal tungsten deposition has successfully been used to fill the gratings with the absorber material.

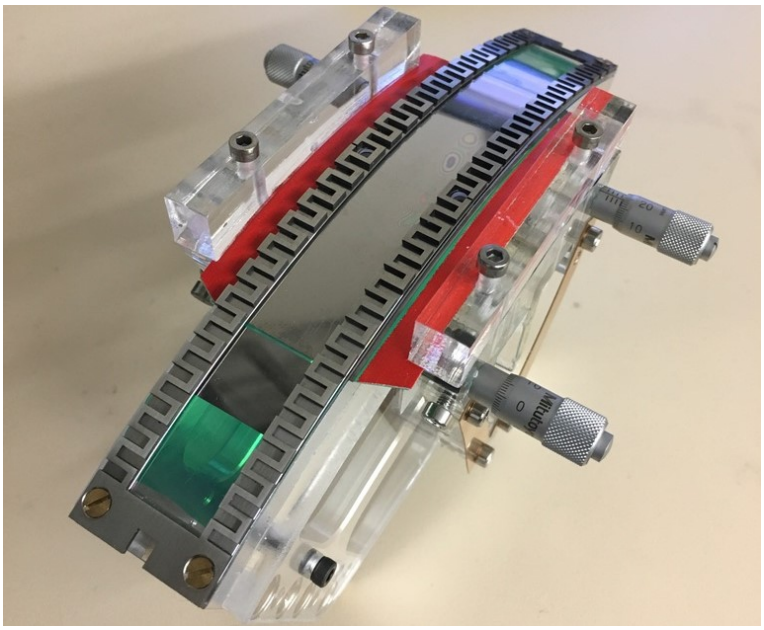

Figure 4.6: Photo of a prototype to evaluate bending and adjustment of 200 µm thick silicon substrates. Multiple differently sized silicon substrates are here bent to a cylindrical shape with radius of approximately 180 mm. The wavers are mounted on a plastic tape (here in green) which stabilizes the process and acts as a splinter protection.

For thinner silicon substrates also smaller radii are possible. For example 200 µm thick wavers have successfully been bent to approximately a radius of 180 mm. However, then the material is in no forgiving state and easily scatters. During the experiments with the thin wavers spontaneous scattering was observed. It was probably caused by internal defects or local stress from, e.g., thermal expansion or mechanical pressure. By mounting the brittle 200 µm waver on a thick plastic tape (200 µm thick PET foil) handling and bending can be relaxed as mechanical stress is better distributed. In Figure 4.6, an example of a bent 200 µm thick silicon waver mounted on a transfer tape is shown.
These experiences with silicon substrates led to the conclusion that it is not an ideal substrate material for designs which require small bending radii. For silicon etching-based grating fabrication processes this is a fundamental problem since the substrate material cannot easily be replaced by a more flexible one. In contrast, the LIGA fabrication method does not strictly rely on silicon as a substrate, thus, alternative materials, which have better mechanical properties, can be used. For example, graphite and polyimide (also referred to as Kapton) have successfully been eventuated as alternatives which also have lower X-ray attenuation than silicon [66]. Both materials are significantly more flexible than silicon and are regularly used for grating fabrication.
The thickness of the substrates can vary with common thicknesses being 0.5 mm and 1 mm for graphite, and 0.5 mm for polyimide. Experiments showed that both materials allow small bending radii because they are flexible and remain stable. The smallest tested bending radius has been 100 mm with substrate thicknesses of 0.5 mm for both materials, an example can be seen in Figure 4.7. It is likely that even smaller radii are feasible. This is an important milestone for bending-based shadowing reduction because the stability of the setup is no longer affected by instabilities of a brittle substrate which might spontaneously scatter.
Alternative grating substrate materials for future evaluation might be the materials which are currently used as filters in CT systems. For example titanium and aluminum are often used to optimize the spectrum. Using those as substrates of the gratings would reduce the attenuation induced by the added components. However, the increase of flux would be comparably small and a significant effort is required to optimize the fabrication process on another substrate material. Hence, the well evaluated graphite and polyimide are currently the most promising choices as grating substrates in clinical CT.

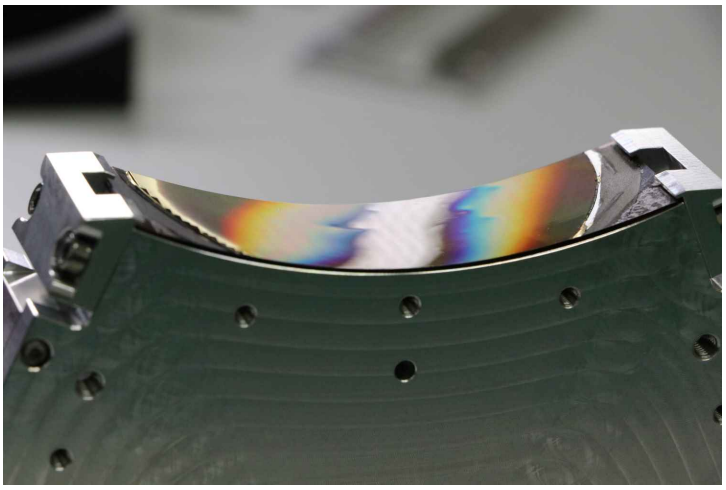

Figure 4.7: Photo of a 500 µm thick graphite substrate with a grating fabricated with the LIGA process. It is bent to a 100 mm radius.

4.3.2 Bending Procedures

As previously introduced, the flat grating is bent to a cylindrical shape by applying mechanical force. While it should ideally have a spherical shape this is not required for 1D gratings which are discussed here because shadowing only occurs perpendicularly to the grating lines. Specialized mounts made of plastic, steel, or aluminum have been used as bending frames. The contact surfaces should be flat or polished and can be covered by a layer of PTFE-tape (Teflon® tape) to reduce friction induced stress during the bending process. Additional layers of, e.g., tape, however, can lead to inaccuracy of the final grating position, particularly as such tapes are often compressible.
The particular mechanical realization to bend the grating to the desired radius depends on the setup design and the requirements to be able to adjust the grating.

Clamp-Based A common construction uses curved clamps to grab the substrate from two sides [111]. This is advantageous because the bent grating is firmly gripped by the clamps and can still be adjusted by moving it including the clamps. A drawback is that the clamps and the adjustment frame must remain as a part of the setup, consequently, this design requires some space around the grating. In Figure 4.8, an example of 3D-printed clamps bending a graphite substrate is shown. The clamps grip the substrate next to the structured area to have a large contact surface with the substrate but not reach into the X-ray beam.
When a larger grating surface is required one option is to switch to plastic clamps which then also grip the grating within the structured area and the X-ray beam. The material must then be chosen to have sufficient mechanical stability and simultaneously have low X-ray attenuation. Besides plastic also thin carbon reinforced parts might be an option. As long as the polymer-resist remains as a stabilizing matrix between the gold structures clamping within the structured area is feasible. Otherwise, the structures can easily be damaged by the pressure from the clamps.
A rather technical disadvantage of this approach is the constraint to a specific thickness of the grating, i.e., combined thickness of substrate and structure. This means that a given pair of clamps can only be used with a specific grating thickness. Furthermore, it has only little tolerances as a too loose fit leads to instability and wrong curvature and a too tight fit can destroy the grating. While the thickness of the substrate is usually relatively stable the resist thickness can easily vary by several tenths of micrometers. When the clamps only grip in the unstructured area this problem can be minimized by removing any residual resist in the clamping area.

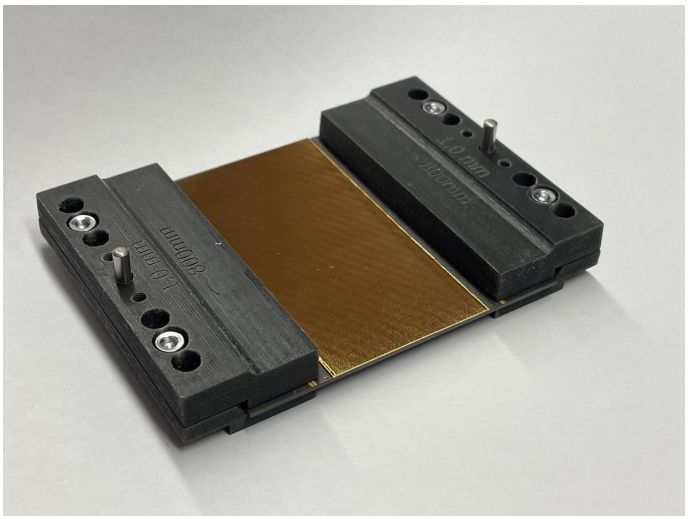

Figure 4.8: Photo of a **clamp-based mount** with a 1000 µm thick graphite waver bent to a radius of 800 mm. It is forced to the cylindrical curvature by large curved clamps which grip the substrate next to the structured area. When using silicone substrates the applied pressure must not be too large as the brittle material might scatter if it is squeezed between the two clamps. Other substrate materials, such as polyimide or graphite, are more tolerant which simplifies the installation process.

Manipulator-Tape-Based An alternative is the use of a manipulator-tape which is attached to the grating substrate. Previously it has been introduced as a stabilizing tape for thin 200 µm silicon substrates and is here adapted to also allow adjustment of the grating. An early prototype has been shown in Figure 4.6 and a more advanced implementation is presented in Figure 4.9. The bending is realized by pushing the grating and manipulator-tape construction onto a curved surface, e.g., using a spring-loaded mechanism.
For adjustment of the grating motorized stages can be used to move the manipulator-tape. These allow translation and rotation of the grating in all degrees of freedom on the cylindrical surface. Once the position and alignment of the grating is optimal, the motorized stages can be removed. Then the spring load can be increased to ensure that the grating does not move. If

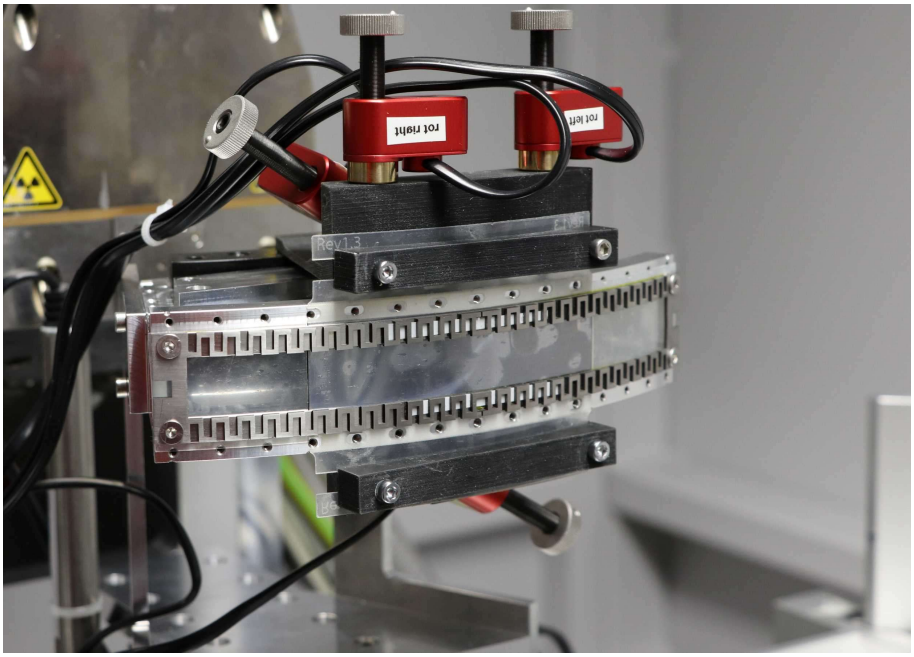

Figure 4.9: Photo of a **manipulator-tape-based mount** which is used to simultaneously bend and adjust a grating mounted on a manipulator-tape. The tape allows motorized stages to push and pull the grating to the correct position. After adjustment is finished the mechanical parts can be removed and the protruding flaps of the manipulator tape can be cut away. Then the aluminum mount and the bent grating are an extremely compact and stable construction.

required, screws can be added to establish an even better connection between manipulator-tape and the holder. Ultimately, the protruding ends of the manipulator-tape can be cut away.
The advantage of this procedure is the small size of the bent grating and mounting unit once the alignment is done. Furthermore, it realizes that the grating is always bent to the center of the curved surface onto which it is pressed. This cannot be achieved by the previous alternative method which is based on clamps only. The spring-loaded bending mechanism has the advantage of being compatible with a wide variety of different grating thicknesses. Only when differently thick substrates are placed next to each other the compression mechanism no longer works and bending fails. This can be solved by adding, e.g., additional spacers to compensate the differences.

Clip-Based An even more compact bending method inserts the grating like a clip between two radially pushing clamps. These keep the bent grating under compression, so it cannot move. An example implementation is shown in Figure 4.10 with a small bending radius of 100 mm.
While this construction has a minimal footprint, it is difficult to initially bring the grating into the bent state and then attach the clamps with the appropriate torque. Furthermore, once the grating is positioned, it cannot be adjusted in any way, except by moving the entire construction.
This method relies on precise slicing of the grating to the required dimensions. If the width is not correct or the two edges are not parallel to each other the bending procedure will fail, or the result will not be stable. As shown in Figure 4.10, it is possible to adapt the clamps to the length of the grating if it is longer as the support surface. Here, the clamps have been 3D printed which allows fast optimization of the prototype design as different clamp lengths are evaluated.

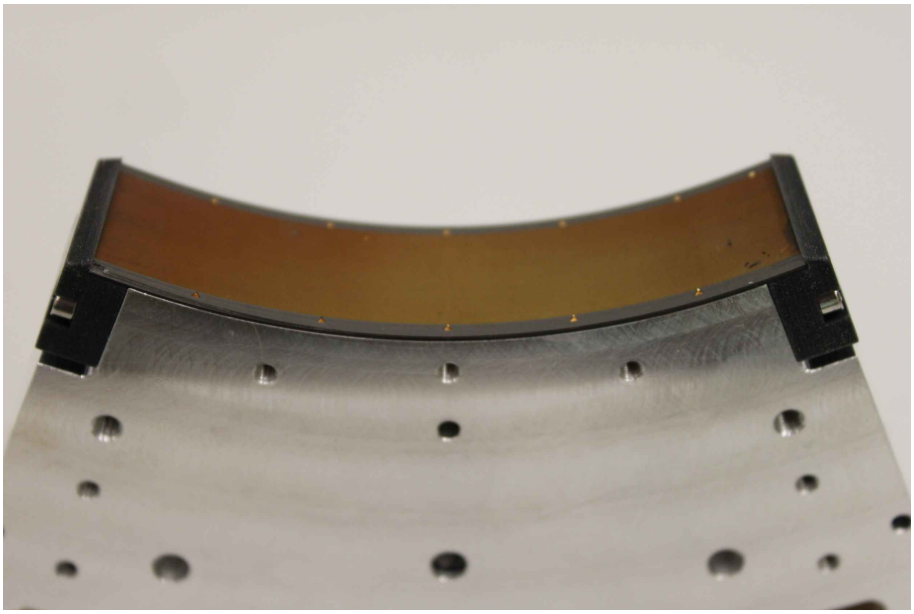

Figure 4.10: Photo of a **clip-based mount** of a bent grating. It is installed between two clamps (black) which hold the grating like a clip under sufficient tension. Thereby it is pressed onto the curved aluminum surface with the demanded bending radius. This concept has a minimal footprint and offers a high stability once the grating is in place. However, the installation process to bend the grating and apply sufficient pressure through the clamps is a challenge.

4.3.3 Internal Stress and Defects in Gratings

The concept of bending a planar grating to a cylindrical form clearly relies on some sort of deformation of the grating structure and of the substrate. In an earlier sketch in Figure 4.4, this has been illustrated in an exaggerated way for ease of visualization. In this section, the deformations from internal stress in a LIGA process fabricated grating are discussed. This evaluation then leads to the analysis of what kind of deformations occur during mechanical bending of such gratings.
Currently, the precise deformation processes within a grating are not clear and only with an angular X-ray transmission analysis (AXT) [41] some insights are possible. This evaluation method, however, requires the grating to be planar and is not yet available for bent gratings. Direct analysis based on microCT are difficult because of the high attenuation in the gold lamellae. Common artifacts are beam starvation which make the interpretation of the reconstructions difficult. Evaluation using optical and electron microscopy are limited to the surface and provide no information on the inner structure of the gratings.
Furthermore, the mechanical properties of the polymer-matrix into which the gold lamellae are embedded, i.e., the former photosensitive resist during the LIGA process, are unknown. The fine structure, the various chemical processing steps, and aging of the polymer-matrix make it difficult to be analyzed.
The current hypothesis is that, in contrast to the substrate and the gold lamellae, the polymer-matrix can be easily compressed during the bending process. This is motivated by observations that the grating structures tend to shrink after the fabrication. Similar as in a bi-metal the shrinkage of the grating structure which is mounted on the substrate leads to a bending. This is illustrated in Figure 4.11. Here, a thick grating structure ($h > 300\,\mu m$) is fabricated on a thin graphite substrate which is 500 µm thick. During the fabrication process the whole structure is forced to be flat to ensure a stable grating period and the intended inclination of the lamellae. However, after the fabrication is finished and the grating is diced to its final rectangular shape a significant deformation can be observed. An example is of such a deformed grating is shown in Figure 4.11. It bends along the grating lines which is probably caused by shrinkage of the

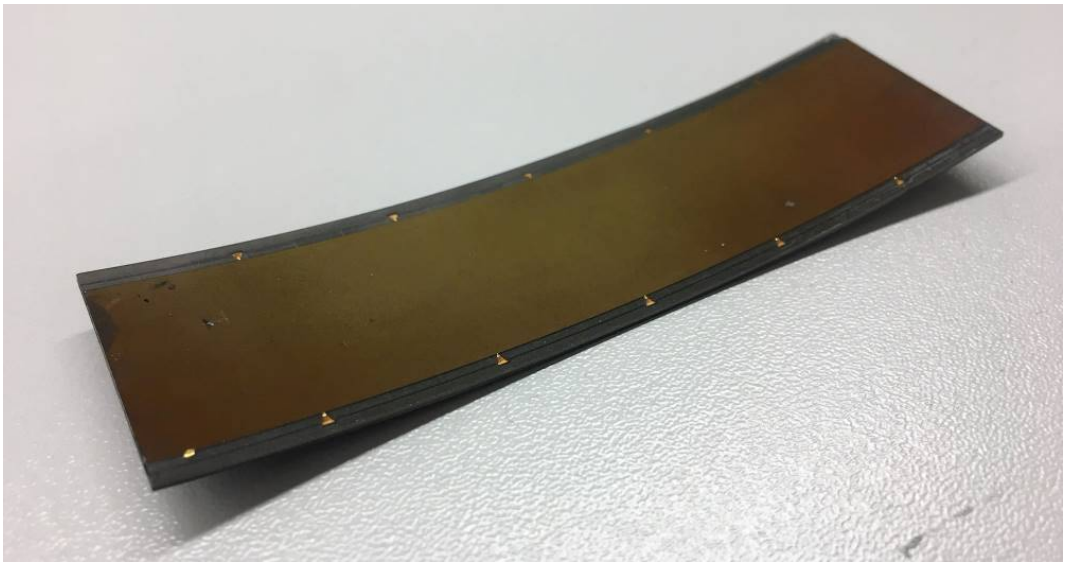

Figure 4.11: Photo of a grating fabricated on a 500 µm thin graphite substrate with a relatively thick polymer-matrix for a grating with a height larger 300 µm. It is assumed that the shrinkage of the polymer-matrix leads to the deformation and bends it similar as in a bi-metal.

grating structure and no sufficient stability of the substrate to keep the grating in its original flat shape.
The shown example is an extreme case where a thin graphite substrate, which is relatively flexible, cannot counter the shrinkage of the thick polymer-matrix layer. For a better illustration of the deformations in Figure 4.12 three cases are shown to demonstrate the possible changes to the grating structure. In Figure 4.12a, an ideal grating where the polymer-matrix shrinks without deforming the structure is shown. However, due to the bonding between grating lamellae and polymer lamellae, and bridges (not included in the sketch for ease of visualization) this behavior is not realistic. The alternative case, in Figure 4.12b, where the shrinking of the polymer-matrix is relaxed through deformation of the whole grating includes that the length of the substrate remains constant. In consequence, assuming a flexible substrate, this leads to a bending of the grating to relax the stress induced by the shrinkage. If the grating, however, is forced to be on a flat substrate, i.e., by a stiff and stable substrate, the stress can also lead to defects as indicated in Figure 4.12c. The cracks form to reduce the internal stress locally and deform the grating lamellae in the respective area. This leads to a change of grating lamella inclination depending on their position relative to the neighboring cracks. In the center between two cracks the lamellae remain perpendicular to the substrate surface but close to the cracks the inclination is changed away from the crack. Certainly, also a mixed state between Figure 4.12b and c is possible.

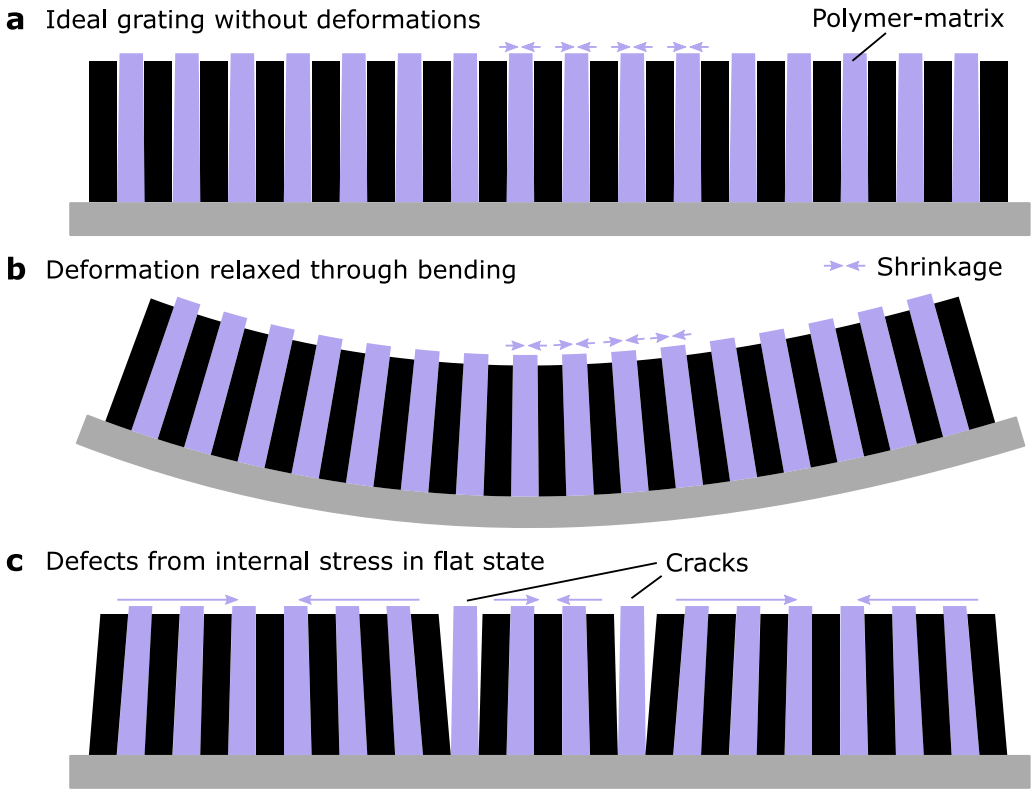

Figure 4.12: Effects how shrinkage of the polymer-matrix, i.e., resist, deforms the grating profile visualized in a cross-section of a grating. In an ideal grating the lamellae should remain in their original vertical inclination. However, the bounding forces between the grating lamellae walls and the polymer-matrix walls are not easily broken apart, thus, either the entire grating is bent or cracks are formed to relax the internal stress. This depends on the stability of the substrate, i.e., whether it can maintain the flat state.

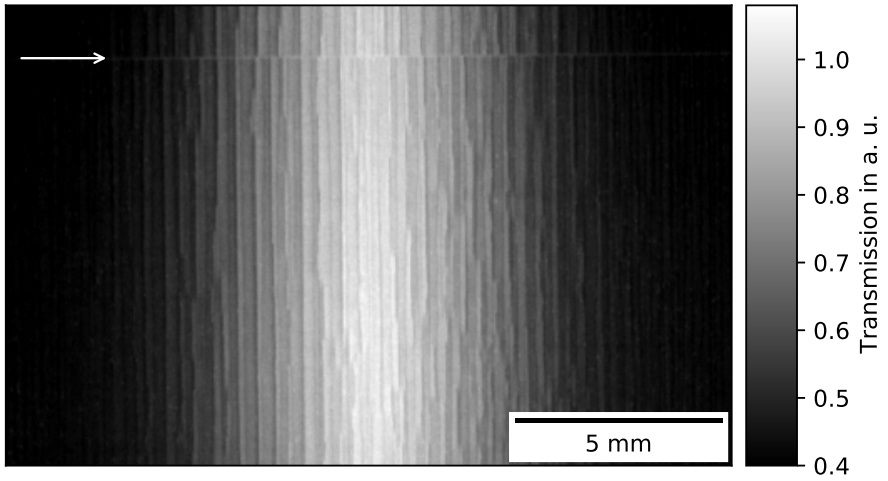

Figure 4.13: Transmission image of a flat grating with crack-like defects parallel to the grating lines. Besides typical shadowing from the divergence of the X-ray beam fine variations in the transmission are visible. These are caused by local changes of lamella inclination between cracks which leads to more or less shadowing depending on the direction of inclination, i.e., towards or away from the source. The white arrow indicates a stress release line which is part of the grating layout. A line plot through the center of this image can be found in Figure 4.15.

While this description is purely hypothetical, there are many observations supporting this model. Clearly, the grating shown in Figure 4.11 is an extreme example for the bending from internal stress. However, regularly also gratings with thicker substrates show defects which are likely being induced by internal stress. These manifest either as some minor bending of the grating, occurrence of crack-like defects, or a combination of both.
An example of a flat grating with crack-like defects is shown in Figure 4.13. This absorption grating with a period of 4.8 µm has been evaluated at a microfocus X-ray source and a high-resolution detector. To achieve a high geometrical magnification the grating was positioned close to the source. The scale bar in the figure relates to the position in the grating plane. A strong transmission variation with its maximum in the center, i.e., where X-rays transverse vertically through the grating slits, is visible. The transmission decreases towards the left and right, i.e., perpendicular to the grating lines. As has been discussed earlier in this chapter, this behavior is referred to as shadowing. It regularly occurs when planar high-aspect-ratio gratings are used in divergent beam geometries and has been illustrated in Figure 4.2. In the following discussion we refer to this shadowing as global shadowing because the transmission profile covers the entire grating area.
Besides the global shadowing the high resolution of the image also reveals finer structures. While the system cannot resolve single grating lamellae it can show characteristic transmission variations on a length scale around several hundred micrometers. This allows to resolve transmission variations caused by several hundred grating lamellae. The observed patterns are primary vertically aligned, and thus, parallel to the grating lines. Similar to the large-scale or global shadowing also the fine pattern consists of gradient like changes of transmission These are, however, on a much shorter length scale and come from local variations in the grating lamella inclination angle. The varying inclination leads to local increase or decrease in shadowing depending on the direction the lamellae are bent. If several lamellae are bent towards the X-ray source spot the transmission increases, otherwise it decreases. Thus, the change of measured intensity can be related to a variation of the mean inclination angle of the grating

lamellae. One can extend this evaluation by applying the AXT analysis method [41]. This exploits this effect to actually retrieve quantitative information from those images.
Besides the global and the local shadowing from beam-geometry and varying lamella inclination, respectively, also a horizontal line is visible. It is indicated by a white arrow in Figure 4.2. This is one of several stress release areas in the grating layout which discontinue the fine line pattern. This should help to stabilize the overall structure by discontinuing the defect lines.
One should note, that the discussed local defects are unique for each grating and depend strongly on the specific fabrication parameters. In most interferometer implementations the shadowing from the divergence of the beam geometry is the most dominant artifact. It degrades the system performance particularly in the outer regions. The local defects and stabilization areas contribute usually only minimal to a visibility loss and are easily blurred away by a large X-ray source spot. This is possible, as the defects and stabilization areas are on a small length scale and are difficult to resolve in most imaging setups.

4.3.4 Deformation during Bending

The previous section revealed that gratings fabricated by the LIGA process can undergo internal changes which lead to stress and subsequent deformation or defects. The formation of crack-like defects can be seen as a consequence of the grating structure not being able to deform into a curved state because the substrate is too stiff. Therefore, the concept of actively bending a grating to reduce the shadowing of radiation can counteract these defect structures and increase grating performance.
Given these considerations the only reasonable orientation of the grating for bending is *source facing*. This means, that the structured grating surface faces the X-ray source spot while the substrate is towards the detector. In this case, the bending process leads to a compression of the grating structure. As a side-effect this can then revert the crack-formation process by closing the gaps and bending the lamellae back to a straighter inclination angle. In contrast,

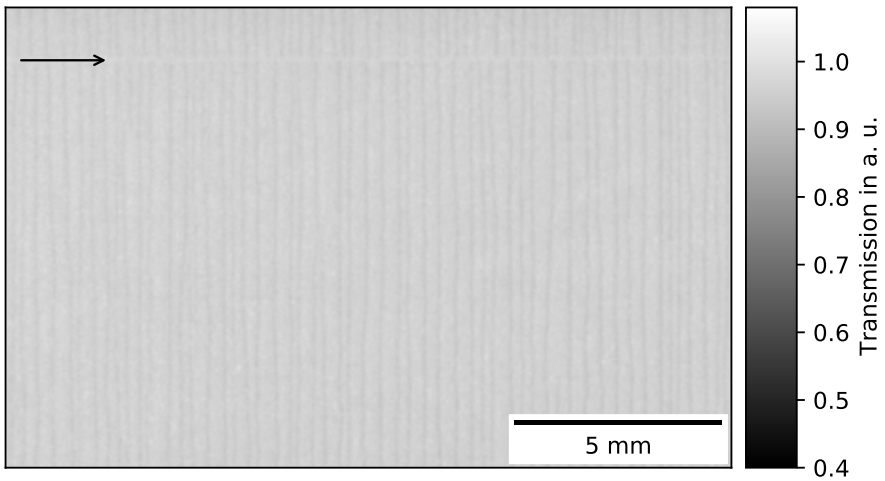

Figure 4.14: Transmission image of a bent grating with remaining defects from former cracks seen in Figure 4.13. The shadowing from the divergent geometry and most of the local shadowing due to crack-like defects are removed by bending the grating. The black arrow indicates a stress release line which is part of the grating layout. The color bar and magnification is the same as in the previous image in Figure 4.13, which represents the unbent state. A line plot through the center of this image can be found in Figure 4.15.

if the orientation was reversed, i.e., the grating structures would face towards the detector, the cracks would extend further. For gratings with small aspect-ratios this *detector facing* bending might work as there the deformation processes are smaller.
To demonstrate the performance of the concept of bent gratings the previously analyzed flat grating is bent to a 100 mm radius. In Figure 4.14 the transmission image through this bent grating is shown. The global shadowing, previously caused by the divergence of a cone-beam, is completely removed. The transmission is homogeneous and as high as previously only in the central area.
Since the grating is source facing, the crack-like defects have also been reduced. Only a faint residual defect pattern of the vertically aligned lines with slightly lower transmission remains. These can also be found in the line plots shown in Figure 4.15. It reveals that by bending the overall X-ray transmission can be significantly increased. The blue curve shows that flux decreases rapidly for increasing fan angles in the flat grating case. In contrast, with a bent grating the transmission profile is almost independent of the fan angle.
In both line plots in Figure 4.15 the local shadowing from the crack-like defects can be found. In the bent state these fluctuations are significantly smaller than in the unbent case. This can mean, that the induced compression is not yet sufficient to close the gaps entirely. It possibly requires a smaller bending radius or it might indicate that the crack-like defects are not entirely revertible.
Clearly a defect and shadowing free transmission profile would be preferred. Nevertheless, the achieved increase in total transmission and reduction of defects by cylindrical bending is a milestone. It allows to realize high performance Talbot-Lau interferometers with a large coverage perpendicular to the grating lines. The fundamental idea to bend gratings has regularly been demonstrated in previous work, e.g., [100], [112], [132]. However, in most setups just one or two gratings have been bent. Recently Wu et al. [150] demonstrated a non-interferometric setup with three bent gratings. Unfortunately no experiences on the bending process or a characterization of the bent gratings performance have yet been published on this setup.

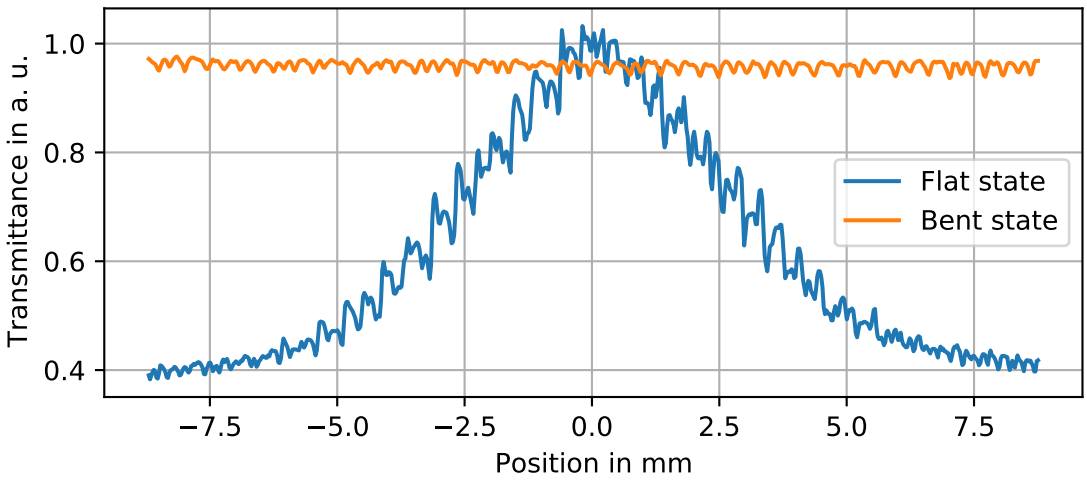

Figure 4.15: Line plot horizontally through the center of the transmission data shown in Figures 4.13 and 4.14. The strong loss in transmission for a flat grating due to shadowing from the divergent geometry can efficiently be compensated by bending the grating. The crack-like defects also get reduced when the grating is bent as can be seen by the decrease in local variation between the line plots.

4.3.5 Change of Grating Period

In Talbot-Lau interferometry the grating parameters, particularly the grating pitch, are important and are usually considered to be constant. To evaluate whether thermal expansion and mechanical compression have an influence on this sensitive parameter the orders of magnitude of these effects are estimated in the following paragraphs.

Thermal Expansion Effects from thermal expansion can usually be neglected as the expansion coefficients of the used materials lies in the range of 5 to 20 µm/m/K [31]. Thus, the change of the period is only 0.005‰ to 0.02‰ for every Kelvin of temperature drift. Thermal expansion has therefore only the potential to invoke period variation in the sub-nanometer range:

$$\Delta p = p \cdot \tau \tag{4.3}$$
$$\Delta p = 4.8\,\mu\text{m} \cdot 20\,\mu\text{m/m/K} \tag{4.4}$$
$$\Delta p = 0.1\text{nm/K}\,, \tag{4.5}$$

with τ denoting the thermal expansion coefficient of Kapton (20 µm/ m/K) and a grating period p of 4.8 µm. For other materials used in grating fabrication this coefficient is usually even smaller. Considering system-wide temperature stability within a couple of Kelvin the effect of thermal expansion of the gratings can safely be neglected in the system design.
Particularly as also other parts of the setup, e.g., mechanical parts, are easily affected by thermal expansion slow phase-drifts due to thermal expansion can not be avoided. These must be compensated by measuring references and appropriate processing, or active thermal stabilization of the entire system.

Mechanical Compression In contrast to thermal expansion, mechanical compression as induced by bending the gratings can easily lead to a change of the grating period. Here, a simplified model is introduced to demonstrate that the deformation from bending can change the grating period. In the following discussion also a rough estimate on the length scales is presented. We expect the grating to be in flat state, i.e., without a curvature from polymer-matrix shrinkage, and the substrate being of constant thickness. The substrate thickness is denoted by s and the grating structures being of height h. For clarity, the detail that the polymer-matrix is usually slightly higher than the gold filling is neglected. It is expected that this aspect has only minimal influence on the deformation.
During the bending process the grating is deformed to a specific radius, which is inaccurate because the grating extents in radial direction. More precise is that the surfaces of the grating are eventually given as inner and outer radii, r_i and r_o, respectively. When the grating is bent, this process can be separated in two areas which are divided by a line referred to as *neutral line* or *neutral fiber*. In Figure 4.16, the model is illustrated and shows that the neutral line lies between the two radii. From the neutral fiber towards the inner radius the material gets compressed, while towards the outer radius the material is stretched. Consequently, the neutral fiber is the layer which is not deformed along the curvature and remains at the same length as in the flat state, here, referred to as length L_n.
If the bending radius is large the neutral fiber lies approximately in the center of the object. For stronger bending the neutral fiber shifts towards the inner radius as shown in Figure 4.16. In the process of single material bending, e.g., bending of metal sheets, this concept is well established, and empiric solutions are available to describe the behavior of the material. However, bending of gratings is an extraordinary field for which those empiric solutions are not available.

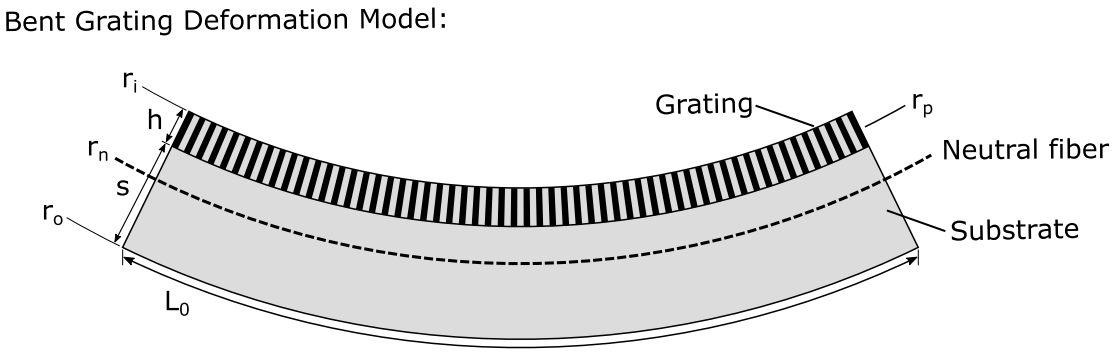

Figure 4.16: Model to describe deformation of the grating period due to bending. The neutral fiber represents the layer which gets neither compressed nor stretched and thus remains in its original length, i.e., as long as it was in the unbent state. For large bending radii the neutral fiber usually lies in the center of the object. For small bending radii it shifts towards the inner radius as indicated here. It strongly depends on the material properties of the substrate and how easily the attached grating can be compressed.

With the large variance of substrate properties, i.e., various materials and pre-processing variants, different grating heights and bridge fractions its evaluation is difficult. Therefore, the radius of the neutral fiber r_n remains unknown, nevertheless, the model allows an initial assessment of the approximate length scale and variance of the induced grating period compression one can be expected from bending a grating.
In the worst-case scenario, in which the change of the grating period would be largest, the neutral fiber lies in r_o. This represents a hypothetical case of a substrate material which is not stretchable but compressible. The surface length L_o along the outer radius thus is also the neutral length L_n of the grating. For the surface length L_i along the inner radius this means:

$$\frac{L_i}{2\pi r_i} = \frac{L_n}{2\pi r_n} \tag{4.6}$$

$$\frac{L_i}{L_n} = \frac{r_i}{r_n} \tag{4.7}$$

Inserting an outer bending radius $r_o = 100\,\text{mm}$ and a total grating thickness of 1 mm this leads to a compression of L_i by 1% of its unbent length. In this conservative evaluation, the effective grating period is interpreted at the inner grating surface. Consequently, a grating with 4.80 µm period would shrink by 48 nm to an effective grating period of 4.75 µm.
In a more realistic evaluation the neutral fiber is positioned 2/3 into the substrate,

$$r_n = r_o - 2/3\ s\ , \tag{4.8}$$

and the effective grating period in the bent state is given by the period in the center of the grating structure, i.e., in the central grating fiber at radius r_p. Thus, the grating length L_p along the layer with radius r_p must be analyzed,

$$r_p = r_i + 1/2\ h = r_o - s - 1/2\ h\ . \tag{4.9}$$

This leads to a slight variation of Equation (4.7):

$$\frac{L_p}{L_n} = \frac{r_p}{r_n} \tag{4.10}$$

$$\frac{L_p}{L_n} = \frac{r_o - s - 1/2\ h}{r_o - 2/3\ s} \tag{4.11}$$

Inserting the same grating properties as in the previous evaluation ($r_o = 100\,\text{mm}$, $s = 0.6\,\text{mm}$, $h = 0.4\,\text{mm}$) the compression of the grating structure is 0.4%. For a 4.8 µm grating this represents a shrinkage of 19 nm to an effective grating period of 4.78 µm.
Ideally, the grating period should remain unchanged or at least change as little as possible. This could only be realized by having the neutral fiber in the middle of the grating structure. However, this is not in accordance with previous observations where the polymer-matrix was found to shrink and form crack-like defects. Therefore, the most ideal case would be a neutral fiber in the inner substrate surface, hence,

$$r_n = r_o - s \ , \tag{4.12}$$

which yields a compression of the grating along the central grating fiber at radius r_p given by:

$$\frac{L_p}{L_n} = \frac{r_o - s - 1/2\ h}{r_o - s} \tag{4.13}$$

Inserting the same grating properties as used in the previous case the compression of the grating structure is 0.2%. For a 4.8 µm grating this represents a shrinkage of 10 nm to an effective grating period of 4.79 µm.
Based on these evaluations we can conclude that the bending induced compression of the grating period can be expected to be in the single digit per-thousands range. It depends, however, strongly on the bending radius, the substrate thickness and material, and the grating structure height and bridge-fraction. For simulation of Talbot-Lau setups with bent gratings in this thesis the neutral fiber is positioned 2/3 into the substrate from the outer radius, as evaluated in the second example.
Unfortunately, quantitative evaluation and validation of this model is difficult. As previously stated, the variety of grating parameters is large, which makes development of a model challenging. Particularly, when considering that even in metal sheet bending mostly empirical values for different materials are used. Furthermore, for a quantitative assessment, the change of the period must be precisely measured which is difficult as the deviations are expected to be in the nanometer range. Even if a high-resolution imaging technique would be easily available to measure the periodicity with sufficient resolution, this would only be able to measure a couple of lamellae, but not the overall periodicity of the entire grating, which consists of thousands of lamellae. Such a large area could only be evaluated in an interferometric approach where interference between patterns from two different gratings are analyzed. However, since in such a setup at least one additional grating is involved, it is unclear whether differences in the nanometer scale can be resolved quantitatively in such an experiment. Particularly, as also the additional grating might come with an unknown period and inaccuracies from the geometry and positioning of the gratings.

Suppression of Mechanical Compression To keep the change of the grating period to the minimum the neutral fiber must be in the center of the grating. This can be achieved for example by removing the substrate after the grating fabrication, or at least vastly reduce its thickness. Then the mechanical properties of the grating structure would dominate the bending process as the neutral fiber no longer lies in the substrate, but it should now lie within the grating structure. Obviously, this would come at the cost of a significantly reduced stability and might allow previously unseen internal stresses to deform the grating.
An alternative, which does not risk the stability of the grating, is to attach a second substrate on top of the grating structure. By encapsulating the grating structure from both sides the stability is actually increased. Based on the neutral fiber model this should shift the neutral

fiber into the center between the two substrates, i.e., into the center of the grating structure. The pile-up of additional substrate material, however, can be problematic as more overall thickness reinforces the grating. Thus, the increased overall stability might no longer allow to bend the new grating to the desired radius. Another issue might be caused by the two different kinds of bonding which will be involved in such a construction. Between primary substrate and grating structure, i.e., the parts processed during the LIGA fabrication, the connection is based on adhesion of the resist and electroplating of the lamellae to the substrate. In contrast, the additional substrate must be glued on top of the grating structure which might have an influence on the bending properties. While this challenge can certainly be solved, it is likely to be a rather resourceful evaluation process. It will require ready-to-use gratings and reversal of the gluing process might not be possible.

Deformation of the Grating Slits In the previous discussion the effective grating period has been defined as the compressed state in the center of the grating structure. The grating surface facing the focal spot gets more compressed than the bottom which is attached to the substrate, in a source facing grating. Considering the neutral fiber model, introduced in Figure 4.16, the change of grating period within the grating structure is given by,

$$\frac{p_i}{p_o} = \frac{r_i}{r_i + h}\,, \tag{4.14}$$

where p_i and p_o denote the grating period at the grating surface and at the interface to the substrate, respectively. Thus, the deformation depends purely on the bending radius and the grating height. For a grating with height $h = 0.4\,\text{mm}$ and a relatively small bending radius of 100 mm this yields a relative deformation of 4‰ between top and bottom. This reveals that in contrast to the visible macroscopic deformation, i.e., bending to a 100 mm radius, the actual microscopic deformation is rather small. The impact of this deformation on the interferometer performance is assumed to be minimal as it is comparable to a slight deviation from the binary grating profile. Such deviations can also occur due to variations in the electroplating.

4.4 Other Solutions for Divergence-Induced Shadowing

The combination of divergent radiation and high aspect-ratio gratings is the reason why shadowing becomes a challenge for Talbot-Lau interferometry and grating-based imaging in general. Certainly, by reducing the aspect-ratio the negative effects of shadowing would vanish. Unfortunately, however, there is no material with the required X-ray stopping power in the specific energy range suitable for clinical CT. With gold as grating material already one of the densest and best X-ray attenuating materials is in use. Therefore, as long as the energy range is maintained the use of smaller grating heights is no viable option for the absorption gratings G_0 and G_2. However, for phase-gratings this approach works well because here the aspect-ratio is relatively small. Those gratings require only some micrometer high structures to induce the phase-shift. Consequently, use of a phase-grating G_1 is advantageous to make at least one of the three gratings largely unaffected by any shadowing.
Besides tuning the grating structure height, a potential to reduce shadowing lies in an optimized orientation of the grating lines. Shadowing has a strong direction dependence perpendicular to the grating lines but not along the lines. This can be seen in Figure 4.13 where the intensity loss is only towards the left and right edges but not towards the top or bottom. This relation is rather obvious because even under an extremely shallow angle a ray parallel to the grating lines can pass through a grating slit. A drawback of this approach is that a Talbot-Lau interferometer

is only sensitive to scattering and phase-shifts perpendicular to the grating lines. Furthermore, this is no actual solution to reduce shadowing but merely shifting it along the smallest extent of the field of view. This approach is feasible for long but narrow fields of views, but up-scaling to larger, i.e., less narrow, coverage would not work. However, such dimensions are required for full-field radiography systems which have an almost rectangular field-of-view.
More radical approaches work on removing the G_0 grating of a Talbot-Lau interferometer. To still achieve the required coherence for interferometric imaging one concept is to produce a sufficiently small X-ray source spot. This is possible with, e.g., a liquid metal jet X-ray source [160]. Alternatively, also recent work on a structured anode target as demonstrated by Zan et al. [157] is promising. Here, multiple small source spots in a grating like pattern are generated. Both approaches are still restricted to laboratory setups with comparably soft X-ray energies and a small flux.

4.5 Acceptance-Induced Shadowing

A fundamental requirement for Talbot interferometry is coherent radiation. At synchrotrons the long propagation distance to the interferometer and the small size of the source spot lead to highly coherent radiation. If beam coherence is not sufficient, e.g., at an X-ray tube, a source grating G_0 can be added to the setup. It converts the incoherent wave field into a set of coherent slit sources which constructively superimpose their interference patterns in the G_2 plane. This has earlier been introduced in Section 2.3.2.
In the previous section, the shadowing in high-aspect ration gratings due to the divergence of the radiation has been evaluated. With the bending of the gratings a promising approach has been identified which can compensate this issue. However, until now a point-like X-ray source has been considered, which is a sufficient approximation for laboratory setups, but fails for clinical sources.
In this section, the performance of G_0 is evaluated and challenges of its implementation in a clinical X-ray system are revealed. The problem lies in the combination of the large source spot size and the required high aspect-ratio for the hard X-ray spectrum. The identified issues can vastly reduce interferometer performance and therefore must be considered during system design. As this effect is based on the G_0 acceptance this effect is referred to as acceptance or source size induced

4.5.1 Multi-Slit Contribution

The size of the X-ray source spot can vary strongly between X-ray tube models. While there are special versions with extremely small focal spots in the micrometer range, often referred to as microfocus tubes, most sources operate in a source size regime of several micrometers to some hundred micrometers. Increasing X-ray flux is usually accompanied by an increase in source spot size.
A Talbot-Lau interferometer is – by design – independent of the source size and thus, its performance does not depend on the applied source technology. The geometry is chosen in a way that all rays which contribute to a specific point in the G_2 plane intersect G_1 at a common phase of the grating pattern. This is illustrated in Figure 4.17 where in two examples the rays contributing to two points in the G_2 plane are highlighted. Only direct rays from the extended source which can pass a G_0 slit and reach the specific sampling point in the G_2 plane are considered. While each ray has its unique trajectory all rays project the same G_1 pattern into the G_2 plane. This means, the G_1 interaction points of the rays are always

shifted 2π along the G_1 pattern, i.e., by one full period, for rays from neighboring G_0 slits. Consequently, the interference patterns from each G_0 slit, which are independent of each other, overlap constructively in the G_2 plane.
This geometrical concept efficiently adapts the interferometer to a variable source size and the only difference for the interferometer between two different source sizes is the number of G_0 slits which contributes to a sampling point in the G_2 plane. As an example, in Figure 4.17, an extended source spot close to the G_0 shows that four slits contribute directly to the interference pattern in the G_2 plane. If the same focal spot would be placed further away from the G_0 or would be smaller, also fewer slits would contribute.
The approximate number of G_0 slits which lie on the path between the source and a G_2 sampling point can be calculated based on the G_0 period p_0, the source to G_0 distance s and the source width w:

$$N_{\mathrm{G_0\ slits}} = \frac{w \cdot T}{s+T}\,\frac{1}{p_0}\,, \tag{4.15}$$

with $T = L + d$ as the total interferometer length. For conservative approximation this does not include the actual intensity profile of the source spot but uses an upper bound of the source width.
As an example, the number of contributing G_0 slits for a Talbot-Lau interferometer in a clinical CT geometry (approx.: $s = 100\,\mathrm{mm}$, $T = 900\,\mathrm{mm}$) with a G_0 period of $4.8\,\mu\mathrm{m}$ is analyzed for different source sizes. When such a setup is operated at a laboratory X-ray source with a source width of $100\,\mu\mathrm{m}$ already about 19 G_0 slits superimpose in the G_2 plane. If larger source sizes are used this number increases linearly and is around 190 for a 1 mm wide source spot, which is within the approximate range of a clinical CT X-ray source.

4.5.2 Sensitivity to Local Period Variation

The numbers calculated in the previous section reveal that for large focal spots a significant number of grating periods must constructively superimpose in the G_2 plane. While ideally

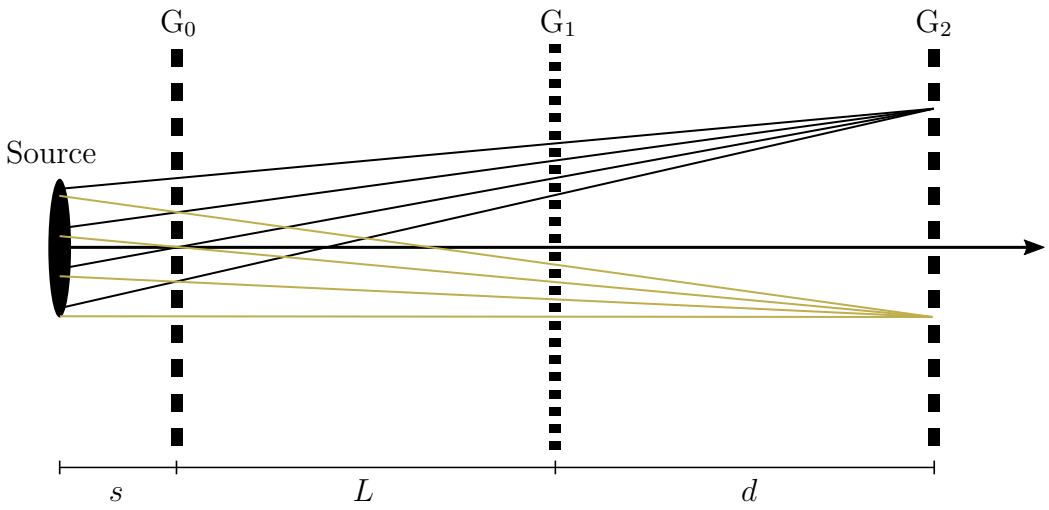

Figure 4.17: Illustration of a Talbot-Lau interferometer with an extended X-ray source. As highlighted by some ray paths every sampling point in the G_2 plane is directly illuminated from several G_0 slits because the source spot is large. For the ease of illustration a symmetric geometry has been chosen but the same relation is also found in asymmetric or inverse geometries.

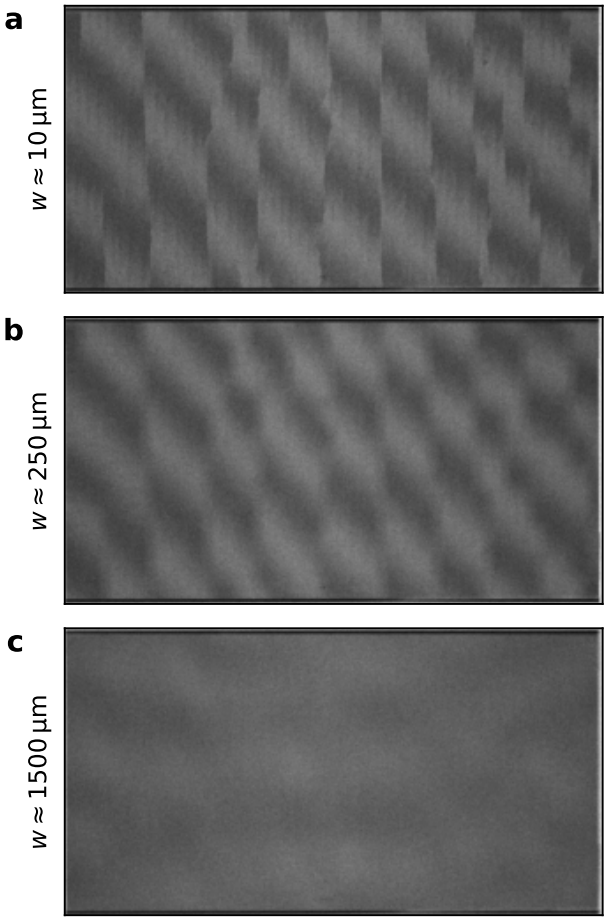

Figure 4.18: Three projections of the fringe pattern with different source sizes. A G_0 with extreme defects (vertical crack-like defects) is chosen for demonstration. **a,** Using an approximately 10 µm small source spot keeps the number of active G_0 slits for a G_2 sampling point small. Consequently, the defects do not degrade the interferometer performance and can be resolved and included in the reference phase image. The mean visibility in this configuration is around 20%, except at the sharp defect lines where visibility loss is unavoidable. **b,** For larger source spots the number of active G_0 slits increases and in the vicinity of the defect lines the lack of constructive superposition between the increasing number of G_0 slits leads to a performance loss. The visibility decreases with increasing source size and here is around 15%. **c,** For extremely large source sizes this example demonstrates a total loss of visibility.

gratings should have a constant grating period, hence usually referred to as *grating constant*, defects during or after the fabrication process or distortions along the beam axis can lead to changes of the grating period or shifts of the grating pattern. The latter is actually easily possible if cracks are formed as discussed in Section 4.3.3.

If such defects occur in a setup with a small source size the defects can be resolved when a detector with sufficient resolution is used. Then the defects are visible as phase-variations in the measured data. An example of this situation is shown in Figure 4.18a where a small focal spot with $w \approx 10\,\mu\text{m}$ is used at a Talbot-Lau interferometer in a clinical CT geometry (approx.: $s = 100\,\text{mm}$, $T = 900\,\text{mm}$) with a G_0 period of 4.8 µm. Consequently, only about two G_0 slits contribute to a point in the G_2 plane and thus besides the defect lines in the G_0 where the interferometer phase jumps the interferometer visibility is stable.

For larger source sizes the number of slits increases and thus the probability that defect grating areas are superimposed increases. The defects disturb the consistency of the pattern projected into the G_2 plane and consequently the visibility of the interferometer is decreased. This effect can also be interpreted as a kind of source blurring of defects in the gratings. Its impact is limited to the system's visibility and does not affect the projection of the sample attenuation properties.

By de-focusing a laboratory microfocus tube the interferometer response can be evaluated in a controlled environment. As an example several projections with various source sizes have been measured at a laboratory setup and are shown in Figure 4.18. The G_0 grating used here has been selected because of its remarkable strong vertical crack-like defects which were induced accidentally by a handling error. The fringe pattern of the interferometer is still recognizable in Figure 4.18a and b where the fringes go from top left diagonally to bottom

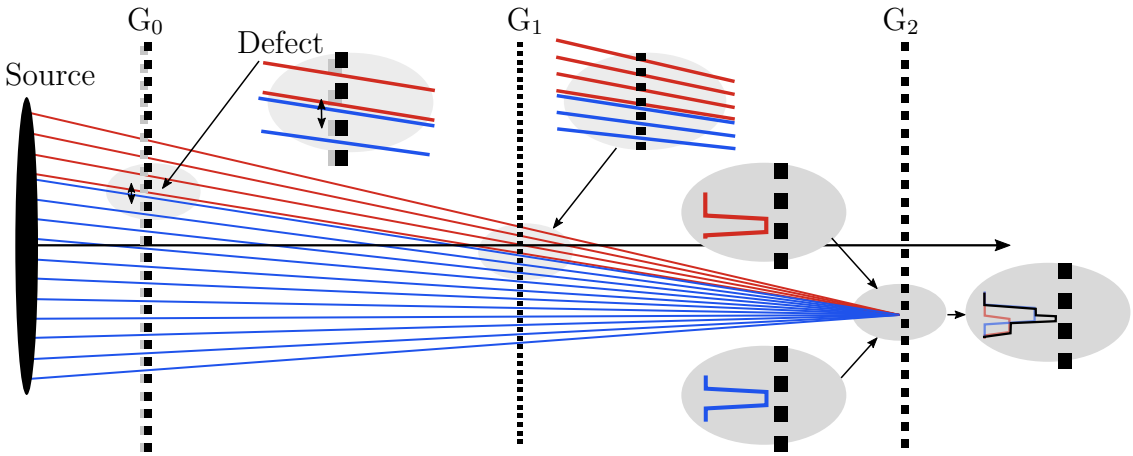

Figure 4.19: Illustration of a Talbot-Lau interferometer with an extended X-ray source and a crack-like defect in the G_0 which discontinues the periodicity of the structure at the indicated position. Only rays through the center of the G_0 slits are highlighted and two insets illustrate the interference patterns produced by the two types of rays (red and blue). The shift of the G_0 pattern–caused by the defect–leads to a shift of the resulting patterns. As illustrated in the rightmost inset the superposition of all G_0 slit contributions is not constructive and a wide and deformed pattern results. This does not fit to the G_2 slit and leads to a visibility loss.

right, but are regularly discontinued by the vertical crack-like defects where the fringe-phase jumps significantly. As discussed in Section 4.3.3, the cracks occur from internal stress in the grating and here discontinue the periodic structure of the grating. The periodicity is still the same in the homogeneous areas but at the crack-like defect line an additional gap is in the grating pattern, distorting it locally. This can be seen best in Figure 4.18a where the vertical defect lines induce jumps of the interferometer phase. Since here a small focal spot is used, the defects only lead to sharp jumps and the configuration still performs well with a mean visibility around 20%.
For a larger focal spot the number of active G_0 slits for each G_2 sampling point increases. Starting from areas with defect lines, no longer constructive superposition in the G_2 plane is achieved. Consequently, the visibility degrades starting at the former sharp defect lines which can be interpreted as the previously mentioned effect of source blurring. In areas where the grating pattern is defect free over a sufficient width the visibility remains constant even for the larger focal spot. This can be observed in Figure 4.18b between the defect lines.
As an extreme example, where all visibility is lost, a projection with a 1500 µm source spot is shown in Figure 4.18c. The combination of extreme phase jumps induced by the G_0 defects and the extreme blurring leads to an extinction of the fringe pattern. Eventually, this reduces the interferometer visibility to zero.
For a schematic description in Figure 4.19 an illustration of a symmetric interferometer design with a large source spot and a crack-like defect is shown. The rays which pass from the source through the G_0 slits can be separated in the ones above the defect (red) and the rest below the defect (blue). Their interference pattern in the G_2 plane is illustrated in two insets as well as their combination. In the combined intensity profile, the degradation of the final pattern becomes obvious as it no longer fits to the G_2 slit width and consequently can no longer be analyzed by, e.g., a stepping procedure.
From this discussion, we can conclude that local period variations in the grating structure can easily decrease the visibility of an interferometer. To some extent, this effect always degrades the visibility because there is probably no *perfect grating* but always some defects. However,

mostly the defects should be minor and spectacular examples as shown in Figure 4.18 are rare or remain unseen as the setup resolution or X-ray source size is too large. The important take-away from this discussion is that performance only decreases for larger source sizes if defects are present. Thus, in absence of any defects the visibility remains source size independent. In the following section the impact of the source sizes will further discussed.
A second important conclusion is that the presence of defects and changes of the source size during a measurement can lead to a complex artifact. When these deviations occur during a measurement the visibility can undergo local changes, i.e., pixel-wise changes, starting around the defect lines. It is therefore advisable to perform a grating inspection or a test implementation at a stable X-ray tube with a high-resolution imaging setup. Such a reference implementation then allows to assess whether the final implementation actually reaches the maximum feasible performance.

4.5.3 Impact of Source-Size on Shadowing

In the beginning of this chapter, the effect of the cone beam has been discussed and compensated by introduction of, e.g., bent gratings or divergent lamellae. Similar to this beam divergence also an extended source spot can be interpreted as a set of many divergent point-like sources. The angles of incidence though the grating planes vary between the ray paths originating from different positions in the source spot. Particularly for absorption gratings like the G_0 the relatively large aspect-ratio leads to shadowing already at small deviations from a perpendicular incidence angle.
In contrast to cone beam related shadowing the range of incident angles from an X-ray source spot is significantly smaller because the focal spot is usually not larger than a few millimeters. The maximum incident angle α for an (un-bent) G_0 can be derived from the source spot size and the geometry of the setup as,

$$\alpha \quad = \quad \arctan\left(\frac{w/2}{s+T}\right) \ , \tag{4.16}$$

with source width w, source to G_0 distance s, and $T = L + d$ as the total interferometer length. Comparing this to the maximum angle of incident α_m, for which the grating structure would be completely lost as introduced in (4.2), shows that the source size induced incident angle is significantly smaller.

$$\alpha = \frac{w/2}{s+T} \ll \frac{p}{h} = \alpha_\mathrm{m} \ , \tag{4.17}$$

with $\arctan(x) \approx x$ for small x.
For example, for a clinical CT geometry (approx.: $w = 1\,\mathrm{mm}$, $s = 100\,\mathrm{mm}$, $T = 900\,\mathrm{mm}$) with a 200 µm high and 4.8 µm period G_0 the maximum incident angle $\alpha = 0.029°$. Consequently, the source size induced incidence is a factor 48 smaller than α_m and the effective shadowing would be minimal. Only for much larger source spots a substantial influence must be expected. It is important to note that for this example the gratings are not bent.
In Figure 4.20, an illustration shows how a large source spot is subject to shadowing when the rays pass, e.g., a G_0 absorption grating with high aspect-ratio. Central rays pass the grating as intended, but for larger incident angles the increasingly more diagonal trajectory leads to shadowing as the gaps become virtually more narrow. This leads to undesired attenuation in G_0 and reduction of the total X-ray flux available for imaging. Furthermore, the ratio between primary beam passing through the grating slits and the radiation leaking through the grating

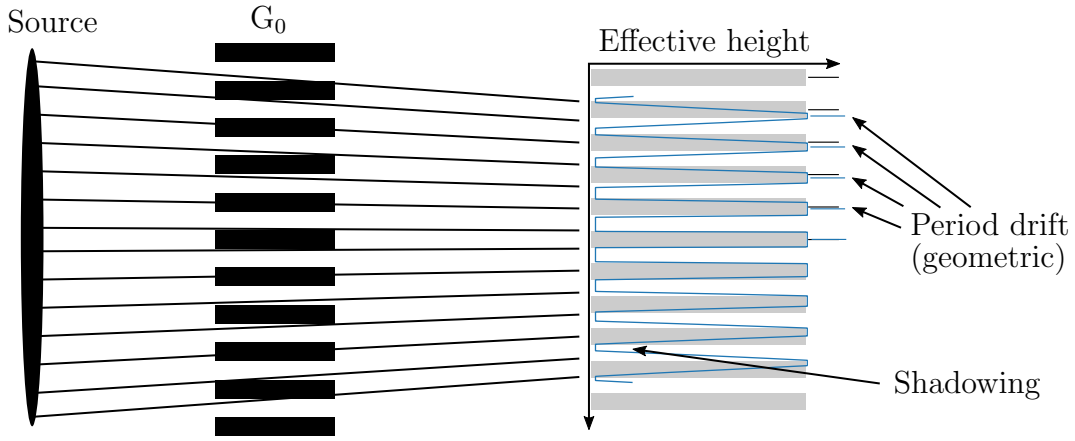

Figure 4.20: Illustration of rays from an extended source to a point in the G_2 plane where the combination of a high aspect-ratio grating and the large source size leads to shadowing for off-center rays. Since here a flat grating is analyzed the effective period between the G_0 slits can drift as indicated by displacement of the blue marks relative to the black ones.

structure shifts towards the latter. This leads to a decrease in coherence in the system and consequently to visibility and performance loss.
The projection of the source through the flat G_0 in Figure 4.20 also reveals that the grating period can vary. The grating period becomes finer for rays originating from further off the center of the source.

4.5.4 Grating Acceptance

Simulation results in Figure 4.21 reveal the incidence angle dependence of the G_0 grating profile. The plot shows in orange the effective height profile of a high aspect-ratio grating. In blue a reference curve is plotted for a grating with small aspect-ratio and no shadowing. This reveals, that only for almost perpendicular transmission through a grating the effective height and shape is imprinted into the wavefront as intended. At $\pm 0.5\alpha_\mathrm{m}$ the rays pass the grating lamellae diagonally which leads to a triangular structure. At $\pm\alpha_\mathrm{m}$ the rays traverse the lamellae and corresponding grating slits diagonally, consequently, this leads to a total loss of the grating pattern. In between these two characteristic situations the profile can be approximated by some trapezoidal structure.
To minimize the impact of the acceptance induced shadowing in an interferometer, ideally a small X-ray source should be used. This keeps the maximum angle of incidence small. For larger sources a solution is to increase the distance between interferometer and source, i.e., increase s. This has a similar effect as using a smaller X-ray source spot and might be unfavorable in terms of flux efficiency and setup geometry.
To quickly assess the risk for source size induced shadowing and following performance loss one can introduce an empiric measure,

$$\alpha < 0.1\ \alpha_\mathrm{m}\ . \tag{4.18}$$

If a setup fulfills this, it is assumed that the changes induced by source size induced shadowing are only minimal, based on the simulation results in Figure 4.21. Reshaping of (4.17) then yields a formula to calculate the range within which the source size w should lie for a given interferometer configuration:

$$w < 0.1 \cdot \frac{2\,p\,(s+T)}{h}\ , \tag{4.19}$$

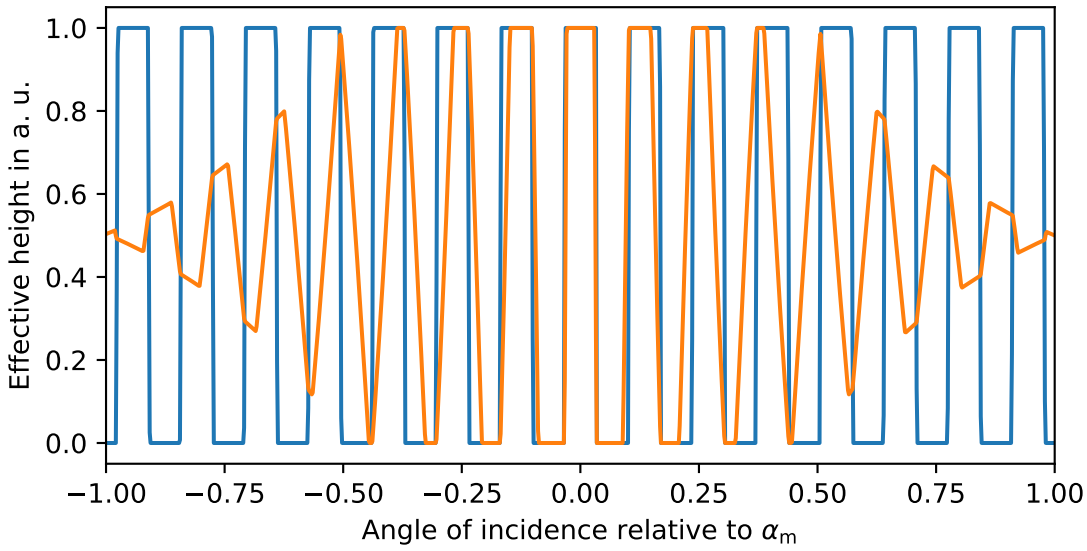

Figure 4.21: Simulation results similar to the line shown in Figure 4.20, however, here over a wider range of incidence angles. In blue a low aspect-ratio grating is shown as a reference where no shadowing due to the extended source size occurs. The orange curve reveals that due to increasing angles of incidence the grating profile becomes more trapezoidal. At $\pm 0.5\alpha_m$ the grating profile is momentarily triangular. For even larger angles the grating pattern is more and more lost until it vanishes at α_m because the rays traverse the lamellae and gaps diagonally. These results are for a 50% duty-cycle grating.

where the period p and structure height h of the grating with the larges aspect-ratio is inserted. A setup fulfilling this relation should not suffer from significant acceptance induced shadowing. The system parameters in this evaluation have been selected conservatively. Thus, it is easily possible that in practice also larger factors than 0.1 work well. A further evaluation on this parameter, i.e., including experimental implementations with different geometries and source sizes, has not been done yet, particularly because this is only applicable to flat gratings. When gratings are bent a different approach is required, which will be discussed in the following section.

4.5.5 Source Magnification by Bent Gratings

While for flat gratings the source size induced shadowing is a minor issue, it becomes a critical issue when gratings are bent. Introducing the cylindrical curvature to focus the grating slits into the source spot leads to an inclination of the grating structures. This is visualized in Figure 4.22. The illustration is clearly exaggerated and will, probably, not occur to this extent in any experimental implementation. Nevertheless, it demonstrates how the deformation, which was initially intended to reduce shadowing, ricochets when combined with an extended source spot. The added inclination of the lamellae by the bending process then lead to more source size induced shadowing.
The maximum effective angle of incidence can be calculated based on the construction shown in the sketch in Figure 4.23 as:

$$\alpha_{\mathrm{eff}} = \alpha + \alpha_{\mathrm{b}}, \tag{4.20}$$

where the maximum angle of incidence α of the flat grating is extended by α_{b} which depends

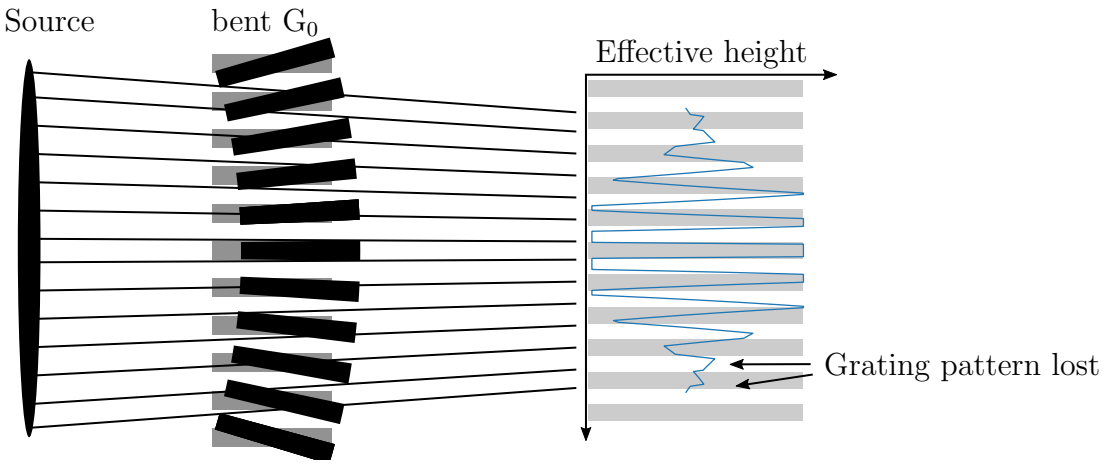

Figure 4.22: Illustration of rays from an extended source to a point in the G_2 plane through a bent absorption grating, i.e., G_0. In gray the unbent lamellae are shown which have been analyzed in Figure 4.20. The plot of the effective grating height for the different rays reveals that only the central rays interact with the periodic grating pattern as intended. Towards the outer regions the rays quickly begin traversing the high aspect-ration lamella diagonally and soon the pattern is completely lost.

on the geometry. The latter includes the distance s between the source and the grating as the bending radius. With $x = s \cdot \cos(\alpha_b)$ and $y = s \cdot \sin(\alpha_b)$ we can insert into the geometrical construction,

$$\tan(\alpha) = \frac{w/2}{s+T} = \frac{y}{s-x+T} = \frac{s \cdot \cos(\alpha_b)}{s - s \cdot \sin(\alpha_b) + T} , \tag{4.21}$$

$$\alpha(\alpha_b) = \arctan\left(\frac{s \cdot \cos(\alpha_b)}{s - s \cdot \sin(\alpha_b) + T}\right) . \tag{4.22}$$

Unfortunately this equation cannot easily be brought into the form $\alpha_b(\alpha)$ but can be solved by a numerical evaluation and interpolation.
A simpler method, however, is based on an alternative interpretation of the observed effect.

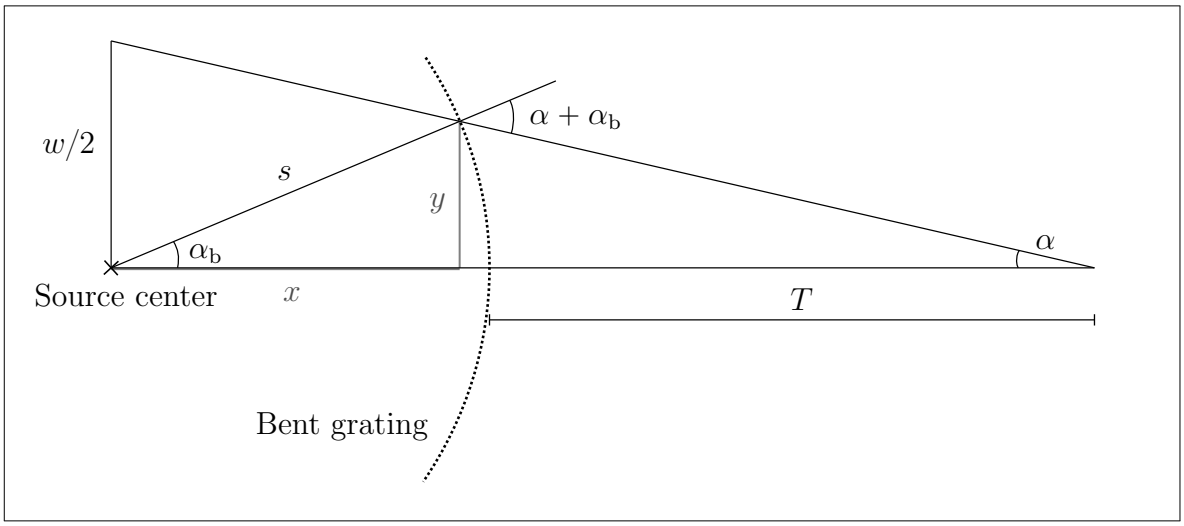

Figure 4.23: Sketch for calculation of the effective incidence angle in a system with a bent grating. The grating is bent to a cylinder with radius s around the source center. The corresponding half source width is indicated by $w/2$.

One can consider the bent grating as a lens-like element and then work with a flat grating instead of a bent one. Obviously, this model is restricted to the discussion of effective incidence angles and no actual magnification is realized. The fundamental idea is that the focal-length of the bent grating leads to a virtual magnification of the source spot. In consequence, rays from the magnified source spot intersect a virtual flat grating instead of the bent grating. In this case the angle of incidence is the same as for the outermost rays in the real geometry from the original X-ray source spot.
This approach is sketched in Figure 4.24. It demonstrates the extreme magnification of the virtual source which is required to achieve the same α_{eff} incidence angle for a flat grating. The substitution of the bent grating by a magnified source and a flat grating is particularly useful for simulation frameworks which have superior performance when operating with flat objects and wave-fronts.
To calculate the virtual magnified source size w_{mag} one can insert into,

$$w_{\text{mag}} \quad = \quad 2\,(s+T)\cdot\tan(\alpha_{\text{eff}})\;. \tag{4.23}$$

Alternatively an approximate solution can be calculated from,

$$w_{\text{mag}} \quad \approx \quad w\,\frac{s+T}{s}\;, \tag{4.24}$$

which only works for small source sizes w and should always be validated with the previous approach. When working with the virtual magnified source width w_{mag} the formula from (4.16) can be used as $\alpha_{\text{eff}} = \alpha$.
As an example the same setup as previously used in the example in Section 4.5.3 is reconsidered. However, here, the grating is bent according to its distance from the X-ray source. Evaluating this setup (clinical CT geometry approx.: $w = 1\,\text{mm}$, $s = 100\,\text{mm}$, $T = 900\,\text{mm}$ with a G_0

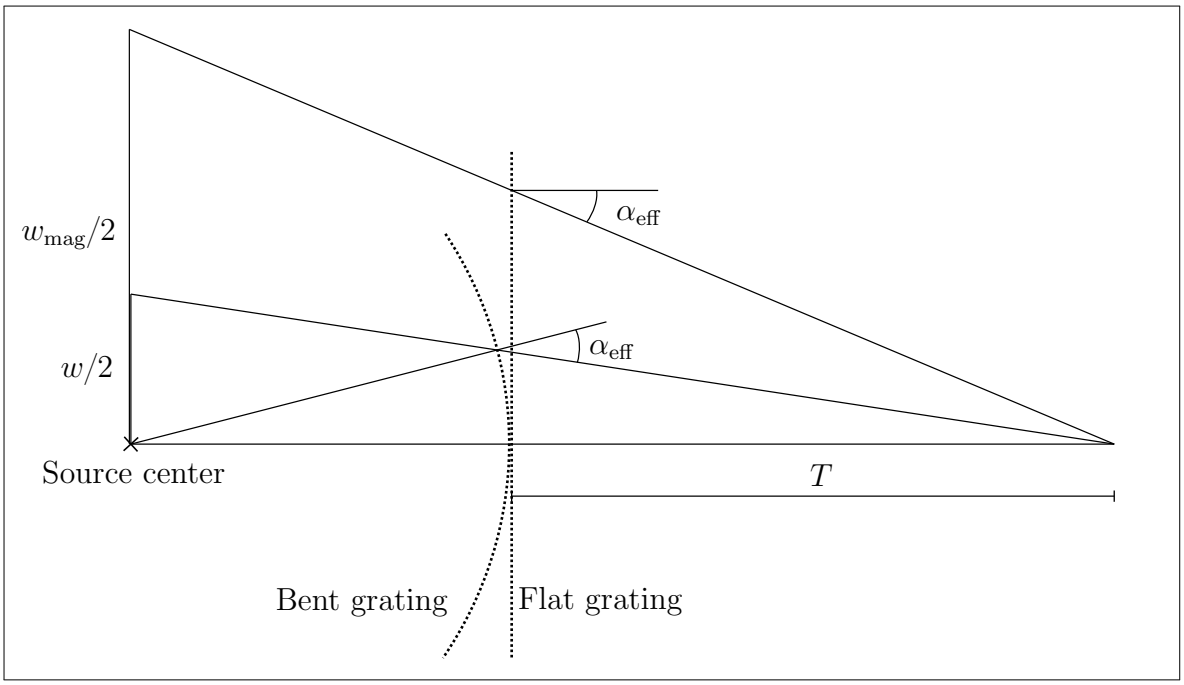

Figure 4.24: Concept of magnified source with a virtual flat grating as a substitute for a regular extended source with a bent grating. The magnified source size w_{mag} can be calculated with Equation (4.23).

$h = 200\,\mu m$, $p = 4.8\,\mu m$) reveals that the virtual source size is $w_{mag} = 10\,mm$. Consequently, the maximum incidence angle in this design is $\alpha_{eff} = 0.286°$. This result is a factor ten larger than for the example with a flat grating and considering $\alpha_m = p/h = 1.37°$ the suggested acceptance limit from (4.18) is violated by a factor of two.
These results demonstrate that while the impact of a large source size can usually be ignored in flat grating systems it quickly gains importance when gratings are bent. The combination of a bent high-aspect-ratio grating with a large source spot can then easily lead to significant performance loss due to shadowing.
Options to decrease this effect are to use a smaller source spot, a smaller aspect-ratio, or placing the source further away from the interferometer. Since source spot sizes are usually predefined by the X-ray tube manufacturer it is important to consider this issue during development of a system, e.g., by selecting a tube with a small source spot. The requirement for smaller aspect-ratios contradicts the requirement for absorption gratings in hard X-ray spectra which require high grating structures. This can be interpreted as an upper limit for the design of such gratings. Usually, the maxim is to maximize aspect-ratio because higher absorption structures stop the high energy X-rays better. However, the results in this chapter revealed that higher aspect-ratios can also lead to performance loss due to source size induced shadowing. A compromise between absorption and shadowing must be found, giving a limit for the structure height of absorption gratings.
Another aspect of source size induced shadowing is that changes of the X-ray source size during a measurement or between scans can easily change the system performance. The acquisition procedure and the data processing then must be adapted to compensate for these fluctuations. Such a processing pipeline which is capable of correcting for intensity and visibility fluctuations of the interferometer will be presented in Chapter 7.

5 Design of the Interferometer

In this chapter, the translation from laboratory based grating-based dark-field imaging to clinical CT is discussed. Experiences with laboratory experiments, recent large-scale radiography implementations, and a small animal dark-field CT are evaluated to identify upcoming challenges for clinical dark-field CT. Then the available design options are introduced and discussed in detail. This analysis then selects the optimal design for the proposed dark-field CT gantry whose realization is described in Chapter 6.

5.1 Know-How from Previous Experiments

To prepare the discussion of the various design options for a Talbot-Lau interferometer in a clinical dark-field CT gantry an overview over some existing implementations is presented. It highlights already achieved milestones and on which concepts new designs can be built on. Certainly, it is important to be aware of already identified limitations and problems so that they can be considered right from the beginning of the design process.

5.1.1 State-of-the-Art Laboratory Dark-field Imaging

Experiments with Talbot-Lau interferometers to retrieve phase-contrast and dark-field images of samples are available at synchrotron facilities but have also been realized at conventional X-ray sources and at compact light sources (e.g., MuCLS). The variety of setups is mostly purpose built to evaluate specific questions and concentrate either on material science or biomedical imaging.
In the majority of the phase-contrast and dark-field experiments a limitation to small sample sizes applies. Usually, the geometry of the Talbot-Lau interferometer sets this limitation, despite perhaps at synchrotron beam lines where the beam width is an earlier limit. At conventional X-ray sources the maximum size of the gratings and the divergence of the radiation limit the active area of the interferometer. Particularly if flat gratings are used the shadowing in the high aspect-ratio grating structures is a limitation. For some scientific X-ray detectors also the active area or gaps within it can limit the usable field of view. However, the available fields of view are often sufficient for laboratory studies and methods such as off-axis-tomography and combining of several interleaving projections can further increase the field of view.
Most laboratory phase-contrast and dark-field imaging systems are optimized for effective energies between 25 and 50 kVp since the performance of grating structures is best in low energy X-ray spectra. This allows laboratory Talbot-Lau interferometers to achieve extremely high sensitivity and visibility. However, as such soft radiation is also attenuated strongly in the sample this limits the penetration depth. As usually small samples are imaged – due to field of view restrictions – the soft X-ray spectrum is sufficient. Nevertheless, X-ray flux is often one of the most prominent design issues in laboratory X-ray setups.

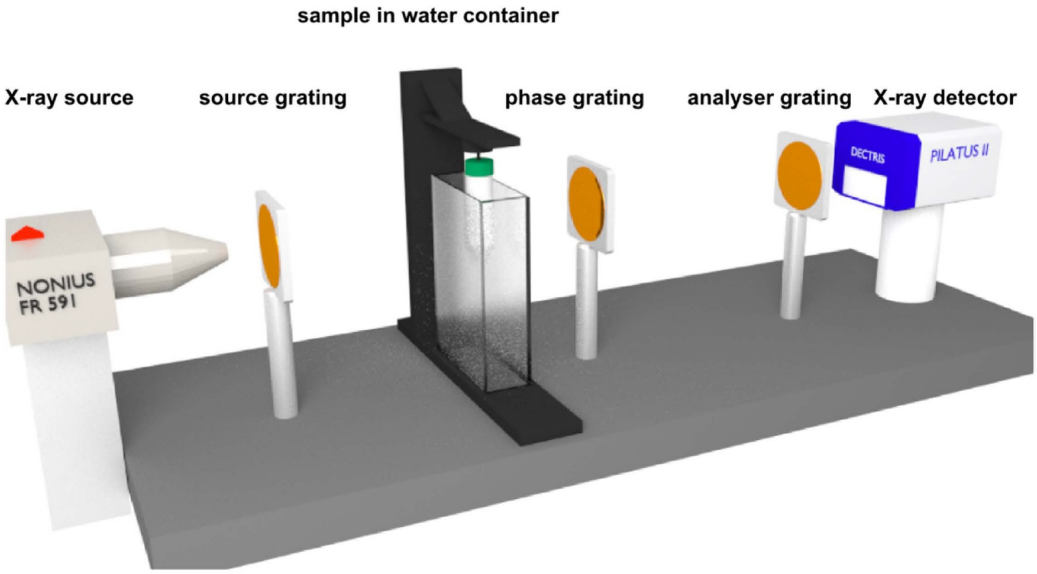

Figure 5.1: Rendering of a laboratory Talbot-Lau interferometer. A rotating anode X-ray source generates poly-chromatic X-ray radiation which traverses the three gratings of the interferometer and then is measured on the detector. The sample is positioned close to the G_1 grating inside a water tank which is used to suppress beam-hardening and phase-wrapping artifacts. A motorized sample stage allows rotation and positioning of the sample, which is inside a cylindrical plastic container, during the tomography scan. Image adapted from [13] CC BY.

Having sufficient X-ray flux in a Talbot-Lau interferometer is an important aspect as not only the sample attenuates a variable portion of the radiation but also the absorption gratings G_0 and G_2 absorb roughly 75% of the incident flux. The restriction to comparably small sample sizes is therefore acceptable as thinner samples tend to absorb less radiation. Nevertheless, most laboratory X-ray setups are commonly flux limited. Depending on the setup optimization, e.g., high-resolution or high-sensitivity, the distance between the gratings must be relatively large. This leads to a long total setup length and reduces the flux which reaches every detector pixel. Introducing high-resolution detectors reduces the individual pixel size which also leads to less flux per pixel. Furthermore, the generated X-ray flux is also limited as usually small X-ray focal spots are required, which can only deliver a small X-ray flux.
A solution for laboratory studies lies in longer exposure times which can transform most flux-related problems into a time-related problem. This requires that in time domain the setup can be assumed to be stable and there are no mechanical and thermal drifts in the components. Based on this assumption phase-stepping-based acquisition is possible and simplifies processing of the measured data. However, particularly on long time scales temperature drifts in the interferometer can hardly be avoided. Additionally, also changes in biological samples can occur even in fixated samples, e.g., formation and movement of bubbles. These two effects are often the upper limit for the scan duration, besides practical limitations.

5.1.2 Dark-field Radiography at Large Scale

To realize dark-field imaging for larger objects recently several specialized setups and machines have been developed. All these devices concentrate on radiography only and usually use some kind of scanning approach along one image axis to cover a large field of view with a small slot as illustrated in Figure 5.2. Example implementations for this are the first clinical dark-field

chest X-ray system [146] and its predecessor [37] or a material testing setup [6].
Clearly full field designs, i.e., with gratings covering the full field of view and no need to scan, would be preferred. However, the scanning approach has several advantages and was a major milestone. It allowed to bring dark-field imaging quickly to the clinics, even though grating fabrication was not yet ready to supply full field of view gratings.
The fabrication process of the gratings remains a bottleneck for development of dark-field imaging systems and the scanning approach minimizes the required area of structured grating surface. The fabrication based on the LIGA process has for a long time been optimized for round 100 mm diameter substrates with either rectangular 50 mm × 50 mm or round 70 mm active grating areas (approximate values). By combining several of those gratings to a large one full field systems can be achieved, but the process of stitching is complex and errors can pile up [111], [112]. For scanning systems usually only one-dimensional stitching is required

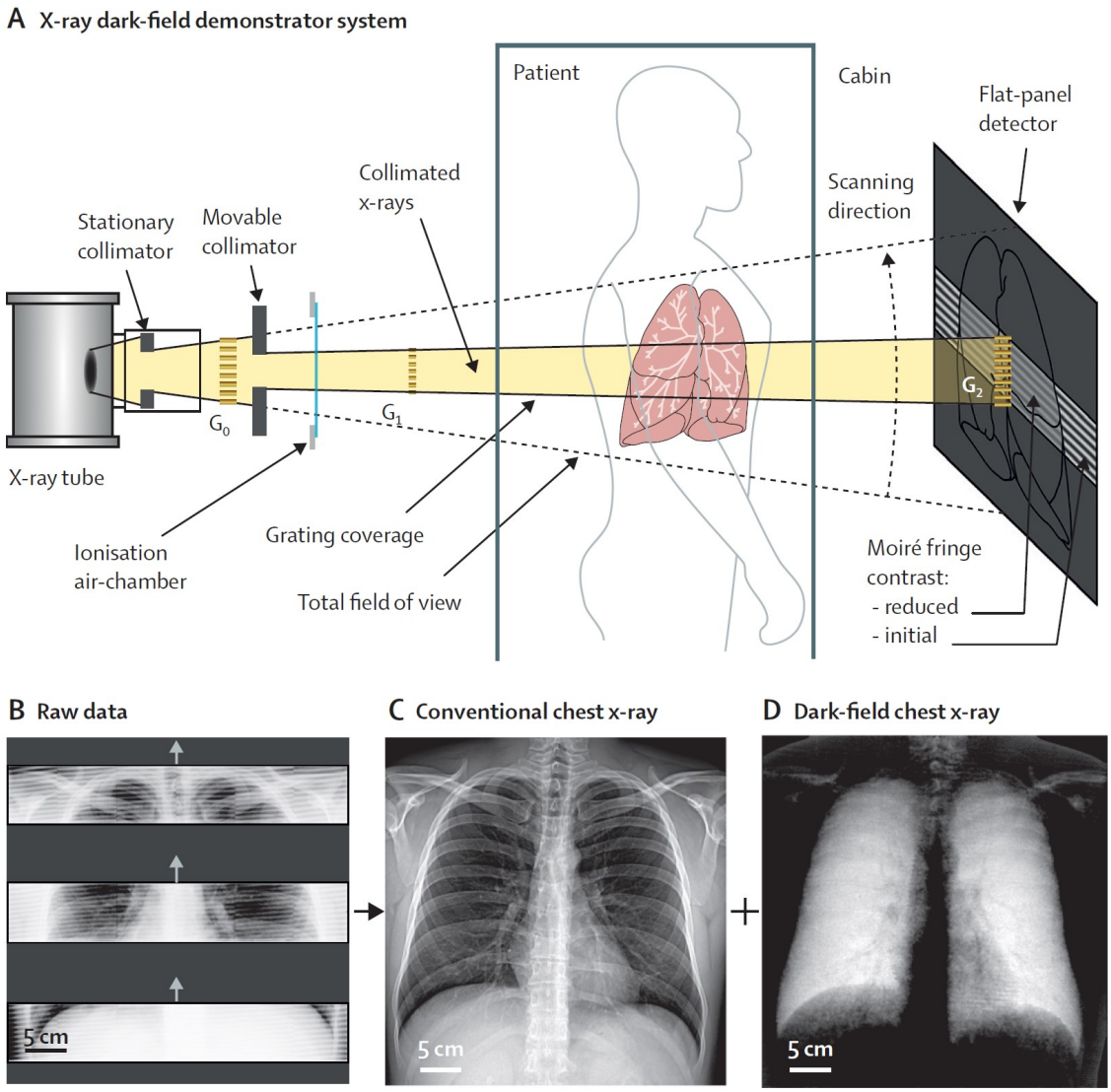

Figure 5.2: Slot scanning approach utilized at the dark-field chest radiography system. **A,** To achieve a large coverage for the whole human chest with a relatively small total grating area the setup is moved along the vertical axis. **B,** During the scanning procedure continuously images are acquired. **C and D,** The measured data is then processed and conventional attenuation chest X-ray and additional dark-field radiographs are retrieved. Image adapted from [146] CC BY.

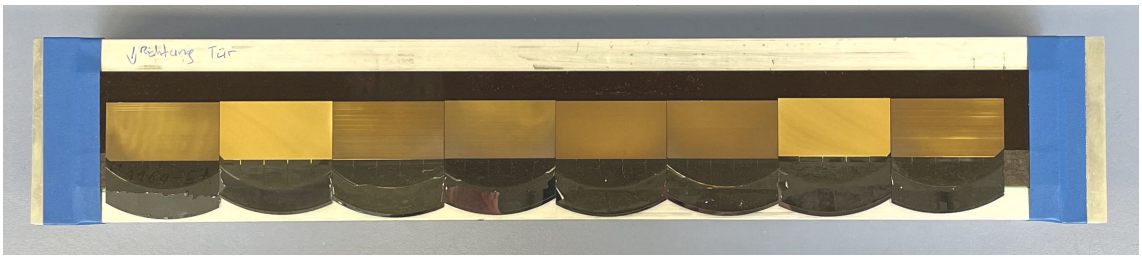

Figure 5.3: Combined X-ray grating covering an area of 384 mm × 24 mm. Eight individual grating tiles have been combined to achieve a wide grating which is then used in a scanning based dark-field radiography system. After stitching, i.e., combining and adjusting the tiles, all components have been glued to a large basis substrate. Fabrication details can be found in Schröter et al. [111].

which simplifies the manufacturing and assembly of the combined grating. An example of such a grating which is combined from multiple small grating tiles is shown in Figure 5.3.
The acquisition procedure at scanning systems is more complicated than at laboratory systems because no stepping curve is measured, but instead the system is continuously moved along an axis. The coverage of the slot must be large enough that for each detector pixel several images with different interferometer positions are acquired. From this data set a processing algorithm can extract the attenuation, differential phase-shift, and dark-field signal which has been induced by the sample or patient.
Since only the area of the slot is irradiated during the acquisition the X-ray dose on the patient is the same as in a full field system. Only the acquisition time is longer as the system must be scanned over the field of view. In theory the scanning speed can be extremely fast as long as the stability of the system is maintained, and the X-ray flux is sufficient. The first prototype dark-field chest X-ray machine which uses conventional radiography equipment is capable of doing a scan within seven seconds at an effective dose of 0.035 mSv [146].

5.1.3 Small Animal Gantry-based Dark-field CT

At laboratory Talbot-Lau interferometer setups radiography imaging is usually only done for mammography studies [105], evaluations concentrating on the direction dependence [61], or time resolved studies. At laboratory Talbot-Lau interferometer setups mostly computed tomography is done to retrieve a three-dimensional reconstruction of the different imaging modalities. This

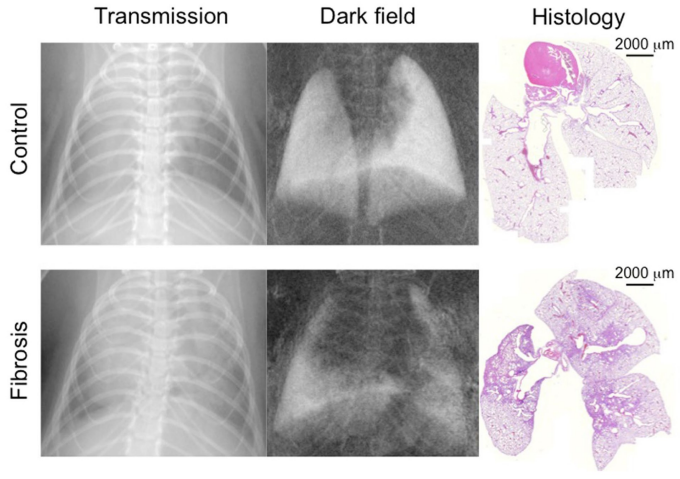

Figure 5.4: Pre-clinical results on lung fibrosis in mice imaged with dark-field radiography. Dark-field, transmission and histology images of murine lungs. The healthy lung from the control group produces a strong dark-field signal, whereas the fibrotic lung clearly shows degradation in the dark-field channel. In the transmission these changes are more difficult to access, particularly because the rib cage overlaps with other structures.
Image adapted from [51] CC BY.

allows reconstruction of quantitative values and can reveal significantly more information about the sample without any overlapping features. Since the sample size is usually rather small, tomographic scans can easily be realized by rotating the sample with a dedicated rotation motor during the acquisition protocol. This means, that no changes to the interferometer are necessary, and the system stability is unaffected. The only requirement is, that the sample must be stable during the rotation, which can easily be achieved for most biological samples or solid objects.
For in-vivo experiments, however, rotating the sample, e.g., a small animal, during a computed tomography scan is rather impractical. Consequently, a gantry-based system for small animal dark-field CT has been developed [121]. The system design follows closely conventional laboratory based Talbot-Lau implementations with the only difference that here the mouse lies on a stationary bed while the X-ray source, Talbot-Lau interferometer, and detector rotate around it. While these components are all assembled rigidly to a gantry the stability of the system is worse than in laboratory implementations, where those components usually rest on an optical board. Nevertheless, the results proved that the system delivers good tomographic reconstructions in all image channels – attenuation, differential-phase, and dark-field – and set a major milestone by demonstrating the first in-vivo dark-field CT of mice [135].
The system uses a fixed target tungsten X-ray tube which is a stable and lightweight solution but comes with limited X-ray flux. The acquisition follows a step and shoot protocol where the gantry is not rotated continuously but from one projection angle to the next. At each gantry angle a conventional phase stepping measurement is done. This procedure leads to comparably long can times for a full tomographic scan or around 40 minutes [132]. A side effect of such a long scan time is that the interferometer can start to drift due to thermal changes, particularly as the X-ray tube is cooled with the air inside the gantry housing. Furthermore, long scan times are problematic in in-vivo applications as it is a health-risk for the mouse to be kept under anesthesia for long time.
This initial gantry based dark-field CT results demonstrated that in a compact and moving design Talbot-Lau interferometry is feasible. Some stability issues during gantry rotation, related to deformations due to the changing direction of gravitational force on the components, were found but could be compensated by reference scans and data processing. The acquisition protocol used at this system is directly adapted from laboratory setups but as it leads to long scan times it is not ideal for in-vivo imaging. A continuous rotation acquisition would be a solution but comes with the drawback that then no conventional phase-stepping is possible. This demonstrates that stability, speed, and a continuous acquisition protocol are most important for advanced gantry-based CT designs.

5.1.4 Conclusion for Development of Clinical Dark-field CT

The previous sections clearly show that optimization of available technology, i.e., introduction of combined gratings or advanced processing to do scanning acquisition, recently led to several milestones in dark-field imaging. Initially large scale dark-field radiography seemed unrealistic, nevertheless, a decade after the initial dark-field results at a laboratory X-ray source by Pfeiffer et al. [91] the technique reached the clinics.
The question when dark-field CT will be available in the clinics arises naturally as the step from radiography to tomography seems obvious. As recently published in an editorial contribution of the RSNA, for most researchers the realization of dark-field CT "remain[ed] in the realm of future research and development" [47]. Surely, parallel to the development process of clinical dark-field radiography also solutions for specific CT related problems were solved [133], [127]

but little progress on experimental realization of clinical dark-field CT was made. The only significant development towards clinical CT realization was recently published by Wu et al. [150]. Their bench top system extended the field of view to 160 mm– significantly larger than the small animal CT – but requires rotation of the sample and is over two meters in total length. Positive is, however, that they report on a significant speedup compared to the small animal CT and need only seven minutes for one tomographic scan.
The main topics and aspects which are critical for a dark-field radiography or CT system are,

- X-ray spectrum
- X-ray flux
- Setup length
- Sample size
- Sample position
- Field of view
- Acquisition protocol
- Grating periods
- Aspect-ratio
- System stability
- Applicable dose
- Total scan duration
- Integration time
- Pixel size

Critical system specifications like total system length, acquisition procedure, patient or sample position, and X-ray spectrum are relatively loosely confined in radiography systems. This allows that these parameters can be chosen beneficial for dark-field imaging, i.e., a softer X-ray spectrum, a long setup length, and a scanning acquisition instead of a full field system. When using a clinical CT gantry as a platform for dark-field CT, however, there is no or only very little margin for adaption as most changes would require the development of a new CT gantry. Obviously, a change of system length would require a differently shaped detector and a new gantry structure. Changing the acquisition protocol from continuous rotation to step and shoot is also infeasible. Given the complexity, cost, and safety concerns in development of a new CT gantry, purpose built for dark-field application, is beyond the scope of academic research. Therefore, the challenge lies in development of a Talbot-Lau interferometer which is fully adapted to the specifications of an existing clinical CT.
The true challenge of clinical dark-field CT development is probably that there is hardly any translation process, but it is more like a large step. All concepts and design ideas, whether they have previously been tested in laboratory setups or not, must be integrated into one system and work harmonically. While previous evaluations are extremely valuable their direct translation into clinical CT must be dealt with caution. Experiments like those by Wu et al.

Priority 1	Priority 2	Priority 3
Feasibility	**Sensitivity**	**Clinical Application**
• Safety • Grating fabrication • Stability	• Fine periods • System length	• Large field of view • Low patient dose • Scan speed

Table 5.1: Priority guideline for the design process of the first dark-field CT. Highest priority lies in demonstration of feasibility which is mainly related to good grating fabrication results and a stable implementation. Parameters such as fine grating periods and maximum system length for maximization of the sensitivity are less prioritized. While certainly the main objective and motivation of the design is clinical application, the related specifications are of low priority. Obviously, meeting those, e.g., a large field of view, would have no value if the prior categories would be neglected.

[150] which demonstrates that a clinical X-ray tube and CT detector can be used for dark-field CT are hardly transferable to a rotating gantry which is much less stable. The demonstration of bent gratings, which can compensate shadowing artifacts as the lamellae are aligned with the divergent beam by Revol et al. [100], might not be compatible with a large X-ray focal spot or might have problems at small bending radii.
One can therefore conclude that the development of a Talbot-Lau interferometer and an appropriate processing and reconstruction protocol for clinical dark-field CT is a set of well-chosen compromises. All available experiences from previous experiments must be considered and combined, which is complex as not all uncertainties and dependencies can be evaluated beforehand. Therefor, the priority for the first dark-field CT prototype lies in demonstration of the feasibility of dark-field CT in clinical scale. This sets the optimization for highest possible dark-field sensitivity to second position, before large field of view and highest dose efficiency. An overview over these considerations and priorities is summarized in Table 5.1.

5.2 Sensitivity Requirements

The primary focus of the dark-field CT currently lies on imaging of the lung, initially motivated by promising results found in pre-clinical studies with the small animal dark-field CT and at similar setups. A variety of studies demonstrates that with dark-field imaging an enhanced image contrast, particularly useful for detection of diseases in the lung, can be achieved [107], [154], [152], [135], [106], [50], [132]. Similar studies are available for dark-field radiography showing that the retrievable signal is strong enough to increase diagnostic value, however, with the limitation that radiography imaging is no quantitative method and suffers from overlapping of structures [76], [49], [51], [146].
In conventional attenuation-based radiography and CT the contrast from the lung is usually very low because of the low density of the tissue as it is mostly porous air-filled tissue. As the spatial resolution of clinical and even most micro-CT setups is insufficient to resolve the porous structure, no structural changes of these pores can be retrieved in the attenuation channel. Therefore, the finding that dark-field radiography and CT can extract information on changes in the sub-resolution range is a breakthrough for lung related imaging.
To investigate the origin of the strong dark-field signal the interaction process has been studied in great detail in several works [156], [72], [118]. The lung tissue's porous structure, i.e., the lung alveoli, can be modeled as spherical interfaces refracting the radiation which allows an analytical analysis of the interaction process. This approximation is required, as reliable information on the microstructure of alveoli is difficult to obtain. Only in the in-vivo state a realistic inflation by negative pressure from the rib cage and the diaphragm is established. Unfortunately, in this state high-resolution CT or histology is difficult, particularly, as the lung tissue has almost no contrast in conventional attenuation micro-CT. Therefore, this vast approximation of the lung as spherical interfaces is required. It allows to derive that a Talbot-Lau interferometer has a geometry and wavelength dependent response to spherical interaction-surfaces. This behavior can be described by a characteristic value referred to as the *correlation length*. If the sample contains structures in this length-scale the interferometer is particularly sensitive and a strong dark-field signal will be retrieved [156], [72], [118]. Tests with different interferometer sensitivities and pig lungs as samples could verify that this model helps to find optimal interferometer sensitivity for lung imaging [71].
The angular sensitivity S is commonly used as a performance measure for Talbot-Lau interfer-

ometers and characterizes the minimal resolvable refraction angle. As derived in [27] it is,

$$S = \left(\frac{1}{L} + \frac{1}{d}\right)^{-1} \frac{1}{p_1}\left(1 - \frac{x}{d}\right) = \frac{d}{p_2}\left(1 - \frac{x}{d}\right) \ , \tag{5.1}$$

for a Talbot-Lau interferometer in inverse geometry, where the distance between G_1 and the sample is denoted x. It leads to a linear scaling between the highest sensitivity at the G_1 position and lowest at the G_2. An analysis of this formula reveals that in general a long geometry, a more symmetric geometry (at a given total length), and small grating periods increase the sensitivity and thus lead to a better interferometer performance.
Another important design measure is the correlation length ξ, which can be calculated from the previously introduced sensitivity S and the wavelength λ of the radiation [156], [118], [71], [72] as,

$$\xi = S \cdot \lambda \ . \tag{5.2}$$

This now includes the energy dependency of the small-angle scattering sensitivity. Since at most dark-field imaging setups a poly-chromatic X-ray spectrum is used the mean energy of the spectrum is used to specify the wavelength of the setup. It is important to note that the correlation length goes beyond the spectral performance of the interferometer components themselves. It, however, does not consider the performance of the gratings for different energies which underlie, e.g., the energy dependent attenuation coefficient.
In Table 5.2, the geometry and grating parameters of various Talbot-Lau interferometers are listed. Based on these values the correlation length for each setup is calculated and a wide range from 0.48 to 3.5 µm reveals that their sensitivities vary significantly. For consistency a wavelength of 23 fm, which corresponds to 53 keV photons, i.e., the mean energy of a clinically filtered 80 kVp tungsten spectrum, has been used for all evaluated setups. The last entry in the table is the dark-field CT prototype designed in this thesis. Clearly laboratory setups, which are optimized for high sensitivity, can use a low-energy X-ray spectrum, fine grating periods, long setup geometries, a rather symmetric interferometer design, and position the small samples as close to the G_1 as possible. However, as soon as large field of views or a particularly short total setup length is prioritized the maximum correlation length drops significantly. In theory finer grating periods can compensate for this but this is limited by the micro-fabrication process of the gratings.
The findings of previous studies on lung imaging at mice, pigs, and human patients are rather unspecific which correlation length is optimal. For example, a comprehensive study using inflated pig lungs at three different setup configurations has been published by Ludwig et al. There the conclusion is that ideally an interferometer with a correlation length around 1 µm should be used for dark-field imaging of lung tissue. Contrary, there are also setups which achieve comparable dark-field imaging results, but with significantly lower sensitivity at correlation lengths around 0.5 µm [135], [37], [146]. These inconsistencies suggest that the correlation length and the sensitivity should not be the only design specification for dark-field radiography and CT setups.
One can conclude that in general higher sensitivity and longer correlation lengths are preferred. As can be seen in Table 5.2, all large scale dark-field radiography implementations use relatively fine grating periods and very long total setup lengths. It surprises that these implementations loose most of their sensitivity because the sample or patient is positioned relatively far away from G_1 which degrades the sensitivity. This, however, is probably in most designs a necessary compromise due to a limited detector size.
In case of the small animal dark-field CT the total length of the interferometer is very short. Nevertheless, sufficient sensitivity is achieved by using the finest available gratings (4.8 µm

Description	L	d	p_0	p_1	p_2	Sample distance	Corr. Length	Setup Length
	mm	mm	µm	µm	µm	mm	µm	mm
[13] Laboratory CT High Sensitivity	857	857	5.4	5.4	5.4	30*	3.5	1714
[120] DF CT Small Animal	300	150	10	3.24	4.8	50	0.58	450
[3] Animal DF Radiography	1599	231	68.72	8.73	10	160*	0.48	1830
[146] Clinical chest DF Radiography	720	1380	7.725	10.14	14.77	1066	0.489	2100
[71] Conf. A DF Radiography	123	1250	2.4	2.19	22.39	610	0.60	1373
[71] Conf. B DF Radiography	403	970	4.8	3.39	11.54	330	1.28	1373
[71] Conf. C DF Radiography	728	970	10	5.71	13.31	330	1.11	1698
[150] DF CT Non-interferometric	300	1200	30	24	120	140	0.20	1500
[136], [140] DF CT Clinical Prototype	87	812	4.8	4.338	45	383	0.22	899

Table 5.2: Setup geometries and correlation lengths of various dark-field radiography and CT setups. Laboratory setups can achieve extremely high sensitivities and consequently long correlation lengths as they can be long, use a symmetric geometry, and have fine grating periods. When adapting Talbot-Lau interferometers to a small animal gantry-based CT or scaling it up to animal or human chest dark-field radiography compromises reduce the sensitivity. The last line represents the dark-field CT prototype whose design considerations are covered in this thesis. For the calculation of the correlation length a wavelength of 23 fm, i.e., mean energy of a clinical 80 kVp spectrum, is used for all setups. Distances labeled with an * are approximate values when no more specific information was available in the setup description.

for an absorption grating as G_2) and keeping the distance between G_1 and iso-center, i.e., the sample, relatively short. In this design the area for the sample, the sample bed, and the housing separating the gantry from the sample area is only 40 mm in diameter, which is just enough for a small animal CT.

5.3 Technical Specifications of Clinical CT

The discussion in Section 5.1.4 concluded that for initial realization of clinical dark-field CT the implementation of a Talbot-Lau interferometer into an existing conventional clinical CT system

is the most feasible option. Consequently, decisions for the interferometer design must consider the layout of the CT gantry into which the grating setup should be implemented. For the dark-field CT prototype the Brilliance iCT gantry will be the base system and in the following sections the design and concepts of this commercially available gantry are evaluated. The focus is on the detector module, the collimator box, and the X-ray source and is based on analysis of system drawings provided by the manufacturer. Since most clinical CT gantry layouts are similar, the conclusions might be transferable to CT systems of other manufacturers.

5.3.1 Detector Unit

In Figure 5.5 a sketch derived from the system drawings shows most important parameters of the CT gantry geometry related to the detector unit, referred to as *Data Measuring System (DMS)*. In contrast to laboratory and radiography systems here the detector is spherically shaped, which means that all detector pixels are 1040 mm from the source spot and each pixel surface is perpendicular to the beam direction. Since the covered area is large, the detector is combined from 42 individual detector modules along the fan direction. Each module is 16 pixels wide (in fan direction) and tight tolerances ensure that the gap between two adjacent modules is negligible. In total this sums up to 672 pixels in one detector row covering a 52° fan angle.
The anti-scatter grid is directly integrated into the detector modules and important for the imaging performance of the CT system as it absorbs most of the Compton scattered photons, which is the dominant interaction process. The aspect-ratio of anti-scatter grid openings is about 21 which collimates the incident radiation to ±1.4° but requires about 30 mm of space in front of the detector surface as shown in Figure 5.5. A 0.3 mm thick aluminum sheet is used as a detector cover towards the center of the gantry as a mechanical protection for the fine anti-scatter grid and as a shielding for the detector electronics.
Ideally all these core components of the DMS should remain unmodified as any changes can quickly degrade the overall imaging performance. For example, the thermal stability of the detector units is ensured by heating elements at the air inlet of the DMS. If the removal of, e.g., the detector cover would change the ventilation, temperature drifts can degrade the image quality or even damage the system if the thermal controller is operated outside its specifications.
Right above the detector cover the ultra-high-resolution comb (UHR comb) is positioned. It is a tantalum comb which can block the radiation from half the detector pixel surfaces as described by Flohr et al. [33]. This allows to reconstruct higher resolved tomographic images by combining the virtually smaller detector pixels and a flying focal spot at the cost of lower statistics as part of the flux is absorbed in the comb. The UHR comb covers only the central 25° which corresponds to a field of view with 250 mm diameter. This small field of view is sufficient for the ultra-high-resolution applications in the clinics, which focus for example on imaging of the bones of the ear.
For standard CT the UHR comb is not required and can be moved out of the beam path with a motorized mechanism. Since the comb only needs to cover the central region of the detector this mechanics and the housing of the DMS are optimized for this coverage. Left and right from the area where the comb is positioned reinforcements stabilize the DMS and prevent wider coverage of the UHR comb. These are shaded in light gray in Figure 5.5. The UHR comb is an optional component and can easily be removed from the system as it is attached to the DMS only by some positioning pins and screws.
There are two configurations of the Brilliance iCT detector which differ in the number of detector lines, hence, coverage in z-direction. For a Brilliance iCT SP with 64 lines each

detector module consists of four detector tiles with 16×16 pixels each; Otherwise, it comes with eight tiles per detector unit summing up to 128 detector lines. It is important to note that the detector is spherically shaped with equal pixel spacing along rows and columns.
For the implementation of the Talbot-Lau interferometer the available space between detector cover and bore cover is of particular importance. Under the assumption that the UHR comb is removed for the implementation of the interferometer the illustration in Figure 5.5 shows only a 80 mm area along the beam axis which is available. Another limitation for installation of custom parts is that the DMS housing closely wraps around the beam path at the far left and right of the detector, i.e., at the light gray shaded areas. This can make reaching the detector surface difficult.

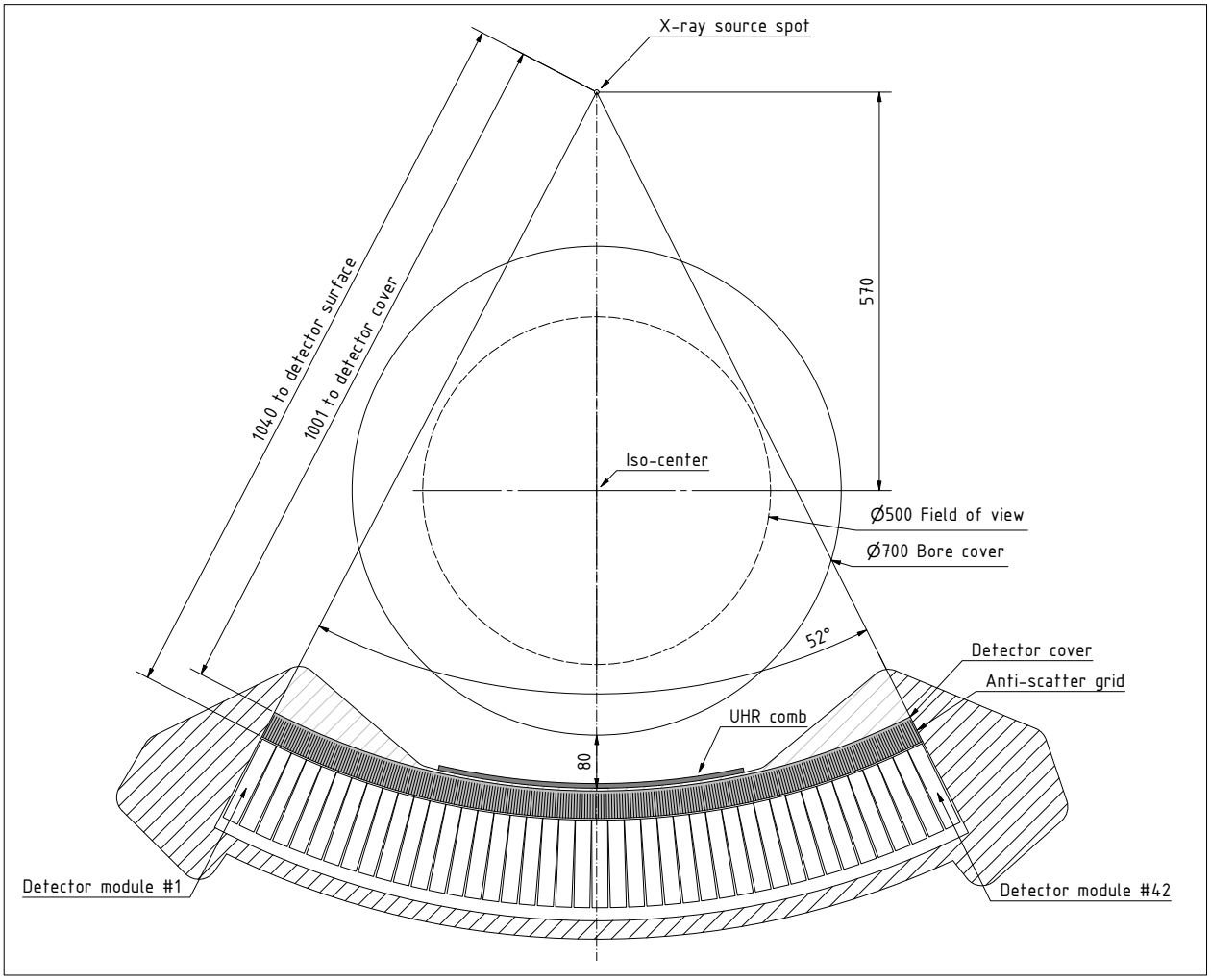

Figure 5.5: Geometry of clinical CT gantry along the detector rows. The detector unit (DMS) is curved following the spherical detector surface at 1040 mm from the X-ray source spot. It consists of 42 individual detector modules along the fan angle, each contributing 16 pixels to the detector row of 672 pixels. The modules are shifted by four pixels along the fan direction, referred to as the detector offset. The full fan coverage of 52° allows reconstruction of a field of view with 500 mm diameter. With the ultra-high-resolution comb, which is required for enhanced spatial resolution scans, only a 250 mm diameter field of view can be reconstructed. It can be removed from the gantry to free the area between detector cover and bore cover which is about 80 mm along the beam path.

5.3.2 X-ray Source and Spectrum

Another core component of the CT gantry is the radiation source which is positioned on the other side of the gantry opposing the detector. In this section, the relevant aspects for the development of dark-field CT are summarized based on the literature by Behling [11] and Behling [10] in which a comprehensive explanation and discussion of modern X-ray tubes for medical imaging can be found. Similar to the detector also the CT X-ray sources are highly optimized devices for the special working conditions of clinical CT. They must withstand the centrifugal forces of the gantry rotation and simultaneously produce massive amounts of radiation for a significant time span. This means that high thermal and structural stress act on the rotating anode as X-ray production is a rather inefficient process and most energy goes to heat.
Only with a rotating anode setup the required X-ray flux can be realized in the compact form which fits onto a CT gantry. A special target material, optimized thermal expansion grooves, and fast rotation speed help to distribute the heat load and maintain the stability of the anode plate. Since the target must sit in a vacuum for free electron propagation it is well insulated and cooling is the main challenge of X-ray tube design. A sophisticated cooling process combines absorption of back-scattered electrons in the housing, heat radiation, and heat conduction as the three available cooling channels. At the Brilliance iCT system the generated heat is ultimately transferred into a water-based cooling circuit and then via a heat exchanger to air. This circuit, also referred to as cooling unit (CLU), includes a continuously running pump for the cooling fluid.
The iMRC X-ray tube, which is implemented in the Brilliance iCT, has an anode with 200 mm diameter and rotates continuously as long as the CT system is initialized. The target rotation is realized by an asynchronous motor which generates a rotating electromagnetic field at a frequency of 189 Hz. It induces an eddy current in the target shaft which leads to a Lorenz force and consequently rotates the anode. This allows contact free transfer of momentum from outside the vacuum chamber and is free of wear on the components. Due to slippage, caused, e.g., by friction in the bearings, the actual rotation frequency of the target is some Hz below the electromagnetic driving frequency. Consequently, while the electromagnetic drive operates at 189 Hz the actual rotation frequency of the target is smaller, i.e., at around 180 Hz but can vary ± several Hz [10, Chapter 6.3.2.1].
An important feature of modern CT X-ray tubes is an adjustable focal spot based on quadrupole coils which are used to focus and adjust the area where the electrons hit the target and generate X-rays. This can also be used to reposition the focal spot position for each measured projection, realizing a *flying focal spot* [62]. It can be used to double the spatial resolution of the detector by displacing the focal spot along the detector rows, i.e., the x-axis, by one pixel width between each projection. Furthermore, a displacement along the detector columns, i.e., the z-axis, can reduce windmill artifacts in helical CT [62]. Since the anode is round and the anode surface is inclined by 8° a shift of the focal spot in x or z-direction also leads to a change in y-direction, i.e., towards or away from the detector. This effect is particularly pronounced for z displacement. At the Brilliance iCT system the focal spot deflection in x direction is limited to approximately ±650 µm and in y direction to ±0.5 µm.
There are two focal spot settings available at a Brilliance iCT system:

Large focal spot for high X-ray flux with 1.1 × 1.2 (IEC).

Small focal spot for high resolution but lower X-ray flux with 0.6 × 0.7 (IEC).

The size of these source spots is characterized based on the IEC 60336 [25] which gives the width and height of the spot for the reference beam which goes through the iso-center, i.e., at

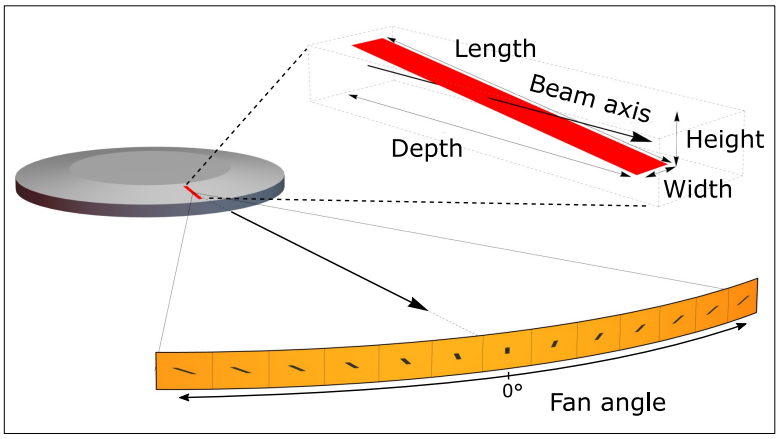

Figure 5.6: Rendering of the projected focal spot for different fan angles. The physical source spot is elongated on the anode surface and leads only under the 0° fan angle, i.e., projected through the iso-center, to an almost quadratic spot. For the outer rays the effective focal spot distorts to a parallelogram. Image adapted from [140] CC BY.

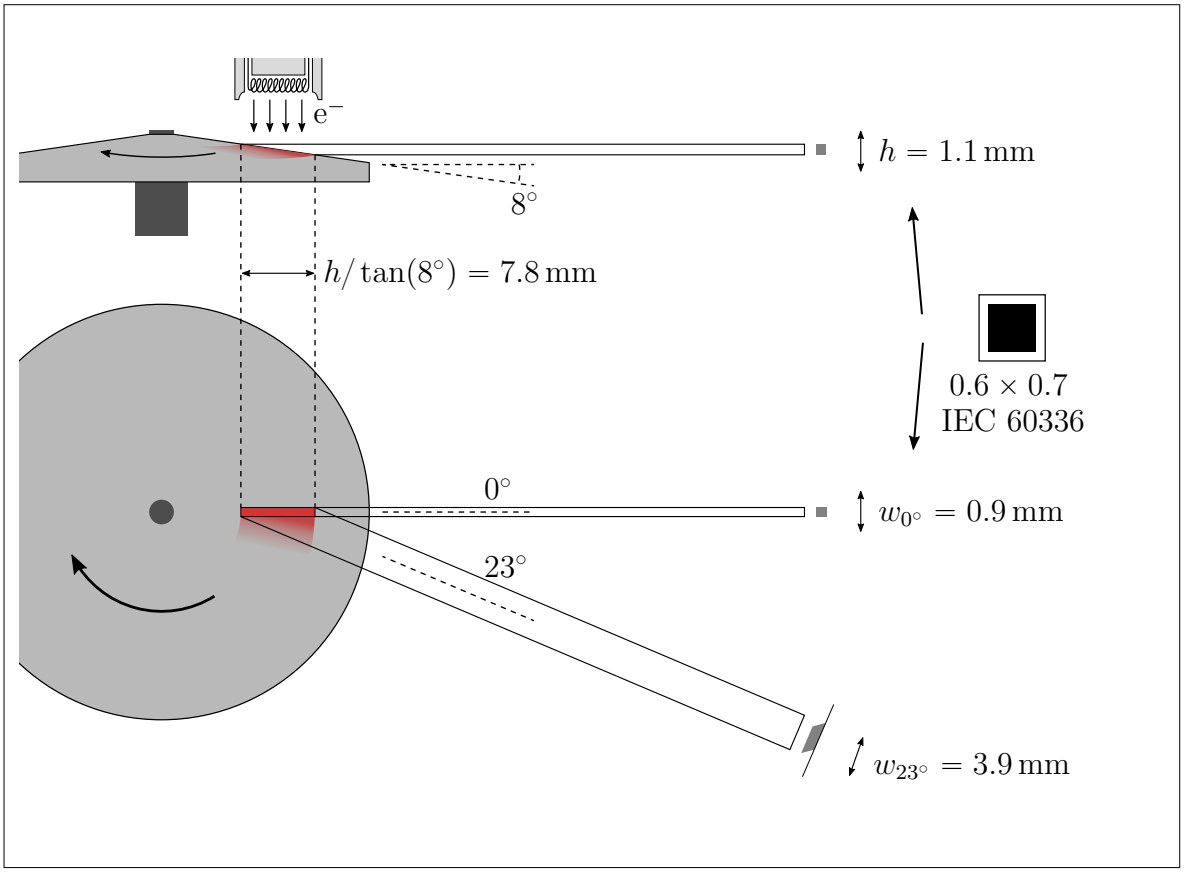

Figure 5.7: Generating an almost quadratic X-ray source spot with a rotating anode tube. The size of the X-ray focal spot is defined following IEC 60336 as, e.g., 0.6×0.7 for the small source spot, which converts to 0.9 mm × 1.1 mm (width×height) according to [25, Table 3]. Since the anode surface is inclined to 8° the electrons are accelerated onto an elongated area on the rotating anode target. This line like physical (electronic) focal spot is $1/\sin(8°)$ longer than the resulting X-ray focal spot is in height. While this works well for the central beam, which goes through the iso-center, rays to the outer fan angles suffer from extensive source blurring. As illustrated in the lower sub-figure the elongation leads to a distorted source spot which is approximately $\sin(23°) \cdot 7.8\,\text{mm} + \cos(23°) \cdot 0.9\,\text{mm} = 3.9\,\text{mm}$ wide.

0° fan and 0° cone angle. The dimensionless numbers are converted based on Table 3 column one and two in [25] to, e.g., 0.9 mm × 1.1 mm (width×height) for the small focal spot.
As illustrated in the rendering in Figure 5.6 the source profile looks only as specified by IEC

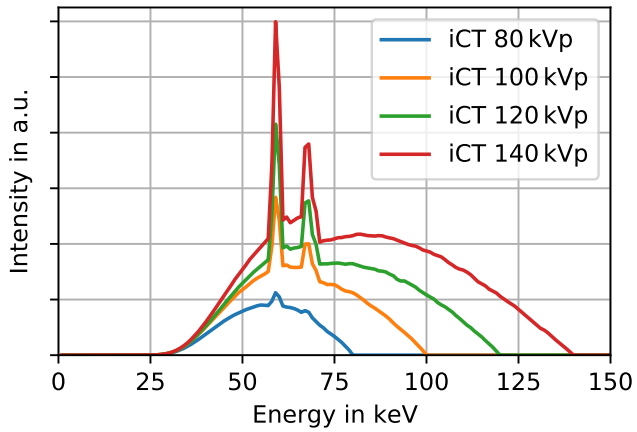

Figure 5.8: Brilliance iCT X-ray spectra for the four common clinical energy settings. These spectra include filtration from aluminum and titanium filters as well as the bowtie filter and the detector response. The continuous bremsstrahlung spectrum and the characteristic K_α and K_β lines of the tungsten anode material at 59 and 67 keV are visible. These spectra have been simulated based on TASMICS as introduced in [52].

60336 under the 0° fan angle, but varies significantly for the outer fan angles. This is because the anode target has an inclination of 8°, consequently, the physical source spot on the surface is elongated radially as shown in Figure 5.7. This means that the electrons are projected onto a line-like area, which in case of the small focal spot is 0.9 mm wide and over 7.8 mm long [10, Chapter 6.2.1.6]. Besides the reference beam, however, the projected X-ray source spot gets distorted as shown in Figure 5.7 for a ray under a fan angle of 23°. There the height is still unchanged, but the width is extended to about 3.9 mm.
The X-ray spectrum for clinical CT imaging is usually generated from acceleration voltages of 80, 100, 120, or 140 kVp. Example spectra are shown in Figure 5.8 where the broad bremsstrahlung spectrum and the characteristic emission lines of the tungsten target material can be identified. Various filters are integrated into the beam path to remove unwanted low-energy photons, which would not contribute to any image information as they are too easily absorbed by the sample.
To mimic the CT X-ray spectrum at a laboratory source, which often comes with almost no filtration, the following filters can be added:

- 0.57 mm titanium,
- 2.9 mm water,
- 3.0 mm aluminum,
- 1.0 mm polyetheretherketon (PEEK).

The Heel effect, i.e., deviations of the spectrum depending on the emission angle, is mostly compensated by specially formed filters which are integrated into the exit window of the clinical X-ray source [10, Chapter 2.13].
An important difference between radiography and CT X-ray tubes is the operating mode. For radiography systems the exposure time is rather short and a precise timing between source and detector makes sure that the integration time of the detector and the X-ray production is synchronized. During the read-out phase of the detector and the time between two frames no X-rays are generated.
In CT, the acquisition must be continuous, since the gantry keeps moving, consequently also the X-ray tube is operated continuously and the detector integration time of the detector is coupled to the rotation encoder of the gantry. Naturally, the readout time and the integration time is kept extremely short to avoid wasting X-ray flux and minimize blurring due to the movement. To compensate flux variations a reference detector sits right behind the exit window of the X-ray tube and measures the intensity before the sample can introduce a variation of the flux. These reference values, which are acquired for each projection, are then used to normalize the measured projections during pre-processing of the data.

As previously illustrated in Figure 5.5, the position of the X-ray focal spot is 570 mm from the iso-center and lies in the focal center of the detector curvature with radius 1040 mm. There is a 84 mm distance between the X-ray focal spot and the tube exit window as shown in Figure 5.9. The exit port is flat and directly attached to the collimator box, which is discussed in the following section.

5.3.3 Collimator Box

Before the X-rays traverse the bore the radiation is filtered and shaped by the components inside the collimator box. It is a unit attached to the X-ray source window and fills the remaining space between bore cover and X-ray source.
Its primary function is the collimation of the radiation to the active detector rows which limits the applied dose and reduces scattering artifacts. For this task two motorized collimator blades are installed close to the outlet of the so called A-plane box. These components are crucial to achieve dose efficiency and have a high priority to remain unchanged by any modifications of the system.
The filtering of the X-ray spectrum is done by several components. A fixed filter is implemented in the X-ray source, i.e., into its exit port, which can not be changed. To optimize the filtration for specific imaging cases there are two motorized filter trays integrated in the collimator box

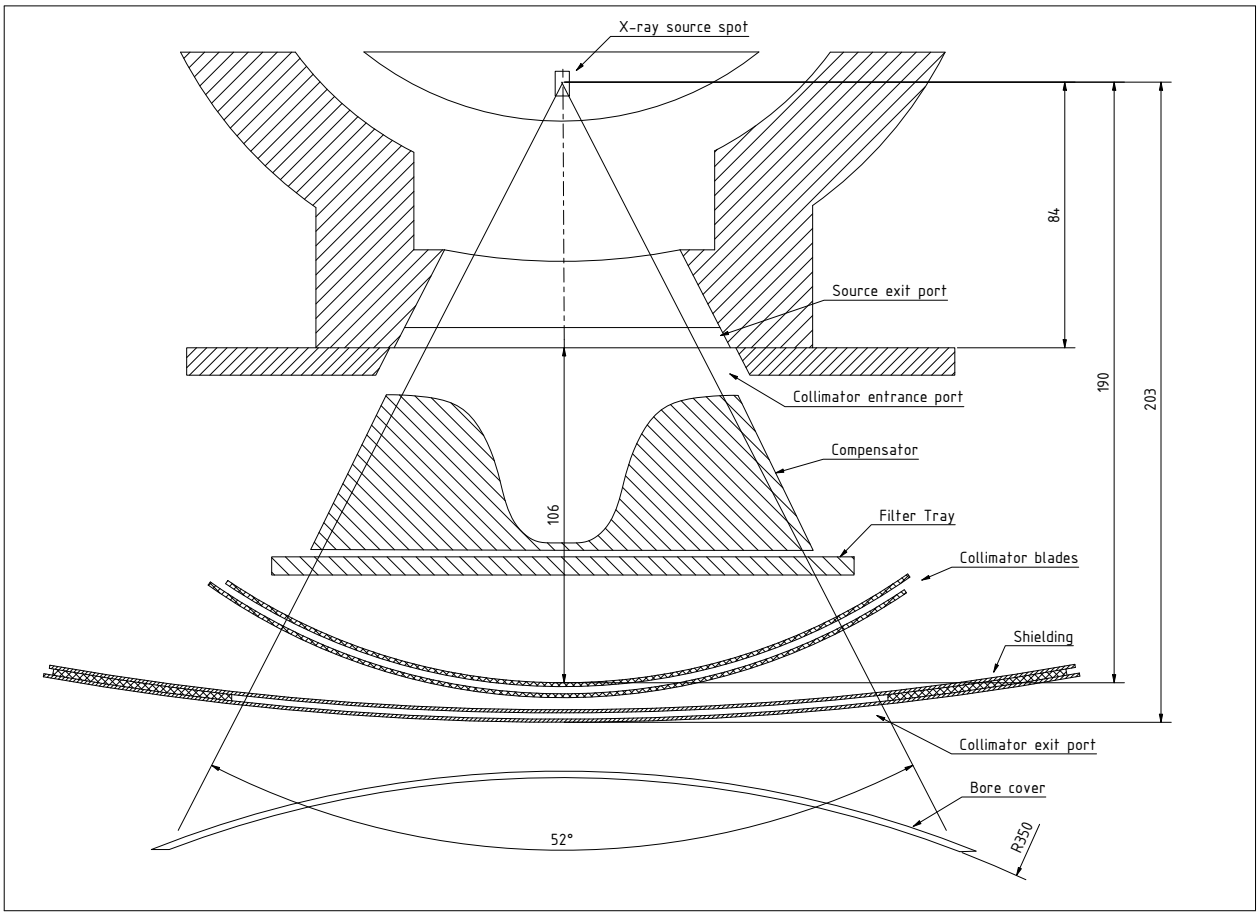

Figure 5.9: Layout of the X-ray tube and collimator box of the Brilliance iCT. Between the exit port of the source and the first of the two collimator blades is a distance of approximately 106 mm. Here, the filter tray and the compensator tray (i.e., with the bow tie filters) are located. The reference detector sits at the entrance port of the collimator box but is not shown here.

The first filter unit is a set of three different plates:

- 0.6 mm titanium,
- 1.25 to 5.00 mm aluminum (wedge shaped, thinnest in the center),
- no filter.

Most clinical exams are performed with the 0.6 mm titanium filter, but for children and intervention other filters might be used. The function of these filters is to harden the X-ray spectrum before it reaches the patient. The harder and more narrow spectrum undergoes less hardening due to the sample interaction can reduce beam hardening artifacts.
The second motorized filter tray is a set of three different bow tie filters, also referred to as compensators or wedges, optimized for different patient sizes. Also, here, most scans are performed with the setting "large wedge", which means the largest of the three bow ties. The other two bow tie filters are designed for children and infants. The purpose of the bow tie filter is to shape the intensity of the radiation to lower the applied patient dose. Maximum intensity is required through the iso-center because there is the longest mean path length through the patient. With increasing distance from the center, i.e., for larger fan angles, lower intensities are sufficient because here the path lengths through, e.g., the extremities are shorter.
Both these filter trays have an impact on the dose and image quality of the CT, but they are no crucial component and can be modified. Obviously, any changes will also change the patient dose as the removal of a filter will increase the X-ray flux and soften the spectrum which reaches the patient. By dose calibration measurements following the constancy test protocol [59] the changes can be quantified and compensated, e.g., by using different mAs settings.
Important for the design of the dark-field CT is the available space within the collimator box. Since the collimator blades should remain unchanged these curved structures and the tube exit port define a 109 mm long area into which parts of the interferometer can be integrated if the two filter trays are discarded. However, it must be noted that the exit port of the X-ray tube is flat – perpendicular to the central beam – and the collimator blades are curved focusing into the focal spot. Additionally, there is the reference detector which uses some space close to the X-ray source exit port. All dimensions and the internal design of the collimator box are sketched in Figure 5.9.
Changing the outer dimensions of the collimator box is also beyond the scope of this work. The sophisticated shielding integrated into it would raise safety issues, furthermore, there is only a gap of about 15 mm between the exit port of the collimator box and the gantry cover. This is an even smaller gap between rotating and stationary frame than between DMS or UHR comb and gantry cover. Therefore, no alterations of the outer shape of the collimator box seem reasonable.

5.3.4 Scan Modes and Data Acquisition

For tomographic scans with the Brilliance iCT system the gantry rotates with a constant speed between 1.5 and 0.27 s rotation time during the acquisition. As previously discussed, the X-ray source is operated continuously and with the flying focal spot technology the position of the focal spot can be changed for each projection. Depending on the angular sampling setting and the rotation time the number of projections is either 4800 or 2400 projections per cycle. Only for 1.5 s rotation time 4800 projections with integration periods of 312.5 µs are acquired, all faster rotation speeds are sampled with 2400 projections per cycle. This means that for the

fast rotation time of 0.30 s one integration period is only 125 µs long which equals a sampling rate of 8 kHz.
In this continuous rotation, a blur of the measured projections is unavoidable because the detector and source move during the integration period. As the central detector pixel sits 470 mm from the iso-center the distance it moves during one exposure of a scan sampled with 2400 projections is,

$$\frac{2\pi \cdot 470\,\mathrm{mm}}{2400} = 1.23\,\mathrm{mm}\ . \tag{5.3}$$

This is almost as far as a detector pixel is wide. A similar number can be found for the movement of the X-ray source spot. While there is no blurring of any object in the iso-center of the system, for off-center details the parallax effect leads to some blurring. This effect is known and accepted in clinical CT.
In axial acquisition mode the patient couch remains stationary and a scan over a full rotation (360° gantry rotation) is measured. There is also the option to perform multiple cycles at the same patient couch position, which is usually used for perfusion imaging. These scans are not concatenated continuously as there is always a short pause between two cycles in which the gantry rotation continues. Therefore, the resulting data stream of projections is not continuous which must be considered during processing.
In helical acquisition mode the patient couch is moved continuously during the scan which results in a spiral trajectory of the source and detector around the patient. While the same sampling settings apply for each rotation, the data stream is now continuous and the pitch, i.e., the speed of the couch, specifies how often a point in the sample is visible in a projection. The pitch can be set freely to, e.g., 1.0 for very fast acquisition or 0.34 for better resolution and higher applicable dose.
The last scan mode, which is actually no CT acquisition, is called surview or scout scan and is used for patient positioning and planning of CT scans. For a surview the gantry rotation is stopped and positioned either in vertical or horizontal beam direction and the patient couch is moved through the beam path. The measured data is processed and yields a 2D image similar to a radiography, however, due to the strong divergence of the beam the image is distorted and not intended for diagnostic purposes. In this scan mode only the central detector lines are used and the collimator blades in the a-plane box make sure that only radiation for this narrow slot irradiates the patient.
Before tomographic reconstruction the acquired data must be pre-processed to correct a variety of setup-specific effects. For example, dead pixels and flux variations measured by the reference detector are corrected. Furthermore, calibration results from air scans, i.e., reference scans with no sample, are used to normalize the detector sensitivity.

5.4 Evaluation of Interferometer Geometries

From previous experiments with Talbot-Lau interferometers it is known that their geometry can be rather flexible, but various advantages and limitations must be considered. The choice of the interferometer geometry is a fundamental design decision and directly affects a cascade of parameters and specifications. As discussed in Section 2.3, a comprehensive study on interferometer geometries by Donath et al. [27] concludes that there are tree different design geometries of Talbot-Lau interferometers: Symmetric, asymmetric, and inverse geometry. In the following sections each variant is reviewed for application within the previously discussed CT geometry constraints and the arising advantages and problems are discussed.

5.4.1 Symmetric Geometry

The simplest interferometer geometry is the symmetric one where the distances L and d are equal, and thus, G_1 is positioned halfway between G_0 and G_2. In this geometry, the periods of G_0 and G_2 are the same, and depending on the G_1 design, i.e., for a π-phase-shift design, also G_1 can have the same grating period. This is particularly convenient when grating fabrication is difficult because when all gratings have the same period they can be produced from the same lithography mask. This can make the fabrication process more efficient and thus a bit easier. The sensitivity, which can be achieved in symmetric setups, is comparably high because usually a small grating periods and a long sample to G_2 distance can be chosen.
However, for an implementation in a CT gantry this geometry comes with several drawbacks. Given a minimal G_0 distance to the source (100 mm) and a minimal G_2 distance to the detector (40 mm) the symmetric geometry in a most optimistic estimation is shown in Figure 5.10. The geometry is only realizable when the bore diameter is decreased to about 300 mm, which is significantly smaller than the original 700 mm. This means that imaging of the human chest is not possible with such a geometry.
Another drawback of this geometry is that the sample is positioned not particularly close to G_1 and thus the effective sensitivity is strongly reduced. The sensitivity is roughly half the maximum value because the center of the sample is halfway between G_1 and G_2 and also extends into the area where it is closer to G_2 than to G_1. Furthermore, the sensitivity gradient through the sample is here the steepest of all available geometries.
There is also an alternative implementation with G_1 and G_2 both behind the patient possible, but then the field of view would be even smaller (around 280 mm diameter). Furthermore, such a design would require even larger gratings than in the design shown in Figure 5.10, where G_1 and G_2 are both relatively large compared to laboratory setups.
One can conclude that a symmetric geometry is not feasible for clinical CT as long as no major changes to the gantry (e.g., source and detector distance) are considered. The inefficient use of the available space on the CT gantry, a reduced sensitivity because the sample is close to the G_2, and the significantly smaller bore radius cannot outweigh the simpler grating fabrication and smaller grating periods.

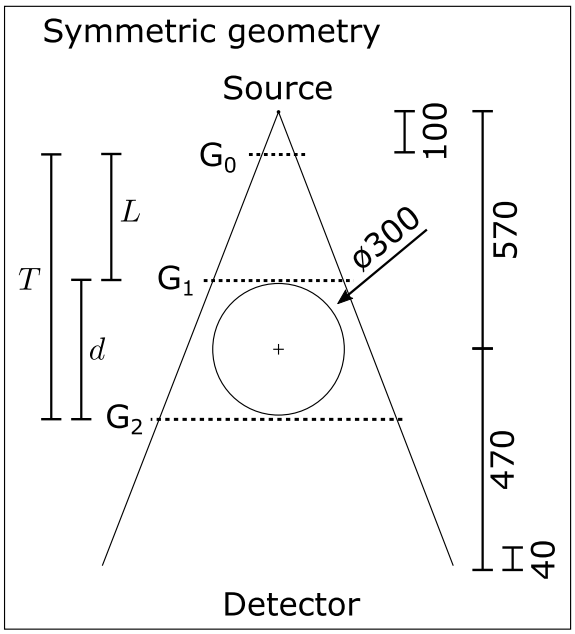

Figure 5.10: Symmetric interferometer geometry. It results in a smaller field of view with 280 mm diameter and requires larger gratings. Besides these shortcomings the geometry comes with the advantage that the grating periods of G_0 and G_2 are the same. With G_1 positioned behind the patient the patient dose is increased, compared to geometries, where the G_1 is before the patient. The total size of the gratings is rather large, compared to the relatively small reconstructable area.

5.4.2 Asymmetric Geometry

As derived by Donath et al. [27] the geometry of the Talbot-Lau interferometer can be freely re-scaled as long as the grating periods are adapted accordingly. While in a symmetric geometry the original bore-diameter cannot be maintained, this is possible with an asymmetric geometry but comes with several drawbacks.
In Figure 5.11, the sketch shows the re-scaling of the three-grating interferometer which leads to relatively small grating periods for G_1 and G_2. Since finer structures are difficult to manufacture, G_1 and G_2 are the crux in such a design. Furthermore, both are extremely large, i.e., almost as large as the entire detector surface which is about 80 cm wide. Only for G_0 this geometry offers an advantage because it has a coarse period, and it is relatively small, both making fabrication easier. A drawback of the G_1 position behind the patient can arise from its absorption and thus increase in patient dose.
The sensitivity of this design can be discussed under two separate aspects, namely the dependency on small periods and the influence of the geometry. For a high sensitivity finest grating periods are required, but due to the large area which G_1 and G_2 must cover their fabrication might be difficult. For such large areas coarser periods where yield of the fabrication is higher are preferred. Hence, it is assumed that for such a geometry a trad-off to coarser periods is required at the cost of system sensitivity.
Decoupled from the grating parameters the sensitivity also depends directly on the distance between sample and G_1. While the symmetric geometry is the worst-case-scenario in this relation and achieves only about 50% of the maximum sensitivity in the iso-center, the asymmetric geometry is slightly better. The sample is here positioned closer to the G_1 grating and consequently the asymmetric geometry can achieve a 14% higher sensitivity than the symmetric geometry – based on its geometry alone.
One can conclude that the asymmetric geometry is better suited for clinical dark-field CT than the symmetric geometry. It can produce a sufficiently large bore diameter compatible with the clinical requirements. In this geometry, the fabrication of the gratings is clearly the bottleneck because two gratings with fine periods and huge outer dimensions are required. Such large gratings with fine grating periods can then ultimately also run into stability issues because rigid mounting can become an issue.

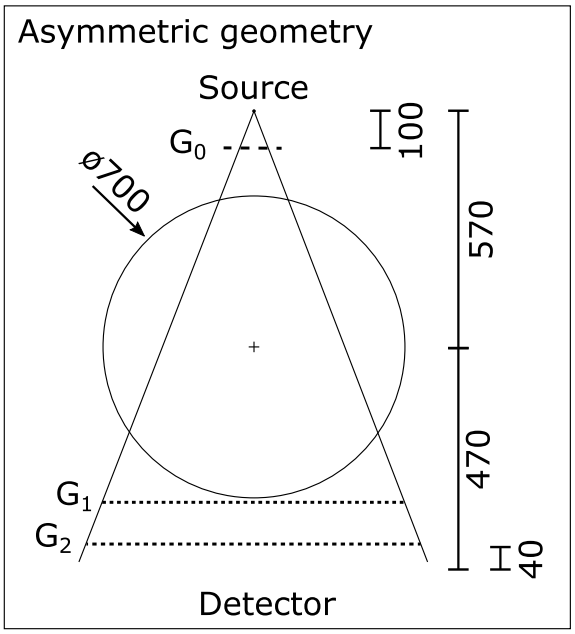

Figure 5.11: Asymmetric interferometer geometry. It allows to maintain the original bore diameter of 700 mm by placing G_1 and G_2 behind the patient. Due to the asymmetry the grating periods vary significantly and G_1 has the finest grating period. Furthermore, G_1 and G_2 must cover a large area. A positive aspect is that there is only one grating close to the source which is simple to fabricate because it is small and has a comparably coarse period.
Image adapted from [140] CC BY.

5.4.3 Inverse Geometry

Another geometry for Talbot-Lau interferometers is the inverse geometry which uses the reversed beam path of an asymmetric geometry. As illustrated in Figure 5.12 it also allows realizing a 700 mm bore diameter. It has the same asymmetry in the grating periods, but here the small periods are in G_0 and G_1.
In contrast to the asymmetric geometry where G_1 and G_2 have to be positioned very close to each other (with only about 70 mm inter grating distance) the distance between G_0 and G_1 in inverse geometry can use 120 mm space which is available in the collimator box. This is advantageous because it increases the sensitivity almost by a factor of two without the need for finer gating periods compared to the asymmetric geometry.
Positioning G_1 in front of the patient is also positive to optimize the dose efficiency. In such a geometry even an absorption grating as G_1 could be used with no negative impact on the patient dose. Furthermore, the sizes of G_0 and G_1 are both relatively small compared to the other two geometries and the only large grating is G_2. As for G_2 only a relatively coarse period is required its fabrication becomes simple even though it is large. For the two gratings with fine gating periods a low yield in the production can be tolerated as the quantity, i.e., area, of those is comparably small.
A drawback in this geometry is that the two most fragile gratings are positioned close to the X-ray source. Degradation caused by thermal stress and radiation damage might appear in these parts. Furthermore, the X-ray tube is known to be a source of vibrations due to the rotating anode, and placing fine-period gratings close to it might not be ideal. Rigid mounting is therefore important to avoid resonance between these gratings and the vibrations from the X-ray tube.
One can conclude that the inverse geometry is advantageous in almost all aspects which previously could not be sufficiently met by the symmetric and the asymmetric geometry. The inverse geometry makes efficient use of the available space within the CT gantry and maximizes the sensitivity that can be achieved without requiring finer grating periods.

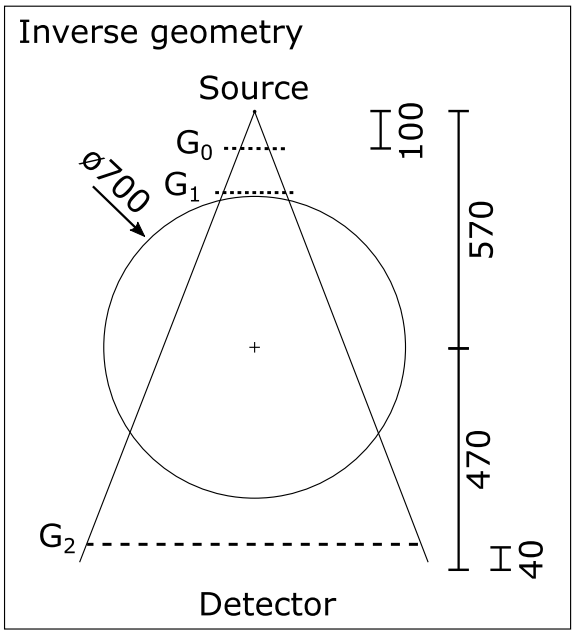

Figure 5.12: Inverse interferometer geometry. It is the reverse version of the asymmetric geometry and also maintains the original bore diameter of 700 mm. The two gratings close to the source are comparably small but also have the finest periods in the setup. The G_1 is positioned before the patient which makes patient dose independent of the G_1 design. Only one large G_2 is required but here with rather coarse periodicity. Image adapted from [140] CC BY.

5.4.4 Conclusion on Prototype Design Geometry

For the prototype design of the dark-field CT system clearly the feasibility of the design, its performance, and also the clinical relevance must be balanced. While the symmetric geometry would not require a grating close to the X-ray tube and its grating fabrication could profit from at least G_0 and G_2 having the same periods, it comes with the significantly reduced bore diameter which is not suitable for clinical chest imaging. This is an unacceptable restriction which disqualifies this geometry for the initial dark-field CT prototype. Consequently, a compromise towards asymmetric or inverse geometry must be found. Between those two alternatives, the inverse geometry is clearly advantageous. It requires the smaller total grating area to be fabricated, it positions G_1 in front of the patient, and it maximizes the sensitivity within the geometrical restrictions of the CT gantry. The disadvantages, such as positioning fragile and fine-period gratings close to the X-ray source is difficult to assess and must be considered during the design process of, e.g., the grating mounts.

Source to G_0	99.9 mm
Source to G_1	99.9 mm + 86.65 mm
Source to G_2	99.9 mm + 899.0 mm

Table 5.3: Grating positions used for prototype development for the geometry of the Brilliance iCT. Tolerances are ±1 mm for, e.g., fine-tuning of the final positions.

For the further discussion of the prototype development the inverse geometry with optimized grating positions tabulated in Table 5.3 is used. These values deviate slightly from the results in Section 5.3 because during the implementation process some adaptations became necessary. For example, some safety margins between the custom made mounts in the collimator box could only be guaranteed by selecting slightly different grating positions. These are important to avoid collisions and allow adjustment of the components.
From the values in Table 5.3 these interferometer geometry parameters follow,

$$T_{\text{dfCT, inverse}} = 899.0\,\text{mm}\ , \tag{5.4}$$
$$L_{\text{dfCT, inverse}} = 86.65\,\text{mm}\ \text{, and} \tag{5.5}$$
$$d_{\text{dfCT, inverse}} = 812.35\,\text{mm}\ . \tag{5.6}$$

Nevertheless, the alternative geometries should also be kept in mind for future dark-field CT implementations. As soon as modifying the X-ray source or detector position is within the scope here new possibilities might become available.

5.5 Grating Orientation

As discussed in Chapter 4, one-dimensional gratings, which are commonly used in dark-field X-ray imaging induce a strongly direction dependent shadowing artifact. It arises from the high aspect-ratio used in the setups and usually is most dominant in G_0 and G_2, i.e., the absorption gratings, as usually G_1, as a phase-grating, has only a relatively small aspect-ratio.
Another important aspect related to grating orientation is the direction dependence of the signal sensitivity. Only phase-shifts and small-angle scattering perpendicular to the grating lines can be resolved. From pre-clinical studies performed with mice no direction dependence of the small-angle scattering in the lung is known [154], [152], [135], [106], [50], [132].

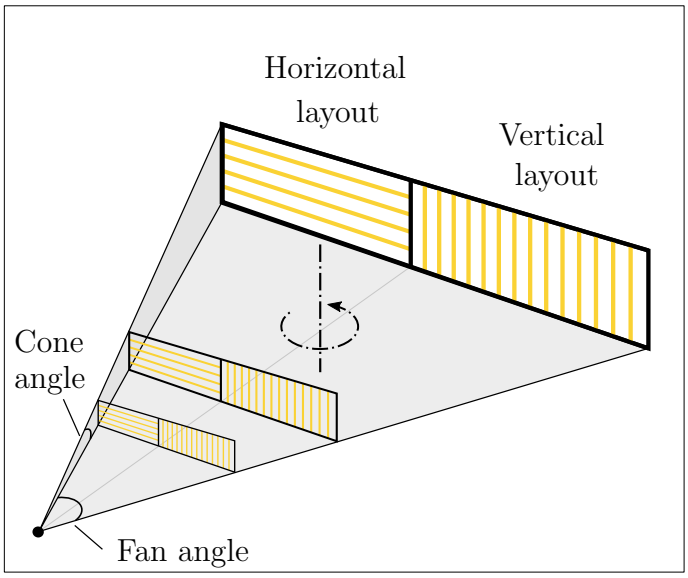

Figure 5.13: Sketch of horizontal and vertical orientated gratings. The grating lines in the vertical layout are parallel to the rotation axis of the CT, respectively the horizontal layout is perpendicular to it. Image adapted from [140] CC BY.

Consequently, there are two options of grating orientation, namely, *vertical layout* and *horizontal layout*, as illustrated in Figure 5.13. The first-mentioned has the grating lines oriented parallel to the CT rotation axis and the horizontal grating orientation perpendicular to the rotation axis. Advanced designs with tilted [14] or bidirectional patterns [39] are not considered for now as they require more complex processing of the data.
The horizontal layout comes with the advantage that in a CT implementation where the detector field of view is broad but only small in height no shadowing occurs along the detector rows, i.e., for varying fan angles. Depending on the actual height of the field of view shadowing can, however, become an issue as even for clinical CT machines with relatively small coverage of only 20 mm in the iso-center the cone opening is already around $\pm 2°$. For example, a G_0 grating with 4.8 µm period and 200 µm height, which has a maximum incidence angle $\alpha_m = 1.4°$ according to Equation (4.2), would have severe shadowing issues in most of the detector field of view. Consequently, if the dark-field CT should not be restricted to a few central detector lines the grating must be bent to compensate the shadowing. Since the spacial limitations in the CT gantry also require the gratings to be bent along the vertical axis this means that for a horizontal layout the gratings must be bent spherically. This has not yet been realized or published, and it is assumed to be difficult to achieve properly which is a significant drawback of the horizontal layout.
This is rather unfortunate because the horizontal layout actually has an important advantage over other grating orientations. As discussed in Section 4.5, the source size can have a significant influence on the interferometer performance. Since the source spot size of a clinical CT X-ray tube varies in width, i.e., along the horizontal grating lines, for increasing fan angles, but not in height, there would be no negative impact from this variance in a horizontal layout.
For now, the only solution, which works around spherical bending, is to fabricate divergent grating lamella as illustrated in Figure 4.3. This has recently been demonstrated by Pinzek et al. [97] for 10 µm gratings. However, further optimization of this approach is required to reach aspect ratios relevant for clinical dark-field CT.
The remaining alternative is the vertical layout. It is currently the only feasible design for the clinical dark-field CT prototype. After bending the grating along the vertical axis shadowing is vastly reduced and, since no shadowing for increasing cone angles occurs, this cylindrical bending is sufficient. Even large coverage, i.e., large cone angles, can be realized with this layout. A drawback is the previously mentioned increase in the X-ray focal spot width for

larger fan angles. It leads to performance loss due to source size induced shadowing in high aspect-ratio gratings (see Section 4.5). An advantage of the vertical layout over the horizontal one is the compression during the bending process which can close cracks in the grating structure as illustrated in Figure 4.12.
We can conclude on a vertical layout for the clinical dark-field CT prototype because it is currently the only feasible option. The horizontal layout, however, would come with promising advantages and should be considered once appropriate fabrication methods are available to solve the shadowing along the cone angles.

5.6 Evaluation of Grating and Interferometer Designs

As introduced in Section 2.3.2 a Talbot-Lau interferometer must fulfill certain geometrical requirements. We concluded on Equations (2.25) and (2.31), which can be reshaped to the underlying geometric constraints:

$$p_0 = \begin{cases} \frac{T}{d}\, p_1 & \text{for } \pi/2 \text{ shift and absorption grating} \\ \frac{1}{2}\frac{T}{d}\, p_1 & \text{for } \pi \text{ shift grating} \end{cases}, \tag{5.7}$$

$$p_2 = \begin{cases} \frac{T}{L}\, p_1 & \text{for } \pi/2 \text{ shift and absorption grating} \\ \frac{1}{2}\frac{T}{L}\, p_1 & \text{for } \pi \text{ shift grating} \end{cases}, \tag{5.8}$$

$$T = L + d\,. \tag{5.9}$$

This sets the inter-grating distances L and d from G_0 to G_1, and G_1 to G_2, respectively, into relation to the grating periods p_i for the respective gratings G_i.
While these equations also hold for the poly-chromatic X-ray spectrum, i.e., in a clinical CT machine, the formation of the Talbot-carpet, as discussed in Section 2.3.2 for monochromatic radiation, becomes less explicit. This makes it difficult to select, e.g., the structure height of G_1, based on a $\pi/2$ or π phase-shift for a specific fractional Talbot distance.
This problem can be solved by simulation-based search for the optimal parameter configuration. In Chapter 3, the simulation framework on which the following discussion builds on has been introduced. It performs several mono-energy propagation-based simulations of the interferometer with the given set of design parameters and combines them to a poly-chromatic result. This allows to optimize a large variety of parameters and can also give an educated guess on the interferometer performance one can expect from the design upon realization.
Since we concluded in Section 5.4.4 on an inverse geometry for the dark-field CT prototype, all simulations focus on this geometry and use the grating positions as defined in (5.4), (5.5), and (5.6). To keep the parameter-space of the simulations compact the initial parameter studies are performed with G_0 and G_2 as ideal absorption gratings. This means, they have a duty-cycle of 50%, no stabilizing structures, i.e., bridges, and their grating bars are 300 µm high which almost fully absorbs any radiation in the 80 kVp spectrum. This simplification is reasonable for identification of trends and most promising parameter combinations. Afterwards, realistic values must be set to evaluate the regions of interest in detail. The X-ray spectrum for the simulations is the 80 kVp spectrum of the iCT system which is filtered with 150 mm polyoxymethylen (POM) which represents the sample.
In the following sections, several design parameters are evaluated, first the most fundamental parameters such as grating period, profile, and height. After the most promising configurations are identified details such as duty-cycle, support structures, and spectral response are optimized.

5.6.1 Grating Profile and Structure Height

As an initial step, different grating profiles, i.e., binary and non-binary, and interferometer designs, i.e., $\pi/2$ phase-shift and π phase-shift designs, are evaluated with the simulation framework introduced in Chapter 3. We start with binary grating profiles which are the most common gratings in current Talbot-Lau interferometers and their shape has been introduced in Section 2.3.2.
Since the grating positions are fixed to the values listed in Section 5.4.4, the grating periods are defined by Equations (5.7) and (2.31), and thus, depend solely on p_1 and on the $\pi/2$ or π phase-shifting design. As discussed in Section 2.3.2, the difference between the two designs is that the period of G_2 is a factor two finer in the π phase-shift design than in the $\pi/2$ phase-shift design.

$\pi/2$ Phase-shift Design

By simulating interferometers with different G_1 periods and heights the best parameter configuration for a given X-ray spectrum can be identified. For every simulation, the respective grating periods of G_0 and G_2 are calculated based on Equations (5.7) and (2.31) considering a $\pi/2$ phase-shift design. Each simulation then yields the visibility which can be reached with the given parameter setting and the results are plotted in Figure 5.14. The simulation reveals that there is only one configuration with a significant performance for a $\pi/2$ phase-shift design. For a G_1 period of 1.9 µm and a height of about 4.4 µm (for gold as grating material) the visibility reaches a maximum. The simulation results indicate a maximum visibility of 33%, but this value is not quantitative and can only be used as a rough estimate because some grating parameters are not modeled realistically in this initial simulation. The full parameter configuration of the design is tabulated in Table 5.4.

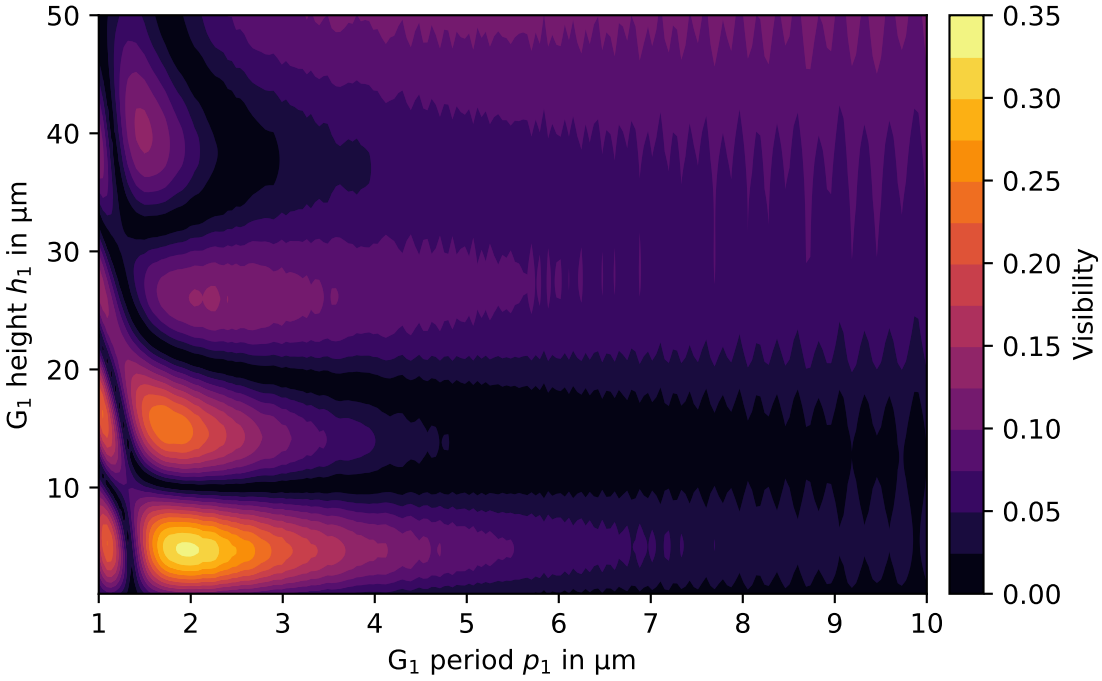

Figure 5.14: Simulation of interferometer performance for a $\pi/2$ phase-shift design with a binary G_1. The maximum performance arises for $p_1 = 1.9$ µm and $h_1 = 4.4$ µm. The simulation is based on the 80 kVp spectrum of the iCT with a filtration by 150 mm POM.

Grating	Period	Comment
G_0	2.10 µm	absorption grating, $h_0 \geqslant 300$ µm
G_1	1.90 µm	phase-grating, 4.4 µm high gold
G_2	19.7 µm	absorption grating, $h_2 \geqslant 300$ µm

Table 5.4: Best performing binary grating configuration in a $\pi/2$ phase-shift design.

For a further analysis and to evaluate why there is a performance minimum for 1.3 µm G_1 period, a visibility spectrum is shown in Figure 5.15. By simulating every energy separately, an energy resolved visibility can be generated and is plotted next to the 80 kVp power spectrum. This can reveal the visibility of the Talbot patterns before they are combined and add up to the resulting poly-chromatic visibility which is shown in Figure 5.14.
In the configuration which leads to the performance maximum ($p_1 = 1.9$ µm and $h_1 = 4.4$ µm) the energy resolved visibility is relatively high, wide-spread, but it is not ideally aligned with the spectrum indicated in gray. The maximum visibility is found at 48 keV, but the mean energy of the spectrum is around 55 keV. Nevertheless, a promising performance can be reached with this configuration, but it would profit from a softer X-ray spectrum. An interesting aspect is the comparably high performance above 80 keV, i.e., above the K-edge of gold, which, however,

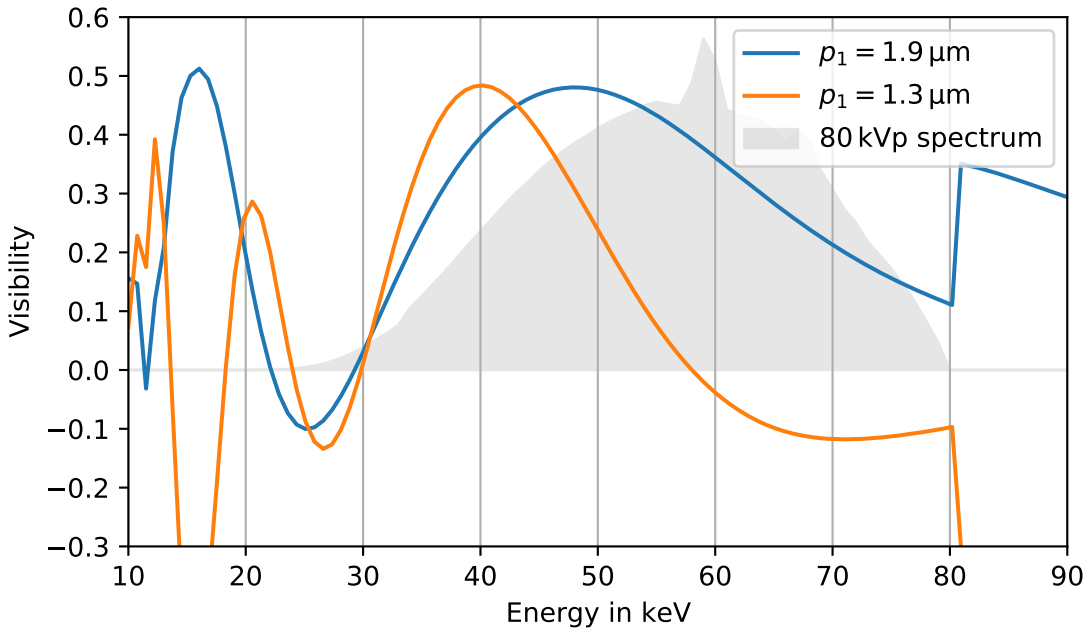

Figure 5.15: Simulation of energy resolved interferometer performance for a $\pi/2$ phase-shift design at two points of interest in Figure 5.14. The performance maximum for $p_1 = 1.9$ µm and a local performance minimum for $p_1 = 1.3$ µm are analyzed, both cases with $h_1 = 4.4$ µm (gold). In the background the 80 kVp spectrum is illustrated in arbitrary units. In the 1.9 µm configuration, the good overall performance arises from the wide and high visibility which is found for all energies between 35 and 80 keV, i.e., where the spectrum has a high intensity. For the other configuration we find a visibility minimum at 58 keV, i.e., the mean energy of the spectrum, and the Talbot carpets below and above this energy have an opposite phase-relation–plotted as negative visibility–which leads to contrast destruction when the Talbot carpets are combined.

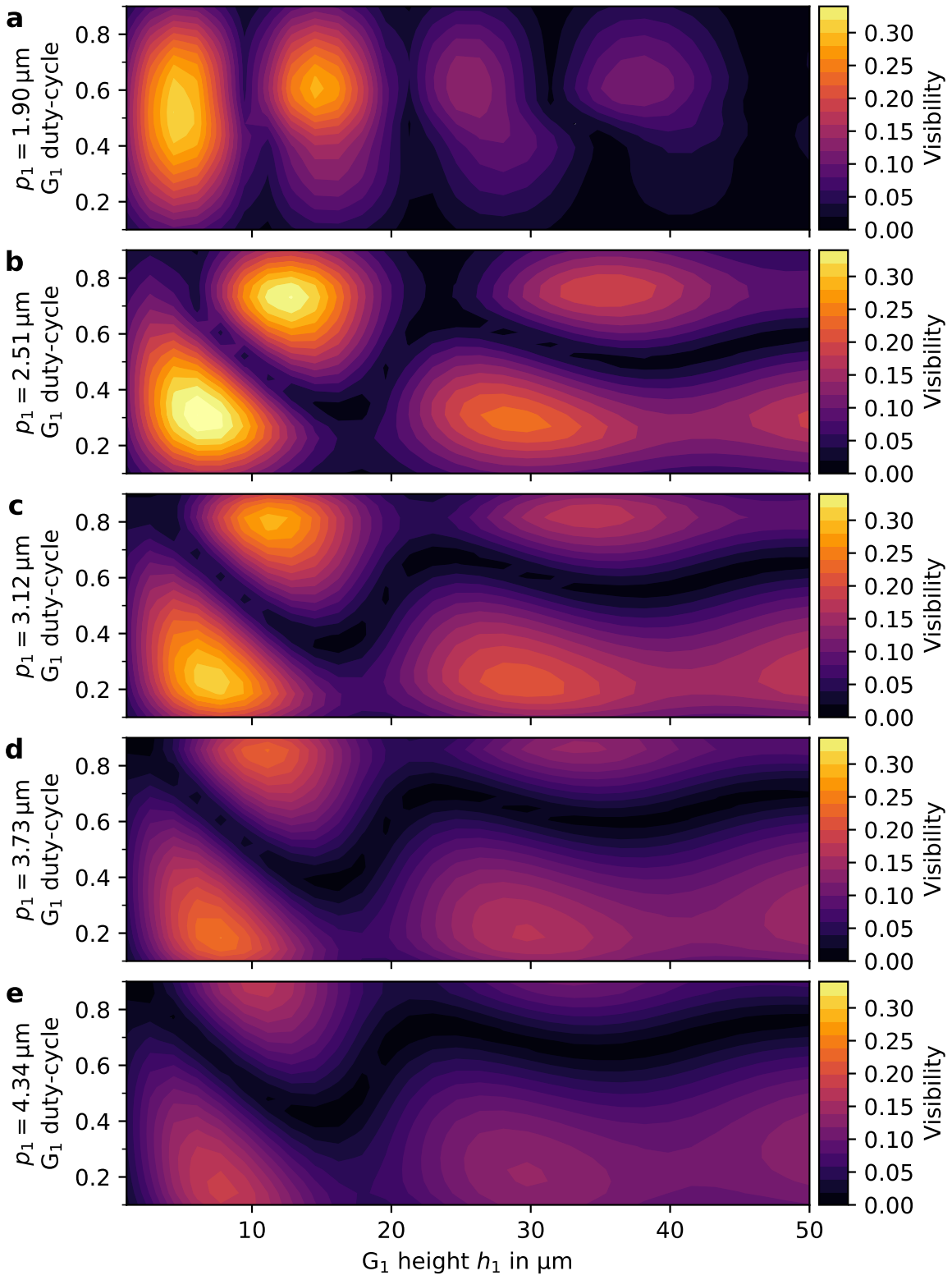

Figure 5.16: Simulation to analyze the impact of the G_1 duty-cycle and G_1 height in binary $\pi/2$ phase-shift design for different G_1 periods. **a,** Simulation of the performance maximum from the initial simulation in Figure 5.14 where only the 0.5 duty-cycle has been evaluated. **b,** The performance fluctuates and there are several plateaus with significant visibility for asymmetric duty-cycles, i.e., $\neq 0.5$. **c - e,** The pattern remains asymmetric, however, performance vanishes for larger p_1.

is not relevant for the prototype design which targets a 80 kVp spectrum.

As a counter example, the second configuration with $p_1 = 1.3\,\mu m$ and $h_1 = 4.4\,\mu m$ shows in Figure 5.15 that the visibility has a minimum at 58 keV in the center of the spectrum. Furthermore, another problem arises from the phase-inversion of the fringe patterns in the G_2 plane which is indicated by the change of sign at 58 keV. This means that the Talbot carpets do not add up constructively and are shifted in phase by 1π which leads to destructive interfere and an even lower overall visibility. This behavior is common in $\pi/2$ designs and can also be seen in Figure 2.13.

In a comprehensive study on the impact of the duty-cycle Rieger et al. [102] simulated and verified in experiments that, particularly in $\pi/2$ phase-shift designs performance maxima can be found for asymmetric duty-cycles. In Figure 5.16, a simulation is used to evaluate the impact of the duty-cycle around, e.g., the previously identified performance maximum at $p_1 = 1.9\,\mu m$ ($h_1 = 4.4\,\mu m$ and duty-cycle 0.5). While in Figure 5.16a the maximum performance is found at duty-cycle 0.5 as expected from the previous evaluation, in the other panels **b–e** asymmetries arise and maxima are revealed which were not within the parameter space of the initial evaluation. Particularly for a G_1 period of 2.51 µm (in Figure 5.16b) an extremely high performance for a 0.3 or 0.7 duty-cycle can be found. For larger G_1 periods the asymmetry of the overall pattern remains, but the total visibility decreases continuously. In Figure 5.16e, a configuration with $p_1 = 4.34\,\mu m$ and $p_0 = 4.8\,\mu m$ is evaluated which yields only a maximum visibility of 0.19, which is a rather low-value considering that ideal G_0 and G_2 are assumed.

Conclusion on Binary $\pi/2$ Phase-shift Design There is only one grating parameter configuration which yields a significant performance for a symmetric G_1 duty-cycle of 0.5 (listed in Table 5.4). It requires relatively fine gratings with a G_0 period of only 2.1 µm and is therefore not feasible for clinical dark-field CT implementation with current fabrication limitations. In a duty-cycle evaluation which also included larger G_1 periods additional performance maxima have been identified. Their grating periods, however, are not significantly coarser, and they require extremely asymmetric duty-cycles which can also introduce problems during fabrication. No promising grating configuration for clinical dark-field CT based on a binary $\pi/2$ phase-shift design has been identified.

Absorption G_1 Design

A variant of Talbot-Lau interferometers uses an absorption grating instead of a phase-shifting grating as G_1. As introduced in Section 2.3.2, in the absence of any rays transmitted through the grating bars of G_1 solely the unperturbed rays from neighboring slits interfere and lead to an interference pattern. In Figure 5.17 simulation results for this design are shown, where G_0 and G_2 periods are set as in a $\pi/2$ phase-shift design. It reveals that a wide range of configurations with high G_1 structures perform well in the given geometry. For small G_1 structure heights, i.e., smaller 25 µm, the phase-shift-driven visibility maximum as found in Figure 5.14 can be identified. The focus, however, lies on the higher G_1 structures where purely the absorption in the grating bars leads to an interference pattern and configurations with G_1 periods around 1.5 µm and above 4 µm generate a significant visibility. For larger G_1 periods above 4 µm the design smoothly transitions into a non-interferometric design where visibility is purely generated by the cast shadow behind the G_1 slits. These non-interferometric designs come with rather coarse grating periods but can produce significant visibilities.

The performance minimum around the G_1 period of 2.1 µm arises because of the structure of the resulting Talbot-carpet behind the G_1 grating. By comparing Figures 5.26c and 5.27c it

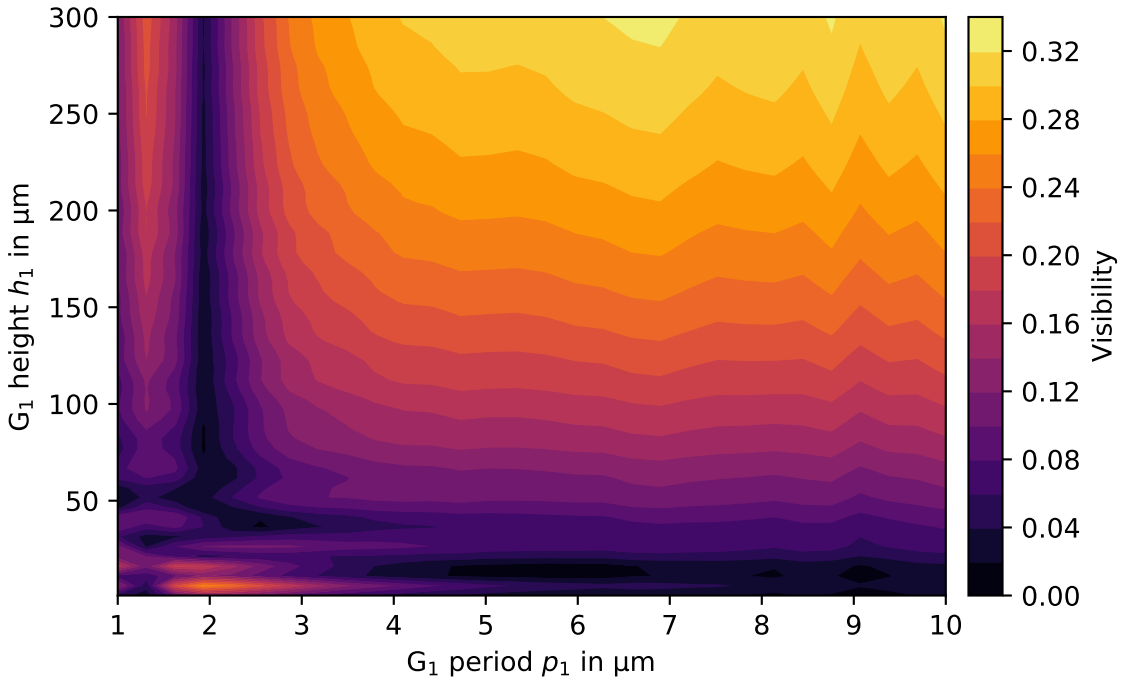

Figure 5.17: Simulation of interferometer performance for a $\pi/2$ phase-shift design with a binary absorption G_1. A wide performance maximum for high G_1 structures with periods larger than 4 µm is found. The simulation is based on the 80 kVp spectrum of the iCT with a filtration by 150 mm POM.

Grating	Period	Comment
G_0	4.80 µm	absorption grating, $h_0 \geqslant 300$ µm
G_1	4.34 µm	absorption grating, $h_1 \geqslant 250$ µm
G_2	45.0 µm	absorption grating, $h_2 \geqslant 300$ µm

Table 5.5: Example configuration for an absorption G_1 based design with good performance.

can be found that in the $p_1 = 2.1$ µm case the carpet is evaluated at an unfavorable position. As expected for every absorption grating, the results in Figure 5.17 demonstrate that in for an absorption design higher G_1 structures lead to better visibility because of the increased stopping power of the G_1 grating lamella.

Conclusion on Binary Absorption G_1 Design This design is highly flexible as it allows a wide variety of grating period configurations with good performance. However, due to the hard X-ray spectrum the G_1 structure height must be comparably large, i.e., in the range of 250 µm and higher to produce a significant visibility. This makes its fabrication even more difficult than for G_0 because due to the geometry, it must cover a larger area. Another potential issue is the loss of flux in absorption gratings, which is unavoidable for G_0 and G_2 but unusual for G_1. This can be easily compensated by increasing the generated X-ray flux if the source has sufficient power overhead.
If the high aspect-ratio was no limitation this design would be very promising. In Table 5.5 an example configuration which might be feasible with state-of-the-art grating fabrication technology is listed. An energy resolved visibility evaluation for this configuration is shown in Figure 5.21 as a part of the discussion in Section 5.6.1.

π Phase-shift Design

An alternative to the previously discussed $\pi/2$ phase-shift design is the π phase-shift design. In the parameter study on p_1 and h_1, shown in Figure 5.18, we can identify one performance maximum at $p_1 = 3.8\,\mu m$ for a G_1 height of $9.8\,\mu m$. While this coarser G_1 period is advantageous for fabrication, it must be kept in mind that in a π phase-shift design the G_0 and G_2 periods are reduced by a factor of two compared to a $\pi/2$ phase-shift design. The best performing configuration therefore requires a $2.1\,\mu m$ fine G_0 period as tabulated in Table 5.6.
In comparison to the $\pi/2$ phase-shift design evaluated in Figure 5.14 the performance maximum of the π phase-shift design is slightly shifted towards larger G_1 periods. In Figure 5.19, the visibility spectra for the configuration of maximum performance and a configuration where the G_0 period is $4.8\,\mu m$ are plotted. The latter is chosen as an example because this configuration lies within the specification of state-of-the-art grating fabrication technology. In contrast to the $\pi/2$ phase-shift design results no negative visibility appear in π phase-shift designs. Therefore, by aligning the visibility spectrum sufficiently to the setups power spectrum results in a good performance as we can see for the $p_1 = 3.8\,\mu m$ curve in Figure 5.19. The alternative case where $p_1 = 8.7\,\mu m$ (and $p_0 = 4.8\,\mu m$), however, performs significantly worse due to lower overall visibilities.

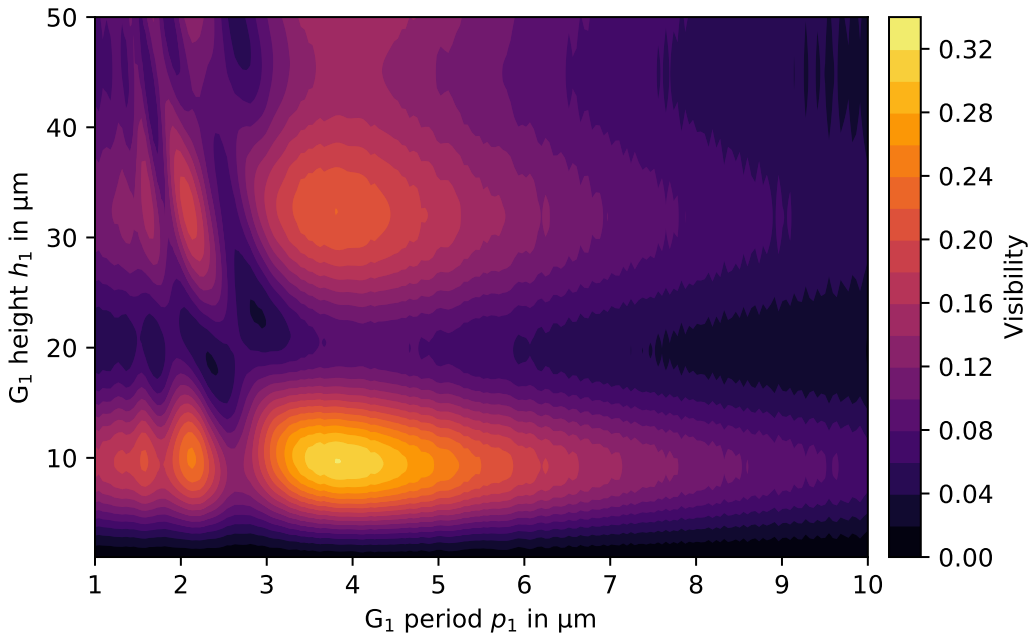

Figure 5.18: Simulation of interferometer performance for a π phase-shift design with a binary G_1. Maximum performance is found at $p_1 = 3.8\,\mu m$ and $h_1 = 9.8\,\mu m$. The simulation is based on the 80 kVp spectrum of the iCT with a filtration by 150 mm POM.

Grating	Period	Comment
G_0	$2.10\,\mu m$	absorption grating, $h_0 \geqslant 300\,\mu m$
G_1	$3.80\,\mu m$	binary phase-grating, $9.8\,\mu m$ high gold
G_2	$19.7\,\mu m$	absorption grating, $h_2 \geqslant 300\,\mu m$

Table 5.6: Best performing binary grating configuration with a π phase-shift design.

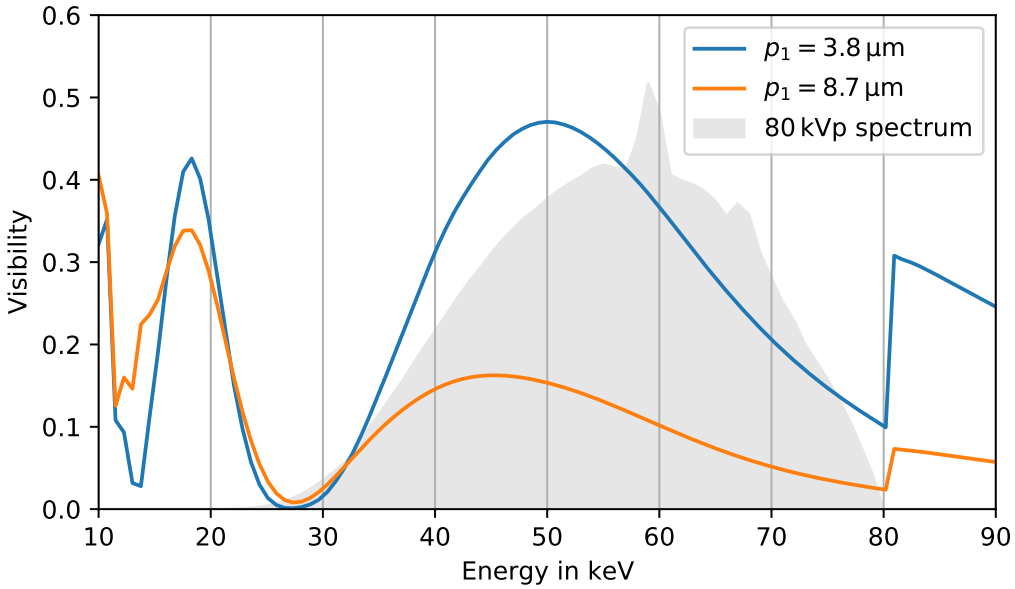

Figure 5.19: Simulation of the visibility spectrum for a π phase-shift design for $p_1 = 3.8\,\mu m$ and $p_1 = 8.7\,\mu m$, both with $h_1 = 9.8\,\mu m$ (gold). In the background the 80 kVp spectrum is illustrated in arbitrary units. Both curves have a wide visibility maximum which is almost aligned with the spectrum and primarily differ in their maximum height which is significantly higher for the $p_1 = 3.8\,\mu m$ design.

Conclusion on Binary π Phase-shift Design Similar to the $\pi/2$ design also in a π phase-shift design only fine grating periods yield a significant performance. While the G_1 period is coarser still a very fine G_0 with $p_0 = 2.1\,\mu m$ is required. An advantage is the wider performance maximum and that the visibility spectrum has no inversions. Consequently, when finer absorption grating periods are feasible this design might become interesting. However, currently there is no binary π phase-shifting design which is promising for a clinical dark-field CT prototype.

Triangular Grating Profile

An alternative to the binary grating profile are triangular gratings which are only available as phase-shifting gratings, i.e., with relatively small grating heights. They are also referred to as non-binary gratings as introduced in Section 2.3.2 and have for example been evaluated by Yaroshenko et al. [153].
In a simulation, a wide parameter range of p_1 and h_1 have been evaluated where periods for G_0 and G_2 are set as in a $\pi/2$ phase-shift design and the resulting system visibility is plotted in Figure 5.20. Clearly these results differ from the classical binary $\pi/2$ and π phase-shift designs as not a local maximum is found but a rather large and flat performance area. It covers a range of G_1 periods from 2 to 7 µm for structure heights from 6 to 50 µm and seems to continue for even higher periods and heights.
The simulated performance for the triangular gratings lies here above 30% and thus is comparable with previous results from the other designs. It is important to note that the triangular grating profile leads to a similarly flexible configurations as found for an absorption G_1 design. In contrast to the absorption G_1 design, as proposed in Table 5.5, with a triangular G_1 the fabrication is easier. This is because the G_1 structure heights are comparably low.
In Table 5.7 an example configuration for the peak performance with a triangular G_1 grating is listed. It is based on a 4.8 µm G_0 period, which is currently the minimum period for hard X-ray

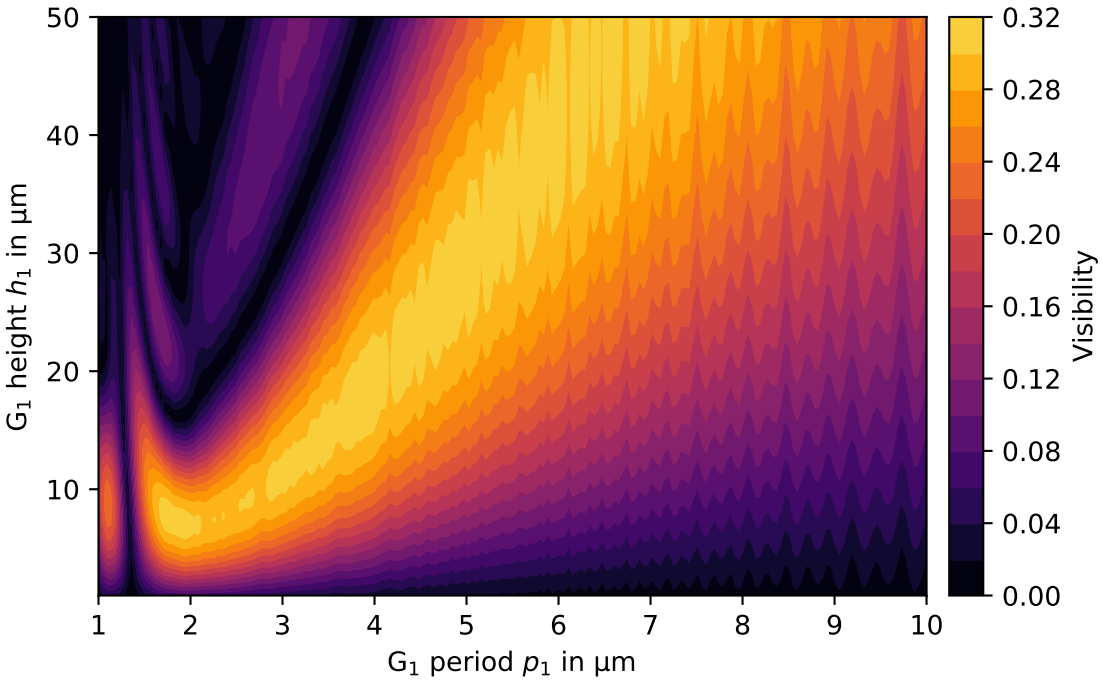

Figure 5.20: Simulation of interferometer performance for a $\pi/2$ phase-shift design with a triangular G_1 profile. A wide performance maximum for various G_1 periods larger than 2 µm is found. The simulation is based on the 80 kVp spectrum of the iCT with a filtration by 150 mm POM.

Grating	Period	Comment
G_0	4.80 µm	absorption grating, $h_0 \geqslant 300$ µm
G_1	4.34 µm	triangular phase-grating, 20 µm high gold
G_2	45.0 µm	absorption grating, $h_2 \geqslant 300$ µm

Table 5.7: Grating configuration based on a G_0 period of 4.8 µm with a triangular G_1 profile and $\pi/2$ phase-shift design.

Grating	Period	Comment
G_0	2.05 µm	absorption grating, $h_0 > 250$ µm
G_1	1.85 µm	triangular phase-grating, 8 µm high gold
G_2	19.2 µm	absorption grating, $h_2 > 250$ µm

Table 5.8: Best performing grating configuration with triangular G_1 profile and $\pi/2$ phase-shift design. The fine grating periods allow the highest angular sensitivity but are currently not feasible to be fabricated for the hard X-ray spectrum of clinical CT.

compatible gratings. The corresponding G_1 then must have a period of 4.34 µm and should have triangular structures with a maximum height of 20 µm (for gold as grating material). At this height, a 2π phase shift is induced for X-rays at around 52 keV which is close to the mean energy of the used spectrum.
An alternative configuration is presented in Table 5.8 which uses finer periods and consequently achieves a higher angular sensitivity. Obviously, here the fabrication of the fine G_0 period with

high aspect-ratio is the bottleneck in current grating fabrication technology.
Similar simulations in π phase-shift design lead to no significant performance.

Conclusion on Triangular Grating Profile In Figure 5.21, the visibility spectra for the two triangular grating configurations in Tables 5.7 and 5.8 are plotted in comparison to the absorption G_1 design proposed in Table 5.5.
All these configurations have very similar performance characteristics which only deviate significantly for energies above 80 keV (for which none of the designs has been optimized, thus this can be ignored for now). Since the 80 kVp spectrum used at the system has only a small intensity around 35 keV the visibility minimum in the triangular $p_1 = 4.34\,\mu m$ configuration at this energy has only a small impact on the overall system performance.
The advantage of the triangular grating profile is clearly the simpler fabrication of the G_1 which is only 8 or 20 µm high and thus has a relaxed aspect-ratio. Nevertheless, the absorption design remains a promising candidate because it has a robust spectral response and has previously been used in other designs. The triangular G_1 profile, in contrast, has not yet been implemented in a dark-field CT system.

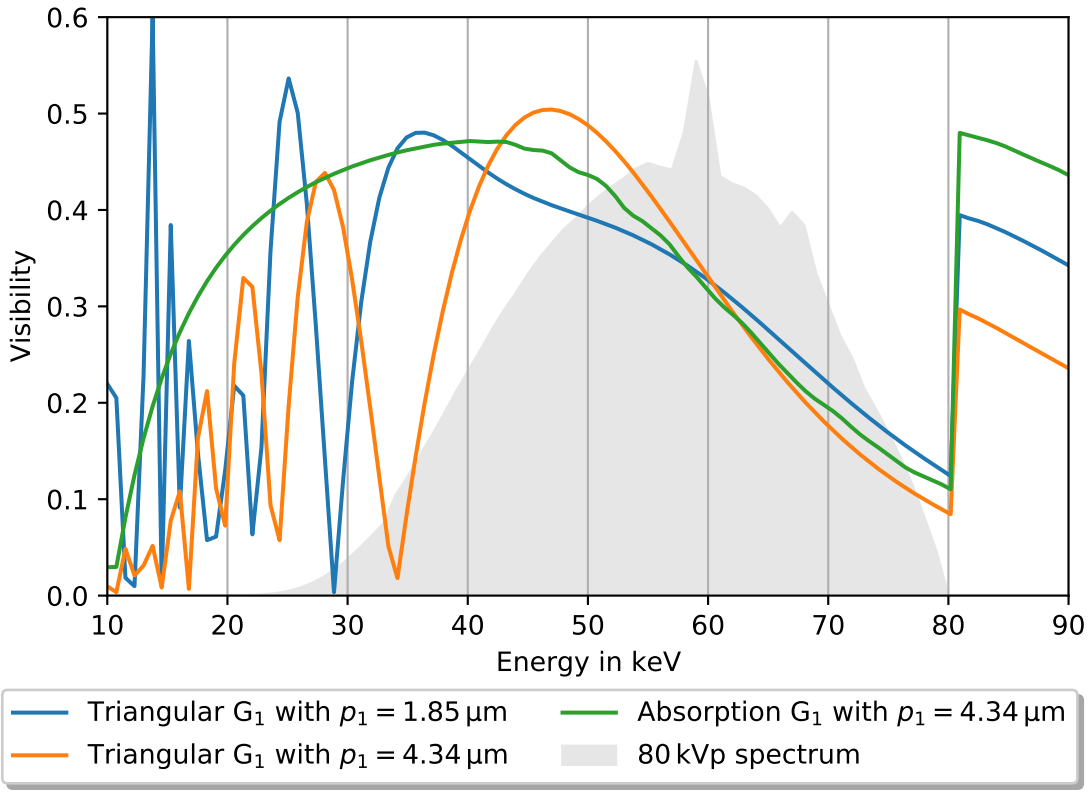

Figure 5.21: Simulation of energy resolved interferometer performance for a $\pi/2$ phase-shift design with triangular and absorption G_1. All variants lead to a high and similar performance in the range of the 80 kVp spectrum. Only above 80 keV, i.e., at the gold K-edge, and at 35 keV deviations occur, which have only a minor impact on the total system performance as they lie in areas where the 80 kVp spectrum has low power.

5.6.2 Duty-cycle of G_0, G_1, and G_2

From studies by Thuering and Stampanoni [129] and Rieger et al. [102] the huge impact of duty-cycle variations is known and has previously been seen in Figure 5.16 for the binary $\pi/2$ phase-shifting design. In this section, the influence of this parameter in all three gratings, i.e., G_0, G_1, and G_2, is studied for the two most promising designs with the triangular G_1 profile or the absorption G_1). For all simulations, the absorption gratings are configured as 300 µm high gold structures and the 80 kVp spectrum with 150 mm POM filtration is used.
In Figure 5.22, the simulation results show the peak performance around a duty-cycle of 0.5 for both G_1 profiles. Only for absorption G_1 at structure heights above 200 µm a slightly increased duty-cycles towards 0.6 becomes advantageous. For the design with a triangular G_1 profile clearly a 0.5 is the optimum duty-cycle. A minor performance asymmetry is found for extremely high triangular grating structures with a 0.2 duty-cycle. Presumably this arises as high aspect-ratio triangular gratings with small duty-cycle become similar to binary profiles with small duty-cycle.
These results demonstrate that duty-cycle variations, which are common defects in microfabrication processes and can be in the range of a couple of percent, are acceptable. For the

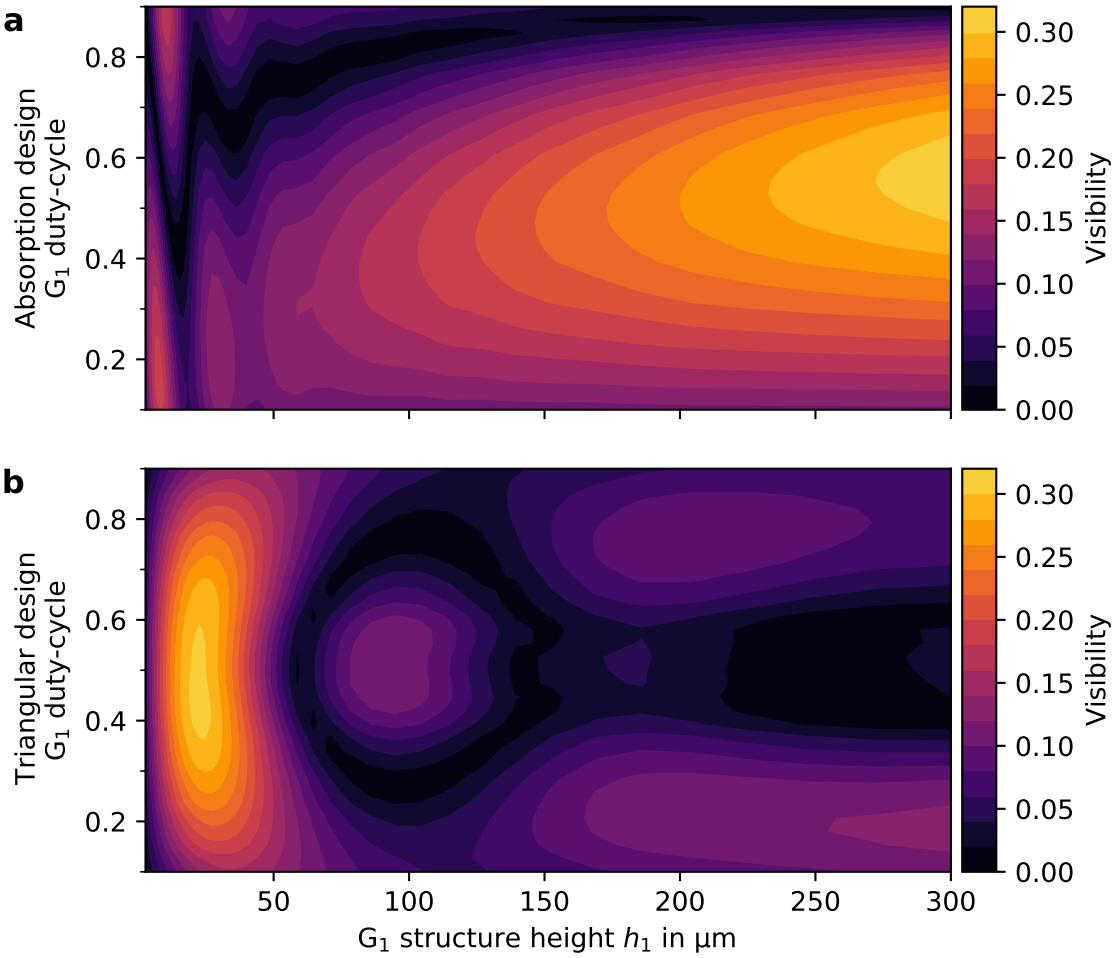

Figure 5.22: Simulation to analyze the impact of the G_1 duty-cycle and G_1 height in the triangular and absorption G_1 design. **a,** In an absorption G_1 design for increasing grating heights a duty-cyle of 0.58 slightly increases the visibility. **b,** The triangular G_1 profile works best at a height around 20 µm and at a duty-cycle of 0.5 .

absorption G_1 design a slightly increased duty-cycle between 0.5 and 0.58, depending on the height of the grating structures, might be advantageous.
For the other two gratings Figure 5.23 shows that there lies significant potential in optimization of the duty-cycles of G_0 and G_2. Both can achieve a better interferometer visibility with a peak at G_0 and G_2 duty-cycles of 0.72 . While the common duty-cycle of 0.5 also performs well with a visibility of 0.34, an optimization of both grating duty-cycles would lead to a relative visibility increase of almost 50% .
As derived by Thuering and Stampanoni [129] the optimum duty-cycles depend on the height of G_0 and G_2 and here, for 300 µm high gratings it is a duty-cycle of 0.72. The rest-transmission, i.e., radiation which leaks through the gold lamella since there is no perfectly absorbing material, has a significant impact. For gratings with higher rest-transmission the optimal performance is closer to a symmetric duty-cycle of 0.5, only if good gratings with low rest-transmission are used a performance boost can be achieved with larger duty-cycles.
This significant visibility optimization potential, however, comes at the cost of flux and feasibility. Since gratings with extreme duty-cycles above 0.6 are rather uncommon, there is only little experience in the microfabrication available. For asymmetric duty-cycles the aspect-ratio of either the resist or the grating lamella increases which potentially leads to problems and limitations in the fabrication. Another problem is that for imaging sufficient X-ray flux must reach the detector. Naturally, a larger duty-cycle leads to more X-ray absorption in the grating and consequently the absorbed photons no longer contribute to the signal. In Figure 5.24, the transmitted intensity behind the interferometer is analyzed in a simulation. It shows that for a standard 0.5 duty-cycle configuration the transmission T is,

$$T(\mathrm{dc}_0 = 0.5, \mathrm{dc}_2 = 0.5) = 0.5 \cdot 0.5 + 2\tau = 0.25 + 2\tau \ , \tag{5.10}$$

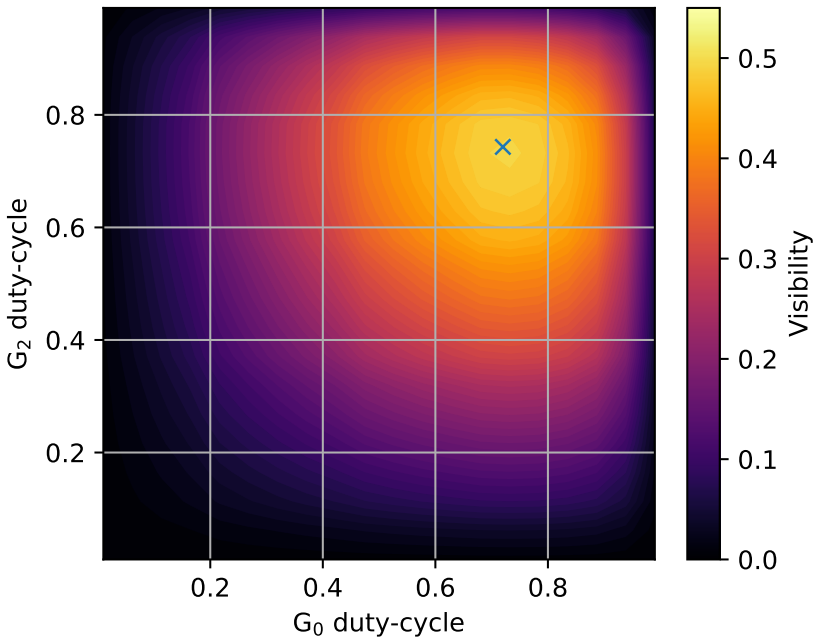

Figure 5.23: Simulation of G_0 and G_2 duty-cycle impact on the visibility for a design with a triangular G_1. The maximum is found at a duty-cycle of 0.72 for both gratings. In comparison to the standard duty-cycle of 0.5 an optimization can yield a relative performance gain of almost 50% . The precise position of the optimum depends on the rest-transmission of the absorption grating. Here, the rest-transmission is rather low because 300 µm high gold gratings are evaluated which can almost fully absorb the radiation of the 80 kVp spectrum.

with τ as the rest-transmission of each absorption grating. For clarity, $\mathrm{dc}_0 = \mathrm{dc}_2$ is used, but certainly also different rest-transmissions for each grating are possible. The configuration with the best visibility, in contrast, yields only

$$T(\mathrm{dc}_0 = 0.72, \mathrm{dc}_2 = 0.72) = (1 - 0.72) \cdot (1 - 0.72) + 2\tau' = 0.08 + 2\tau' \,, \tag{5.11}$$

with τ' as the rest-transmission of each absorption grating with duty-cycle 0.72 . This reveals that the optimization towards larger duty-cycles is accompanied by a significant loss in X-ray flux. Consequently, the best visibility is not necessarily equal to best performance because the imaging performance also depends on the number of photons reaching the detector.
To evaluate this relation and optimize the design for best imaging performance the signal-to-noise ratio is a common measure. In attenuation imaging this is purely intensity I dependent:

$$\sigma_{\mathrm{att}} \propto \frac{1}{\sqrt{I}} \,, \tag{5.12}$$

For dark-field imaging also the visibility V must be included and Weber et al. [143] derived for the noise level,

$$\sigma_{\mathrm{df}} \propto \frac{1}{V\sqrt{I}} \,, \tag{5.13}$$

which allows us to find a trade-off between visibility, which increases with larger duty-cycles, and intensity, which decreases with larger duty-cycles.
The simulation results shown in Figure 5.25 reveal for a design with 300 µm high G_0 and G_2 gratings that the best dark-field signal-to-noise ratio is reached for duty-cycles of 0.59 and 0.60, respectively. The results also demonstrate that these parameters form a wide peak,

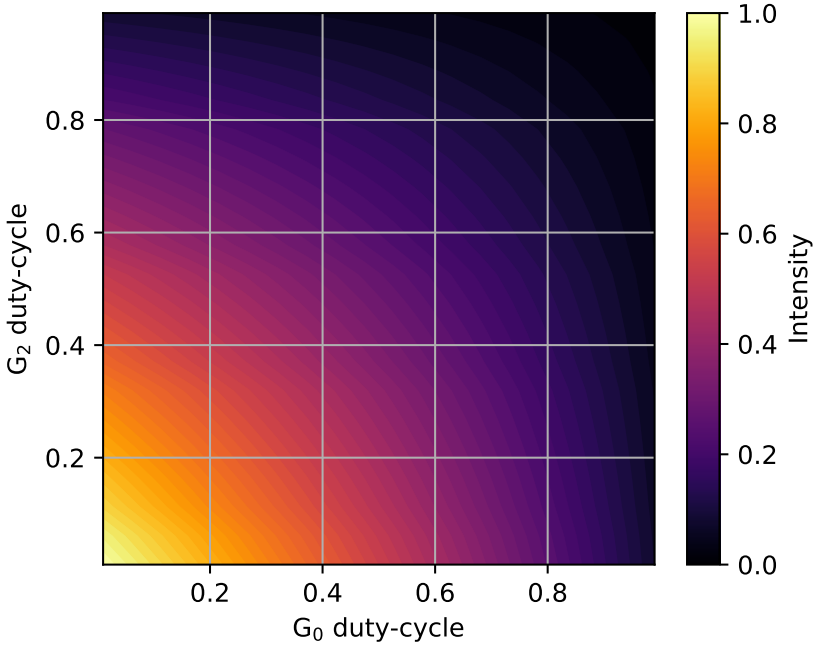

Figure 5.24: Simulation results of G_0 and G_2 duty-cycle variation show the associated reduction of the transmission for larger duty-cycles as the absorption gratings stop more radiation. Here, 300 µm high grating structures made of gold and the 80 kVp spectrum of the iCT filtered by 150 mm POM are simulated. For G_0 and G_2 duty-cycles 0.5 the transmission is about 27% and for the visibility maximum found in Figure 5.23 at duty-cycles 0.72 the transmission is about 11%.

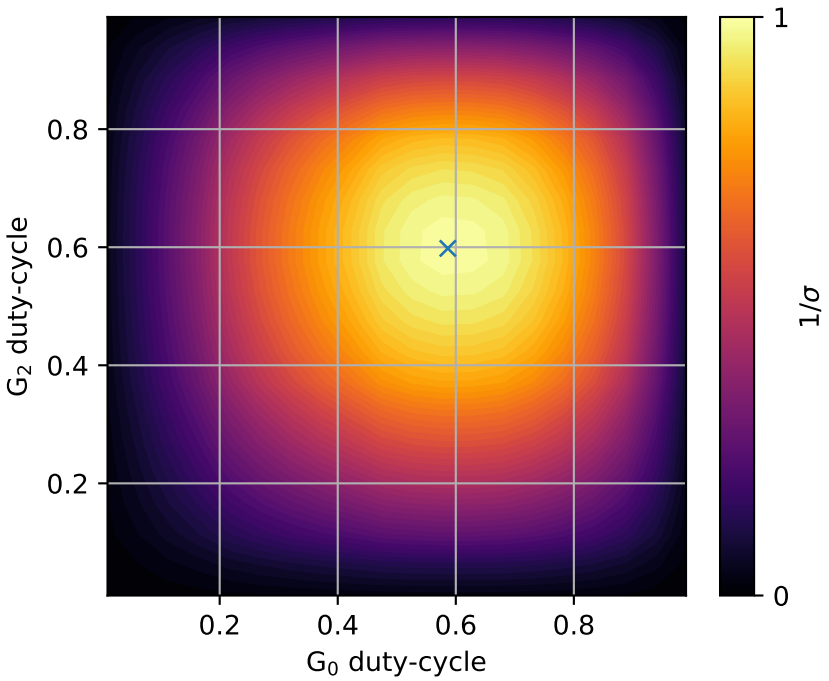

Figure 5.25: Signal-to-noise ratio simulation results of G_0 and G_2 duty-cycle variation based on Equation 5.13. This representation combines the visibility and intensity results from Figures 5.23 and 5.24. It reveals that for dark-field imaging the optimal duty-cycle configuration is 0.59 and 0.60 for G_0 and G_2, respectively. Image adapted from [140] CC BY.

consequently, deviations in the duty-cycle by some percent can be tolerated. While these numbers clearly indicate that G_0 should be fabricated with a 0.6 duty-cycle, a more careful consideration is required for the G_2 duty-cycle. For G_2 the potential duty-cycle deviations from the fabrication process can lead to an unnecessary increase in patient dose if the duty-cycle exceeds 0.6. Therefore, the nominal duty-cycle should be around 0.56 which ensures that deviations do not lead to an additional patient dose without an improvement of the signal-to-noise ratio.
It is important to note that Figures 5.23, 5.24, and 5.25 show results for the triangular design which are almost identical to the results for an absorption G_1 with one exception. For an interferometer design with an absorption G_1 more X-ray flux is absorbed by the G_1 which decreases the intensity reaching the detector. While this does not lead to a shift of the optimal G_0 and G_2 duty-cycles around 0.6, the signal-to-noise ratio is affected significantly. From simulation result follows that in a design with a triangular G_1 the signal-to-noise ratio is 27% higher than in an absorption G_1 design. This reveals an additional argument why a triangular G_1 is advantageous over an absorption G_1 design.

Conclusion on Duty-Cycle Optimization The evaluation of the impact of G_0, G_1, and G_2 duty-cycles revealed significant potential and must be considered for fine-tuning of the grating design. Optimization of the interferometer visibility alone is not sufficient as also the change in X-ray transmission has an impact on the imaging performance. Best signal-to-noise ratio is achieved for a G_0 duty-cycle of 0.6, a G_1 duty-cycle of 0.5 to 0.58 depending on the design, and for G_2 a value between 0.56 and 0.6 is ideal. Considering the signal-to-noise ratio, the analysis also revealed a significant advantage of the triangular G_1 design over the absorption G_1 design. When generated X-ray flux is kept constant the triangular G_1 design comes with a 27% higher imaging performance than the absorption G_1 design.

5.6.3 Talbot Carpet Evaluation

In the previous sections the various grating profiles and designs have been evaluated by simulations of the interferometer in the compact CT geometry and calculations of the system visibility or the signal-to-noise ratio. To validate the results and demonstrate why the absorption and the triangular design are the most promising candidates, the poly-chromatic Talbot-carpets for several designs are shown in Figure 5.26. Here, all simulations are performed for 4.34 µm period G_1 gratings with duty-cycle 0.5 but different heights, e.g., 4.9 µm representing a $\pi/2$ or 10 µm for a π phase-shift design, as discussed in Section 5.6.1. The simulation of the Talbot-carpets uses a poly-chromatic yet perfectly coherent X-ray beam and the 150 mm POM filtered 80 kVp spectrum of a clinical CT as in the previous sections. Consequently, the divergence of the beam and the impact of G_0 are omitted as well as the analyzer grating G_2. This allows us to resolve the interference effects in the Talbot-carpet over a longer propagation distance, beyond the propagation limit implied by the divergence. In orange the virtual analyzer plane, i.e., where

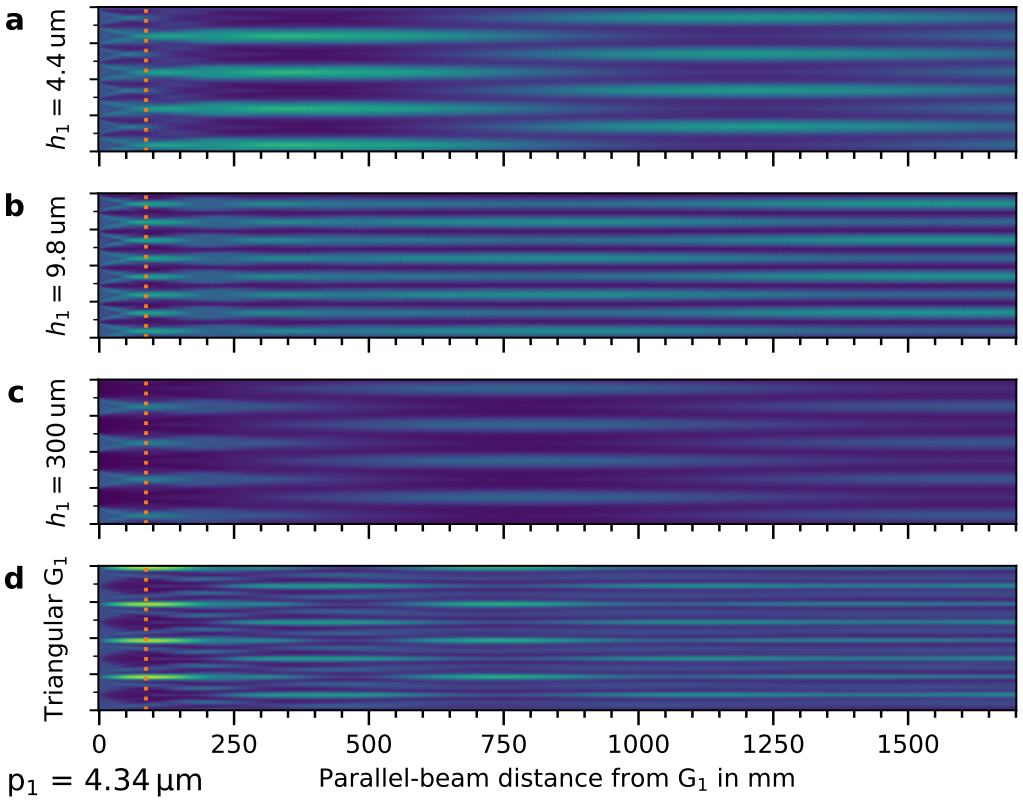

Figure 5.26: Poly-chromatic Talbot carpets for different G_1 heights with otherwise constant configuration (period 4.34 µm, duty-cycle 0.5, G_1 material gold, 80 kVp spectrum filtered with 150 mm POM) in parallel beam. **a,** With the $\pi/2$ phase-shifting G_1 the first high contrast fringes are found after a relatively long parallel propagation distance of about 350 mm. In the inverse CT geometry (orange line) the performance is degraded due to additional local intensity maxima. **b,** In the π phase-shifting configuration the carpet is very stable for varying distances, but the frequency of the fringe pattern is doubled. **c,** An absorption G_1 grating leads to a similar pattern as the $\pi/2$ phase-shifting G_1 in panel a, but it is shifted towards G_1, has no additional local intensity maxima, and due to the absorption in G_1 the overall intensity is reduced. **d,** The triangular G_1 is simulated with height 20 µm and leads to a pattern which contains details from $\pi/2$ and π phase-shifting designs. It focuses particularly well for the short propagation distances where narrow intensity maxima are generated.

G_2 is positioned in the CT implementation, is highlighted at the scaled propagation distance,

$$d_{\text{parallel}} = \frac{L}{T} \cdot d_{\text{cone}} = \frac{L_{\text{dfCT, inverse}}}{T_{\text{dfCT, inverse}}} \cdot d_{\text{dfCT, inverse}} = 78.30\,\text{mm}\ , \tag{5.14}$$

with the lengths defined in Equations (5.4) to (5.6). For further information on this re-scaling see Section 3.2 and the comprehensive work by Paganin [88].
The simulated Talbot-carpet in Figure 5.26a shows that a $\pi/2$ phase-shifting G_1 produces the first high contrast fringes at a parallel-beam propagation distance of about 350 mm. Such a propagation distance is beyond the feasible length within a CT gantry. In the proposed inverse CT geometry, indicated in orange, additional intensity maxima between the high contrast fringes occur and degrade the interferometer performance.
In Figure 5.26b, the advantage of a π phase-shifting G_1 in a poly-chromatic spectrum is demonstrated. This configuration is known to perform well in these spectra because of the little contrast variation along the different propagation distances. This can be seen in these results where

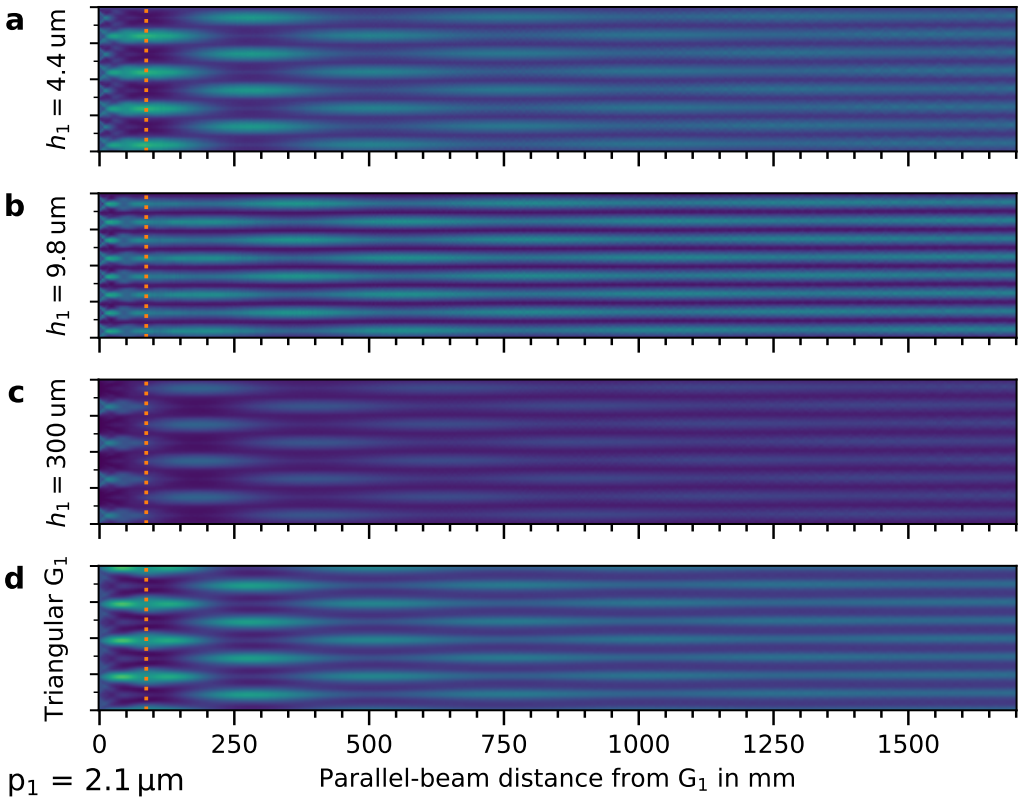

Figure 5.27: Poly-chromatic Talbot carpets for different G_1 heights with otherwise constant configuration (period 2.1 µm, duty-cycle 0.5, G_1 material gold, 80 kVp spectrum filtered with 150 mm POM) in parallel beam propagation. **a,** With the $\pi/2$ phase-shifting G_1 the first high contrast fringes are found approximately at the propagation distance which can be realized in a clinical CT gantry (orange line). This is in accordance with findings in Figure 5.14. **b,** In the π phase-shifting configuration the carpet is very stable for varying distances, but the frequency of the fringe pattern is doubled. **c,** The absorption G_1 design achieves almost no visibility at the orange line which is in accordance with the visibility minimum which has been found in Figure 5.17. **d,** The triangular G_1 design, however, performs well. Its height is adjusted to 8 µm which leads to an intense interference pattern at the proposed CT geometry. The height of the triangular grating structure here has been optimized according to results shown in Figure 5.20.

the pattern becomes almost continuous beyond 350 mm of propagation. The first significant fringe contrast is found around the propagation length of the inverse CT geometry indicated in orange. The drawback of the design is the frequency doubling of the pattern period which requires a factor two finer G_0 and G_2 gratings than in a $\pi/2$ phase-shifting design.
As previously highlighted, the absorption G_1 design produces a good fringe visibility in the inverse CT geometry and its Talbot-carpet shown in Figure 5.26c also demonstrates this. It has similarities to the $\pi/2$ phase-shifting G_1 case, discussed in Figure 5.26a, but the intensity maxima are shifted closer towards the G_1 which is beneficial for the CT design. Consequently, in the CT geometry at the orange line the fringe contrast has a maximum. It is important to note that this pattern is actually an interferometric effect, and we can find re-occurrences of the interference pattern at further propagation distances. This separates the proposed absorption G_1 design from non-interferometric imaging as it is proposed in [150] or edge-illumination imaging where the cast shadow of a grating-like structure is utilized. Due to the strong attenuation in G_1, i.e., G_1 stops about 50% of the incoming X-ray flux, this design has a significantly lower transmission than the other designs which use phase-shifting gratings. This leads to the reduced intensity values of the Talbot-carpet in Figure 5.26c but not necessarily means that the visibility is lower.
The second promising design comes with a triangular G_1 profile and leads to a fundamentally different behavior in the Talbot-carpet as revealed by the simulation results in Figure 5.26d. It has focused intensity maxima after a short propagation distance which then reappear in slightly reduced intensity and becomes an almost constant pattern for propagation distances beyond 1000 mm. Particularly interesting for the inverse CT geometry is the strong fringe contrast at the propagation distance for the inverse CT design. It is important to note that the 'focusing distance' of the triangular grating can be optimized by changing the height of the

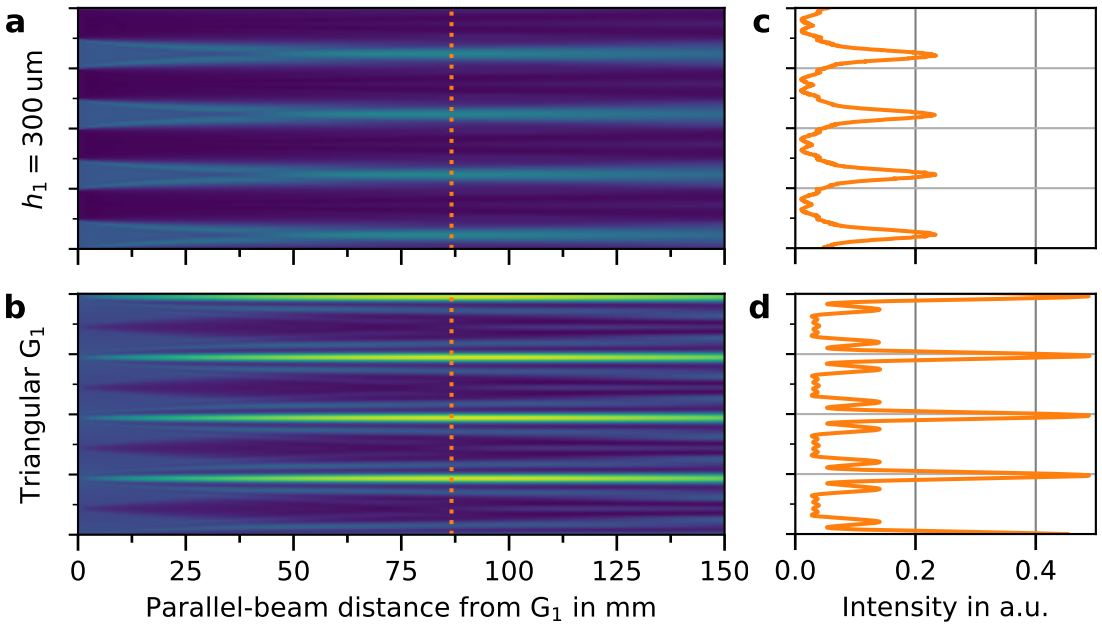

Figure 5.28: Poly-chromatic Talbot carpets and fringe pattern in the G_2 plane of the inverse CT geometry. **a and b,** Interference behind an absorption and a triangular G_1 simulated as in Figure 5.26c and d, respectively. **c,** Resulting intensity pattern in the G_2 plane shows peak like maxima for the design with an absorption G_1. **d,** The focusing behind a triangular G_1 leads to narrow intensity peaks and also secondary maxima besides them.

G_1 structures. Here, a triangular structure height of 20 µm leads to good performance for the inverse CT geometry (see Table 5.7). To demonstrate this, a similar evaluation of the different G_1 designs is repeated with G_1 period 2.1 µm and the results are shown in Figure 5.27. These demonstrate that by changing the grating height of the triangular G_1 to 8 µm the 'focusing distance' can be optimized to the new grating periods. This is not possible for the absorption G_1 design, which does not perform well for a grating period of 2.1 µm.
A comparison between the Talbot-carpets of the absorption and the triangular G_1 reveals that the latter comes with an uncommon interference pattern in the target plane of the inverse CT geometry. In Figure 5.28, an enlarged illustration shows the area of interest and the intensity profile of the fringe pattern in the target plane, i.e., at the G_2 position. While in the absorption G_1 design the wavefront is a succession of maxima and minima formed by distinct intensity peaks, the triangular G_1 grating design leads to more sharply focused intensity maxima with secondary maxima in between. To analyze the impact of those side maxima on the data processing a detailed analysis is presented in the following section.

5.6.4 Higher-Order Components in Moiré Pattern

The side maxima in the Talbot carpet behind a triangular G_1 shown in Figure 5.28b might cause problems during data processing as it is expected that the stepping curve is no longer following a sinusoidal shape. Since the default model for Talbot-Lau interferometer data, as introduced in Section 2.3.4, is based on the assumption of a sinusoidal curve, any deviation can lead to unexpected results and artifacts in the data processing. The following analysis of the side maxima has been published in [140] and is here extended by some additional details.
To analyze the additional maxima and find their impact on the Moiré pattern simulated stepping curves for the two grating designs, i.e., triangular and absorption design, are generated with the simulation framework and are evaluated via a Fourier analysis as introduced in Section 2.3.5. The stepping curve results shown in Figure 5.29a reveal that both G_1 profiles deviate from a simple sinusoidal shape, which is usually expected in Talbot-Lau interferometry. For the binary G_1, the deviation is small but increases significantly in the triangular G_1 design.
These deviations can be identified as a higher order sinusoidal signal by the Fourier analysis, shown in Figure 5.29b, where the third and fifth Fourier coefficient is increased compared to the stepping-curve obtained from an absorption G_1 setup. Note that the amplitude is shown on a logarithmic axis and for a perfectly sinusoidal curve only the components 0 and 1 should be non-zero.
When a G_0 is added to the interferometer the convolution with the extended slit sources leads to a decrease of the higher orders. Nevertheless, for a triangular G_1 they remain higher than for a binary G_1.
This analysis reveals that when working with triangular G_1 gratings the higher Fourier coefficients do not decay as fast as at common binary G_1 setups. Conventional data processing approaches in Talbot-Lau interferometry usually only consider the first order because of the rapid decay [26] but this might not be sufficient for a setup with a triangular G_1 grating. The Fourier processing, as defined in [91], can efficiently separate the higher-order contributions and these end up in the residuum of the standard sinusoidal model of the stepping curve. Other methods, however, which for example also optimize the stepping position or fluctuations in the system might heavily exploit the prior-knowledge about the data model and thus can easily optimize artifacts into the output signals. While this behavior leads to a further minimization of the residuum between measured data and the first order sinusoidal data model, the output images become corrupted with, e.g., fringe-like artifacts.

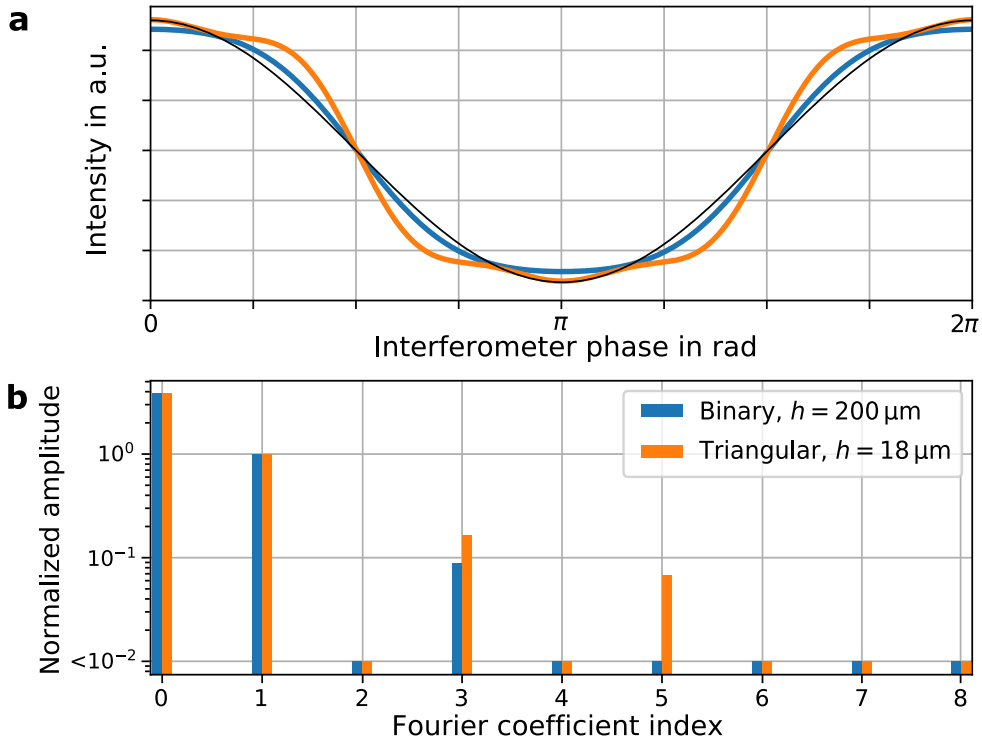

Figure 5.29: Stepping curve simulation for 200 µm high binary and 18 µm high triangular G_1. All gratings are made of gold and have duty-cycles of 0.5. G_2 is 300 µm high. **a**, Stepping curves obtained behind a G_2 grating deviates from the expected sinusoidal shape (black). **b**, Fourier analysis reveals that a triangular G_1 implementation contains significant higher-order contributions than a binary G_1. Data is normalized to the first Fourier coefficient. Image adapted from [140] CC BY.

Since the amplitude of the higher orders is still small compared to the first order we see no problem for use of a triangular G_1 in clinical dark-field CT. Nevertheless, the aspect of higher orders must be considered during the data processing, and it might become necessary to adapt the data model to a more extended form.

5.6.5 Stabilizing Bridge Structures

In the previous sections the most important grating parameters have been evaluated assuming that the gratings are free of defects and a stable X-ray spectrum is used. In reality, however, fabrication requires stabilizing structures within the grating layout which lead to a performance decrease as the lost area does not contribute to the interference pattern. These structures are often referred to as bridges, as they connect fragile parts of the layout which then increases the stability. While for absorption gratings this effect can be treated as a contribution to rest-transmission, as introduced in Section 5.6.2, the impact of bridges in phase-gratings cannot be included as easily. The simulation is therefore extended to evaluate the visibility of the interferometer with realistic bridges in all three gratings.
As an initial result, the simulations revealed that there is no correlation between the visibility and the bridges in the individual gratings. If a grating has a certain non-zero bridge fraction or defect area through which primary beam leaks, this leads to a total performance decrease independent of the other gratings quality. Consequently, defects cannot be compensated by a change of geometry or another grating configuration.
In Figure 5.30, simulations of the triangular and the absorption design show the performance

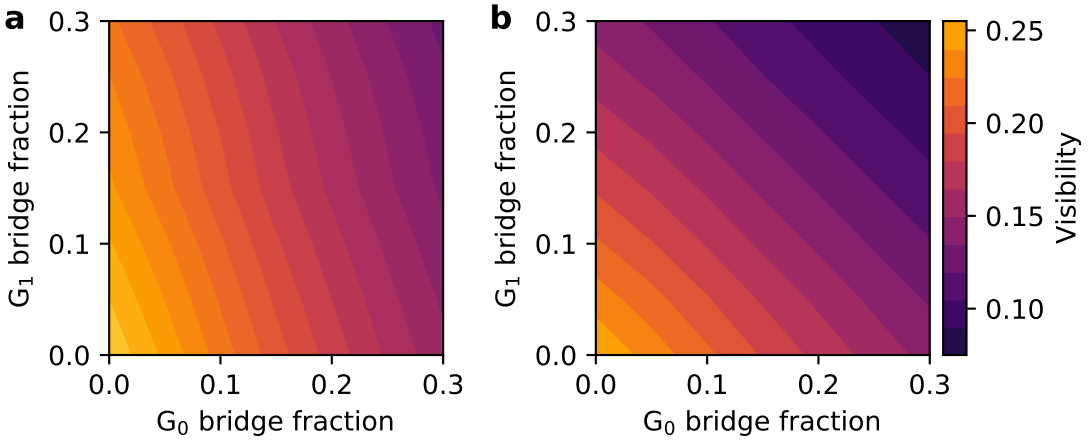

Figure 5.30: Simulation of various bridge fractions in G_0 and G_1 with duty-cycle 0.5 for all gratings. **a,** In the triangular G_1 design the performance loss due to bridges in the phase grating are smaller than for bridges or defects in absorption grating. **b,** With an absorption G_1 a symmetric performance degradation caused by bridges or similar defects in G_0 and G_1 are visible. This also demonstrates that the performance loss is independent between different gratings.

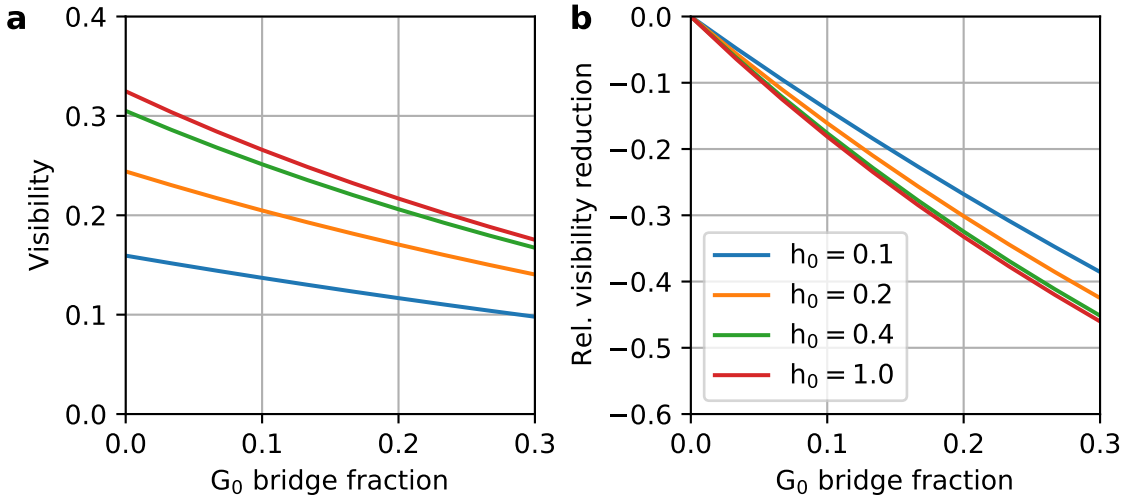

Figure 5.31: Simulation of different G_0 heights in a triangular G_1 design to evaluate the impact of rest-transmission through the lamella versus the additional transmission through the bridges. **a,** The absolute system visibility increases with higher G_0 structures and lower bridge fractions. **b,** For absorption gratings with smaller height the initial rest-transmission is already relatively high. Thus, additional bridges do not reduce their performance as rapidly as it can be seen for higher structures.

impact due to non-zero bridge fractions. The results reveal that the impact of bridges in phase-gratings such as the triangular G_1 in Figure 5.30a have less impact on the visibility than bridges or leak-like defects in an absorption grating, here represented by G_0. In Figure 5.30b, where both gratings are absorption gratings, hence, a symmetric decrease in the visibility is found. These simulations are performed with 300 µm high absorption gratings for which rest-transmission through the lamella is rather small, even for the hard 80 kVp spectrum with 150 mm POM filtration. To analyze the dependency between bridge fraction and absorption grating height a dedicated simulation in Figure 5.31 analyzes different G_0 heights in an otherwise constant interferometer design. As expected, the absolute system visibility increases for higher G_0 gratings with fewer bridges. However, if bridges or rest-transmission inducing defects are

added the system visibility drops. This effect is more pronounced for high grating structures because those profit in the bridge-free case from the absence of any rest-transmission. For lower absorption gratings, where the performance without any bridges is already lowered due to rest-transmission, the additional leakage through the introduced bridges does not lead to such a strong visibility loss.
While defect free gratings with no bridges are certainly preferred, this is not feasible for most high aspect-ratio gratings, such as the G_0. These require a significant fraction of stabilizing bridges of up to 10% which must be considered in the design. For phase-gratings, such as the triangular G_1, in general, no bridges are required as the structures are relatively low. However, due to the novelty of this design, i.e., slanted lithography, bridges are required to ensure stability while the fabrication process is not yet fully optimized.

5.6.6 Spectral Design Response

As discussed in Section 5.6.1, the absorption G_1 design comes with the advantage that the contrast formation does not rely on phase-shift related effects which would be wave-length dependent. Instead, this design still relies on absorption gratings, thus rest-transmission leads to performance loss. While until this point all simulations have been performed with the same 80 kVp spectrum with 150 mm POM filtration now the response of the design to variation of the spectrum is evaluated. Obviously, the approximation of the sample by a filtration with 150 mm POM is very rough and in a real CT scan the X-ray interaction path-length through a sample will vary significantly.
To analyze the system response, the visibility of the two most promising designs are simulated for varying spectral filtration from two materials which have the most dominant influence on the X-ray spectrum in a CT scan. We use Polyoxymethylen (POM) in a range between 0 to 150 mm to describe soft tissue attenuation and as an additional material bone as defined in ICRU as *Bone, Compact* [130]. The filtration with bone tissue is applied for thicknesses between 0 and 50 mm which is sufficient for evaluation related to the human chest CT.
Both materials are purely attenuating and thus do not introduce any dark-field signal, but due to their different elemental composition they harden the applied spectrum differently. This

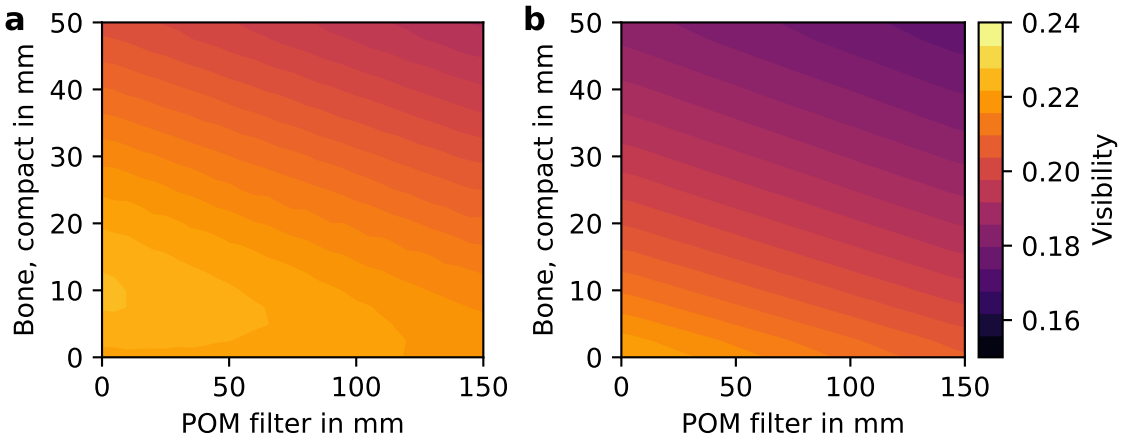

Figure 5.32: Simulation of interferometer response to purely attenuating materials POM, as soft tissue equivalent and bone as defined as *Bone, Compact* in [130] . **a,** The triangular G_1 design has a performance peak at about 10 mm bone, but otherwise the visibility gets reduced due to the beam-hardening induced by the attenuating object. **b,** For the absorption G_1 design a faster visibility loss as in panel a is found, which is caused by the less optimal visibility spectrum of this design.

spectral effect induces characteristic changes of the system visibility as shown in the simulation results in Figure 5.32. In case of the triangular G_1 design the system visibility reaches actually a maximum for approximately 10 mm bone filtration and otherwise looses performance due to the induced changes of the X-ray spectrum.
In Figure 5.32b, a more sensitive response to beam hardening is discovered for the absorption G_1 design. The performance reduces faster than in the triangular G_1 design case, particularly when filtered through bone. To analyze this effect and why the two designs respond so differently to changes in the X-ray spectrum the visibility spectra of the designs are evaluated in respect to the spectral filtration caused by the added materials. In contrast to previous visibility spectra shown in Figure 5.21 here bridge fractions of 10% are included, based on the previous section's conclusion, to make the absolute visibility results more realistic.
Besides the updated visibility spectra, Figure 5.33 also shows three 80 kVp spectra in different filtration states. The progression of the hardening is clearly visible as the spectra are shifted towards higher X-ray energies and the spectrum gets more narrow. The applied filtration would also lead to a significant change of overall intensity but for better visualization this effect was omitted by normalizing the curves to equal height.
For the triangular design there is a visibility minimum at around 35 keV which is problematic when an unfiltered 80 kVp spectrum is used. By a filtration with 10 mm of bone, the spectrum gets shifted to energies above 35 keV and consequently the system performance reaches a

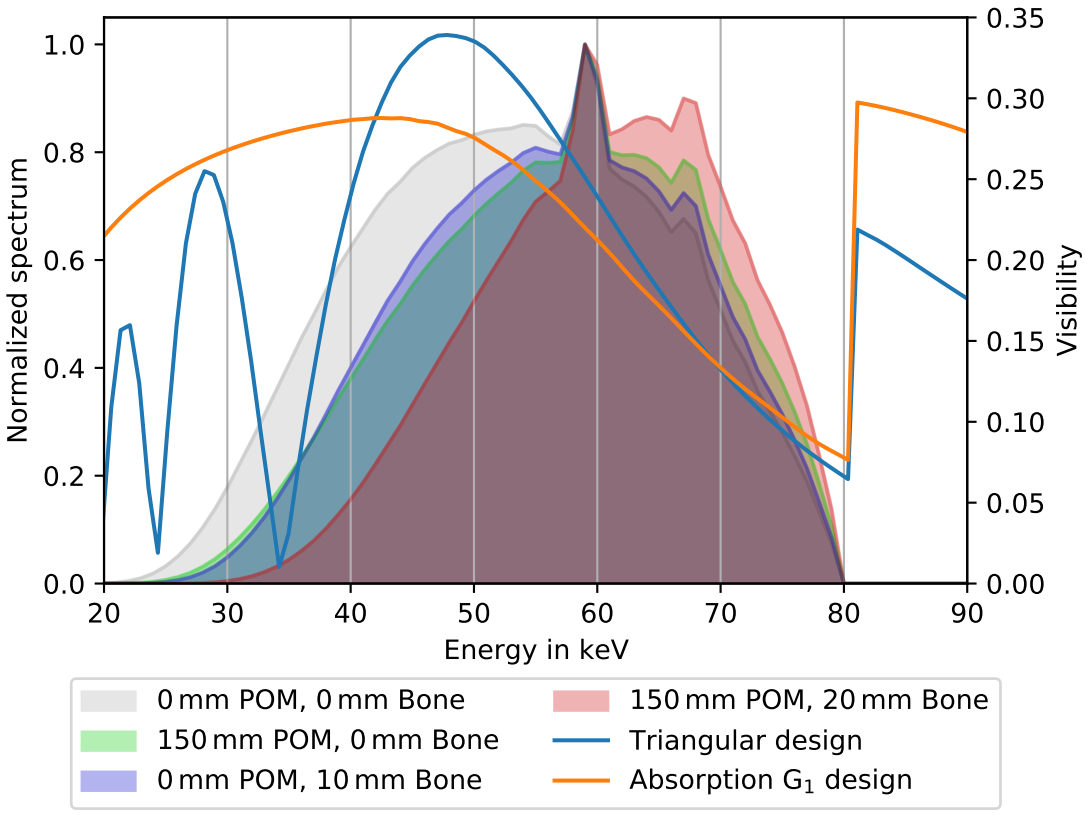

Figure 5.33: Illustration of the beam hardening process of the 80 kVp spectrum with various thicknesses of POM and *Bone, Compact* [130], which are used as soft tissue and bone equivalents, respectively. Intensity reduction due to the attenuation is removed from these curves to better illustrate the shift of the mean energy to higher X-ray energies. Since the visibility spectrum of the triangular G_1 design is higher in the range between 40 and 70 keV this leads to a superior performance of this design, even in hardened X-ray spectra.

maximum as it has previously been identified in Figure 5.32a. As can be seen in Figure 5.32a, this increase is only in the order of 0.6%. For the absorption G_1 design, however, the beam hardening with 150 mm of POM or 10 mm bone leads to a significant loss of visibility because in the absorbed energy ranges a high visibility was achieved. This makes the absorption G_1 design more sensitive to beam hardening than the triangular design. If hardening continues, e.g., towards the 150 mm POM and 20 mm bone case illustrated in red, the spectrum gets shifted further to higher photon energies above 48 keV where the visibility gradually decreases similarly for both G_1 implementations.

5.6.7 Options towards 120 kVp

The dark-field CT prototype is being optimized for a 80 kVp spectrum produced by the clinical CT X-ray tube. This decision is motivated by the better availability of compatible absorption gratings for this comparably soft spectrum. In clinical practice chest CT is mostly done at 120 kVp, therefore, a brief analysis is presented on how well the two most promising designs would perform in this significantly harder X-ray spectrum.
In Figure 5.34, the impact of filtration with POM and bone in the 120 kVp spectrum is analyzed, similar as in the previous section. For these simulations, the same grating configuration, which originally was optimized for 80 kVp, is used. Consequently, the performance of the triangular design is low because its triangular phase grating is not optimized for the 120 kVp X-ray spectrum, as can be seen in Figure 5.34a. As expected further hardening of the spectrum leads to even more visibility loss.
In contrast, the absorption G_1 design performs still reasonably well given the fact that the absorption gratings tend to be insufficiently high for the high-energy photons which are present in a 120 kVp spectrum. While it also suffers from a visibility decrease for additional beam hardening, the reduction is less pronounced than in the triangular G_1 design or in the 80 kVp spectrum. In comparison to Figure 5.32b, the visibility is significantly more stable for varying filtration and stays at a high level around 0.2 .

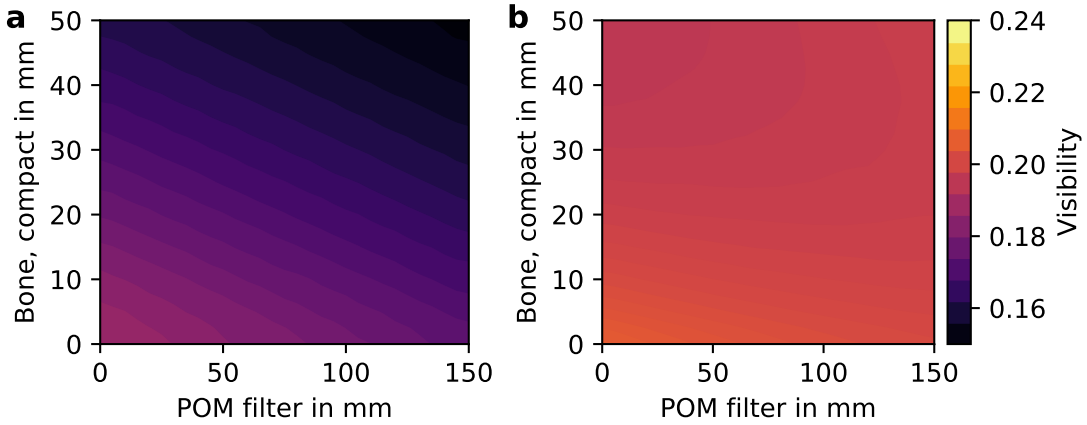

Figure 5.34: Simulation analogously to Figure 5.32 but for an X-ray spectrum with 120 kVp. Filter materials POM and *Bone, Compact* [130] are used as soft tissue and bone equivalents, respectively. **a,** The triangular G_1 design has a significantly reduced visibility because the phase-shifting G_1 is not optimized for the shorter wave-length of the harder X-ray spectrum. **b,** The absorption gratings design performance does not rely on any phase shifts and thus performs better with a visibility around 0.195 . The absence of a strong visibility gradient reveals that this design has a comparably stable spectral response.

In the plots in Figure 5.35 the reason for this changed spectral response can be identified. The visibility spectrum clearly favors the absorption G_1 design as it outperforms the original triangular phase-grating at photon energies above 80 keV. The visibility increase above 80 keV is caused by the K-edge of the attenuation coefficient of gold. It is more pronounced for the absorption design because there all three gratings profit from this effect, not only G_0 and G_2 as in the triangular G_1 design.
As mentioned at the beginning of this section the proposed triangular grating design is optimized for the 80 kVp spectrum. By adjusting the height of the triangular grating structure, i.e., increasing it to about 29 µm an adaption to the 120 kVp spectrum is possible. The dashed line in Figure 5.35 shows that this optimization increases the system visibility to perform better in such a spectrum, but the visibility-drop below 80 keV stays almost unchanged. The former 35 keV visibility minimum is shifted to around 42 keV by this optimization for 120 kVp, which is problematic when this design is used with a weakly filtered spectrum. In Figure 5.36, the simulation results of the optimized 120 kVp triangular G_1 design demonstrates that it performs

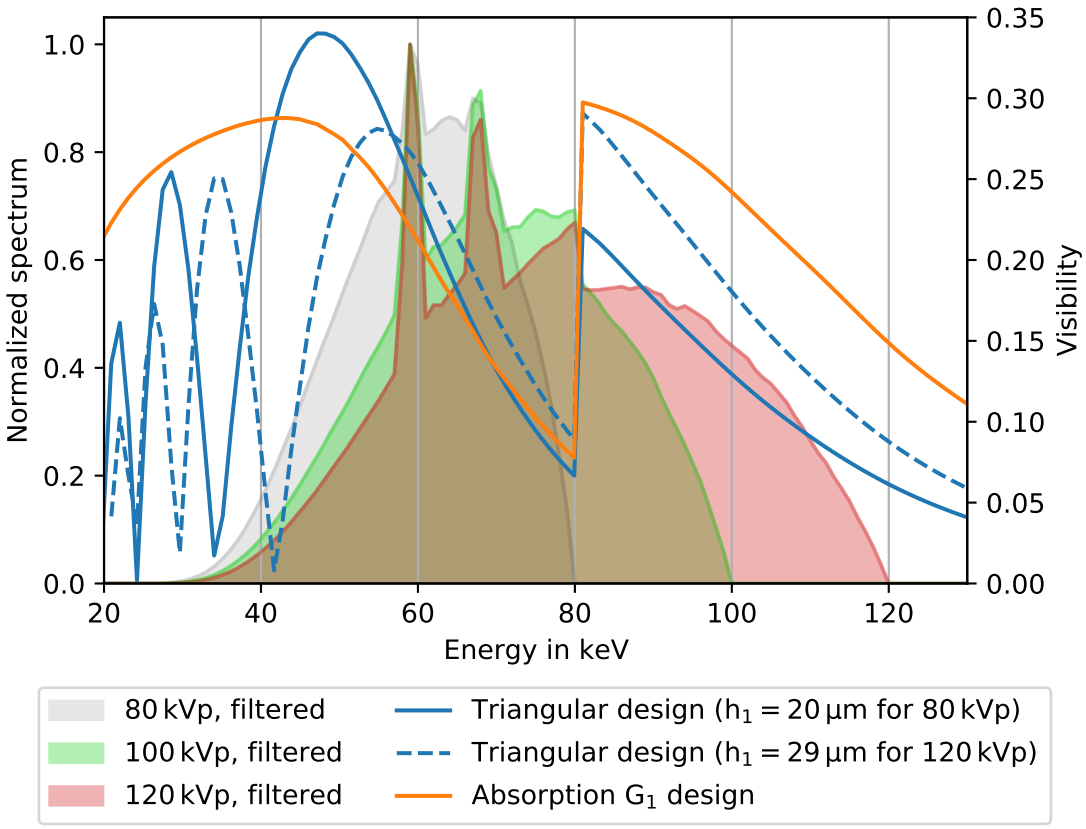

Figure 5.35: Illustration of the spectral visibilities of the triangular and the non-interferometric designs together with hardened X-ray spectra at 80, 100, and 120 kVp. All spectra are filtered by 150 mm POM and 20 mm *Bone, Compact* [130] to simulate beam hardening by a sample. While the proposed triangular design (solid line) mostly outperforms the absorption G_1 design below 80 keV, this relation reverses for higher energies. Due to the spectral optimization of this triangular phase-grating for a mean energy around 56 keV no high visibilities are achieved above 80 keV. In this higher energy range the absorption profits from the K-edge in the gold attenuation coefficient and can utilize the high-energy contributions in the 120 kVp spectrum well. By using an optimized triangular G_1 grating with $h_1 = 29$ µm the visibility spectrum can be adapted to the harder 120 kVp spectrum as demonstrated with the dashed line. This, however, shifts the former 35 keV visibility minimum to around 42 keV further into the 120 kVp spectrum.

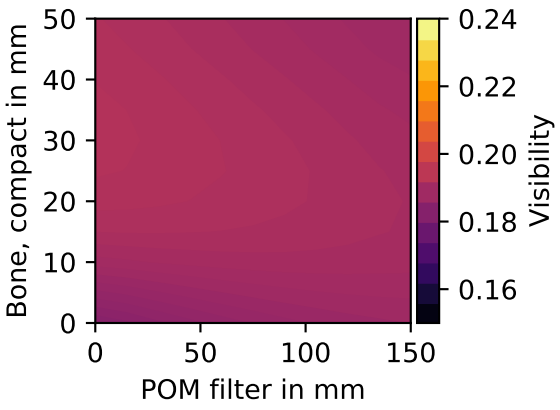

Figure 5.36: Simulation of a triangular design with optimized G_1 height $h_1 = 29\,\mu m$ for a 120 kVp spectrum. The interferometer performance in a 120 kVp spectrum with various filtration based on POM and *Bone, Compact* [130] is evaluated. The optimization of the triangular G_1 to the spectrum increases the performance to a mean visibility of around 0.19 . A visibility drop for unfiltered spectrum is significant but expected.

significantly better than the original 80 kVp version in Figure 5.34a. However, it also reveals a visibility drop for use without any or only little filtration.
These results demonstrate that both interferometer designs are feasible with a 120 kVp spectrum. While the absorption grating design does not require any further optimization, the triangular design requires an adaption of the grating height to 29 µm, which is within grating fabrication capabilities.
Besides the visibility minimum at 35 keV or 42 keV in the triangular design the gold K-edge induced visibility drop below 80 keV reduces the performance of both grating designs significantly. It must be accepted when working with gold as an absorber material, but for example by using another material this performance loss could be removed or at least mitigated to another energy range which lies not that prominent in the center of the 120 kVp spectrum. Materials such as tungsten, lead, or bismuth, which have good X-ray absorption properties are possible options, but they usually cannot be fabricated with state-of-the-art fabrication methods which are optimized for gold.
By Pinzek et al. [96] alternative grating fabrication methods to manufacture absorption gratings have recently been evaluated. There tungsten is used instead of gold and a centrifugal deposition replaces the electroplating during the fabrication. A prototype absorption grating with 207 µm effective tungsten lamella height and a grating period of 45 µm have already been demonstrated. The advantage of using tungsten is its lower K-edge at 69 keV which allows a better use of hard X-ray spectra, i.e., the 120 keV spectrum which is often used in clinical CT. This makes tungsten gratings a promising candidate to improve dark-field CT performance in harder X-ray spectra and is evaluated in the following simulations. A hypothetical 300 µm high tungsten absorption grating is evaluated as a G_2.
In Figure 5.37, the visibility spectrum of the absorption grating design demonstrates the advantage of the combination of gold and tungsten gratings. Instead of an extreme visibility drop for photon energies below 80 keV now the reduction is smaller, but a second drop at the tungsten K-edge at 69 keV is added. In combination, the two visibility drops are moderate, and the visibility always remains above 0.125.
Similar as in the all gold grating design the 120 kVp triangular G_1 design slightly outperforms the absorption grating design again. This design performs particularly well in the 55 to 100 keV range, the visibility minimum at 42 keV, however, remains.
In Figure 5.38 again the sensitivity to beam hardening is evaluated for the two designs, but here with a tungsten instead of a gold G_2. The simulations reveal that the absorption grating design reaches a slightly higher visibility than in a setup with a gold G_2. Similar results are also found for the triangular design which achieves almost the same performance as with a gold G_2. These results demonstrate that in the developed dark-field CT a tungsten G_2 could easily

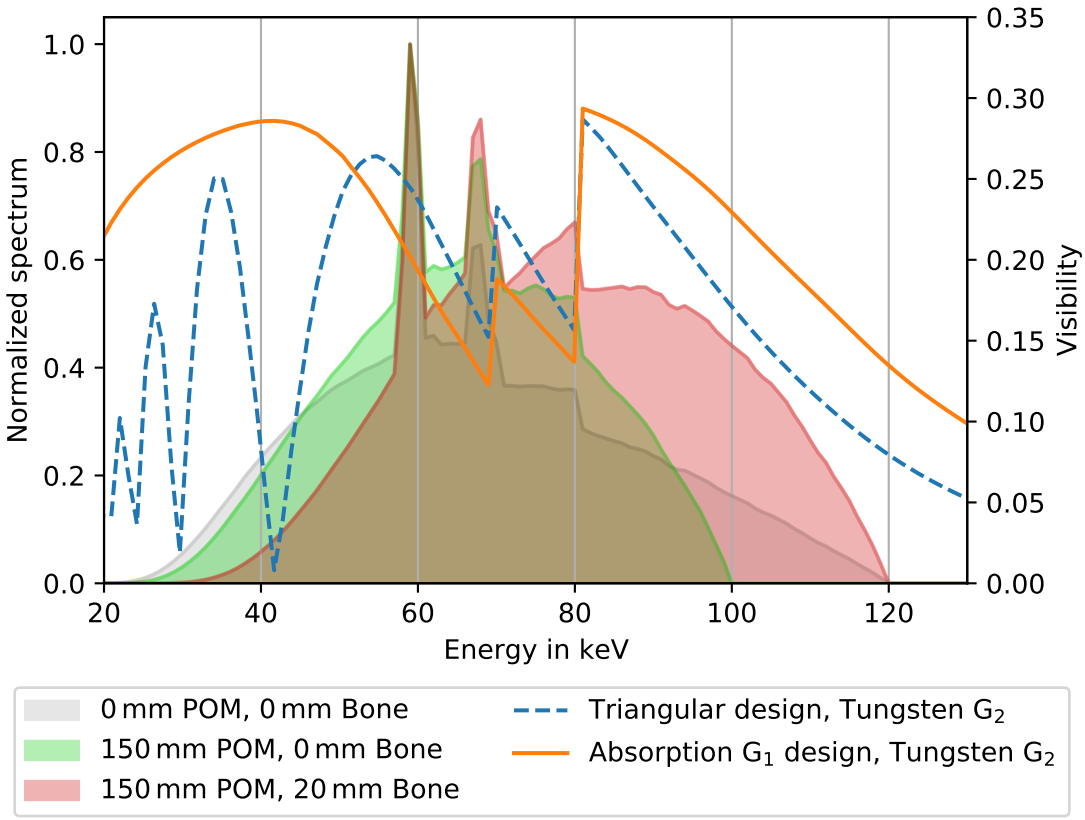

Figure 5.37: Simulation results for a design optimized for 120 kVp based on gold G_0 and G_1, and a tungsten G_2 grating. The normalized X-ray spectra in different filtration states show how beam hardening pushes the spectrum towards higher X-ray energies. The visibility spectrum of the non-interferometric design profits from the tungsten G_2 compared to the results shown in Figure 5.35, i.e., it never falls below 0.125 . In the triangular phase-grating design the optimization for the 120 kVp spectrum yields an optimal lamella height around 29 µm. This leads to high visibilities in the 55 to 100 keV range, but has a minimum at 42 keV due to the spectral response of the phase-grating.

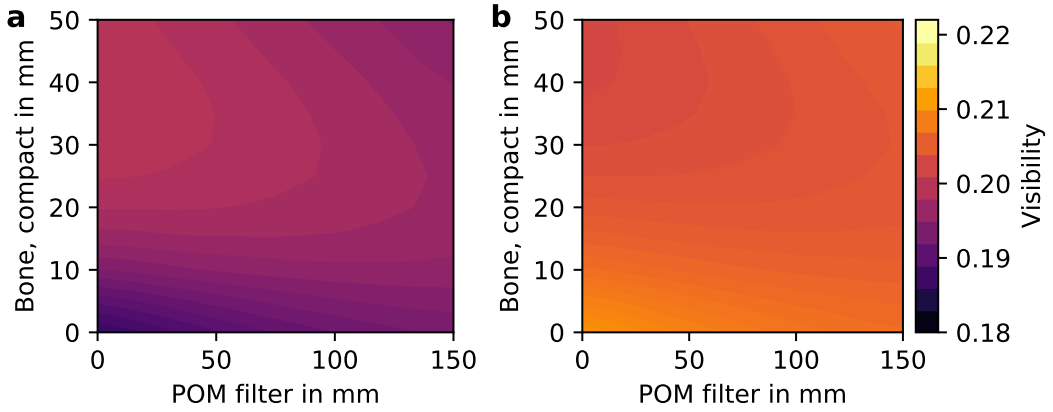

Figure 5.38: Simulation of a combined tungsten G_2 and gold grating G_0 and G_1 interferometer in a 120 kVp spectrum with varying filtration. **a,** A triangular design with a 29 µm high G_1 (adapted to the 120 kVp spectrum) is analyzed. The mean visibility is about 0.196 and stable for the various filter thicknesses. **b,** The non-interferometric design performs similar with a slightly better mean visibility around 0.205 .

replace the gold G_2 once fabrication of 300 µm high tungsten gratings for 45 µm period becomes feasible.
One can conclude that dark-field CT can also be adapted for 120 kVp if the G_1 grating is properly designed. Either an absorption G_1 or a specifically optimized triangular phase-grating G_1 for 120 kVp is required. Based on the presented simulations, the absolute visibility then lies around 0.2 which is only slightly lower than the visibility of 0.215 which can be achieved with a triangular G_1 in the 80 kVp spectrum. These results also reveal that when different kVp settings should be used in clinical dark-field CT, i.e., 80, 100, 120, and 140 kVp as in conventional clinical CT, a single G_1 might not perform well for all spectra. Multiple G_1 gratings for different kVp settings and patient sizes might be required to ensure the best performance similar to the use of optimized metal and bow-ties filters in current clinical CT machines.
The implementation of tungsten G_2 has briefly been evaluated and no significant impact on the overall performance was found. This is a positive result because these gratings might soon become a less expensive alternative to the ones made of gold.

5.6.8 Conclusion on Grating and Interferometer Designs

The previous discussion revealed that there is a large variety of grating parameters which must be carefully selected to achieve a dark-field CT implementation with high performance. Several promising concepts have been identified which work with the specific inverse interferometer geometry which is the best option to fit a Talbot-Lau interferometer into the clinical CT gantry of a Brilliance iCT system. Key features, which have a significant impact on the design performance, are the grating profile, e.g., a triangular or an absorption grating as G_1, and matching grating periods. Other important parameters are grating heights, duty-cycles, and bridge fractions.
Some optimizations are clearly projects for post-prototype designs, once initial know-how is gathered and simulation results are validated. For example, the proposed optimization towards 120 kVp spectra or adaptation to expected filtration based on patient size lacks necessity in a prototype and would increase complexity of the design with only little benefit. Similarly, the advantages of bridge-free gratings and alternative grating fabrication methods are promising, but currently they would jeopardize stability and feasibility of a prototype system.
The simulations revealed that conventional phase-grating based designs, i.e., with binary phase-gratings, are currently not practicable. The given geometry would require an extremely fine grating period for at least one of the two absorption gratings G_0 or G_2. Such fine grating periods at the required high aspect-ratio are currently not available with state-of-the-art grating fabrication methods.
Nevertheless, two feasible and promising designs have been identified beyond the scope of conventional binary phase-gratings:

(1) The *absorption design* with an absorption G_1 performs reasonably well in the simulation results and has practical advantages when it comes to compatibility to harder X-ray spectra.

(2) The *triangular design* with a phase-shifting G_1 with triangular profile yields similar visibility but is more optimized for a specific spectrum. Its G_1 fabrication is less complex as the aspect-ratio is significantly lower than in the absorption design and the evaluation of the signal-to-noise ratio revealed that it outperforms the absorption design by 27%.

An implication of the triangular G_1 might be the uncommon side maxima in the interference pattern, as identified in Figure 5.28, which can lead to uncommon behavior of the stepping

curve. Nevertheless, this aspect is considered to be solvable, e.g., by including the deviations of the stepping curve into the data processing.
While state-of-the-art grating fabrication limits the proposed designs to a certain finest grating period of about 4.8 µm for absorption gratings, further advances in microfabrication might soon unlock finer grating periods which then might require a reconsideration of the grating and interferometer design for clinical dark-field CT. The presented evaluation, for example, revealed that the absorption design cannot be adapted to finer grating periods than about 4.34 µm (see Figure 5.17). Contrary, the triangular design is considerably more adjustable for finer G_1 grating periods which can be scaled down to 1.85 µm. The triangular design, therefore, offers a better perspective for future dark-field CT implementation with improved gratings.
Based on this discussion clearly the advantages of the triangular design prevail. The most important argument remains the practical aspect that fabrication of such triangular gratings is easier than fabrication of absorption gratings with the same grating period. With current state-of-the-art microfabrication fabrication technology only a triangular G_1 can be fabricated as a single piece for the proposed CT geometry, whereas for the absorption design a G_1 combined from several smaller tiles would be required. Another important argument for the triangular design is the significantly better signal-to-noise ratio.

5.7 Dark-field CT Prototype Setup Parameters

The comprehensive evaluations in this chapter covered the various aspects which must be considered for a design of a clinical dark-field CT system. Their results are combined here to conclude on the most promising parameter configuration and are then used in the following chapter for the implementation into a clinical Brilliance iCT system.
The proposed design is based on an inverse geometry which is most convincing for clinical CT implementation. Shown by the analysis of various interferometer geometries in Section 5.4 this design requires only on one huge grating with a relatively coarse period as G_2 and a compact G_0 and G_1 construction, which is integrate-able into the collimator-box of the CT gantry. This keeps fabrication of the gratings and implementation of the interferometer into the gantry as simple as possible.
An analysis of the grating orientation yielded that a horizontal layout would be preferred, but currently only the vertical layout is a feasible option. The evaluation in Section 5.4 identified potential problems concerning the increasing X-ray source size for larger fan angles in the vertical layout. However, since the horizontal layout currently cannot be fabricated or adjusted in the required scale, this performance loss must be tolerated.
In Section 5.6, various interferometer designs have been analyzed in simulations and found two most promising candidates. The triangular design with a respective G_1 profile implemented as a phase-shifting grating is the most feasible option which also yields the highest imaging performance. As an alternative, the design based on an absorption grating as G_1 is promising, but this requires a difficult to fabricate G_1. It is therefore not considered for the prototype implementation and focus is on the triangular G_1 design. Since until now, such non-binary gratings, e.g., triangular grating profiles, have been implemented only based on tilted conventional gratings, e.g., as described in [153], the proposed design is the first-ever implementation based on a genuine triangular grating profile for G_1.
The proposed geometry and grating parameters are listed in Table 5.9 and have previously been published in [140].

	G_0	G_1	G_2
Distance to source [mm]	100	187	999
Period [µm]	4.805	4.338	45.0
Height [µm]	$\geqslant$ 200	18	$\geqslant$ 300
Bridge fraction	10%	10%	1%
Duty cycle	60%	50%	56%
Grating profile	Binary	Triangular	Binary
Grating material	Gold	Gold	Gold
Substrate material	Graphite	Polyimide	Graphite
Substrate thickness [µm]	600	500	1000
Grating orientation		Vertical layout	

Table 5.9: Proposed design parameters for the clinical dark-field CT prototype. It is optimized for a clinical CT spectrum of 80 kVp including a 150 mm POM filtration representing the patient. State-of-the-art grating fabrication limitations and geometrical constraints of the CT gantry are considered. Table adapted from [140] .

Realization of the Dark-field CT 6

The most promising design parameters for the Talbot-Lau interferometer in a clinical CT have been derived in Chapter 5 and here their technical realization is discussed. Several constraints and limitations, which are posed by the gantry geometry and available fabrication technology, have already been considered during the design process and now the focus lies on the practical implementation. Robustness and keeping modification of the basis CT system to a minimum have the highest priority.

6.1 Concept

The implementation of the interferometer into the Brilliance iCT gantry translates the results from the design phase to a clinical dark-field CT prototype as illustrated in Figure 6.1. The developed components and procedures here have to solve several problems which have not been addressed in a previous Talbot-Lau interferometer. Namely, the fast gantry rotation, small bending radii, and wide coverage of the gratings are challenges in this process. Another difficulty, which must be considered for the technical realization, is the limited access to the components once they are implemented into the gantry.
To avoid complex and time-consuming adjustments in the CT gantry the first two gratings, G_0

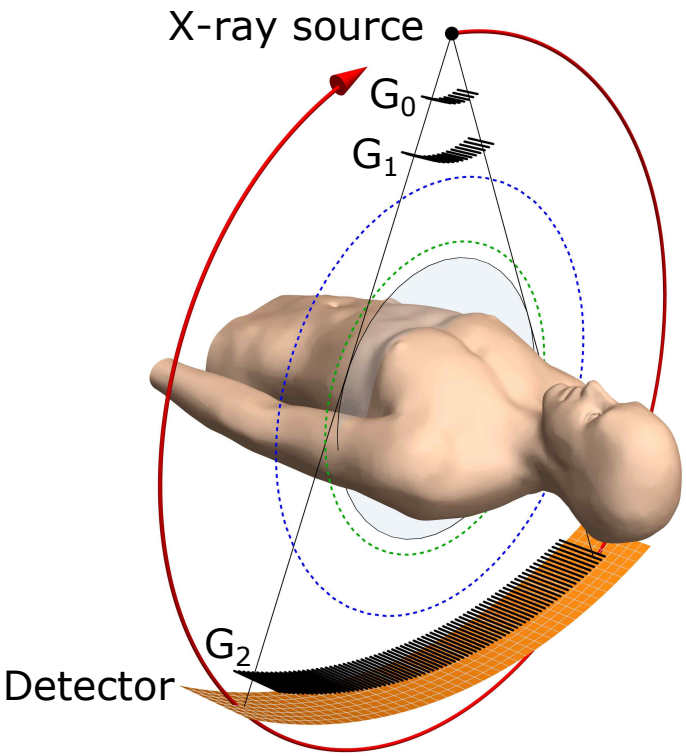

Figure 6.1: Illustration of the dark-field CT prototype implementation. All gratings are bent to adapt to the fan-shape of the divergent beam path. The first two gratings, G_0 and G_1, use all available space between the X-ray source and the bore enclosure (blue dashed line). Behind the patient the G_2 must be comparably large to cover the detector surface. The resulting field-of-view for dark-field reconstructions (highlighted area) is then only 10% smaller than the one of the original CT (green dashed line).

and G_1, are adjusted outside the CT gantry at a laboratory setup. Once these two gratings are aligned, i.e., their grating lines are adjusted to be parallel to each other and their distance is optimized, the assembly of these two gratings is installed into the CT gantry. Then G_2 is implemented into the gantry and adjusted relative to the G_0-G_1-implementation. G_2 is in this workflow the only grating which must be adjusted inside the gantry, which is feasible because it is also the most accessible one and the grating with the coarsest grating period.

6.2 G_0 and G_1 Implementation

The first two gratings of the interferometer are implemented into the collimator box of the clinical CT gantry, which is positioned between X-ray source exit window and the patient. The function and dimensions of the collimator box have been described in Section 5.3.3. To achieve this implementation, some components inside this box must be removed or adapted before the gratings, mounted to a specialized grating holder, can be installed. The interior of the box is easily accessible by removing some parts of the collimator box housing. Since these parts are important for the radiation shielding, i.e., one of the essential functions of the collimator box, they can only temporarily be removed and should not be modified. Consequently, the space inside the collimator box is extremely limited and difficult to access during operation of the system. This leads to the objective to implement G_0 and G_1 in an as simple as possible way which does not require any maintenance and only minimal adjustment.

6.2.1 Modifications to the Collimator Box

There are several components in the collimator box which are not essential for dark-field CT imaging and thus can be removed to clear space for the implementation of the gratings. For example, there is a filter-tray to optimize the X-ray spectrum for specific examinations. It is removed from the system, as this component is not crucial for dark-field CT, particularly as the interferometer design is optimized for the spectrum without those filters.
The collimator box also comes with two motorized tungsten blades, which are used to limit the exposure to specific detector rows. These blades remain unmodified because it is important to limit the beam to only the actively used area. This reduces the patient X-ray exposure and limits the contribution of Compton-scattering. Minimizing the patient dose can become essential for a clinical admission of the prototype system, which is required to be able to conduct a clinical study with patients. Based on the dimensions discussed in Section 5.3.3, the grating design has been selected in a way that the tungsten collimator blades are not in the way for the implementation of the interferometer. This can easily be realized because the blades are further downstream than G_1.
Another important, but not essential, part in the collimator box is the reference detector. It is positioned right at the X-ray source window and measures the X-ray flux during a scan to correct the measured data during the processing. Since G_0 must be positioned as close to the X-ray source as possible, i.e., at a 99.9 mm distance from the source spot, the reference detector must be removed. The flux correction can then, for example, be done based on a pixel of the regular detector whose beam-path is never obstructed by the sample during the measurement.
The remaining component in the collimator box is the motorized bowtie filter or compensator tray which comes with a set of filters for different patient sizes. A modified version of this filter tray has been developed to mount not only several bowtie filters but also comes with a slot into which the G_0-G_1-assembly can be implemented.
A prerequisite for this design is a reproducible and stable positioning of the motorized stage

which could be verified by the manufacturer. Furthermore, basic adjustment features to optimize the angular alignment of the first two gratings around the z- and the x-axis are included in the modified filter tray. These two adjustment features are, however, changed manually only. This is sufficient because such adjustments are only required during initial installation of the gratings and afterwards remain unchanged between all scans.
With this modified bowtie filter tray and maintaining the motorized positioning solution of the original system this easily allows switching the CT prototype between the standard bowtie filters and the dark-field CT mode where G_0 and G_1 are in the beam-path. Furthermore, the positioning along the z-axis allows selecting the optimal position at which the beam-path passes G_0 and G_1. This can become useful to avoid local defects in G_0 or G_1 by shifting the whole assembly to a better performing position.
It is important to note that all proposed modifications are limited to the hardware inside the collimator box only. No changes to the software of the CT system are required, despite a minor reconfiguration of the CT detector. This is required because the CT detector module would otherwise raise an error when no readings from the reference detector are obtained.

6.2.2 Specialized Mount for G_0 and G_1

To implement the first two gratings of the Talbot-Lau interferometer into the CT gantry a specialized mount has been developed. It is a combined holder for G_0 and G_1 which allows simple and rigid implementation of the two gratings into a modified bowtie filter tray. A rendering of the specialized mount is illustrated in Figure 6.2 demonstrating the concept of how the two gratings are attached to the mount.

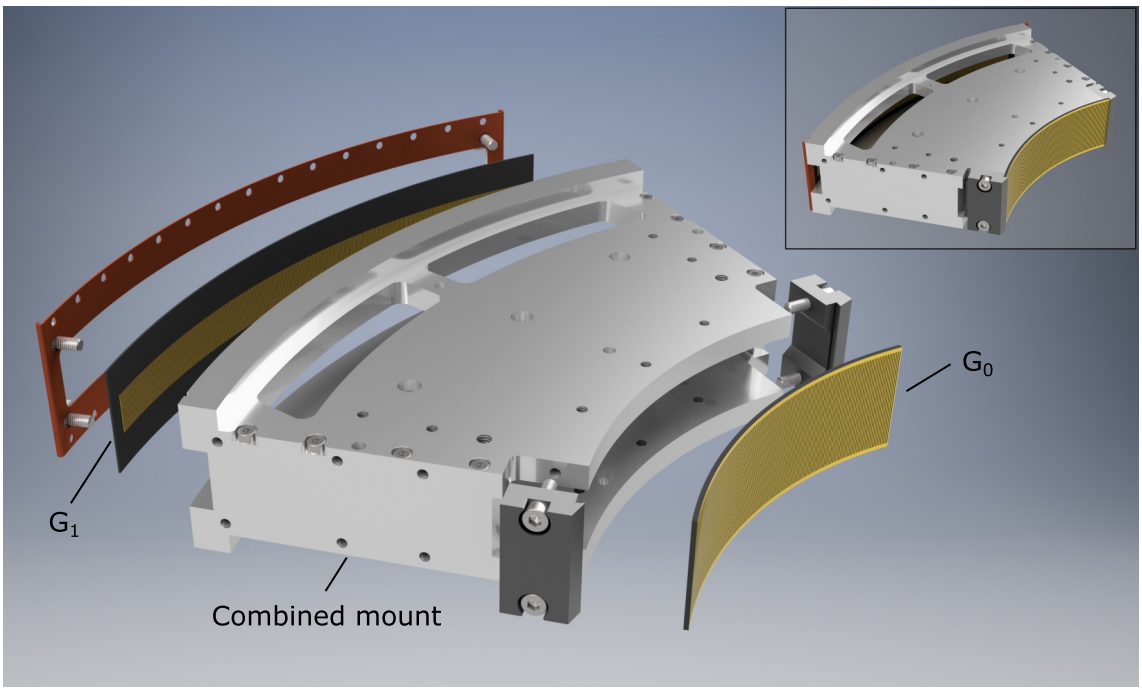

Figure 6.2: Specialized G_0-G_1-mount. The design achieves precise positioning of the two gratings towards each other as the curved surfaces are machined to have the same focal center and a specified radius. Another feature is the precise bending using a clamp-based approach for G_0 with a minimal space requirement towards the X-ray source. For G_1 a conventional approach is applied where the substrate is pressed against the curved surface. Once both gratings are implemented this assembly is installed into the modified bowtie filter tray in the collimator box.

Since G_0 must be positioned as close to the X-ray source as possible a clamp-based bending mechanism (as introduced in Section 4.3.2) is used which needs no additional clearance towards the X-ray source. This method requires the grating to come as a single piece, and it must be on an elastic substrate which can be bent to the radius. Furthermore, the two edges of the substrate which are pressed against the clamps must be parallel to avoid any unwanted deformations or stress in the bent grating. This can easily be realized by the last grating fabrication step in which the large substrate on which the grating has been fabricated is diced to the final rectangular dimensions. Markers in the layout help to ensure parallel edges and alignment to the grating lines. This is important because no adjustment of G_0 is possible once it is implemented into the mount.
As G_0 is early in the beam-path a width of 95 mm is sufficient to cover the entire field of view of the CT detector. In contrast, G_1 must be significantly larger as it is further away from the X-ray source and thus a 152 mm wide G_1 is required. This large grating also comes as a single piece, but the structured area is significantly smaller than the outer dimensions of the substrate as can be seen in Figure 6.2 where the gold color represents the structured area. The large substrate is required to have a large contact surface with the curved mount to ensure precise and rigid implementation. Limiting the structured area only to the part which is actually in the beam path simplifies the fabrication process.
The developed combined mount for G_0 and G_1 precisely defines the distance between the two gratings and ensures that the bending focuses onto the same focal spot. Only the angular

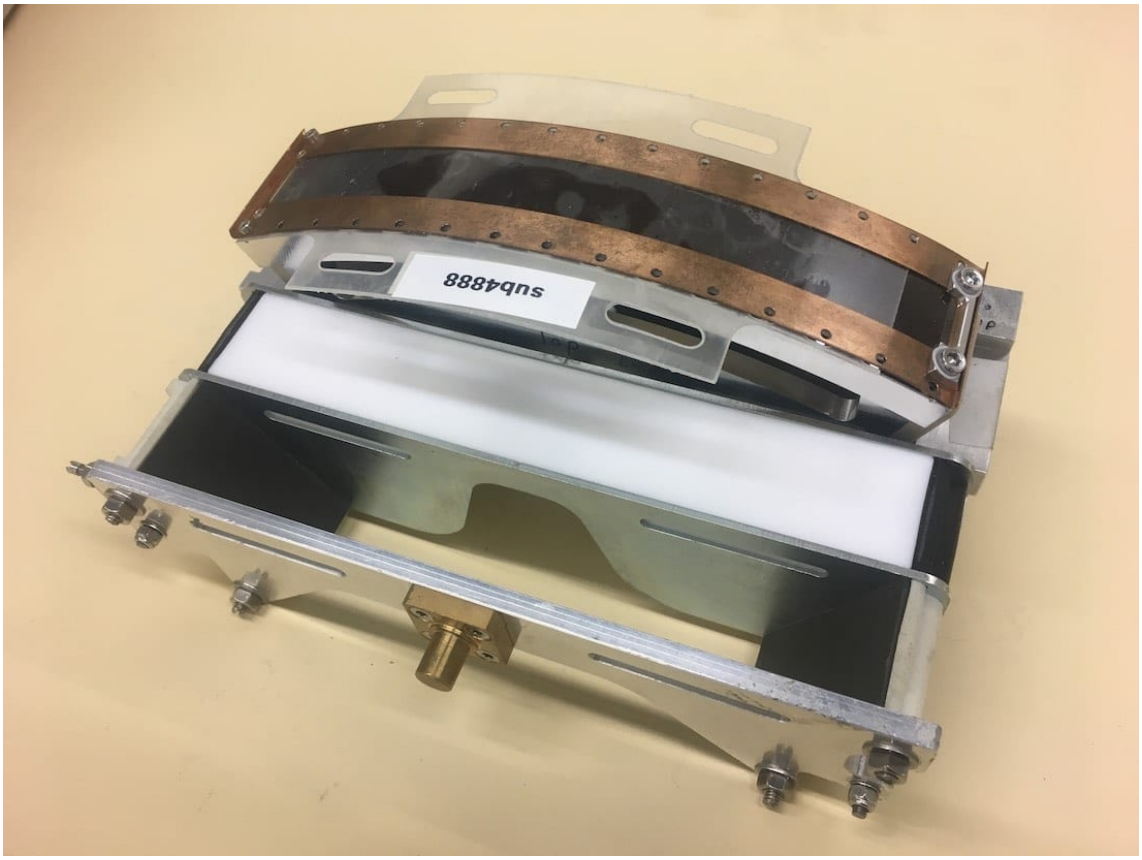

Figure 6.3: Part of the modified bowtie filter tray which offers implementation of up to three different filters or G_0 and G_1 mounts. A combined mount of G_0 and G_1 is here implemented at the very top position and a standard bowtie filter (white) in the center position. The lower slot is empty allowing to perform scans without any gratings or filters in the beam-path of the collimator box.

alignment of the G_1 grating lines relative to the lines of G_0 is not ensured by the design. By an adjustment step with a manipulator-tape (as introduced in Section 4.3.2) the two gratings are aligned to each other and are afterwards fixed. This procedure can be performed at any appropriate X-ray imaging setup and for the presented dark-field CT prototype we use a laboratory setup with a microfocus X-ray tube. There the components are better accessible than in the CT gantry and an adjustment based on a manipulator-tape as described in Section 4.3.2 can easily be realized.
After this alignment at the laboratory setup, G_0 and G_1 are in a compact and rigid assembly which can be easily transported. These pre-aligned gratings are then installed into the prepared slot in the bowtie filter tray as shown in Figure 6.3. In this step different connectors can be used which vary in design and material, and thus come with different stiffness. This allows optimizing the stability of the assembly, e.g., to tune the oscillation amplitudes evaluated later in Section 7.6.

6.2.3 Extensions to the Collimator Box Implementation

The presented approach successfully implements G_0 and G_1 in a convenient and rigid way into the CT gantry. However, it can be further improved to solve some identified problems.
Since the grating mount in the prototype system is made of aluminum and this material has a notable thermal expansion coefficient $> 20\,\mu m/m/K$ any temperature drift in the collimator box leads to a change of inter-grating distance between G_0 and G_1. Such fluctuation of the interferometer state can have a negative impact on the system performance, consequently, such temperature drifts must be avoided. This is difficult to realize as the collimator box is sealed by radiation shielding to all sides and there is no active cooling available. Consequently, the interior of the box, including the G_0-G_1-mount, heats up during a scan, e.g., by thermal load as a result of X-rays being absorbed in the components or thermal conduction to the nearby X-ray source which heats up during a scan. To monitor the temperature drift in the collimator box several temperature sensors have been installed into the box and to different locations on the gantry. A simple cooling approach, based on fans which guide air through the collimator box housing, has been implemented but had no sufficient performance to maintain a stable state. This is particularly because temperature drifts of the entire lab and the varying cooling through different gantry rotation speeds could not be compensated with this implementation. A more promising solution for this problem might be to use another material for the mount which has a smaller thermal expansion coefficient or to implement an active thermal stabilization. The latter can be achieved by a cooling circuit or a thermal regulator which heats the mount to an increased but constant temperature and establishes a heat gradient between the inside of the box and the surrounding.
Data processing can be enhanced by inducing an interferometer phase-shift on a frame-to-frame basis. This can be realized by implementing a motorized unit to the G_0 and G_1 holder. Both gratings are comparably small in outer dimension and period, hence, stepping-like displacement can be realized more easily with G_0 or G_1 than at the large G_2. Such an extension can for example be based on a piezoelectric actuator which comes with a fast positioning speed. However, first a compensation against the intrinsic system vibrations must be found, and thus, such an extension is currently not useful as all stepping-like displacements would be overlaid with the intrinsic system oscillations.
Another interesting extension is the implementation of a transducer mounted to the G_0-G_1-holder which can induce high-frequency displacements when it is turned on to add more oscillation to the interferometer. This can for example be used to increase the phase-sampling if

the system intrinsic vibrations are not sufficient to allow processing of the data. Alternatively, the transducer can be utilized to completely destruct the interference pattern of the interferometer by increasing the amplitude of the oscillations until they can no longer be retrieved by the detector. This then allows to do calibration measurements with the same X-ray spectrum, i.e., filtered through the three gratings, but without any Moiré pattern in the measured detector images. This simplifies data processing as the data model reduces to the conventional attenuation-only case. An implementation of such a transducer has been tested successfully at the prototype dark-field CT.

6.3 G_2 Implementation

The large G_2 is implemented right in front of the detector module where in the original CT gantry an ultra-high-resolution comb is installed. This comb is an optional component, employed for conventional CT imaging with increased spatial resolution, and is not required for dark-field imaging. Hence, it can be removed to make room for G_2.
Compared to G_0 and G_1, G_2 has to cover a much larger area and cannot be fabricated as a single grating with state-of-the-art manufacturing technology. Instead, it is combined from thirteen smaller G_2 tiles which must be stitched to one large area grating. An assembly and adjustment similar as for G_0 and G_1, i.e., at another setup with dedicated infrastructure for the stitching process, however, is not possible. One problem is that the adjustment must be done in its final curved shape. This requires an special X-ray source and detectors as a large opening angle and a extremely wide field of view must be covered. Another problem is the shape of the detector module housing on the CT gantry which does not allow an installation of the large pre-assembled G_2. The orange parts in Figure 6.7 would be in the way. Certainly, these parts of

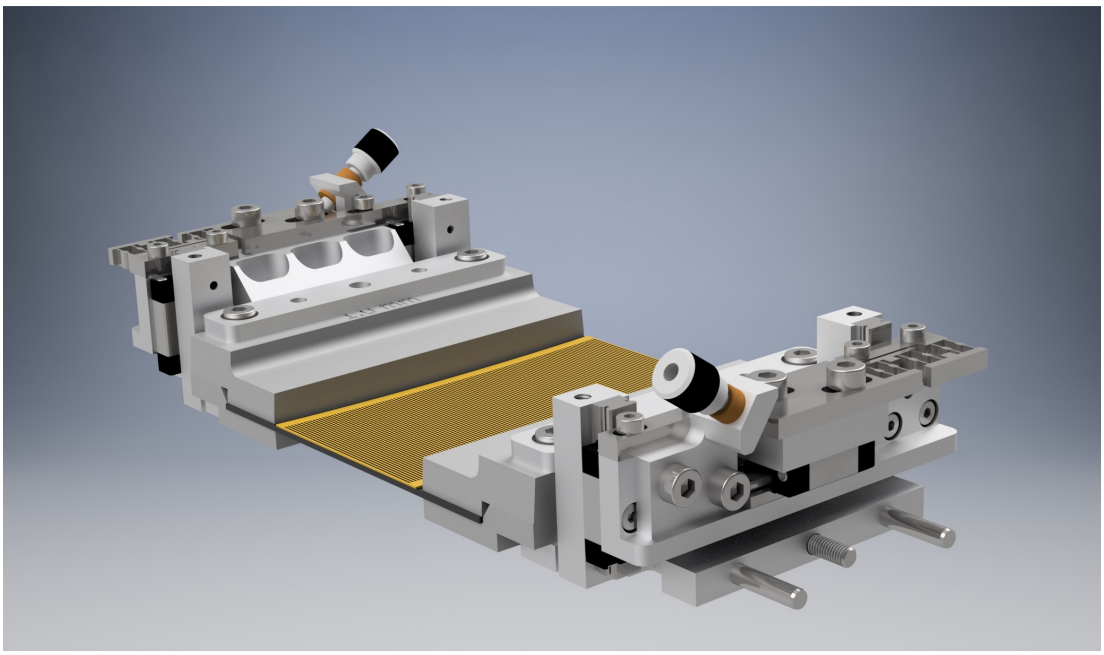

Figure 6.4: One G_2 adjustment module for the dark-field CT prototype. It consists of two identical submodules which hold the G_2 grating in between. The specialized mechanics allow to precisely position the G_2 tile during the implementation and stitching process. Afterwards, the module acts as a rigid mount which has to ensure that the grating is kept at the selected position even during fast rotations of the CT gantry.

the detector module housing can be altered to make a pre-aligned G_2 implementation possible, but this would jeopardize the stability of the detector module. Consequently, the most feasible option for the prototype system is to combine the G_2 tiles inside the CT gantry.
To realize this, the implementation and adjustment of the G_2 tiles has to be after G_0 and G_1 are installed into the system. During the G_2 implementation process each G_2 tile is implemented individually into the gantry and is adjusted to the other already installed gratings by running test scans. Each individual G_2 tile comes with its own adjustment mount which has mechanics that allow to move the tile into the correct position. An intermediate connector between the detector housing and the G_2 adjustment mounts ensures that the curvature of the combined G_2 assembly matches and the gratings are mounted rigidly to the gantry.

6.3.1 Individual Adjustment Mechanics for G_2 Tiles

While G_0 and G_1 can only be tilted along the beam path and moved parallel to the rotation axis the G_2 tiles need more degrees of freedom to be adjustable to each other and to the first two gratings. To be able to adjust each G_2 tile separately a specialized adjustment mount has been developed for the dark-field CT prototype. Each G_2 tile comes with its own adjustment module which holds the grating tile from two opposite sides as illustrated in Figure 6.4. The grating substrate is grabbed from the two opposite sides and is hereby bent to the target radius which is about one meter. This concept allows that the adjustment mechanics and the grating holder remain outside the beam path.
For the interferometer to perform well the three gratings must be aligned to each other, i.e., the

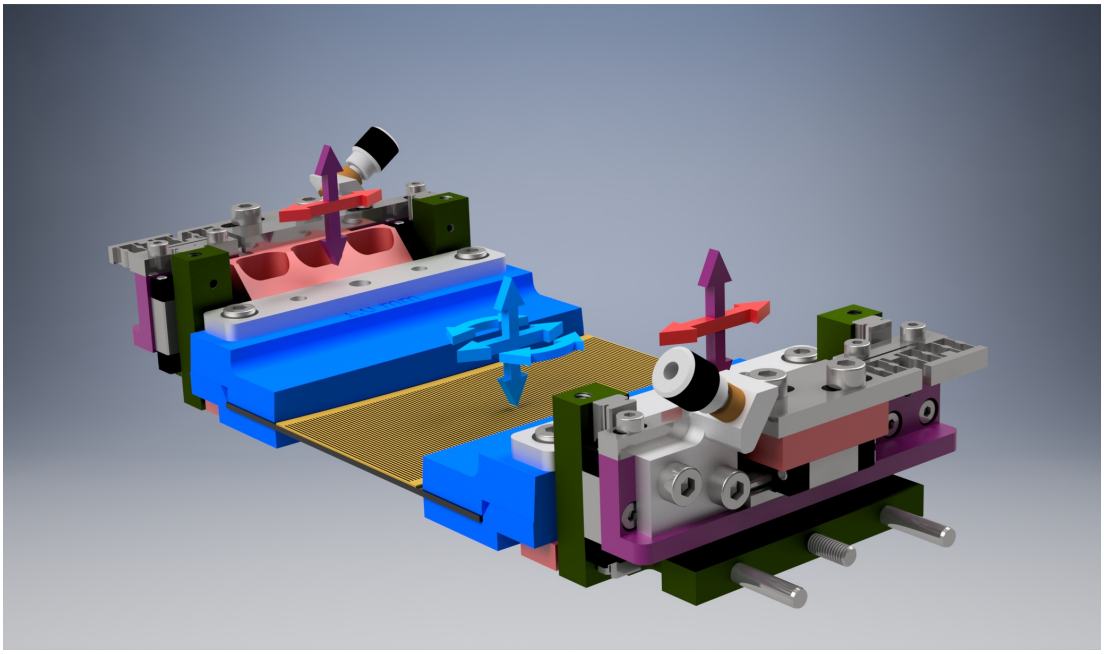

Figure 6.5: Adjustment concept realizes three degrees of freedom for the G_2 tile. The green parts of the two modules are mounted to a stable frame (not visible) by two bolts and a screw. By moving the purple part along the beam axis the height can be adjusted within a range of 8 mm. The red parts are translatable to the left and right as indicated by the red arrows allowing a maximum displacement of 4 mm. Only a single pin connects each of the modules to the blue clamp which hold one side of the G_2 tile, respectively. This allows to rotate and translate the tile as shown by the blue arrows. Particularly important is that the mechanics can be locked after adjustment to ensure a long-time stability of the adjusted assembly.

grating lines of all three gratings must be parallel to each other. While this is ensured for the first two gratings by the prior adjustment at a separate setup, each G_2 tile must be individually optimized during its implementation into the gantry. The specialized grating mount developed for this purpose provides precise rotation of the G_2 tile around the beam axis, translation of G_2 to the left and right, and displacement along the beam-axis.
Most important is the rotation of the G_2 tile around the axis of the beam path until its grating lines are parallel to the ones of G_0 and G_1. This is realized by moving the adjustment modules as indicated with the red arrows in Figure 6.5 in opposite directions. The translation is driven by micrometer screws which push diagonally onto a countering spring, which leads to a high precision and a resetting force. To convert these two linear movements into a rotation of the substrate the two grating holders (shown in blue) are attached to each side of the adjustment modules with only a single pin. These pins are visible in Figure 6.6. Consequently, the two translations are converted into a rotation and a slight change of length between the two grating holders. Since only a fine adjustment of the angle is required the length-change is small and can be neglected.
Besides the angular rotation of the G_2 tile also its position along the beam-axis is important. Only for the specific geometry good visibility is achieved and a useful Moiré fringe pattern can be resolved. For G_0 and G_1 the curved surfaces of the grating mount precisely defined their inter-grating distance but for the distance to G_2 such a high precision cannot be guaranteed based on computer-aided design only. Therefore, as illustrated in Figure 6.5 in purple, the G_2 adjustment modules also come with a movable axis along the beam path to adapt the position of the module within a range of a couple of millimeters. This allows to fine-tune the distance between the G_2 tile and the first two gratings.
The total travel ranges in this design are 4 mm to the left and right along the red arrows in Figure 6.5 and up to 8 mm along the purple arrows, i.e., the beam-axis.

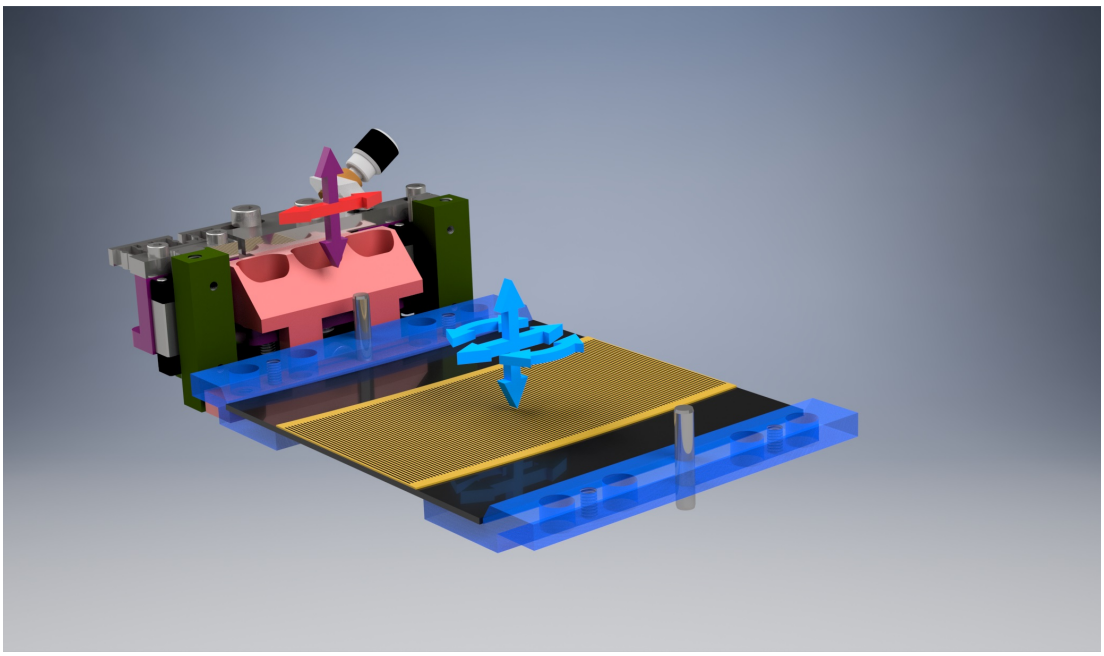

Figure 6.6: Illustration of selected parts to demonstrate the rotation which is realized by translation of two pins. Since only small angular adjustments are required the length-change between the two pins can be neglected.

6.3.2 Combining Multiple G_2 Tiles

Thirteen of the previously discussed G_2 alignment modules are combined to establish a large G_2 for the dark-field CT prototype. The necessary stability for such a construction is provided by a specialized support frame which is attached to the detector module of the CT. It comes with thirteen ports to fix the G_2 adjustment mounts to it and position them at the correct distance from G_0 and G_1. Furthermore, the curvature to focus all G_2 tiles into the X-ray source spot is included in the layout of this support frame.
In Figure 6.7, the support frame is illustrated as it is implemented into the detector unit of the CT gantry with thirteen G_2 adjustment modules and their grating tiles. These adjustment modules have been developed particularly for this purpose and allow that multiple modules can be positioned right next to each other without any gaps in between. This is realized by the only 60 mm narrow footprint of the adjustment modules which is narrower than the about 70 mm wide G_2 tiles.
The thirteen ports to which the G_2 adjustment mounts are attached are placed based on the target radius and the width of the G_2 tiles. The fine-tuning of the gap size is done during the installation and adjustment procedure of the individual tiles utilizing the horizontal displacement as illustrated in Figure 6.5 with the red arrows. This allows to tune the borders of the gratings to be aligned with the detector pixel borders or to establish constant, i.e., matched, interferometer phase over multiple grating tiles. The latter will then lead to the appearance of a continuous G_2 with vanishing performance loss.
To be able to achieve phase-matched adjustment, i.e., constant interferometer phase between neighboring tiles, the adjustment mount must be able to control the position between two G_2 tiles better than the period of the grating pattern. The adjustment uses 200 µm-pitch micrometer fine-adjustment screws which actuate the translation axis under a 45° angle and lead to a displacement of 100 µm per turn of the adjustment screw. With the G_2 period being 45 µm this leads to fine adjustment of the interferometer phase at around half a turn of the adjustment screw, which turned out to be practical. If the grating periods were finer, the

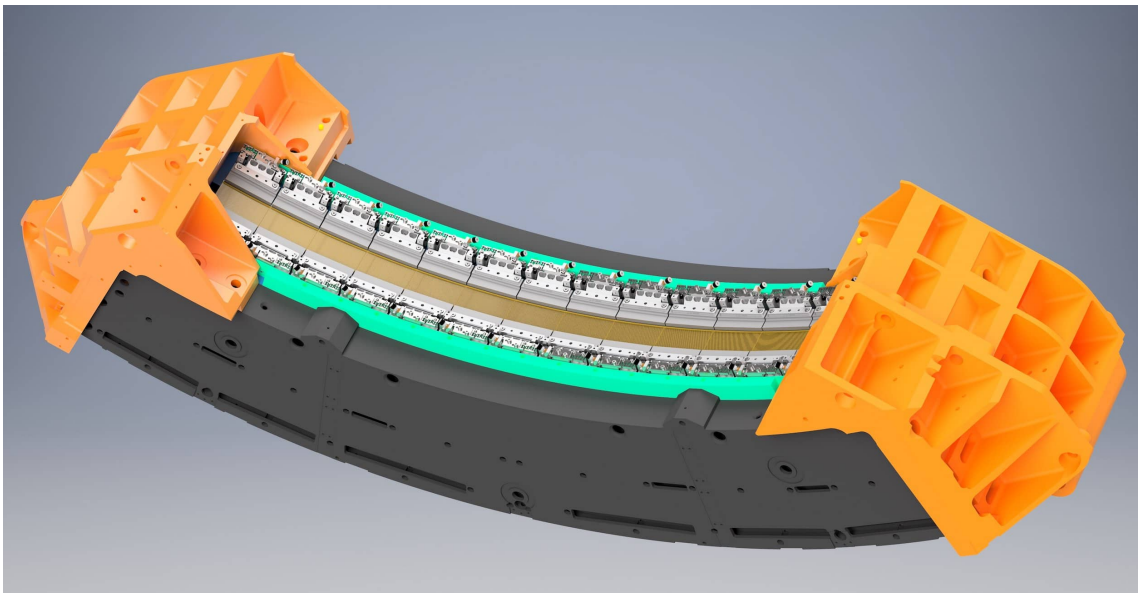

Figure 6.7: Rendering of the G_2 support frame which holds the thirteen G_2 modules. The support frame consists of two parts on either side of the field of view and is colored in teal. It is attached to the detector module (dark gray) by several screws and follows the curvature of the detector surface.

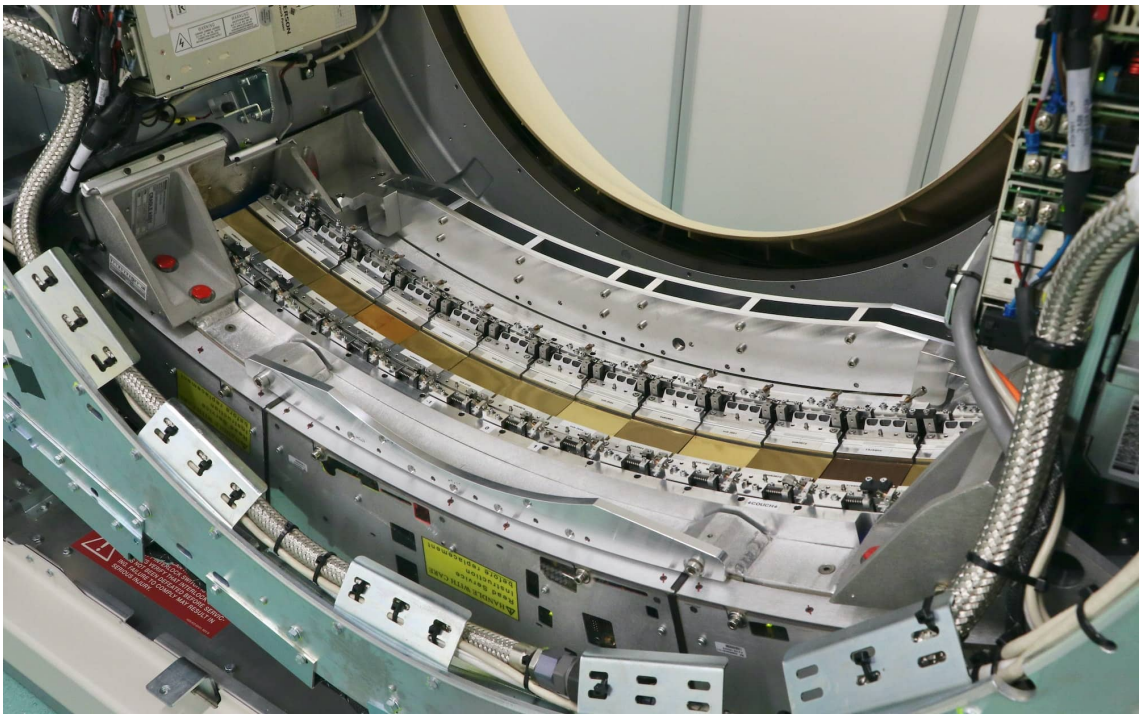

Figure 6.8: Photo of the final implementation of G_2 in the dark-field CT. Thirteen G_2 tiles are combined to cover about 80 cm of ark-length in front of the CT detector. Each tile is bent individually to focus into the X-ray source spot.

adjustment mechanics must be upgraded to use finer micrometer screws or a steeper angle of attack.
For the installation into the dark-field CT prototype the implementation routine starts with the central G_2 tiles and is continued tile-by-tile towards the left and right of the detector. After each adjustment step to the G_2 modules a scan is acquired and the recorded image data is evaluated. These images allow to estimate into which direction the tile must be rotated, whether a shift is required to align the tile edge with a detector pixel edge, and whether the phase of neighboring tiles match. Furthermore, the density of Moiré fringes is measured and can be adapted by changing the position setting of the G_2 adjustment mount along the beam axis.

6.3.3 Extensions to the G_2 Implementation

In an earlier version of the G_2 support frame also an adjustment of the tilt and x-position was included to be able to compensate potential misalignment of the curved G_2 to the X-ray focal spot. However, it was found that based on the computer-aided design the implementation is precise enough to make these features obsolete. As a consequence, the significantly lighter and more stable support frame as introduced in the previous section has been developed and is in use in the dark-field CT prototype.
A potential upgrade for the dark-field CT is a G_2 combined from fewer tiles. The partition into thirteen tiles was initially motivated by the maximum tile width for rectangular gratings on a 4 inch waver, which had been the state-of-the-art substrates when the first G_2 tiles were fabricated. With recent advances in grating fabrication technology now also significantly larger G_2 tiles are possible. Since the fabrication process has been adapted to $6 - 8$ inch wavers tile widths above 130 mm are now feasible. With wider grating tiles a smaller number of total

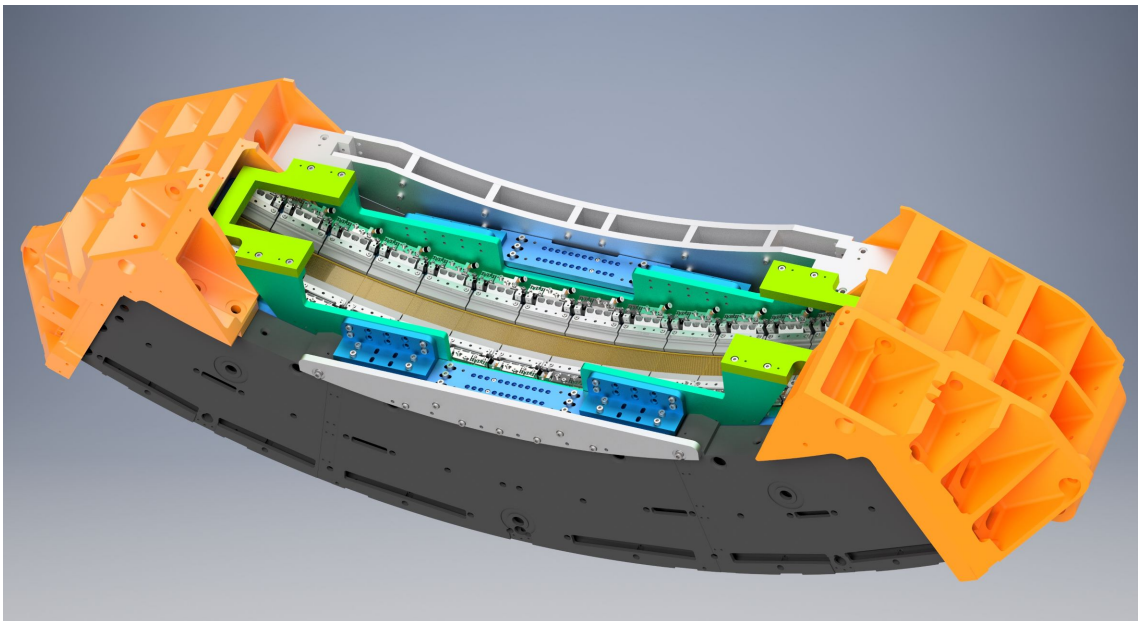

Figure 6.9: Rendering of the initial G_2 support frame which comes with multiple adjustment options in case the focus of the bent G_2 is not aligned with the X-ray source spot. To increase the stability of the support frame two connections go through the outer beam-path connecting the two sides of the frame. This connection could be omitted in the following more lightweight support frame which has been shown in Figure 6.7.

elements would be required. This reduces the number of total tile edges and their adjustment to each other, and ultimately leads to a vast reduction of implementation complexity. Furthermore, the stability of the entire G_2 assembly would increase because each tile would become more heavy and thus less affected by induced high-frequency oscillations.
Another potential extension is an automated removal of the G_2 for non-dark-field CT scans. In contrast to the ultra-high-resolution comb of the conventional CT system, the developed G_2 implementation is not retractable from the beam-path and thus does not allow any scans without the grating. As can be seen in Figure 6.7 and 6.9 at the left and right the detector housing wraps around the beam path (orange parts) and does not allow any displacement of G_2 to retract it from the field-of-view. Certainly, by a redesign of the detector housing a retractable solution can be developed. However, this feature has not been considered for the prototype as it would involve significant changes and could lead to stability issues.

6.4 Dark-field CT Scan Acquisition

The CT system can remain unchanged beside the listed hardware modifications and additions presented in the previous sections. After the adjustment of the gratings, the original bore-covers can be reattached and the laser based positioning system can still be used. Moreover, the original patient couch remains in use for the dark-field CT scans.
For planing and acquiring CT scans the original system software remains fully functional without any adaptations, except, that certain scan modes, i.e., those which require the ultra-high-resolution comb, can no longer be used. Only the results shown after a scan are corrupted as the software uses the standard CT reconstruction pipeline which cannot handle the interferometer data. Instead, the measured raw data must be extracted from the system and then be processed externally in a dedicated processing pipeline. These reconstruction results are then

not transferred back into the CT system but are added to a separate database or a PACS[1]. The review of the reconstructed data is done at a separate workstation which is connected to the database and comes with a specialized viewer application to show the two imaging modalities, i.e., attenuation and dark-field contrast, side-by-side.
While the software itself does not require any modifications, some subordinate configurations were modified to turn off the flying focal spot, which simplifies the data-processing for the prototype system. Furthermore, some adjustments to the configuration of the bowtie filter positions were required to avoid collisions in the collimator box because the modified tray has slightly different dimensions than the original one.

[1]The Picture Archiving and Communication System (PACS) is commonly used to organize medical imaging results. It is a storage and distribute solution between imaging systems and workstations for review.

Experimental Characterization and Data Processing 7

In this chapter, the interferometer performance and the processing pipeline is introduced. This includes an evaluation of the interferometer components as well as introducing the data processing procedure. With this new processing pipeline the transmission, dark-field, and phase-shift signal is extracted from the raw data of only a single axial rotation. From the final and intermediate processing results the system can be characterized, and important performance measures can be extracted. We evaluate the impact of shadowing in the grating structures, the amplitude and frequency of vibrations, and the sensitivity to deviations of the grating periods.

7.1 Initial Characterization of Raw Data Projections

As previously published in [136], the raw data output from the detector shows the expected Moiré fringe pattern. The example image shown in Figure 7.1a represents a single projection measured during a sample-free axial scan with 1 s rotation period. The Moiré pattern is tuned to be vertically aligned and is configured for a fringe density of about 10 pixels for one fringe. This configuration is important for later processing and reconstruction steps as it ensures good phase sampling during sample scans [127], [151].
To analyze the dynamics of the setup during a scan the central pixels are analyzed in a sinogram in Figure 7.1b. This reveals that the fringe pattern oscillates during the measurement and the displacement follows a sinusoidal behavior with a comparably small amplitude. It is assumed, that this oscillation is caused by a displacement of the interferometer gratings perpendicular to their grating lines. This way a shift by a full grating period would lead to a phase change, i.e., movement, of the Moiré fringe pattern, by 2π. However, the precise movements of the individual gratings remain unknown as only their combined effect can be analyzed.
To better assess the vibrations in the sinogram an analysis is shown in Figure 7.1c revealing that there are actually two sinusoidal oscillations superimposed. A fast one with rather small amplitude of only about 0.75π and a much slower one with a large amplitude of about 4π. The frequency of the small amplitude oscillation can be related to vibrations caused by mechanical parts such as fans, the cooling system, and the anode drive. The slow change, however, is induced by centrifugal forces and gravity from the gantry rotation and reoccurs in every scan in the same fashion. An in-depth analysis of the vibration frequencies will be covered in Sections 7.6 and 7.7.
This initial analysis reveals that in contrast to the typical table-top interferometer implementations the clinical dark-field CT system comes with a large variety of drifts and vibrations. These can lead to strong interferometer phase fluctuations as shown in Figure 7.1. Furthermore, also intensity and visibility related fluctuations are found in the prototype system, but cannot be illustrated as easily as the phase fluctuations. This makes the dark-field CT prototype a unique challenge from the data processing perspective because all so far developed processing methods cannot be directly applied.

7.2 Processing Concept for the Dark-field CT Prototype

Besides the identified stability issues also the continuous rotation of the CT gantry is a challenge in the development of the dark-field CT prototype. The X-ray attenuation, refraction, and small-angle scattering must be extracted simultaneously from a set of projections acquired during a single rotation of the gantry. Most conventional signal extraction methods are based on recording a full stepping curve for each projection angle and processing this stepping to a single projection with the three contrast channels. The obtained projections can then be used for tomographic reconstruction. However, since the gantry rotates continuously, acquisition of multiple steps at the same rotor position is not possible. While collecting the steps from multiple rotations, for example described by [150], would be a solution, this is not suitable for a clinical implementation because of the significantly increased scan time. Nevertheless, it might be partially applicable for a helical implementation at a later development stage, but for now, focus lies on axial scans only.
Solutions are for example *sliding window* based signal extraction [158] or novel image reconstruction approaches, such as *intensity based statistical iterative reconstruction* (IBSIR) [127], [151]. Particularly the latter are promising as it can simultaneously process the data and do a tomographic reconstruction, even though no full stepping curve is acquired. Before these signal extraction and reconstruction approaches can be used, however, the reference state of the interferometer must be characterized. This is necessary, so we can afterwards separate the sample signal from drifts and perturbations in the system. By measuring a sample-free scan, also referred to as air-scan or reference scan, and processing it with a specialized pipeline the current state of the interferometer can be evaluated. On this basis, the data model for subsequent sample scans is configured.

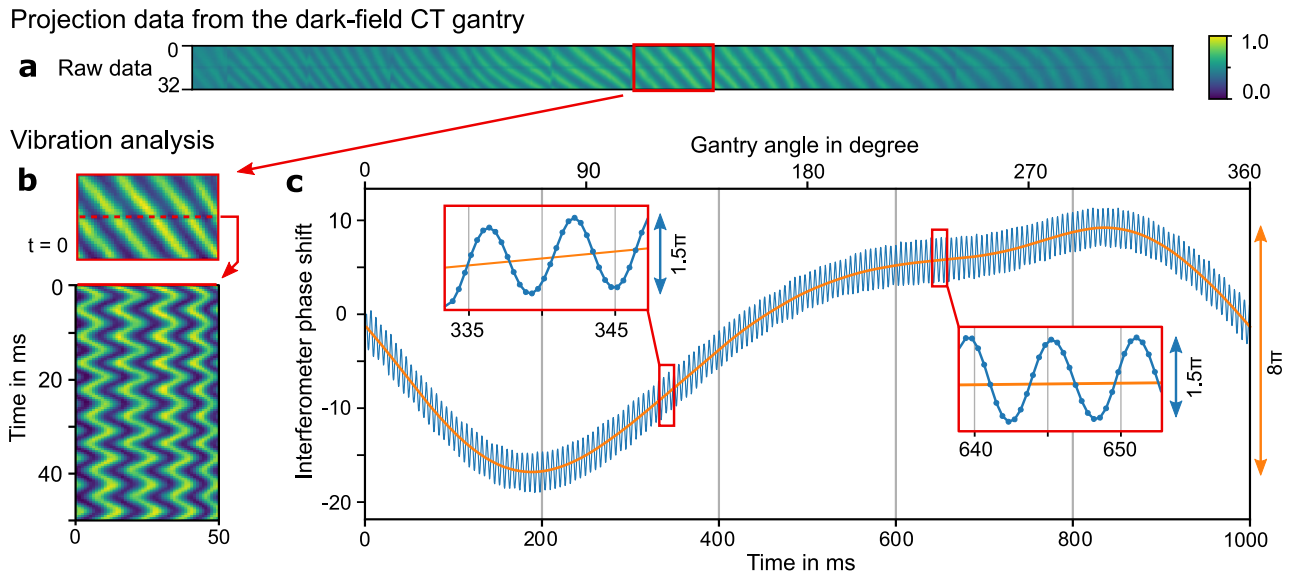

Figure 7.1: Raw data analysis revealing oscillation of interferometer phase. **a,** The projection data from a sample-free scan shows the typical Moiré fringes. By design the pattern is almost vertically aligned and has a fringe density of about 10 pixels for one fringe. **b,** Analyzing the sinogram in the highlighted central area reveals that the pattern changes periodically in a sinusoidal behavior. **c,** A detailed evaluation of the interferometer phase based on this pattern displacement reveals that the phase changes with two dominant frequencies. A slow change over about 4π amplitude and a much higher frequency oscillation with only 0.75π amplitude. Image adapted from [136] CC BY.

During reference processing intensity variations, visibility changes, and interferometer phase oscillations are retrieved and correlated. This allows to find the interferometer performance measures $\boldsymbol{I_0}$, $\boldsymbol{V_0}$, and $\boldsymbol{P_0}$, which represent the intensity, visibility, and interferometer phase for each pixel, respectively. These are important for the later sample processing, to be able to extract sample induced attenuation or small-angle scattering. Simultaneously vibrations and X-ray flux variations occur and are modeled appropriately. Identifying these contributions is only possible in a reference scan where no sample influence leads to similar variations. The gathered knowledge is essential to be able to compensate for vibration- and flux-variation related artifacts in the sample processing. In Figure 7.2a and b the various reference processing steps are shown together with examples for the resulting correction arrays which represent the state of the interferometer and how vibration and drift artifacts can be modeled.
Processing of a subsequent sample scan then utilizes this prior knowledge to remove artifacts and generate a set of intensity, visibility, and differential phase-contrast projections. While conventionally this procedure does not adapt the reference projections to the sample scan we found that generating virtual references, i.e., optimized from the individual correction arrays for each sample projection, is a crucial step to suppress artifacts in the sample projections and the subsequent reconstruction images. In Figure 7.2c and d the sample processing steps are listed. The coefficients for the intensity of each correction array show that there are some vibrations in the interferometer. Since the phase of these oscillations is not the same as during the reference scan the optimization of virtual reference projections is mandatory. This will be discussed in the following more detailed sections on reference and sample processing.

7.3 Reference Data Processing

A sample-free reference scan is used to extract scan-to-scan persistent system characteristics such as the mean interferometer performance measures $\boldsymbol{I_0}$, $\boldsymbol{V_0}$, and $\boldsymbol{P_0}$ following the processing steps illustrated in Figure 7.2a. Linear combinations of correction arrays are used to model the fluctuations in intensity, visibility, and phase which goes beyond previously available data processing approaches for Talbot-Lau interferometers. The following description of developed procedure is taken from [136] and extended by some more details. Further information can also be found in [109] and [108].
Fundamentally the idea of the introduced reference processing is to extract all scan-to-scan persistent information from a sample-free scan and then use this to correct during a sample scan. Fortunately, the presented prototype system has a stable interferometer performance with consistent characteristic vibration patterns over time. This allows that the data-model which has been optimized for a reference scan also works for a following sample scan. The intensity fluctuations, for example, follow a certain frequency, amplitude, and pattern. Since the same pattern appears with the same frequency and amplitude also in a following sample scan its contribution can be corrected during sample processing and reconstruction. A correction solely based on the sample scan would not be possible because differentiation between intensity fluctuation and sample data would be difficult and might lead to cross talk. During reference processing the challenge lies in efficiently identifying and separating the occurring patterns in a way which is useful during sample processing.
As shown in Figure 7.2a, the reference processing is a multistep approach which optimizes the measured data to the Talbot-Lau interferometry data model. It starts with a standard signal extraction, i.e., phase retrieval, which yields the interferometer intensity $\boldsymbol{I_0}$, visibility $\boldsymbol{V_0}$ and phase $\boldsymbol{P_0}$. It is based on the most common model for processing Talbot-Lau interferometry

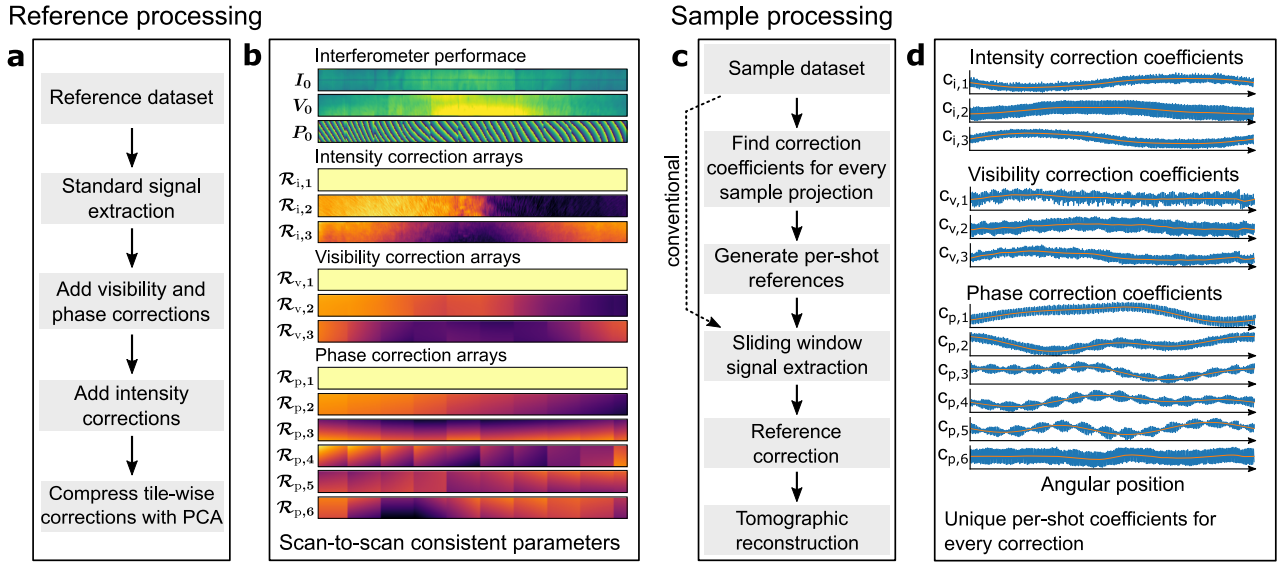

Figure 7.2: Data processing pipeline for the dark-field CT prototype. **a,** The system state is characterized from a sample-free reference scan which extracts scan-to-scan persistent patterns. Extraction of local intensity and visibility fluctuations are important for later processing steps. The gathered information can be compressed using principal component analysis (PCA) for later use during the sample processing. **b,** The revealed performance and correction array results representing the state of the interferometer. **c,** Sample processing is based on the sliding window signal extraction approach. Before this can be applied, the configured model from the reference scan must be used to generate virtual reference projections for each measured sample projection. Only then the sample contribution to the extracted signals can be successfully separated from artifacts and drifts. **d,** Coefficients for a sample scan which are used to generate the virtual references. The optimization process uses prior knowledge from the reference scan to find the best combination of correction arrays for each sample projection. Image adapted from [136] CC BY.

data where the raw data y_{pt} measured by a pixel p is fitted to a sinusoidal curve,

$$y_{pt}^{\text{simple}} = I_p \left(1 + V_p \cos\left(\phi_p + \gamma_t\right)\right) , \tag{7.1}$$

where the index t denotes the time or frame counter during the scan and I_p, V_p, and ϕ_p are related to pixel entry p in $\boldsymbol{I_0}$, $\boldsymbol{V_0}$ and $\boldsymbol{P_0}$, respectively. This has earlier been introduced in Section 2.3.4 and 2.3.5, and the nomenclature has been adapted from [109] for consistency. While in this early step the results are greatly corrupted by the vibrations this result is an initial guess for following steps.

The mechanical oscillations of the system move and deform the gratings relative to each other and hence induce periodic intensity, visibility, and phase fluctuations. As introduced in [109], this can be modeled by adding I_{pt}^{vib}, V_{pt}^{vib}, and ϕ_{pt}^{vib} to form the extended data model,

$$y_{pt} = I_p \left(1 + I_{pt}^{\text{vib}}\right) \left[1 + V_p \left(1 + V_{pt}^{\text{vib}}\right) \cos\left(\phi_p + \phi_{pt}^{\text{vib}}\right)\right] , \tag{7.2}$$

where the additional parts represent the spatial and temporal fluctuations over p and t in the three modalities. Optimizing such a model only works as prior knowledge over pixel-to-pixel correlation is available. For visibility and phase variations, previous work demonstrated that the interferometer phase tends to fluctuate following low-order two-dimensional polynomial functions extending over the detector [26]. This can be extended also to related visibility fluctuations. Consequently, V_{pt}^{vib} and ϕ_{pt}^{vib} can be composed by several 2D polynomial functions

as described in [109]. For the intensity fluctuations, however, initially no such correlation is accessible, but will be introduced at a later stage of the processing. Consequently, for now, it is left unaccounted for by setting $I_{pt}^{\mathrm{vib}} = 0$ and will be revisited in (7.7) when visibility and phase variations have been corrected.
This can be realized by a weighted sum over the low-order two-dimensional polynomial functions in the system. Neglecting the tile-wise character of the G_2 this sum is given as,

$$V_{pt}^{\mathrm{vib}} = \sum_{i,j} \beta_{ijt}\, \mathcal{P}_{ijp}^{\mathrm{global}}\,, \tag{7.3}$$

$$\phi_{pt}^{\mathrm{vib}} = \sum_{i,j} \gamma_{ijt}\, \mathcal{P}_{ijp}^{\mathrm{global}}\,, \tag{7.4}$$

for the visibility and phase variations, respectively. Here, $\boldsymbol{\mathcal{P}}_{ij}^{\mathrm{global}} = (\mathcal{P}_{ijp}^{\mathrm{global}})$ represents the pixel-wise values of a two-dimensional polynomial of order i and j along the two image axes, i.e., width and height, respectively. For pixel p the value is then given as $\mathcal{P}_{ijp}^{A} = w(p)^i \cdot h(p)^j$ with $w(p)$ and $h(p)$ denoting the coordinate of the pixel p along the respective image axis in the area indicated by A. Since we neglected the tile-wise character of G_2, $\boldsymbol{\mathcal{P}}_{ij}^{\mathrm{global}}$ covers the full area of the detector. These $\boldsymbol{\mathcal{P}}_{ij}^{\mathrm{global}}$ are shown in Figure 7.3 until the second order as an example.

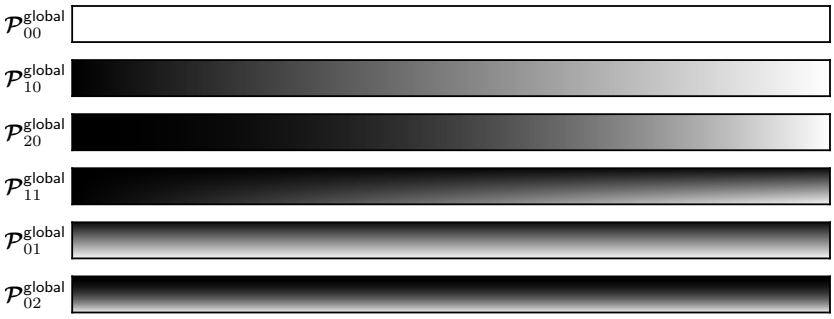

Figure 7.3: Global polynomial patterns $\boldsymbol{\mathcal{P}}_{ij}^{\mathrm{global}}$ until second order. They cover the full area of the detector, indexed as A = 'global'. i represents the polynomial order along the horizontal axis and j along the vertical axis. Gray scale from 0–1.

Since G_2 consists of multiple tiles, these have to be modeled individually with tile-wise polynomial patterns. This can be included by extending Equations (7.3) and (7.4) to,

$$V_{pt}^{\mathrm{vib}} = \sum_{A} \sum_{i,j} \beta_{ijt}^{A}\, \mathcal{P}_{ijp}^{A}\,, \tag{7.5}$$

$$\phi_{pt}^{\mathrm{vib}} = \sum_{A} \sum_{i,j} \gamma_{ijt}^{A}\, \mathcal{P}_{ijp}^{A}\,, \tag{7.6}$$

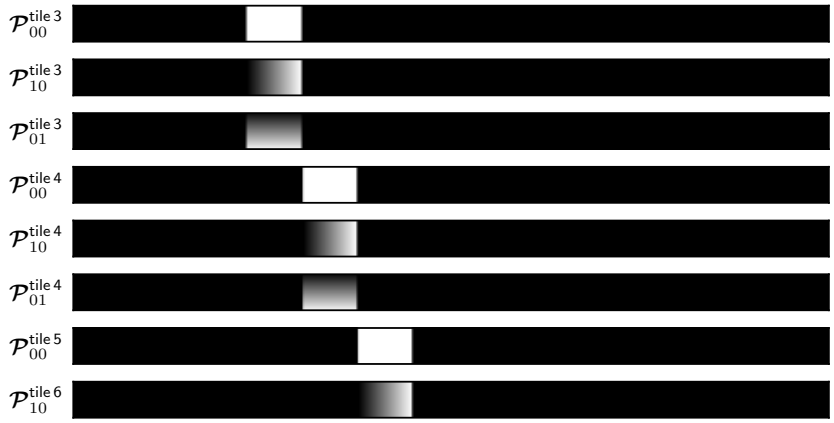

Figure 7.4: Tile-wise polynomial patterns $\boldsymbol{\mathcal{P}}_{ij}^{\mathrm{tile}}$ until first order. They only cover the area of the respective G_2 tile and area labeled accordingly, e.g., as A = 'tile 3'. i represents the polynomial order along the horizontal axis and j along the vertical axis. Gray scale from 0–1.

for the visibility and phase variations, respectively. The introduced index A represents the various areas for which the polynomial patterns are defined. This allows to define areas for each G_2 tile and an example for some of the patterns are shown in Figure 7.4. For clarity, only polynomials until the first order are included in the figure. During reference processing implemented at the dark-field CT polynomials until the second order are used, except $\boldsymbol{\mathcal{P}}_{02}^{\text{global}}$. It was found that this component is not required to improve the model, presumably, because of the small height of the field of view.
This sum over the various areas eventually contains the global and all G_2 tile areas which is sufficient for the further processing steps. While the $\boldsymbol{\mathcal{P}}_{ij}^{A}$ are constant throughout the processing, β_{ijt}^{A} and γ_{ijt}^{A} represent the per-shot parameters which must be optimized during the processing.

With this extension, visibility, and phase fluctuations can be sufficiently well described by the model. Only intensity fluctuations remain in the residuum between measured raw data $\hat{y}_{pt}$ and the model output y_{pt},

$$\hat{I}_{pt}^{\text{vib}} = \frac{\hat{y}_{pt}}{y_{pt}} - 1 \,. \tag{7.7}$$

To separate noise and only the most dominant intensity variation patterns principal component analysis (PCA) is applied to this data:

$$\text{PCA}(\hat{I}_{pt}^{\text{vib}}) \rightarrow (\mathcal{R}_{\text{i},kp}, c_{\text{i},kt}) \,, \tag{7.8}$$

where PCA is a function returning principal components $\mathcal{R}_{\text{i},kp}$ indexed by k and the corresponding magnitudes or intensity $c_{\text{i},kt}$ of each principal component [109, Sec. III-A.3]. Pleas note the differentiation between italic i as an index, e.g., of polynomial order in (7.6), and an upright i representing a label for the intensity channel.
The resulting intensity correction patterns are depicted in Figure 7.2b as $\boldsymbol{\mathcal{R}}_{\text{i},\mathbf{1-3}}$ and the corresponding intensity coefficient per projection $c_{\text{i},1-3}$ (for a sample scan) in Figure 7.2d. Besides the two shadowing induced intensity patterns $\boldsymbol{\mathcal{R}}_{\text{i},\mathbf{2}}$ and $\boldsymbol{\mathcal{R}}_{\text{i},\mathbf{3}}$ there is an all-pixel constant pattern $\boldsymbol{\mathcal{R}}_{\text{i},\mathbf{1}}$ which corrects global intensity variation, e.g., flux fluctuation of the X-ray tube. As found in [109], the first three principal components, besides the constant pattern are sufficient to define the intensity fluctuations in the system as,

$$\hat{I}_{pt}^{\text{vib}} \approx I_{pt}^{\text{vib}} = \sum_{k=1}^{3} c_{\text{i},kt} \mathcal{R}_{\text{i},kp} \,. \tag{7.9}$$

In the final processing step the tile-wise data model and the identified interferometer phase and visibility correction patterns are compressed, also using PCA. This step is required to simplify the patterns and reduce the number of free parameters, i.e., polynomial coefficients, for the sample processing.
For the sample processing it is important to have few globally, i.e., on the entire detector area, defined correction patterns instead of tile-wise defined ones. Working with too small correction patterns would come with a high risk of fitting the locally defined tile-wise patterns to the sample. Furthermore, there is some correlation between the tile-wise patterns expected as, all gratings are exposed to the same system vibrations. It is found that in the dark-field CT prototype this coupling is strong to allow a compression to a small number of globally defined correction patterns. To extract those, all polynomial visibility and interferometer phase correction patterns are summed up as previously defined in Equations (7.5) and (7.6). For clarity, here, the sums from Equations (7.5) and (7.6) are indicated with hats, as $\hat{V}_{pt}^{\text{vib}}$ and $\hat{\phi}_{pt}^{\text{vib}}$,

respectively. This sum is then analyzed with PCA and allows to redefine the former polynomial based V_{pt}^{vib} and ϕ_{pt}^{vib} by a sum of a few globally defined correction patterns,

$$\mathrm{PCA}(\hat{V}_{pt}^{\mathrm{vib}}) \rightarrow (\mathcal{R}_{\mathrm{v},kp}, c_{\mathrm{v},kt}) \;\; \text{redefining} \;\; V_{pt}^{\mathrm{vib}} = \sum_{k=1}^{3} c_{\mathrm{v},kt}\mathcal{R}_{\mathrm{v},kp} \approx \hat{V}_{pt}^{\mathrm{vib}}\,, \tag{7.10}$$

$$\mathrm{PCA}(\hat{\phi}_{pt}^{\mathrm{vib}}) \rightarrow (\mathcal{R}_{\mathrm{p},kp}, c_{\mathrm{p},kt}) \;\; \text{redefining} \;\; \phi_{pt}^{\mathrm{vib}} = \sum_{k=1}^{6} c_{\mathrm{p},kt}\mathcal{R}_{\mathrm{p},kp} \approx \hat{\phi}_{pt}^{\mathrm{vib}}\,. \tag{7.11}$$

Again, only the most dominant components, here, two visibility and five phase correction patterns additional to the constant ones, are used for further processing and are shown in Figure 7.2b.
After all these reference processing steps $\boldsymbol{I_0}$, $\boldsymbol{V_0}$ and $\boldsymbol{P_0}$ are free of any perturbation and X-ray flux variation related artifacts and can be used for correction during the sample processing. We can summarize the results of the reference processing procedure into two categories. Most important are the pixel-wise and scan-to-scan persistent system properties which are listed, e.g., in Figure 7.2b. These describe the interferometer response based on globally defined, i.e., covering the entire detector area, pixel-wise patterns.
The second category are the coefficients which determined the intensity of their respective correction pattern. Examples for these coefficients are plotted in Figure 7.2d. These are not fully scan-to-scan persistent, as, e.g., the high frequency phase of the oscillation is not reproducible between scans. Nevertheless, some scan-to-scan persistent information can be extracted from these coefficients. Examples are the low frequency behavior, which is for example highlighted in Figure 7.5a in orange, and the frequencies and amplitude of the oscillations. The phase of the coefficients' oscillations, however, is unique for each scan and must be optimized during sample processing as will be described in Section 7.8.1.

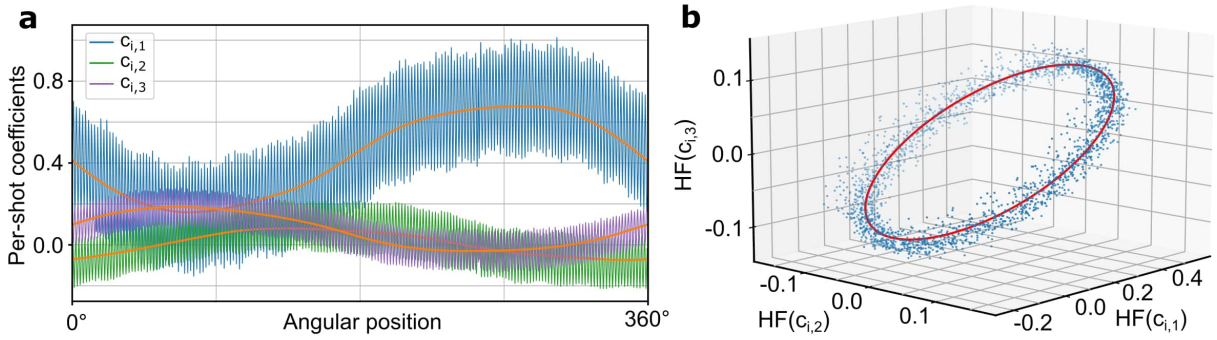

Figure 7.5: Example for correlation between per-shot coefficients. While the three components of intensity variations are orthogonal in their correction array definition (because they are generated using PCA), their per-shot intensity is correlated. **a,** A low-frequency oscillation in orange can be recognized but the high frequency variation seems rather chaotic. **b,** The 3D representation of the high-frequency variation, however, reveals a correlation between the three correction arrays. They form an elliptical curve which persists from scan-to-scan which leads to the assumption that all three correction arrays are caused by the same underlying effect. Image adapted from [136] CC BY.

7.4 Transmission Analysis of G_0 and G_2

Before an in-depth analysis of the interferometer performance is done, the two absorption gratings are evaluated individually. This way potential artifacts and defects from the fabrication or bending process can be identified and associated with a particular grating.
For this analysis G_0 and G_2 are implemented after each other into the CT gantry for test scans of these gratings' transmission. This way the obtained data includes X-ray source spot characteristics of the clinical X-ray tube and the same field of view as during a CT scan is analyzed. The only shortcoming is the limited resolution of the clinical CT detector which cannot resolve fine defects due to its rather large pixel size. Nevertheless, the resolution is sufficient to evaluate shadowing and acceptance artifacts. These are, as discussed in Chapter 4, major issues in this compact and large field of view implementation with bent high aspect-ratio gratings. The following evaluation and results have been published in [139] and their discussion is here slightly extended.
The results for the G_0 transmission in Figure 7.6a reveal that transmission is highest in the center where it exceeds 45% and reduces slightly to the left and right. In the direct vicinity of the left and right edge, i.e., approximately the outermost 50 pixels, the transmission through

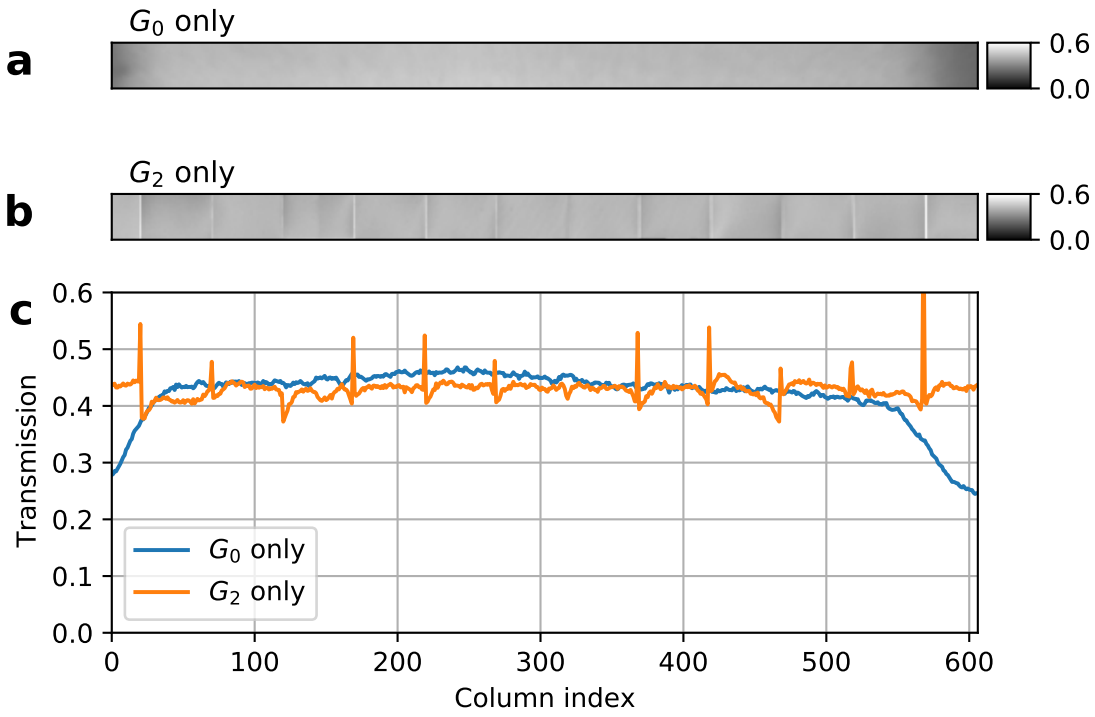

Figure 7.6: Transmission analysis of the bent gratings G_0 and G_2 in the CT gantry without gantry rotation. **a,** G_0 has a mean transmission of 40% which is expected for its grating parameters. Due to grating imperfections and the acceptance effect (i.e., from the high aspect-ratio and large source spot size) the outermost regions on the left and right have reduced transmission. No defects related to the small bending radius of 100 mm are found. **b,** Analysis of the G_2 tiles transmission shows only local variations and tile-wise differences which will be corrected during reconstruction. The mean transmission is around 45%, which is expected for a grating with a duty-cycle of around 56% with a negligible bridge-fraction of only 1%. **c,** Line plots of the central detector row through a and b. Strong transmission peaks occur at the G_2 tile-gaps and for G_0 a decay to the left and right is observed. Image adapted from [139] CC BY.

the G_0 drops significantly. Several reasons lead to this behavior and are difficult to differentiate. Via angular X-ray transmission analysis (AXT), a grating characterization method introduced by Gustschin et al. [41], we found that G_0 has imperfections close to the left and right edges. The results of this analysis are shown in Figure 7.7 where the shape factor should be zero for a perfectly binary absorption grating and a value of one would imply that the structure is inclined to form a triangular grating, as previously introduced in Figure 2.15. From these results, it becomes clear that the very left and right parts of the grating are not optimal, and also in the central and central-upper area some defects are present. As indicated by the red area, the active area in the dark-field CT prototype can be adjusted to only use the best sections of G_0. Since G_0 is so close to the source spot the beam path is rather small and only an approximately 3.5 mm high G_0 area is required. With the motorized adjustment along the z-axis the optimal area can be selected during implementation into the dark-field CT.
Another aspect which must be considered is the shadowing inside the grating structure caused by the extended X-ray source spot as discussed in Chapter 4. We refer to this effect as the *acceptance* of the grating, which depends on the aspect-ratio, the source size, and the bending radius. As introduced in Section 5.3.2, at clinical CT X-ray sources the inclined anode surface leads to a variable source width [10]. It is smallest for the central beam through the iso-center and increases for larger fan angles towards the outer detector columns. Since the aspect-ratio of the grating is constant, the acceptance of G_0 decreases for larger fan angles and consequently transmission and visibility are reduced in these areas.
As a consequence, only in the center, for which the X-ray source spot is smallest, the expected transmission value of 45% is met and otherwise the grating's acceptance leads to a slight intensity decrease towards the left and right. Nevertheless, we conclude that bending of the G_0 minimizes the amount of shadowing to a tolerable level. As G_0 has a bending radius of only 100 mm, this demonstrates that, except for some acceptance-related residual shadowing, bending can be applied at relatively small radii. This approach allows to implement an interferometer with a fan opening of about 47° at the dark-field CT prototype, which is currently not feasible with any other shadowing suppression method.
In contrast to the G_0 results, G_2 has an almost optimal transmittance as only small transmission fluctuations are visible in Figure 7.6b. These are caused by imperfections from the fabrication process and are always localized to a single G_2 tile.
The measured transmission values lie around 45% which matches the expectations for the G_2 design. This shows that this grating works as intended over the entire field of view and

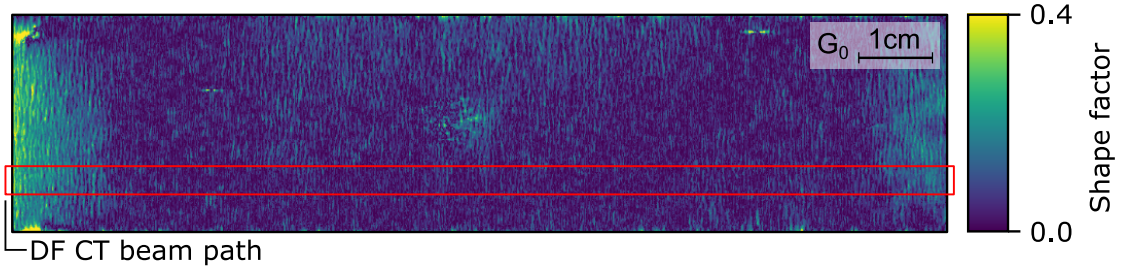

Figure 7.7: Grating characterization of G_0 via angular X-ray transmission analysis (AXT). The shape factor summarizes the inclination and height of the grating structure representing a perfect binary grating where being zero or a triangular grating where one. Defect areas at the very left and right can be identified, and some minor defects are found in the center and the upper half. Since the active beam path in the dark-field CT is relatively small in vertical extent these areas can be omitted as illustrated by the red highlighted area. Image adapted from [136] CC BY.

no shadowing is found. This is important because any additional and undesired absorption, i.e., shadowing or defects, in G_2 would result in an even higher dose penalty than G_2 causes by design, as it is positioned behind the patient. This result demonstrates that cylindrical bending also works well for larger bending radii, i.e., here 1000 mm, and gratings which are combined from several smaller, individually bent, tiles.
The results also show that cylindrical bending is sufficient because no vertical transmission gradients are found. This is because shadowing is strongly direction-dependent and when the angle of incidence is parallel to the grating lines, the performance of the interferometer will not be reduced and no shadowing occurs [100]. For G_1, which is a phase-grating, the transmission analysis is skipped because its attenuation is too low to resolve any artifacts or defects.

7.5 Interferometer Performance Analysis

The previous section demonstrated that G_2 leads to no significant shadowing related transmission losses, but from G_0 at least some shadowing or defect related artifacts and performance losses are expected. To go beyond a component wise evaluation and characterize the interferometer setup in its entirety the following section analyzes the intensity $\boldsymbol{I_0}$, visibility $\boldsymbol{V_0}$, and interferometer phase $\boldsymbol{P_0}$ as defined in Section 7.3 which are yielded by the reference processing of an axial reference scan with 1 s rotation period. While the data processing includes and compensates for influences of the gantry vibrations, this section focuses only on the stable and scan-to-scan persistent interferometer performance measures shown in Figure 7.8. Parts of this section have been published in [139], [137] and their discussion is here slightly extended.
As expected from the previously discussed transmission analysis, the processed system intensity is relatively flat with a wide maximum in the center which is caused by the acceptance of G_0. The apparent intensity variation is similar to the effects of a bow-tie filter in conventional CT, where it is used to reduce patient dose and to achieve a more homogeneous noise level across the image. Therefore, the intensity gradient is actually advantageous for CT imaging, and we can for now omit the use of a bow-tie filter. To further optimize the intensity variation with the fan angle, the implementation of a specifically shaped bow-tie filter can easily be added to the G_0-G_1-assembly.
The system visibility is shown in Figure 7.8b and an evaluation of the three central tiles yields a mean visibility of 0.24 . The same three tiles have also been evaluated at a laboratory setup which resembles a vibration free reference implementation and the results are shown in Figure 7.9. This laboratory implementation has a significantly higher resolution than the clinical CT but comes with a much smaller field of view, consequently only three G_2 tiles can be evaluated. The processing results of a stepping evaluation at this setup reveal a mean visibility of 0.24 over the area of the three analyzed G_2 tiles of the interferometer. While the performance is almost constant over the entire field of view small dot-like defects are visible which come from droplet-like electroplating faults during fabrication of G_1. These are also visible in the high-resolution transmission analysis shown in Figure 7.10. Besides some diffuse vertical lines, which are related to slightly distorted or inclined lamella in G_0 which lead to local shadowing artifacts [41] no further degradation is found in the visibility image in the reference implementation at the laboratory setup. This is an important finding, particularly as this demonstrates that bending the gratings to focus onto the X-ray source spot does not degrade them.
These results demonstrate that a comparable interferometer visibility can be achieved in the clinical CT gantry as in the laboratory setup. Nevertheless, it is important to highlight that this only represents the central region of the CT's field of view, and we clearly see a reduction of

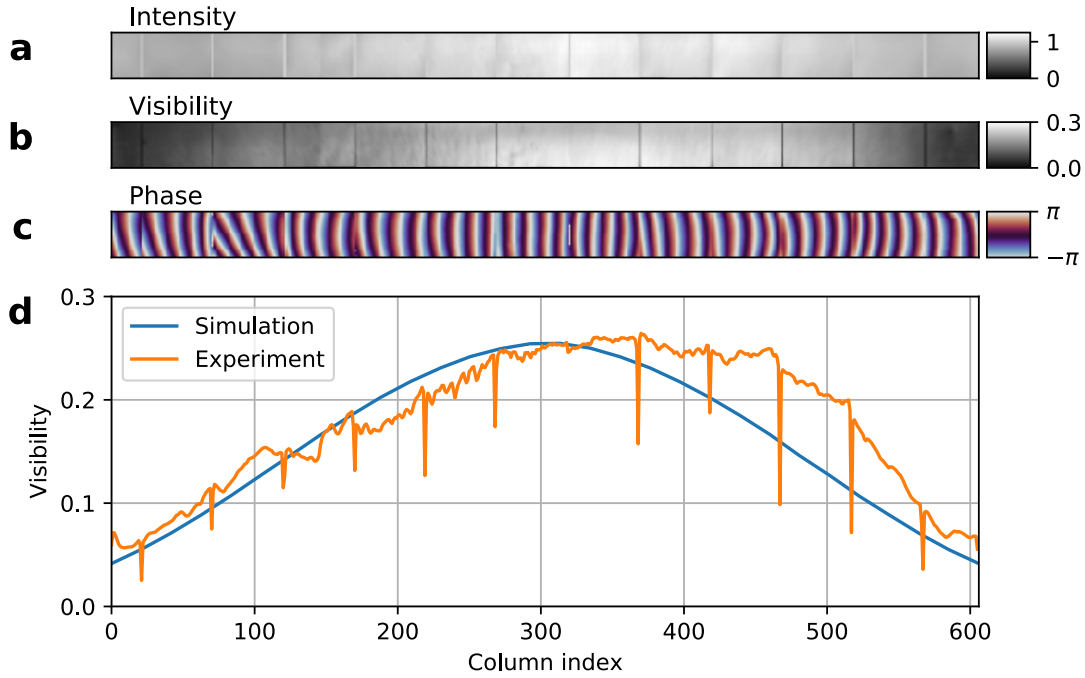

Figure 7.8: Dark-field CT performance in rotating gantry. **a,** The Intensity is homogeneous with a shallow maximum in the center due to the G_0 acceptance. This pattern is similar to the effect of the bow-tie filter regularly used in conventional CT. Thus, this distribution has no negative impact. **b,** Interferometer visibility is highest in the center, exceeding 0.25 . The mean visibility of the central 50% of the field of view is 0.22 and the mean visibility of the whole field of view is 0.18 . **c,** A Moiré pattern with a horizontal fringe period of around 10 pixels, is visible in the phase image. **d,** A line plot of the system's visibility shows the fan angle, i.e., detector column, dependency of the visibility. The visibility drop is related to the limited acceptance of the high aspect-ratio G_0. The experimental results match reasonably well to simulations taking the limited acceptance into account. Deviations from the simulation can be explained by the strong impact of duty-cycle variations and geometry mismatch. Image adapted from [139] CC BY.

visibility towards the left and right edges. These areas had been inaccessible in the laboratory implementation due to the limited field of view.
There are various explanations for these visibility decreases. Quality variations towards the edges from the fabrication are common and can cause such performance losses. Moreover, also a grating period mismatch in combination with a variation of the X-ray source size can lead to visibility decreases. In clinical CT the effective X-ray source size increases towards larger fan angles, hence, the degrading effect increases towards the edges of the field of view. This has previously been introduced in Section 4.5. Both these mentioned aspects are, however, kept to a minimum by thorough inspection and characterization of the fabricated gratings. Consequently, the most dominant effect degrading the visibility in the gantry implementation is the G_0 acceptance.
The quality of the slit-sources which are created by G_0 is degraded by the acceptance in the outer regions of the interferometer. When the source spot is significantly large, i.e., for large fan angles, an increasing fraction of radiation which transverses the grating leaks through the absorbing structures. This leaked radiation subsequently creates an incoherent intensity offset which lowers the system visibility. In the visibility line plot, shown in Figure 7.8, the experimental results are overlaid with simulation results considering the G_0 acceptance. Remaining differences probably arise from quality and geometry deviations between the simulation and

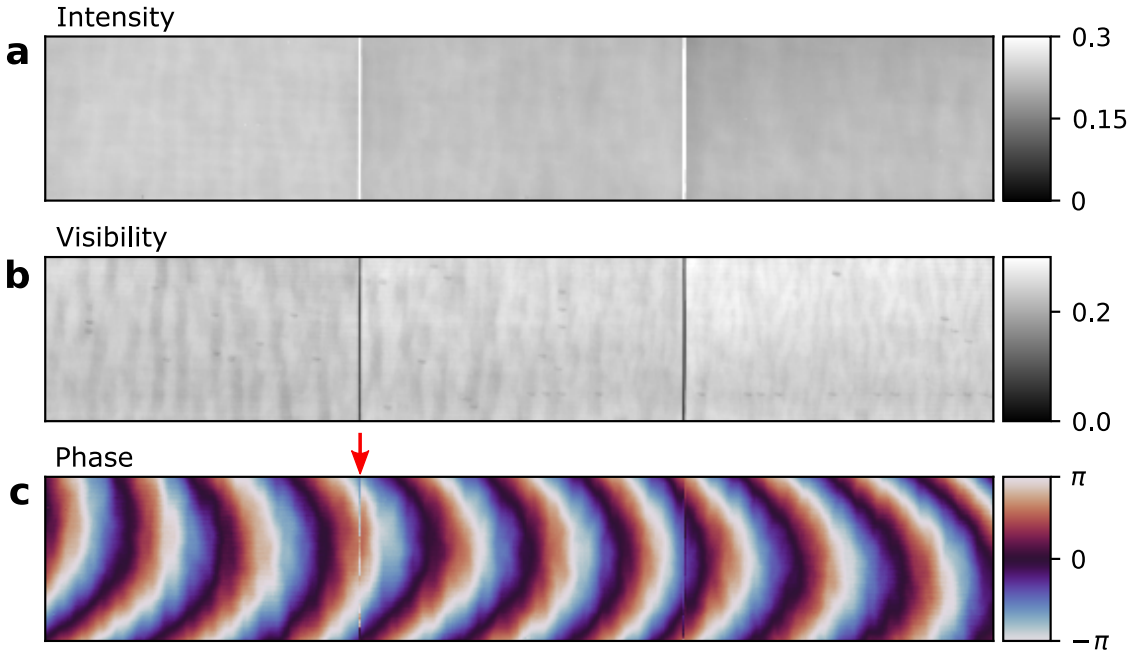

Figure 7.9: Interferometer performance at a laboratory implementation for reference evaluation. **a,** After processing the stepping data, a homogeneous intensity transmitted through the interferometer of 23% demonstrates that cylindrical bending minimizes shadowing. **b,** The mean visibility of the reference implementation is 0.24. It is reduced by small dot-like artifacts originating from defects and some diffuse vertical lines from inclination errors in G_0 and G_1. **c,** The phase can be adjusted to be continuous between G_2 tiles, as demonstrated at the right inter-grating gap. At the left gap, the process was stopped early, showing a local jump in interferometer phase (see red arrow).
Image adapted from [139] CC BY.

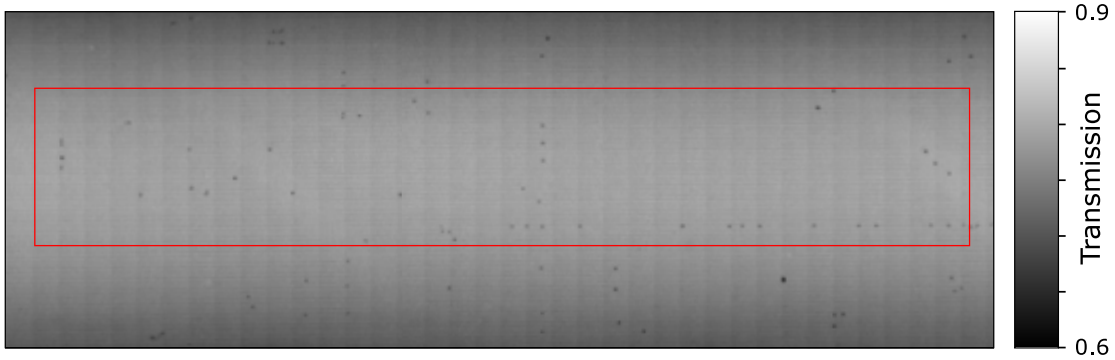

Figure 7.10: High-resolution transmission analysis of G_1 at a micro-CT system with an unfiltered 60 kVp tungsten spectrum provided by Nikolai Gustschin. In red the area as evaluated in Figure 7.8 is highlighted. The dark spots indicate defects which lead to an increased X-ray absorption in the grating structure. These can be related to failed electroplating of individual grating lamellae between two bridges. The number of occurrences is reasonably small, and each defect is extremely localized.

the setup, but the general trend matches.
Between adjacent G_2 tiles, there are one pixel wide columns with reduced visibility because there remain small gaps between the tiles. These are visible as sharp drops in Figure 7.8d. Nevertheless, there are no columns where the visibility drops to zero and the density of the fringe pattern is relatively constant and mostly almost continuous over the tile borders.

This analysis demonstrates that the interferometer performance can – with some restrictions – be reproduced in the hostile environment of a clinical CT gantry. While in the central region a comparable visibility and transmission as in the laboratory is realized, a degradation of the visibility for larger fan angles is caused by the G_0 acceptance. This, however, is not a clinical CT or gantry related problem but a more general issue raised by clinical X-ray tube operated with a large field of view.

7.6 Evaluation of the Vibrations

While usually the aim is to avoid any kind of vibrations in interferometry setups the presented prototype system actually depends on these oscillations. During the reference processing the system intrinsic vibrations of the CT gantry are utilized for random phase stepping. For the sample processing the same vibrations are required to establish a sufficient phase sampling within the small processing windows, as will be discussed in Section 7.8.2. The following analysis of the vibrations and identification of their sources has previously been published in [139] and is here extended by some further details.
Sources of vibrations on the CT gantry are the pump of the cooling unit and the rotating anode of the X-ray source. These are mandatory components of a clinical CT which consist of mechanical parts and continuously induce vibrations as they run. Naturally, these components could be optimized for fewer vibrations, but such developments would go beyond the scope of the objective of upgrading a conventional clinical CT for dark-field imaging. Besides these two primary sources of vibrations also the rotation of the gantry is bound to induce a deformation of the interferometer during the rotation. Contrary to the vibrations from the cooling pump or the X-ray tube, this deformation is expected at a relatively low frequency. While for example the X-ray anode rotates at approximately 175 Hz, the gantry rotation is relatively slow with rotation periods between 1.5 s and 0.27 s.
An important detail concerning vibrations from external sources is the air bearing [24] which is used in the Brilliance iCT system. It lets the gantry float on an air cushion and is assumed to provide an effective decoupling from the surrounding.
The vibrations lead to a displacement of the gratings and consequently fluctuation of the interferometer state. Processing the data of a reference scan models and fits these fluctuations and returns the periodic deviations as has been introduced in Section 7.3 and in [109]. In Figures 7.11, 7.12, and 7.13 these processing results are plotted and analyzed as they allow an evaluation of the fluctuations in the intensity, visibility, and phase channels of the interferometer. They are generated from a scan without a sample with 1.0 s rotation period.
Figure 7.11 shows the analysis of the intensity fluctuations, and we find two dominant oscillation frequencies in these plots: A low frequency oscillation at 1 Hz and a high-frequency at 189 Hz. The Fourier analysis also identifies other frequency contributions, but these are at least two orders of magnitude less intense. The origin of the low frequency oscillation clearly is the gantry rotation, and it is consistent in amplitude and phase between multiple scans. The source of the high-frequency variation has been identified as the X-ray tube driver, which impels the anode. This asynchronous motor is operated at a frequency of 189 Hz (see Section 5.3.2) and induces the observed intensity fluctuations through electromagnetic interference. We assume that the variations might be caused by electromagnetic distortion of the X-ray source spot shape and hence has influence on the total X-ray flux. As we can see in Figure 7.11 the total amplitude of the intensity variations is only in the order of $\pm 4\%$. In conventional CT this is corrected by a reference detector, but due to space restrictions this device has been removed and thus the processing must correct for it.

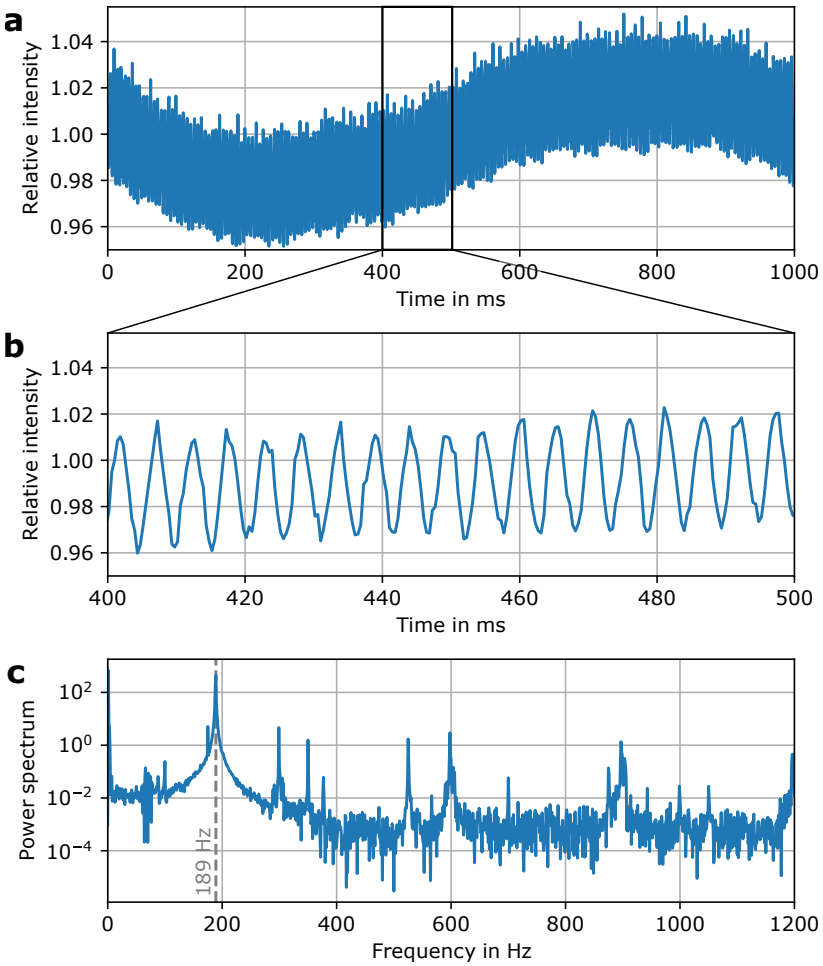

Figure 7.11: Variation in the intensity channel during a scan. **a,** In the 2400 projections measured during one rotation, the intensity varies with a low frequency related to the gantry rotation overlaid with a high-frequency. **b,** Enlarged section from a. The oscillation is dominated by one high-frequency which is stable over the whole scan time. **c,** Fourier analysis of the coefficient yields that, besides the low frequency, 189 Hz is the most dominant frequency. Image adapted from [139] CC BY.

In Figure 7.12, the characteristic vibration properties in the interferometer phase reveal an oscillation at 175 Hz which is again overlaid with the 1 Hz from the gantry rotation. During the rotation, the combination of gravity and centrifugal force leads to slight deformations of the gantry and the grating mounts. The interferometer is highly sensitive to such displacements in the micrometer range and changes its interferometer phase. The high-frequency component here is induced by the rotation frequency of the X-ray tube anode, which is driven by the previously discussed asynchronous motor. It is characteristic for an asynchronous motor that there is a small slippage between the rotating magnetic field excited by the stator coils and the actual rotation of the rotor, i.e., the anode. Consequently, the anode rotates at a slightly lower frequency than the 189 Hz of the driver [10, Section 6.2.3.1]. For verification, we attached a vibration sensor (Model 356A17, PCB Piezotronics, New York, USA) to the X-ray tube housing and analyzed the spin-up phase of the anode, which stabilizes at 175 Hz and never reaches the 189 Hz. This mechanical oscillation from the anode rotation presumably displaces the gratings and leads to the high-frequency phase change of the interferometer visible in Figure 7.12b. Since this displacement is only in the range of a few micrometers it is too small to induce any shadowing artifacts, consequently, we see no influence of this mechanical oscillation in the intensity channel.

It is important to point out that any movement of a grating during the measurement leads to a reduced visibility due to the smearing of the fringe pattern [55]. We therefore expect a visibility variation at double the frequency of the previously evaluated interferometer phase variation (175 Hz) coupled to the absolute speed of the gratings, i.e., the absolute rate of phase change. The derivation of the exact relation can be found in [109, Equation 7]. In

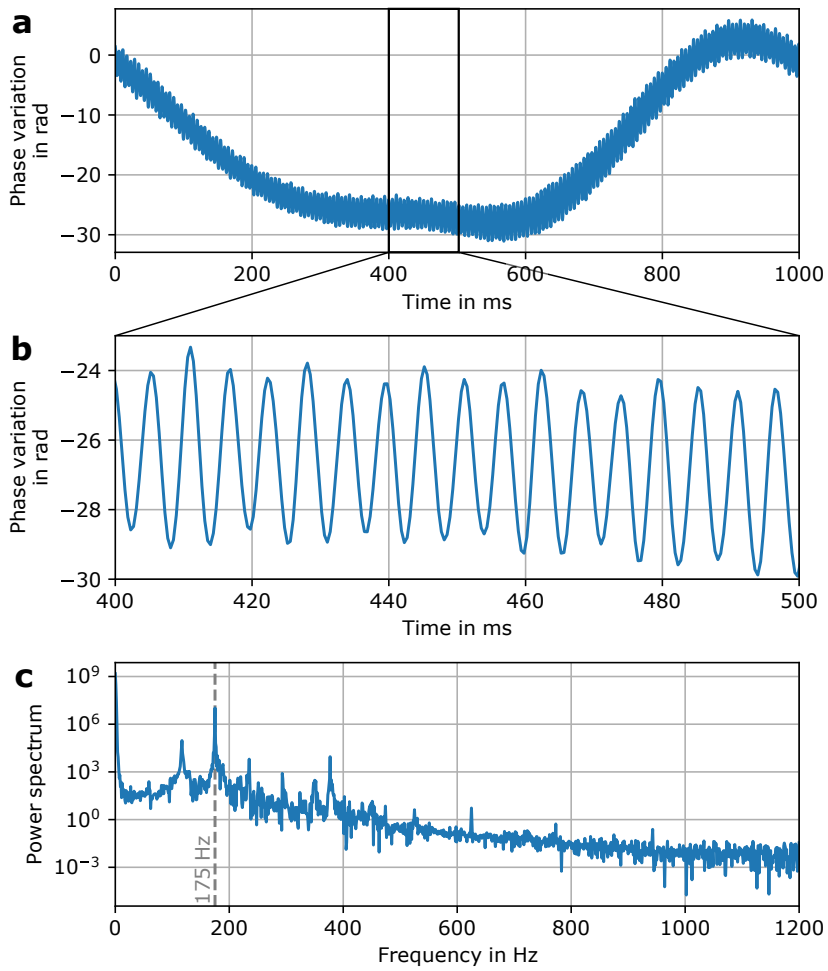

Figure 7.12: Variation of the interferometer phase during a scan. **a,** During one rotation the interferometer phase varies over several π with a low frequency. **b,** Zoom into section from a. An additional high-frequency oscillation is sinusoidal with smaller amplitude and continuous over the whole scan time. **c,** Fourier analysis of the coefficient yields that besides the low frequency the most dominant frequency is at 175 Hz. Image adapted from [139] CC BY.

Figure 7.13c, the processing results of the visibility variation show this effect as there is a peak at 350 Hz in the frequency spectrum. This is double the mechanical oscillation frequency which is induced by the anode rotation, representing the speed of the gratings during the acquisition of the projection. Since the visibility of the system is independent of the position of the interferometer phase, there is no peak at 175 Hz in the visibility variation. Another dominant frequency in the visibility channel is the 189 Hz oscillation which previously was related to the electromagnetically induced change of X-ray flux, which we already found in the intensity in Figure 7.11. This supports the hypothesis that there is an electromagnetic interference between anode motor and interferometer, e.g., by small distortions of the focal spot which can lead to visibility changes if the source size varies. The two frequencies at 189 Hz and 350 Hz have similar strength, consequently, the resulting pattern in Figure 7.13b is a rather chaotic beat pattern as the two frequencies interfere.

Besides the two most dominant base frequencies (175 Hz and 189 Hz) identified in the analyses there are also other frequencies with lower contributions present. Particularly, peaks at some multiples of 59 Hz can be found which are related to the pump of the cooling unit and have also been verified with the vibration sensor. Compared to the impact of the anode drive and the anode rotation frequency, the contribution of other components is small. A rather unfortunate coincidence concerning the cooling pump frequency is the close overlap between the higher order modes of the 59 Hz pump frequency with the 175 Hz anode rotation frequency which makes a clear differentiation between the two sources difficult. In Figure 7.14, results from a measurement with a vibration sensor verify the presence of the mechanical vibrations at 175 Hz and 59 Hz. These results show almost no vibration at the 189 Hz anode drive frequency, but

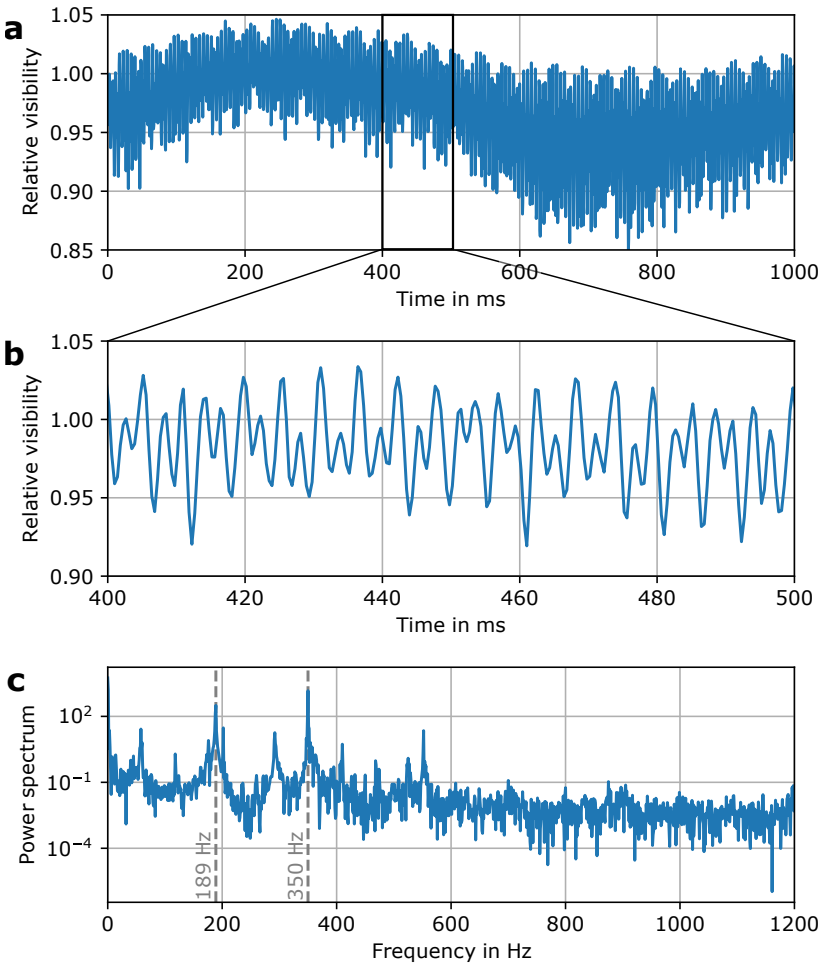

Figure 7.13: Variation of the system visibility during a scan. **a,** In the 2400 projections measured during one rotation the visibility varies moderately with a low frequency related to the gantry rotation overlaid with a high-frequency. **b,** Enlarged section from a. This oscillation is a combination of two almost equally intense frequencies, which leads to a beat pattern. **c,** Fourier analysis of the coefficient reveals that besides the 1 Hz frequency, there are two dominant high frequencies at 189 Hz and 350 Hz. Image adapted from [139] CC BY.

significant intensities of its higher harmonics as indicated with the dashed lines. While the first observation matches the experiences from the interferometer oscillation analysis, the latter cannot be related to any vibrations found during the oscillation analysis of the interferometer data. An explanation might be, that these higher order vibrations are parallel to the grating lines and therefore have only minimal impact on the interferometer performance.
The analysis of the vibrations in the interferometer data demonstrates that the dark-field CT system is clearly in a perturbed state. The underlying characteristics are nevertheless reproducible because the sources of vibration do not change their characteristics from scan to scan. While for the gantry rotation induced variation the amplitude and phase is reproducible from scan to scan, for the high-frequency oscillations only their amplitude can be considered as consistent between scans. The phase of these high-frequency variations is only stable during a single scan, but not on a scan-to-scan-basis. For example, the visibility variation is coupled to the speed of the grating movement, i.e., the first derivative of the interferometer phase. There is clearly a link between those two oscillations, i.e., between visibility and interferometer phase, which can be utilized during advanced data processing. Such correlations between the image channels can become particularly valuable during the data processing of sample scan data where the signal produced by the sample must be separated from the oscillations in the interferometer.

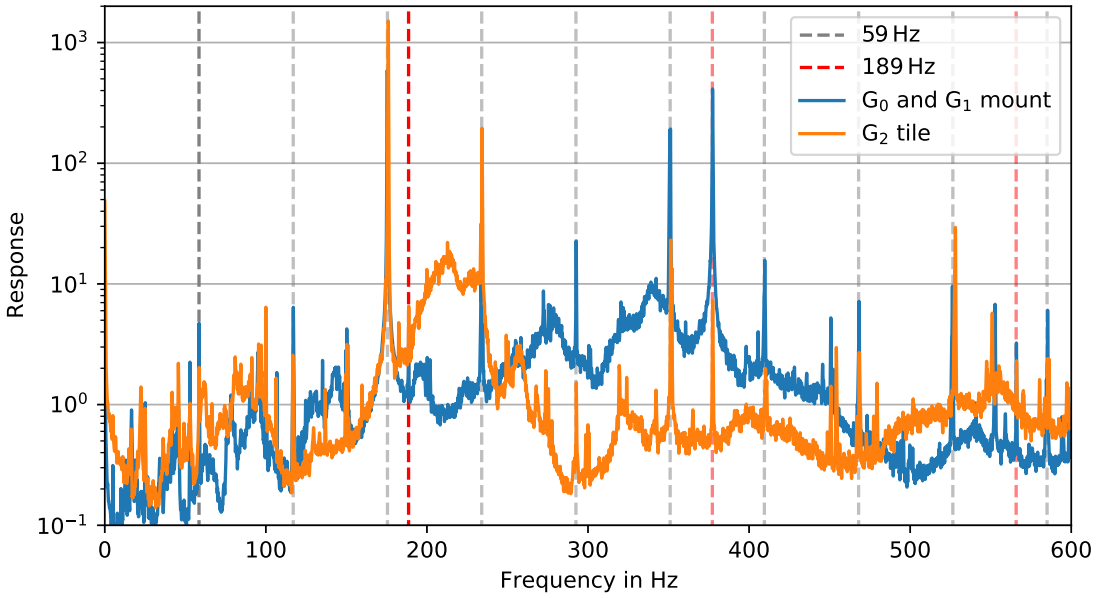

Figure 7.14: Vibration analysis based on a piezoelectric sensor. For one measurement the sensor has been attached to the G_0-G_1-mount, and for another evaluation to the center-most G_2 tile. The dominant vibration frequencies are 175 Hz and 59 Hz, which can be found at both positions. The evaluation has been done without gantry rotation, but with the anode rotating. Higher orders of the 59 Hz and 189 Hz frequencies are indicated with dashed vertical lines.

7.7 Influence of Gantry Rotation

The vibrations in the system have been evaluated in the previous section with focus on the high frequencies. As a side note, also a low frequency component, which is related to the gantry rotation, has there been identified and is now evaluated in more detail.
When the CT gantry rotates with an angular velocity ω the centrifugal force,

$$F = m\,\omega^2 \cdot r\ , \tag{7.12}$$

acts on all rotating parts with mass m on radius r from the iso-center in an outward direction. The acceleration is in the following evaluation given in G representing earths mean gravitational acceleration, i.e., $1\,\mathrm{G} = 9.81\,\mathrm{m/s^2}$. As an example, the G_0-G_1-assembly which is about 430 mm from the center of rotation experiences an acceleration equivalent to 1.6 G when the system rotates at 1 Hz and this value increases to about 7 G for a faster rotation with 0.5 s rotation period, i.e., 2 Hz.
This reveals that during slow rotation gravity and centrifugal acceleration are in comparable magnitudes and the force on the interferometer components vary during the rotation depending on the angular position. These changes on the interferometer components and mounts are assumed to lead to the periodic deformations which lead to reproducible phase variations during the scans. For faster rotations, i.e., shorter rotation periods, the centrifugal force dominates and consequently the relative acceleration on the components decreases. An evaluation for two different rotation periods shown in Figure 7.15 confirms this relation. While at both rotation speeds a similar interferometer phase variation is found their amplitude varies. For the faster rotation the phase variation during one rotation is about 30% smaller than in a scan with 1 Hz rotation. This, however, is limited to the low frequency interferometer phase variations and the high-frequency components, e.g., caused by the X-ray tube, are not affected by changes of

rotation speed.
Another aspect in a clinical CT gantry is that the system must be balanced within tight tolerances to avoid uneven rotation. This would also lead to varying accelerations during the scan and hence can lead to deformations. Modifications to the gantry as done in this dark-field CT system can easily displace the center of gravity, therefore, a balancing routine is required after every modification. This ensures that the system runs within its specifications and imbalance is minimal.
To evaluate whether such an imbalance can have an influence on the interferometer implementation scans within and out of specifications were performed. The results plotted in Figure 7.15 demonstrate that there is only a minimal difference. Naturally, the system must not be operated in such an imbalanced state as analyzed during this test to ensure long-term stability of the system. Nevertheless, this evaluation demonstrated that an imbalance of the rotor has only a rather small impact on the interferometer stability.
For clinical dark-field CT imaging not only stability at various rotation speeds is important but also a sufficient stability over time and over several scans is required. The sample processing, which will be introduced in the following section, relies on some prior knowledge on the system behavior, e.g., that the low frequency variation is the same between reference and sample scan. To evaluate this and verify this assumption a measurement series of 50 axial scans has been acquired with an interval of two minutes between the individual scans. The CT gantry was kept in continuous rotation during the whole time and no sample or table was in the beam path. All these air scans have been processed as described in Section 7.3 to obtain the fluctuation of the interferometer phase $c_{\mathrm{p},0}$. In Figure 7.16 only the low frequency component of this coefficient is plotted. In orange the low frequency phase variation of the first scan is plotted and as a blue envelope, the amplitude of the superimposed high-frequency oscillation. For all following scans only the low frequency variation of the coefficient is plotted and in various shades of red.

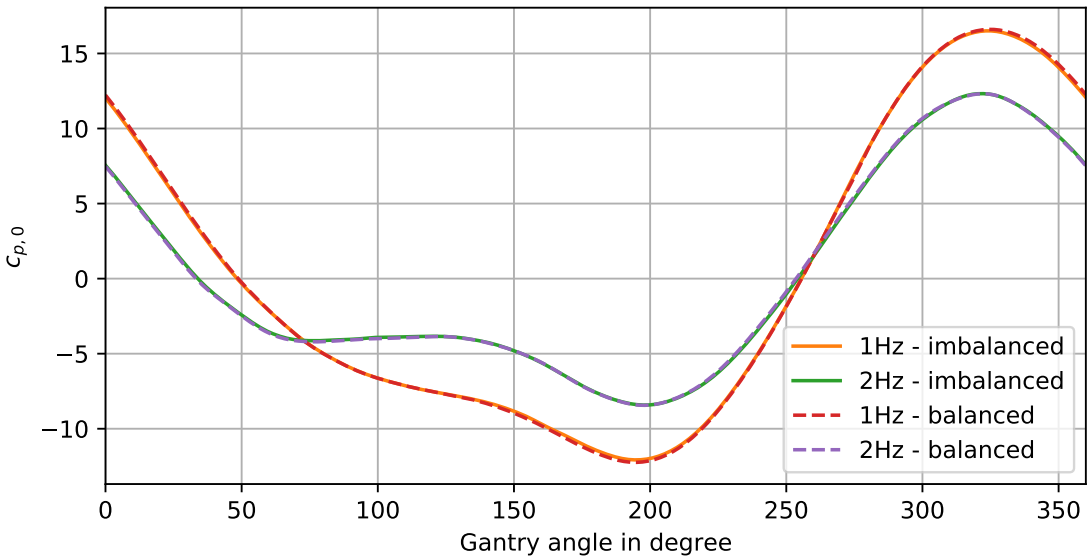

Figure 7.15: Influence of gantry rotation period and balancing on the interferometer. The low frequency interferometer phase variation for different rotation periods is plotted. An interesting observation is the smaller variation for a faster rotation. It is assumed that in a faster rotation the influence of the gravity decreases. Tests where the gantry is imbalanced, i.e., the gantry's center of mass is offset, and operated outside the specifications of the manufacturer reveals that this imbalance has only a minor impact on the interferometer deformation.

The results in Figure 7.16 reveal that no significant deviations occur over the evaluated time span of about 100 minutes. The identified minor deviations do not seem to drift over time, but rather scatter around a common mean curve with a standard deviation of about 0.07 rad. Since the amplitude of the high-frequency oscillation is significantly larger, this deviation can easily be corrected in the same step as the high-frequency oscillation optimization, which will be introduced in the following section.

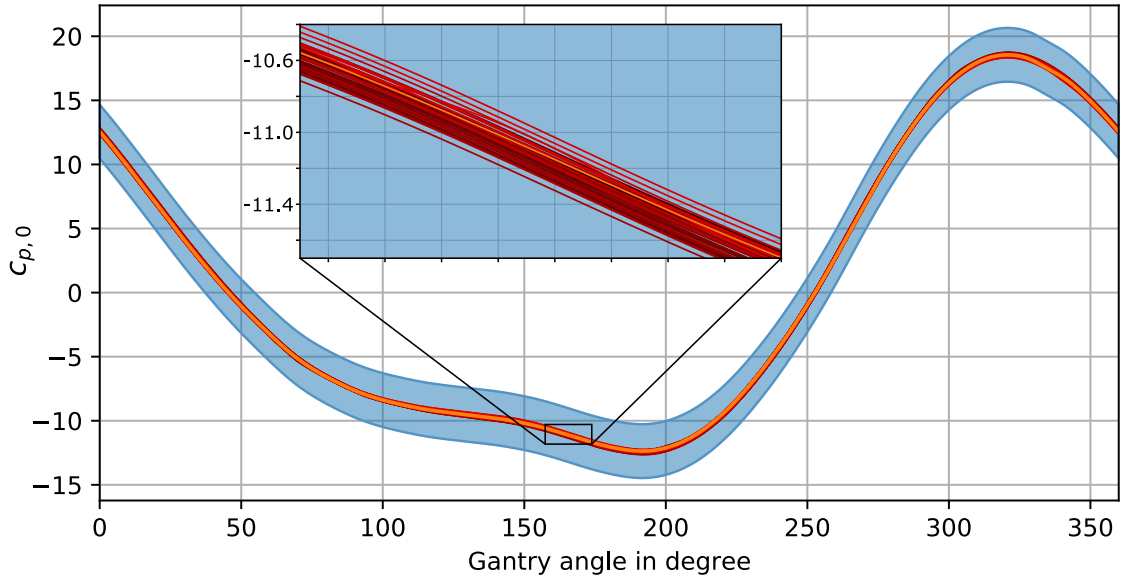

Figure 7.16: Interferometer low frequency phase variation in 50 consecutive scans in a two-minutes interval. The first scan is highlighted in orange and in blue the amplitude of the additional high-frequency variation is indicated (as observed in Figure 7.12a). The low frequency phase variation of the following 49 scans are plotted in red. Minor deviations between the scans are found which are significantly smaller than the amplitude if the high-frequency variation.

7.8 Sample Data Processing

As illustrated in Figure 7.2, the sample scan processing can be separated into two parts. An first optimization part where the free coefficients in the data model are identified and in the end virtual reference projections for the sample scan are generated. The second part is then a signal extraction which can either be based on a sliding window processing or – more sophisticated – a direct reconstruction of the three image channels using IBSIR [127], [151].

7.8.1 Reference Optimization in a Sample-Scan

In most conventional Talbot-Lau interferometer setup no reference optimization is necessary. There a sample scan can simply be converted to intensity, visibility, and phase-contrast projections and then the sample information is extracted via a flat-field correction. This means, dividing or subtracting sample and reference data in the intensity and visibility or phase channel, respectively. In the presented dark-field CT prototype, the instabilities overwhelm such an approach. Consequently, besides the sample information also all vibration induced artifacts would go into the extracted sample projections.
A more sophisticated processing approach is required which uses prior knowledge on the vibration induced artifacts from the reference scan. It assumes that the same oscillation and drifts

which have been identified in the reference data processing are also present during a sample scan. This is legit because for example, the presence of the sample does not interact with the gantry because the patient couch is completely decoupled from the rest of the imaging system. Furthermore, the results in the evaluation in Section 7.7 revealed a good scan-to-scan stability of the oscillation behavior. Therefore, it can be expected that the reference scan's correction arrays are still valid for a sample scan if the time in between is kept sufficiently short.
The reference optimization part of the sample processing uses the calibrated model from the reference scan and adapts its free coefficients to the sample scan. The measured sample data $\hat{y}_{pt}$, however, is also modified by the sample interactions which results in change of transmission, dark-field, and phase-shift signal and are denoted as T_{pt}, D_{pt}, and Φ_{pt}, respectively. This can be modeled by an additional extension of the data model from Equation (7.2) as follows:

$$y_{pt} = T_{pt} \cdot I_p \left(1 + I_{pt}^{\text{vib}}\right) \left[1 + D_{pt} \cdot V_p \left(1 + V_{pt}^{\text{vib}}\right) \cos\left(\Phi_{pt} + \phi_p + \phi_{pt}^{\text{vib}}\right)\right] \approx \hat{y}_{pt} \,. \tag{7.13}$$

While in a reference scan T_{pt} and D_{pt} are 1, and Φ_{pt} is 0 for all pixels p and times t, these parameters can only be used as a vast approximation for the start of the iterative reference optimization procedure. However, as in the initial optimization step the focus lies on exploiting sample-free regions in the projections this assumption works well.
The main challenge during the reference optimization is finding the correct free coefficients in I_{pt}^{vib}, V_{pt}^{vib}, and ϕ_{pt}^{vib} which match to the sample scan. Assuming that the vibration patterns and modes are scan-to-scan persistent the correction arrays $\mathcal{R}$ can be re-used as they are in the sample scan, but the coefficients c for each of those correction components must be recovered. In this step additional prior-knowledge can be used to speed the process up and make it more robust. For example, the low-frequency component in the coefficients is known to remain the same from scan to scan as it is not induced by vibrations, but by the gantry rotation. Thus, e.g., the coefficients for I_{pt}^{vib} can be decomposed into a low-frequency term which is known from the reference scan and a high-frequency part which must be optimized for the sample scan:

$$I_{pt}^{\text{vib}} = \sum_{k=1}^{3} c_{\text{i},kt} \mathcal{R}_{\text{i},kp} = \sum_{k=1}^{3} (c_{\text{i},kt}^{\text{lf}} + c_{\text{i},kt}^{\text{hf}}) \mathcal{R}_{\text{i},kp} \,. \tag{7.14}$$

In Figure 7.5, the $c_{\text{i},kt}$ for the three components are plotted showing the combination of high and low frequencies and in the same figure also their $c_{\text{i},kt}^{\text{lf}}$ are shown in orange, which can be generated, e.g., by low-pass filtering. The same separation of frequencies can be done for the correction patterns in the visibility and phase channel which reduces the complexity of the free coefficients in the extended sample model to $c_{\text{i},kt}^{\text{hf}}$, $c_{\text{v},kt}^{\text{hf}}$, and $c_{\text{p},kt}^{\text{hf}}$. While the exact amplitude and phase of the oscillation in these coefficients remains unknown it can be expected that they should oscillate around zero because their offset is handled by the respective low-frequency components. Consequently, as a start value during the reference optimization step the coefficients can safely be set to zero, as this should be their mean value.
Based on this extended model and the simplifications to the correction coefficients the reference optimization can be formulated as,

$$\hat{c}_{\text{i},kt}^{\text{hf}}, \hat{c}_{\text{v},kt}^{\text{hf}}, \hat{c}_{\text{p},kt}^{\text{hf}} = \underset{c_{\text{i},kt}^{\text{hf}}, c_{\text{v},kt}^{\text{hf}}, c_{\text{p},kt}^{\text{hf}}}{\arg\min} \left(\hat{y}_{pt} - y_{pt}(c_{\text{i},kt}^{\text{hf}}, c_{\text{v},kt}^{\text{hf}}, c_{\text{p},kt}^{\text{hf}})\right)^2 \,, \tag{7.15}$$

where y_{pt} denotes the model defined in Equation (7.13) with the separation of frequencies as, e.g., shown in Equation (7.14). This could also be extended by a term which regularizes the cost based on the frequencies in the coefficients or their oscillation amplitude, which should be

similar to their value during the reference scan. For initial processing this is not required and for the following discussion a least-squares optimization without regularization is used.
After the reference optimization step a unique set of per-shot coefficients for the sample scan is found and for each sample projection a corresponding virtual reference projection y_{pt}^{ref} can be generated. These can be produced by inserting the optimized per-shot coefficient into Equation (7.13) with $T_{pt} = 1$, $D_{pt} = 1$, and $\Phi_{pt} = 0$ to model the sample-free state in a reference scan. These are afterwards used during the next processing step, i.e., the extraction of the sample information from the measurement, to do a flat field correction which separates the sample's transmission, dark-field, and phase-shift signal from the interferometer background and the vibration induced artifacts.

7.8.2 Sliding Window Signal Extraction

For processing and reconstruction of the dynamic interferometer data advanced methods such as IBSIR can be used, but these are still in an early state of development. In this thesis, the focus, therefore, lies on the sliding window approach which is comparably easy to control and well understood. The following description of the sliding window working principle is taken from [136] and extended by some more details.
The sliding window signal extraction is a compromise between feasibility and performance for systems which continuously rotate [158]. While at conventional Talbot-Lau interferometer setups a stepping curve for each projection angle and detector pixel can be acquired this is not possible in the dark-field CT prototype. The compromise therefore is, to treat a set of projections as if they were a stationary stepping. This set of projections consists of several consecutively measured frames under slightly varying projection angles because the gantry rotates during the acquisition. We refer to this set as a window in the sinogram and the size of the window is the number of consecutive projections. During the sample processing each window is converted to a single intensity and visibility projection located at the center of the processed set of projections and the processing method for this decomposition can be freely chosen. At the dark-field CT prototype usually the EM as introduced in Section 2.3.5 is applied.
To minimize motion artifacts, which are caused due to change of projection angle within the window, the size of the window needs to be short. Contrary, the window should be sufficiently large to ensure good phase sampling over ideally 2π. At this point, the setup leverages the high-frequency phase variation from Figures 7.1c and 7.12 in combination with the high frame rate of the detector. The oscillation guarantees adequate phase sampling over at least 1.5π within a sufficiently small window size of only ten projections. Since at least 2400 projections are acquired during a rotation, this rather short window is covered in under 1.5°, consequently, the movement artifacts are kept small. If the intrinsic vibrations of the setup would not be in the required range, either an actuator or further stabilization of the setup would be required.
A limitation in siding window signal extraction is a loss of resolution due to the requirement to combine multiple projections to one. Even though major artifacts are avoided by using a small window, sharp edges remain difficult to recover, particularly if they are off-center. However, this drawback is accepted as the loss in resolution is rather small and spatial resolution is currently not the primary objective.
From a computational perspective, the method is advantageous because it is an extremely fast signal extraction method. It is a linear problem which can be solved analytically and highly parallelized.
In the following equations, the signal extraction procedure is demonstrated for one window at time-stamp t with a window size $2s+1$. The measured sample data within this window is given

as,

$$\hat{\boldsymbol{y}}_{p,t} = (\hat{y}_{p,t-s}, ..., \hat{y}_{p,t+s}) \ , \tag{7.16}$$

and the virtual reference projections, which were generated during the reference optimization step,

$$\boldsymbol{y}^{\mathrm{ref}}_{p,t} = \left(y^{\mathrm{ref}}_{p,t-s}, ..., y^{\mathrm{ref}}_{p,t+s}\right) \ . \tag{7.17}$$

With these inputs then the SPR, as introduced in Section 2.3.5, can be used to retrieve the intensity, visibility, and phase-shift:

$$\mathrm{SPR}(\hat{\boldsymbol{y}}_{p,t}) \rightarrow I^{\mathrm{sample}}_{pt}, V^{\mathrm{sample}}_{pt}, \phi^{\mathrm{sample}}_{pt} \ , \text{ and} \tag{7.18}$$

$$\mathrm{SPR}(\boldsymbol{y}^{\mathrm{ref}}_{p,t}) \rightarrow I^{\mathrm{ref}}_{pt}, V^{\mathrm{ref}}_{pt}, \phi^{\mathrm{ref}}_{pt} \ . \tag{7.19}$$

As a last step a flat-field correction then extracts the sample transmission T_{pt}, the dark-field D_{pt}, and the differential phase-shift Φ_{pt} by,

$$T_{pt} = \frac{I^{\mathrm{sample}}_{pt}}{I^{\mathrm{ref}}_{pt}} \ , \tag{7.20}$$

$$D_{pt} = \frac{V^{\mathrm{sample}}_{pt}}{V^{\mathrm{ref}}_{pt}} \ , \text{ and} \tag{7.21}$$

$$\Phi_{pt} = \Phi^{\mathrm{sample}}_{pt} - \Phi^{\mathrm{ref}}_{pt} \ . \tag{7.22}$$

Unfortunately these results are usually heavily corrupted by artifacts from insufficiently optimized per-shot parameters. This happens when large samples are imaged where sample-free area is rather small. Therefore, the processing must be further refined by the following step before a tomographic reconstruction is reasonable.

7.8.3 Iterative Sample Data Processing

Artifacts are caused by an insufficient convergence of the initial processing step, where the per-shot coefficients $c^{\mathrm{hf}}_{\mathrm{i},kt}$, $c^{\mathrm{hf}}_{\mathrm{v},kt}$, and $c^{\mathrm{hf}}_{\mathrm{p},kt}$ have been modeled under the assumption that the sample influence on the scan can be ignored. Back then, the assumption that T_{pt} and D_{pt} are 1, and Φ_{pt} is 0 for all pixels and times was justified as no better information was available, but after the first pass through reference optimization and sliding window signal extraction a better guess is available.

It turned out that particularly the transmission channel has a dominant influence on the convergence of the reference processing step. Since this channel happens to be one with the least artifacts after the signal extraction, the reference optimization step is repeated starting with the optimized parameters $c^{\mathrm{hf}}_{\mathrm{i},kt}$, $c^{\mathrm{hf}}_{\mathrm{v},kt}$, and $c^{\mathrm{hf}}_{\mathrm{p},kt}$, and the updated T_{pt} from the sliding window signal extraction, but with unchanged $D_{pt} = 1$ and $\Phi_{pt} = 0$. This reference optimization now converges to a better solution than during the first iteration because most of the sample attenuation is now included in the data model. Consequently, the second run of the sliding window signal extraction, with the updated virtual reference projections, leads to significantly reduced artifacts.

This process can be repeated for several more iterations until the update between two iterations vanishes. To further optimize this iterative approach the artifacts, which might be present in the produced T_{pt}, can be reduced before the next iteration starts. One simple option is to blur the artifacts with, e.g., a median filter along the t-axis in the sinogram. The t-axis is the vertical axis, i.e., projection number, in Figure 7.17. This works particularly well for

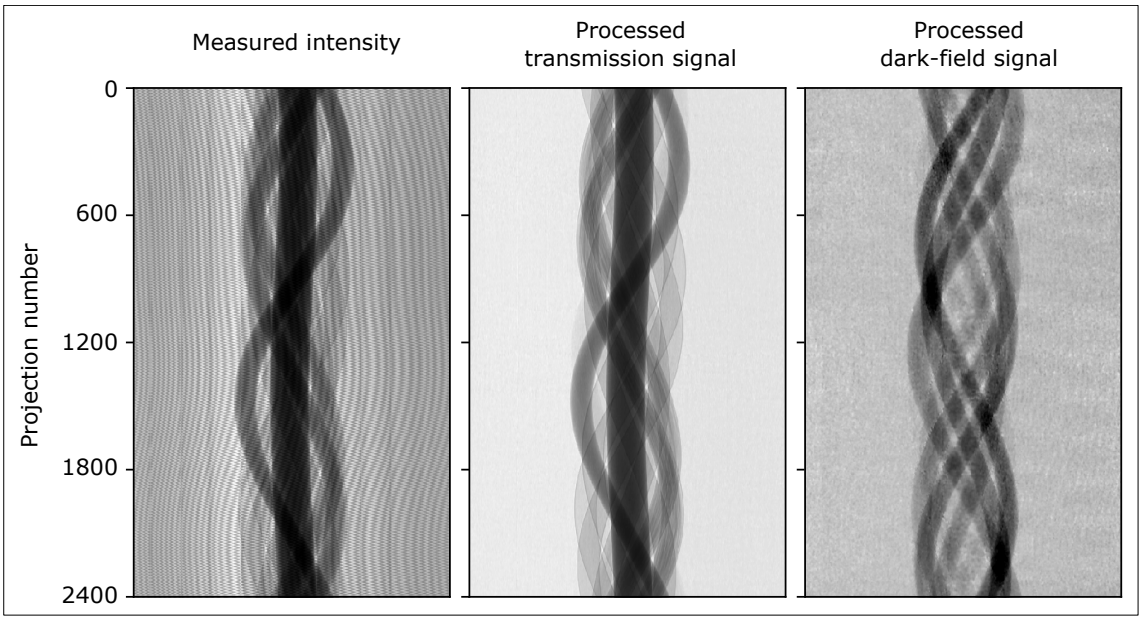

Figure 7.17: Raw data sinogram and the results after processing. In the raw data clearly the Moiré fringe pattern and the sample attenuation in the center can be seen. After the processing the attenuation and the small-angle scattering, i.e., dark-field, have been separated into two channels. The most central object caused attenuation only, but no dark-field, as it is only apparent in the attenuation image as a broad vertical line. It is not found in the dark-field sinogram. Tomographic reconstruction images of these sinograms are shown in Figure 7.18. Image adapted from [136] CC BY.

all artifacts related to the interferometer phase changes which change at a comparably high frequency. Low-frequency changes in the sinogram, such as the sample or slowly changing artifacts, remain almost unaffected by the filter. Additionally, also the most corrupted areas can be identified and weighed down during the reference optimization by extending it to a weighted least squares problem.

More information on the sample processing pipeline can be found in the Master's thesis by Haeusele [42]. There particularly the correlations between the various coefficients are further exploited to achieve a better regularization during the reference optimization step. Furthermore, [44] discusses how the processing makes use of the high-frequency oscillation.

The sample processing pipeline as presented here is used for all datasets shown throughout this thesis. Naturally, the pipeline is continuously optimized and regularly undergoes far-reaching conceptional changes. For example, in an upcoming paper by Haeusele et al. [43] an advanced sample processing approach will be introduced.

With these optimizations only two to three iterations of the sample data processing pipeline are necessary before an almost artifact-free reconstruction of the sample is possible. Example results of the sample processing are presented in Figure 7.17 where the input raw data and the corresponding final attenuation and dark-field channels are shown.

These sinograms can then be reconstructed via, e.g., filtered backprojection to a tomographic image of the examined object as shown in Figure 7.18. This has been briefly introduced in Section 2.4.2. An important step in the data processing pipeline is a beam hardening correction which must be applied to compensate for an overestimation of the linear diffusion coefficient in the reconstructed image. This correction is already included in the results shown in the Figures 7.17 and 7.18, and is introduced in the following section.

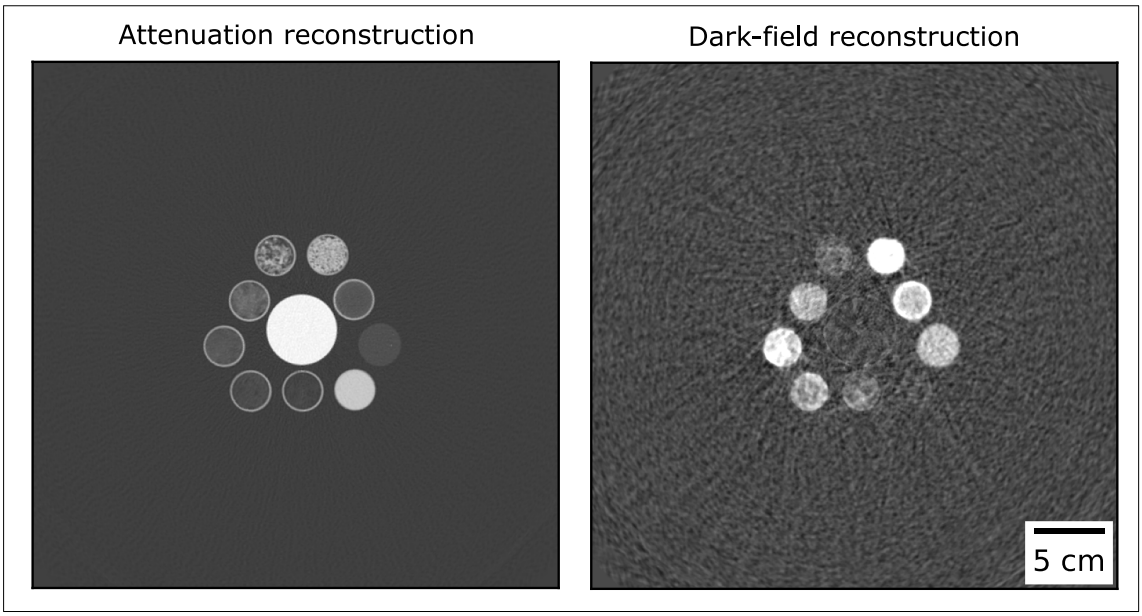

Figure 7.18: Reconstruction results for the sinograms shown in Figure 7.17. Filtered backprojection with a ramp-filter has been used for tomographic reconstruction. In the dark-field channel a beam hardening correction as will be introduced in Section 7.9 has been applied.

7.9 Beam Hardening in Dark-field CT

One of the most common artifacts in conventional clinical CT is beam hardening. It is caused by the poly-chromatic X-ray spectrum and the energy dependent attenuation in the sample [57] and can lead to an underestimation of the sample's attenuation coefficient. Since the visibility of the Talbot-Lau interferometer is also energy-dependent, there is a similar effect which can create an artificial dark-field signal even when no small-angle scattering took place [155]. Additionally, there is analogous to attenuation imaging also an energy dependency of the small-angle scattering in the sample [72], [36] and the effect of visibility hardening, as described in [23]. Most dominant in the prototype system, however, is the beam hardening effect caused by energy-dependent performance of the interferometer which is corrected by the following approach. This has already been observed in Section 5.6.6, where visibility spectra and changes in the X-ray power spectrum have been analyzed. Most dominant is there the impact of the energy dependent stopping power of the absorption gratings G_0 and G_2. It leads to a performance minimum below 80 keV, caused by the K-edge of gold, which is the absorber material in the gratings. The section has previously been published in [139] and is here extended by some further details.

In the attenuation channel beam hardening leads to an underestimation of the sample's attenuation coefficient. Contrary, in the dark-field channel it can lead to an overestimation of the linear diffusion coefficient, i.e., a signal which is not caused by small-angle scattering. This behavior can be seen in the tomographic reconstruction in Figure 7.19a. A phantom consisting of a polyoxymethylene (POM) cylinder with 100 mm diameter in the center and a surrounding 25 mm thick ring of neoprene is shown. While the neoprene has a porous structure which leads to small-angle scattering and thus to a dark-field signal, the homogenous POM should not produce any dark-field signal as it does not generate any small-angle scattering. Contrary, without any correction a significant linear diffusion coefficient is reconstructed for the POM cylinder, as can also be seen in the line plot in Figure 7.19c.

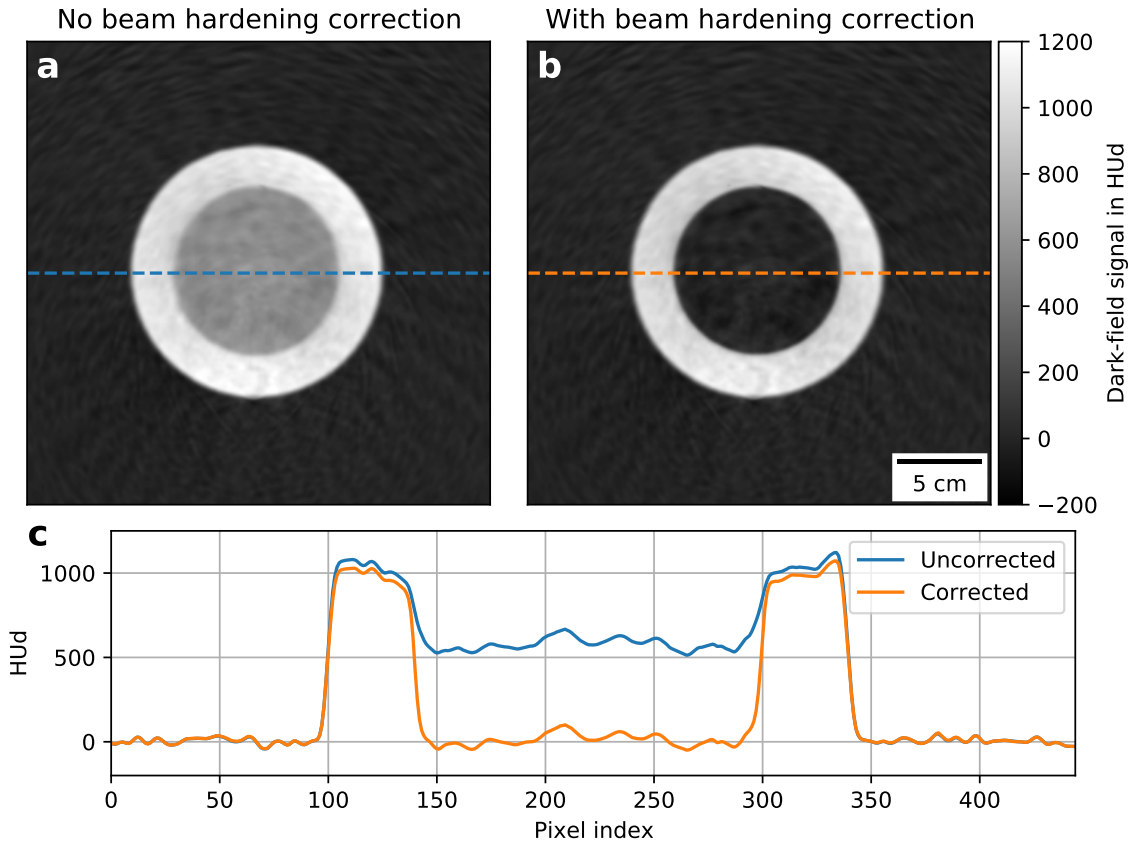

Figure 7.19: Dark-field signal reconstruction before and after beam hardening correction. The phantom consists of two materials; a POM cylinder which only attenuates and a neoprene ring which also generates a dark-field signal. **a,** Without any beam hardening correction a strong dark-field signal is reconstructed for the POM cylinder. **b,** After applying the correction the POM cylinder has no dark-field signal and only the signal of the neoprene ring remains. **c,** The line plot through the reconstruction images demonstrates how the POM cylinder signal is corrected.
Image adapted from [139] CC BY.

We can illustrate this behavior in Figure 7.20 where different POM sample thicknesses are used as spectral filters in a simulation of the interferometer performance, which has been used several times throughout Chapter 5. We find that while measured intensity varies as expected for the different POM thicknesses also a relative visibility reduction appears which is caused by the hardening of the spectrum and not by any small-angle scattering. As an approximation, the relation between measured attenuation and this hardening induced relative visibility reduction can be fitted linearly, which allows us to implement a simple yet effective beam hardening correction.
The proposed correction is similar to previous work by [155], [89], but easier to calibrate because it is based on either the aforementioned simulation in Figure 7.20 or a calibration scan of a non small-angle scattering object such as water or POM. The measured relative visibility reduction,

$$\frac{V}{V_{\text{ref}}} = D_{\text{meas}} \,, \tag{7.23}$$

is treated as a combination of the visibility reduction D_{cor} induced by small-angle scattering and a component $f(T_{\text{meas}})$ from beam hardening. The latter depends on the transmission

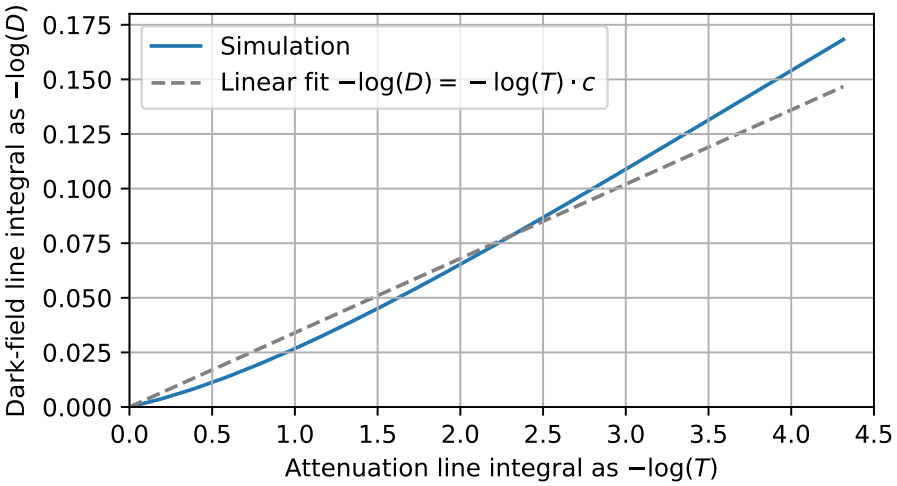

Figure 7.20: Simulation results of beam hardening induced relative visibility reduction, which would lead to a reconstruction of an overestimation of the linear diffusion coefficient. Filtration from different thicknesses of POM samples are simulated, and the resulting -log of the attenuation signal is plotted against the -log of the relative visibility reduction. The retrieved relative visibility reduction comes from hardening effects and does not represent small-angle scattering in the sample. We apply a correction based on the indicated linear fit to reduce the beam hardening in the tomographic reconstruction. Image adapted from [139] CC BY.

$I/I_{\text{ref}} = T_{\text{meas}}$ and hence on the attenuation induced by the sample,

$$D_{\text{meas}} = D_{\text{cor}} \cdot f(T_{\text{meas}}) \; . \tag{7.24}$$

From calibration data as plotted in Figure 7.20 and by implying that the examined sample material should not generate any small-angle scattering, i.e., no visibility reduction and consequently $D_{\text{cor}} = 1$, we can find a correction function based on the linear approximation in the log-log-plot,

$$D_{\text{meas}} = \underbrace{D_{\text{cor}}}_{=1} \cdot f(T_{\text{meas}}) = (T_{\text{meas}})^c \; . \tag{7.25}$$

The calibration factor c can be extracted from a test measurement and is afterwards used to correct sample scans, by applying:

$$D_{\text{cor}} = D_{\text{meas}} \cdot (T_{\text{meas}})^{-c} \; . \tag{7.26}$$

In the prototype system, this calibration factor is a global value for all detector pixels and constant for all scans. Only after changes to the grating configuration or the X-ray spectrum, a new calibration is required.
After the beam hardening correction is applied, only the visibility reduction related to small-angle scattering in the material should remain as D_{cor}. Since the method is calibrated to one material, strongly attenuating materials such as bones can cause artifacts and will require development of a more refined method. For first tomographic reconstructions, however, this single material approach is sufficient because it corrects the overestimation of linear diffusion coefficient and there are no beam hardening related artifacts remaining, as can be seen in the reconstruction results in, e.g., Figures 7.18 or 7.19. Consequently, for now, no further beam hardening corrections are applied to the data for all presented dark-field CT scans in this thesis.

7.10 Tomography Resolution Analysis

The spatial resolution is a crucial feature of CT in clinical routine, and typically is around 10 lp/cm for state-of-the-art CT scanners in the clinics [142]. At the presented dark-field CT, due to the modifications and the extension of the processing currently some restrictions limit the spatial resolution. The section has previously been published in [139] and is here extended by some further details.
In most clinical CT machines, a flying focal spot alternates between slightly displaced source positions for every projection and is used to increase the spatial resolution of the reconstruction [62]. This feature has been deactivated in the presented implementation, and instead a stationary X-ray focal spot is used for maximum stability and to simplify data processing. With an adapted processing, i.e., separate for each focal spot position, dark-field CT with flying focal spot should be feasible, but for now, this simplification comes at the cost of spatial resolution. A significant resolution loss is expected from the processing because it is based on sliding-window signal extraction. As has been described in Section 7.8.2, several consecutive projections are combined to one projection under the assumption that the sample movement is

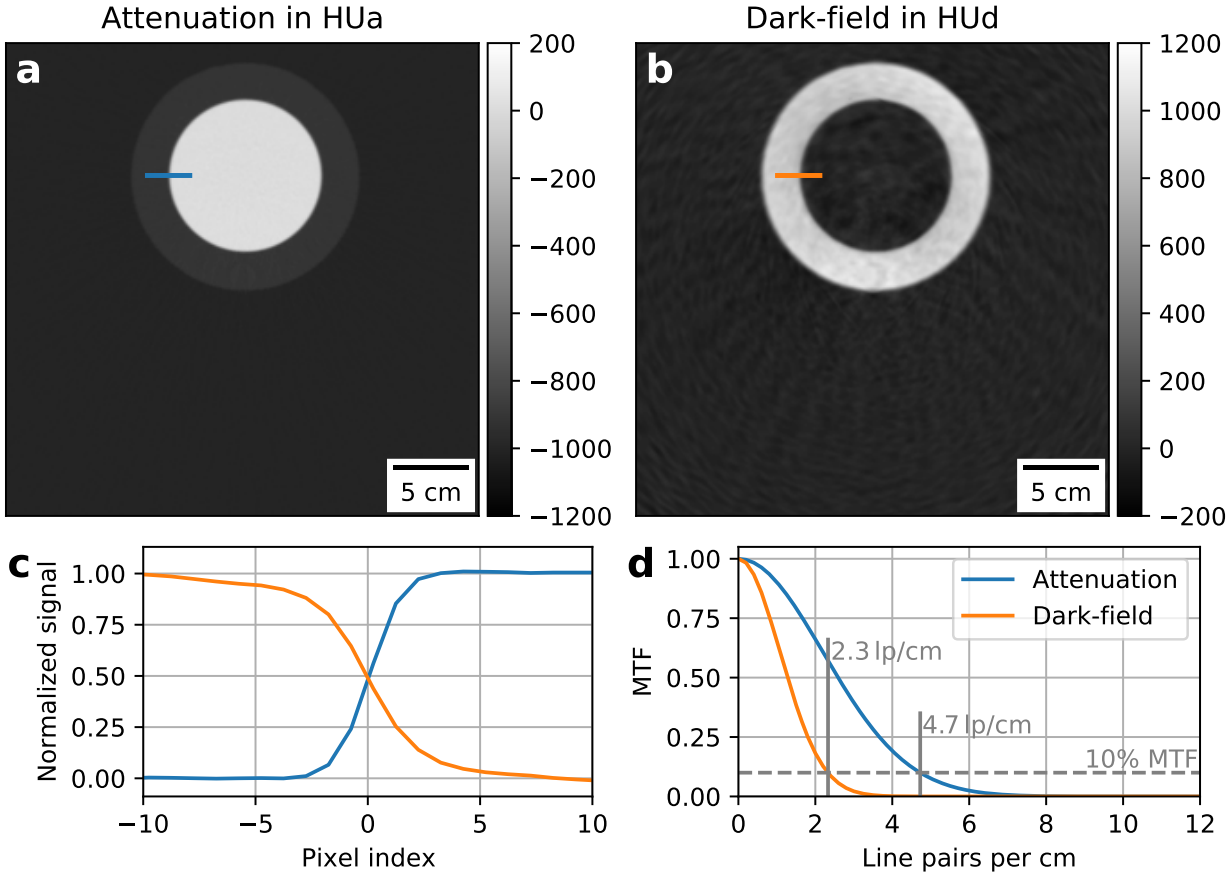

Figure 7.21: Attenuation and dark-field reconstruction resolution analysis. The test sample is positioned 6.5 cm above the iso-center. **a** and **b,** Reconstructions of a neoprene and POM cylinder phantom in attenuation and dark-field, respectively. **c,** The edge spread is analyzed at sharp interfaces in the image highlighted by the line plot in a and b. The values are normalized for better visualization. **d,** The modulation transfer function (MTF) in the two modalities shows that attenuation reaches a resolution of 4.7 lp/cm while the dark-field is less sharply reconstructed with 2.3 lp/cm, both at 10% of the MTF. Image adapted from [139] CC BY.

insignificant [158]. The ignored movement, caused by the system rotation, within a set of projections introduces motion artifacts in the transmission and dark-field signal and leads to a blurring of the reconstructed image. Furthermore, a weighted median filter is applied on the dark-field channel in projection-space, which also lowers the spatial resolution [56]. This filter is adaptive to the count rate and helps to avoid artifacts when X-ray flux is low, e.g., in low-dose scans or when strongly attenuating samples are examined. In these cases, the extraction of the dark-field signal at low count-rate otherwise can become biased and unstable [60].
To analyze the effective image resolution of the presented dark-field CT, we use the filtered back-projection reconstruction of the previously introduced POM and neoprene cylinder phantom. The POM cylider is 100 mm in diameter and the outer diameter of the neoprene ring is 150 mm. The object has been positioned 6.5 cm shifted above the iso-center as can be seen in the reconstruction images shown in Figure 7.21. By this displacement, the blurring effect due to movement artifacts in the sliding window processing is included. This contribution would vanish if the cylindrical objects were placed in the iso-center because then they would appear stationary in the sinogram and in the sliding windows. This scan was measured with 1 s rotation period, 80 kVp, and 300 mA tube current, i.e., at a comparably low radiation dose (see Section 7.11) and a ramp filter is used during the reconstruction. From the sharpness of the

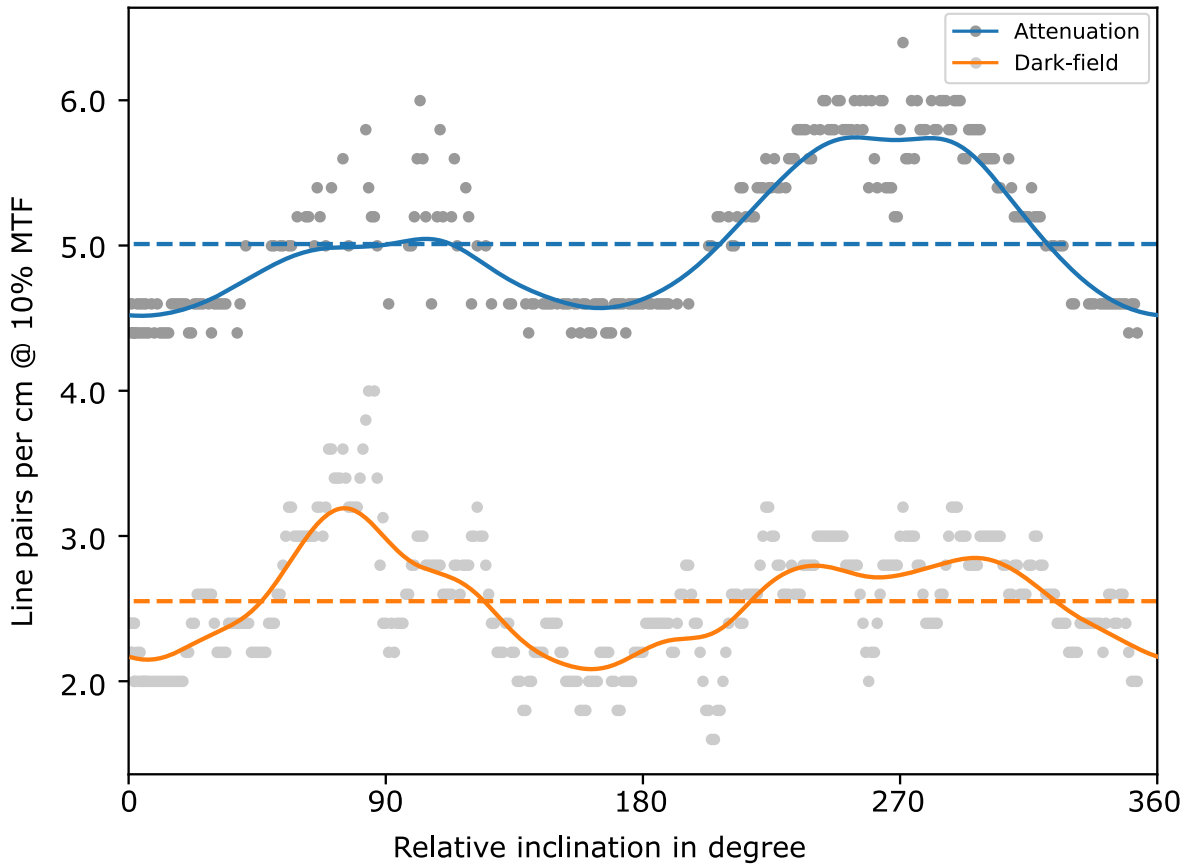

Figure 7.22: Extended resolution analysis. The interface between POM and neoprene is evaluated starting at the line as indicated in Figure 7.21 continuing clockwise. The resolution is relatively stable around the mean values 5.0 lp/cm and 2.6 lp/cm for the attenuation and dark-field channel, respectively. Highest resolution is found for 270°, i.e., where the interface is closest to the iso-center, in the attenuation image. The dark-field resolution results are dominated by noise obscuring any distinct position dependence. The gray dots represent the evaluated values while the colored lines represent running average values.

interface between POM and neoprene, the edge spread function and subsequently the modulation transfer function (MTF) as a measure for the resolution is extracted. The evaluation in Figure 7.21 reveals that in the attenuation image the MTF drops to 10% at 4.7 lp/cm and in the dark-field channel the drop is already at 2.3 lp/cm.
To increase the significance of this analysis also the rest of the POM and neoprene interface is evaluated for the MTF. The results are plotted in Figure 7.22 where the x-axis represents the angle of the evaluated line relative to the highlighted line in the initial evaluation increasing clock-wise. These results reveal some change of resolution along the edge of the test object. For example, the sharpest reconstruction of the edge is found at around 270°, i.e., where the interface is closest to the iso-center. The worst resolution is found for 0° and 180°, i.e., the position evaluated in Figure 7.21 and its mirrored counterpart. This is most evident in the attenuation channel because in the dark-field channel the results are too noisy for such differentiation. There the results are dominated by outliers from the streak-like artifacts in the dark-field image which interfere with the MTF analysis.
Overall, however, the results are relatively stable with a mean resolution of 5.0 lp/cm in the attenuation channel and 2.6 lp/cm in the dark-field reconstruction, using the 10% MTF-cutoff as a resolution measure. The increase of the resolution towards the center can be explained as there the movement of the object within the sliding window is smallest and thus less blurring of the projections occurs. The initially stated 4.7 lp/cm and 2.3 lp/cm for the attenuation and dark-field reconstruction, respectively, are conservative values based on the most blurred interfaces in this test object evaluation.
Besides the clear resolution difference between the two image channels also a notably lower resolution compared to state-of-the-art clinical CT is found. Reasons for the loss of resolution are the missing flying focal spot and the blurring induced by the sliding-window signal extraction which neglects the system rotation. For the dark-field channel additionally the use of a weighted median filter reduces the sharpness of the reconstruction and the increased noise-level also limits the resolution. Nevertheless, the resolution is in the same magnitude as state-of-the-art clinical CT imaging and particularly for the dark-field channel it is not of highest priority in the prototype dark-field CT system.

7.11 Dose Evaluation

For clinical relevance of the presented dark-field CT system, the applied patient dose level must be in a reasonable range. In clinical CT this is measured by the computed tomography dose index $\mathrm{CTDI_{vol}}$ which is the dose applied to a patient to scan one tomography slice. In clinical practice, chest CT protocols have a wide range of applicable $\mathrm{CTDI_{vol}}$ values. They can range from 4 mGy up to 10 mGy [1]. Obviously, lower values are preferred to minimize exposure to ionizing radiation for the patient. The lower limit usually os given by the patient size and the demand for a good signal-to-noise ratio.
In this section, the $\mathrm{CTDI_{vol}}$ values for the dark-field CT prototype are measured for axial scans with 80 kVp spectrum. The results then allow a comparison to the dose range of conventional chest CT protocols. Parts of this section have previously been published in [139] and are here extended by further details.
To analyze the radiation exposition of the patient, the constancy test protocol as defined in [59] is applied. The evaluation uses a standard body phantom of 32 cm diameter and a calibrated dosimeter (NOMEX, PTW, Germany, [84]). The procedure consists of several dose measurements with the probe being placed at different positions in the body phantom. The phantom and dosimeter, inserted at the central position, is shown in Figure 7.23.

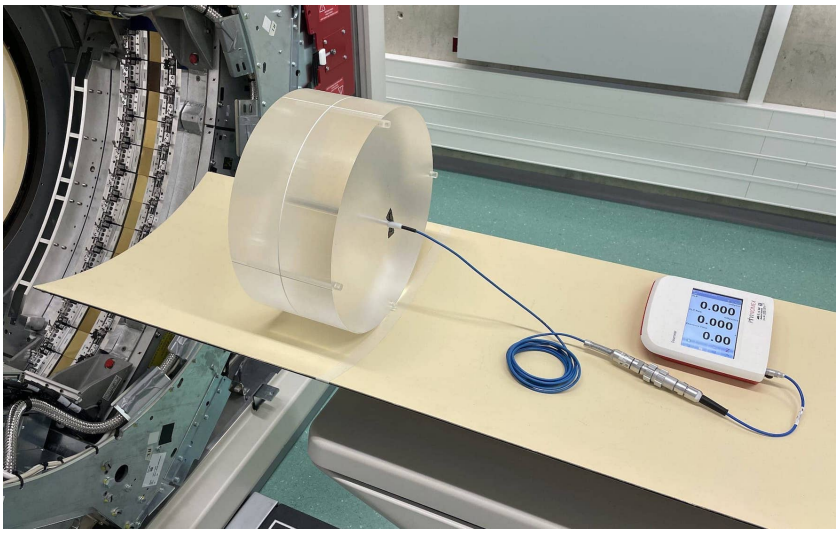

Figure 7.23: Dose evaluation setup. A 32 cm diameter standard body phantom with five ports to insert the dosimeter probe is placed on the couch of the CT. For each position of the probe in the phantom a CT scan is measured and the dose values are combined as defined in [59]. This yields the $CTDI_{vol}$ for the reconfigured scan mode in mGy.

The evaluation revealed that for a scanner setting of 80 kVp and 400 mAs the $CTDI_{vol}$ is 5.38 mGy. A conventional iCT system, without any modifications for dark-field imaging, has at the same settings a $CTDI_{vol}$ of about 9.2 mGy. The reduction of the $CTDI_{vol}$ by about 40% is caused by the absorbed X-ray flux in G_0 and G_1 of the dark-field CT implementation. Consequently, this dark-field CT must be operated at 70% higher mAs settings than a conventional CT system to apply the same X-ray dose to the patient.
Another aspect which must be considered is the influence of G_2 which does not change the $CTDI_{vol}$ but has an influence on the signal-to-noise ratio. Even when $CTDI_{vol}$ are matched a lower signal-to-noise ratio must be expected for the dark-field CT due to the absorption in G_2. It reduces the dose reaching the detector and hence reduces statistics and increases noise in the reconstructed images. This must be considered as a trade-off for being able to retrieve a dark-field CT which provides two different image modalities.
The first published dark-field CT results of a human-sized anthropomorphic body phantom in [136] were measured with a $CTDI_{vol}$ of 7.4 mGy. This corresponds to the scanner settings 80 kVp and 550 mAs, which is the maximum dose that can be applied at 1 s rotation period, 80 kVp, and with the small X-ray focal spot. With the 1.5 s rotation period a higher $CTDI_{vol}$ of about 11.1 mGy can be achieved, which is the maximum dose that can be applied with the dark-field CT system at 80 kVp with the small focal spot.
To demonstrate that dark-field CT works well within the suggested dose index range, a scan with a $CTDI_{vol}$ of only 4.0 mGy has been measured. This corresponds to scanner settings of 80 kVp and 300 mAs with the small focal spot. For this experiment, an anthropomorphic body phantom with a neoprene insert has been scanned. The resulting dark-field CT reconstruction is shown in Figure 7.24. Due to the low X-ray flux in this scan, a strong noise reduction via the adaptive filter in the dark-field channel is required. This leads to a lower resolution in the dark-field channel which is in accordance with the previous discussion in Section 7.10. Nevertheless, the spacial resolution in the dark-field channel is sufficient, e.g., the individual tubes can easily be resolved. For medical imaging we expect that the lower resolution is acceptable and can still provide diagnostic value. As the dark-field signal is sensitive to sub-resolution structures it does not require a high spatial resolution. Moreover, results from previous studies with mice suggest that lung-diseases mostly lead to dark-field signal decrease on a rather large feature size.
This evaluation demonstrates that dark-field CT at 80 kVp is feasible within the full suggested dose range between 4 mGy up to 10 mGy [1] for chest CT. However, for large patients, where

an even higher $CTDI_{vol}$ is required, this can only be realized by slow rotation speeds. This can become an issue when not only a single axial scan, i.e., a single rotation of the gantry, is measured. For helical scans multiple rotations are required and depending on the pitch, i.e., coverage per turn, a slow rotation speed can lead to significant scan times.
Faster scans at constant $CTDI_{vol}$ can only be achieved with an X-ray source which generates more flux. Unfortunately state-of-the-art clinical CT tubes are already among the most powerful tubes and there is no trivial tube upgrade available. The only option is to stitch to a higher acceleration voltage or a larger X-ray focal spot size, which both generate more X-ray flux. For example, using 100 kVp or 120 kVp instead of 80 kVp would be a solution to significantly increase the X-ray flux without any changes to the tube. The evaluation in Section 5.6.7 demonstrated that a change to, e.g., 120 kVp, is possible but requires some optimization of the interferometer. Either an adapted G_1 for the 120 kVp spectrum or an absorption G_1 design must be implemented. While the former should lead to similar $CTDI_{vol}$ values as presented for the 80 kVp implementation, the latter design would deviate strongly. In an absorption G_1 design, two absorption gratings are positioned before the patient instead of only one, which leads to a much larger loss of X-ray flux. To achieve the same $CTDI_{vol}$ as a conventional CT machine, it is expected that an increase of the mAs by up to 300% would be required. This might again limit the available scan speeds. Another option is to use the large instead of the small focal spot of the X-ray tube. This allows to generate more radiation, also at 80 kVp, but comes with drawbacks related to the X-ray source spot size. It is expected that source-size induced shadowing from the G_0 acceptance increases and also issues from fabrication tolerance can become visible. One can conclude that there is demand for higher X-ray flux tubes with small X-ray source spots to allow more flexible scan configurations for clinical dark-field CT. Nevertheless, decent results can already be produced with current state-of-the-art CT X-ray sources. These only come with a minor restriction to small coverage when large patient sizes require an increased $CTDI_{vol}$.

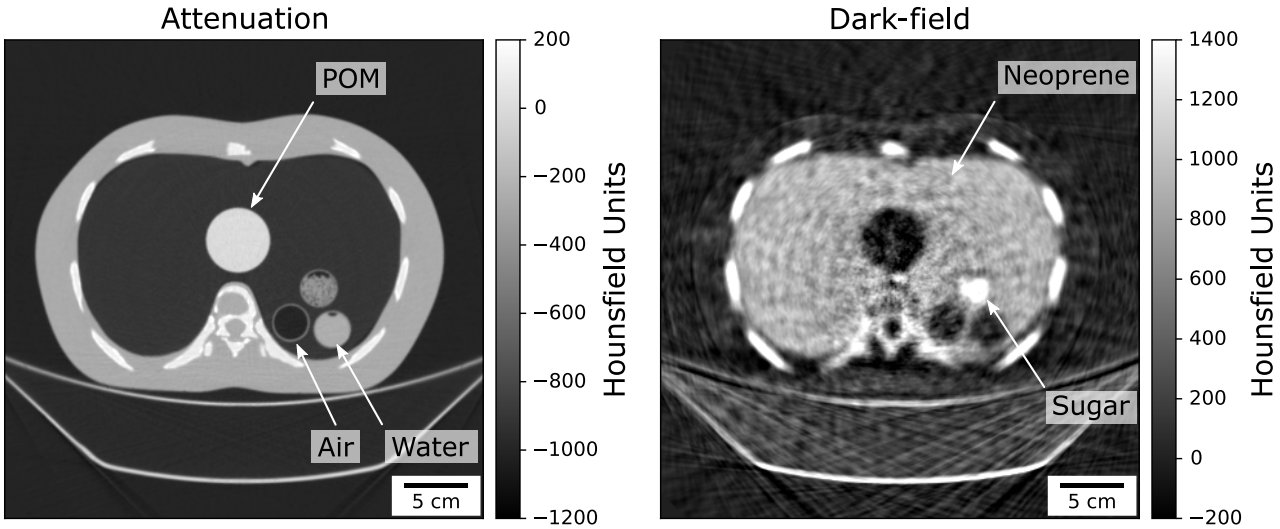

Figure 7.24: Dark-field CT scan with a $CTDI_{vol}$ of only 4.0 mGy. As a sample, an anthropomorphic body phantom with a neoprene insert is scanned at 80 kVp, 300 mAs, and with 1 s rotation period. The resolution in the dark-field channel suffers from strong filtering, but is expected to be sufficient to identify dark-field-signal changes for diagnostics of lung disease. Image adapted from [139] CC BY.

7.12 Dark-field CT Results

To demonstrate the performance and illustrate the capabilities of the dark-field CT system on a clinical scale, several test samples have been developed and scanned. These experiments also include an evaluation based on a ventilated ex-vivo pork lung to investigate the imaging performance for lung tissue. These results allow to identify remaining problems which must be solved in future work. Furthermore, these results can be used to assess the dark-field CT prototype's performance in an initial clinical patient study. Some of the following results have previously been presented in [136], [139], [40].

7.12.1 Cylinder Phantom

To assess the quantitative performance of this first human-scale dark-field CT system, a phantom composed of different materials in plastic tubes is used. A photo of the sample is shown in Figure 7.25. It consists of a 50 mm diameter cylinder made of polyoxymethylene (POM) and nine 30 mm diameter cylinders which are filled with various materials. The scan configuration has been 80 kVp, 550 mAs, and 1 s rotation period. This equals a $CTDI_{vol}$ of 7.4 mGy. These results have previously been published in [136].
The left two panels in Figure 7.25 show the tomographic reconstruction images of the attenuation and dark-field channels. The beam-hardening correction, as introduced in Section 7.9, has been applied during the reconstruction. As gray scale the respective Hounsfield units, introduced in Section 2.4.3, are used.
This scan results demonstrate the advantages dark-field imaging unlocks, as it enables enhanced material identification by combining information from attenuation and the dark-field channel. For example, it is easily possible to differentiate the two top-most cylinders, which have almost identical HUa values, in the dark-field channel. Powdered sugar, as an extremely porous ma-

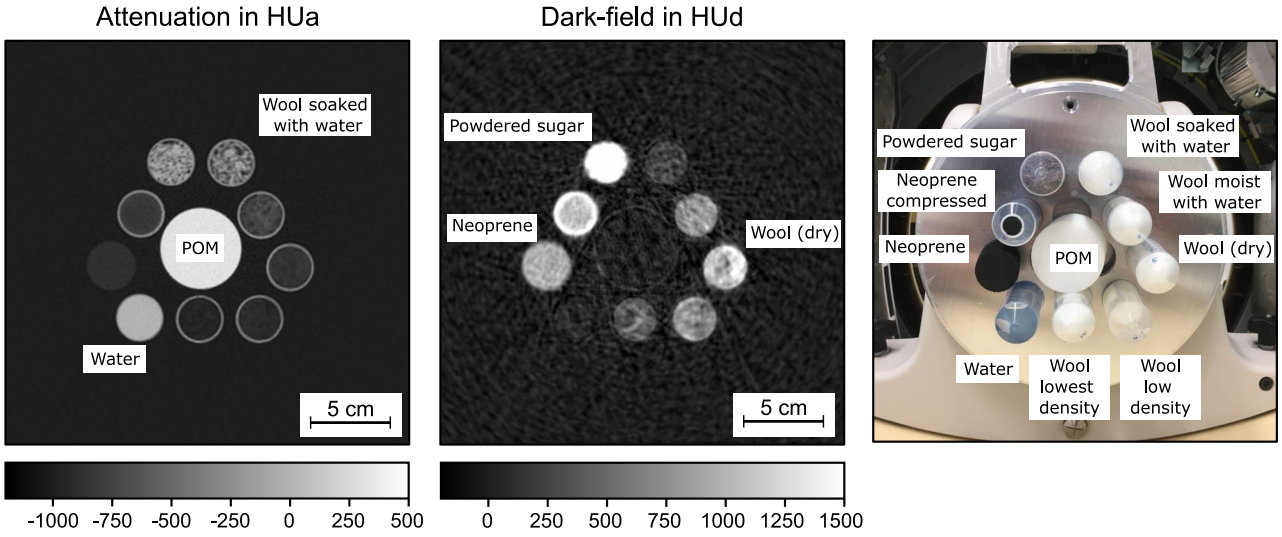

Figure 7.25: Cylinder test sample for attenuation and dark-field CT. One 50 mm diameter POM cylinder and nine 30 mm diameter tubes filled with various materials, as labeled in the photograph of the sample on the right. The CT scan was acquired with 80 kVp, 550 mAs, and 1 s rotation period. During the reconstruction of the dark-field channel the beam-hardening correction has been applied. An isotropic voxel-size of 0.62 mm is reconstructed, hence, the slice thickness of the reconstruction is 0.62 mm. Image adapted from [136] CC BY.

terial, leads to a strong small-angle scattering signal, whereas wool soaked with water leads to almost no dark-field signal. This is because the water closes the interfaces between wool fibers and air, consequently, fewer small-angle scattering occurs in wool soaked with water.
When water content in the wool filled cylinders decreases, i.e., in the tree upper right tubes, the dark-field increases because the water no longer fills all the gaps between the wool fibers. Simultaneously, the attenuation decreases, as wool attenuates rather weakly compared to water. All the tubes on the upper right have been filled with the same amount of cotton wool and are compressed to the same volume to ensure consistent results.
In the bottom row, two tubes with less wool and consequently lower density have been prepared without adding any water, and in both channels the decrease is visible. While in the attenuation channel the reduction of attenuating material causes the decrease, in the dark-field channel we see that the density of small-angle scattering fibers reduces. In the water-filled tube and the POM cylinder no dark-field signal is reconstructed because these homogeneous materials produce no small-angle scattering. These materials, however, are clearly visible in the attenuation image and can be differentiated by their unique attenuation coefficients.
In the remaining two cylinder positions on the left are neoprene foam samples. Both neoprene cylinders are of the same size and material, but one of the neoprene cylinders has been inserted into a plastic tube and thereby got compressed. This compression of the outermost parts of the cylinder is well visible in the dark-field channel as a white ring. In the attenuation image, this deformation of the neoprene is not visible because compression of the low-density neoprene foam only slightly increases its density.
The experiments with this phantom demonstrated that the combination of attenuation and dark-field contrast allows superior material differentiation, particularly when porous structures are involved. This allows to retrieve more information about the sample which otherwise remains inaccessible in conventional attenuation imaging.
Cotton wool is a suitable material to quickly generate test materials of varying porosity but comes with the drawback that it is difficult to ensure a homogeneous result. For example, in the 'Wool (dry)' tube in Figure 7.25, significant variations are visible. Furthermore, compression and adding moisturizing it is complicated and not stable over time because the water diffuses over time and evaporates. A suitable alternative is neoprene foam because it is very homogeneous and more stable. This allows reproducible results and as it is a readily available material it can also be used for calibration of the dark-field CT.

7.12.2 Human Thorax Phantom

For clinical application the capability of reconstructing large sample sizes is important. To evaluate the system regarding clinical application for chest CT an anthropomorphic thorax phantom is employed as a sample. It is based on a commercially available product (Lungman, Kyoto Kagaku, Tokyo, Japan [83]) which accurately models the attenuating properties of a human chest torso. It resembles an adult male chest torso with a girth of 94 cm and is shown in the photograph in Figure 7.26.
Since this Lungman phantom has been developed for conventional CT, it does not model the porous structure of the lung tissue. To use the phantom for test measurements at the dark-field CT, a suitable lung insert is required which models the small angle-scattering behavior of lung tissue. This can be achieved with neoprene inserts which have a similar porosity as healthy lung tissue [124]. In the custom-made neoprene inserts, shown in Figure 7.26, four cylinders with different materials can be inserted. The central one is a POM cylinder that represents additional attenuation by parts of the heart. The other three smaller cylinders are the same as

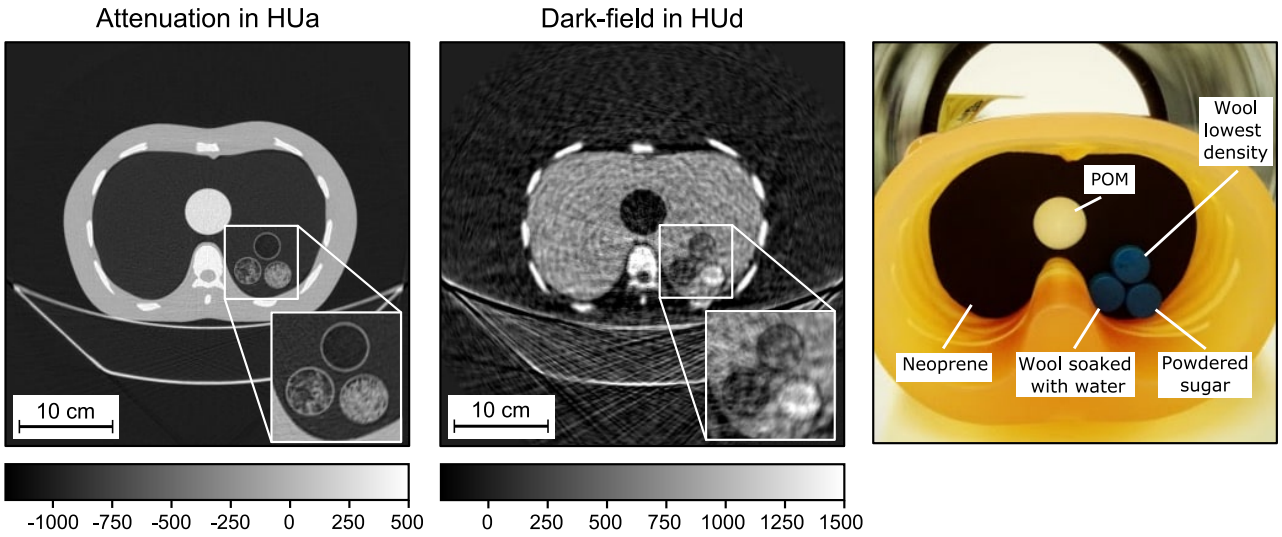

Figure 7.26: Dark-field CT results of Lungman phantom with neoprene insert and test material cylinders. The inside of the chest phantom is filled with a black colored neoprene insert, which resembles similar small-angle scattering as lung tissue. A 50 mm diameter POM cylinder and smaller tubes filled with various materials are also placed in the test sample. They demonstrate that material differentiation by combining the two image contrast channels is also feasible when a human sized object is imaged. The CT scan was acquired with 80 kVp, 550 mAs, and 1 s rotation period. During the reconstruction of the dark-field channel the beam-hardening correction has been applied. An isotropic voxel-size of 0.62 mm is reconstructed, hence, the slice thickness of the reconstruction is 0.62 mm. Image adapted from [136] CC BY.

used in the cylinder phantom, evaluated in Section 7.12.1, and are filled with powdered sugar, or cotton wool. One tube is filled with moist cotton wool, and the other one with only a small amount of cotton wool, which leads to a low density.
In the reconstruction images also the couch of the CT is visible on which the Lungman phantom is placed. The surface of the couch is made of an attenuating and small-angle scattering material, and its infill is weakly attenuating and creates some dark-field signal. The sharp edges of the couch outline and its size lead to streak artifacts, particularly, in the dark-field channel. Fortunately, the streaks mostly do not affect the sample and these streaks can therefore be accepted.
The reconstruction of the Lungman phantom in the attenuation channel primarily shows the bones, i.e., ribs and spine, and the soft tissue in between. Furthermore, the POM cylinder in the center and the three tubes are clearly visible. Again, differentiation between the wet cotton wool filled tube and the powdered sugar becomes trivial when information about the tube's small-angle scattering property is considered from the dark-field channel.
As previously found in the resolution evaluation in Section 7.10 the attenuation image is reconstructed sharper than the dark-field image. Nevertheless, sufficient resolution is achieved in the dark-field to clearly differentiate the falcon tubes and resolve the interfaces between the different materials. This scan has been measured with 80 kVp, 550 mAs, and 1 s rotation period which leads to a $CTDI_{vol}$ of 7.4 mGy. Consequently, almost twice as much X-ray dose as in the similar scan shown in Figure 7.24 is applied here. This leads to a sharper reconstruction with lower noise, which is particularly visible in the dark-field channel. The higher $CTDI_{vol}$ of 7.4 mGy, however, would still be adequate for clinical human chest CT, which should range between 4 and 10 mGy.
A characteristic mid-frequency noise-like pattern is visible in the dark-field reconstructions. It

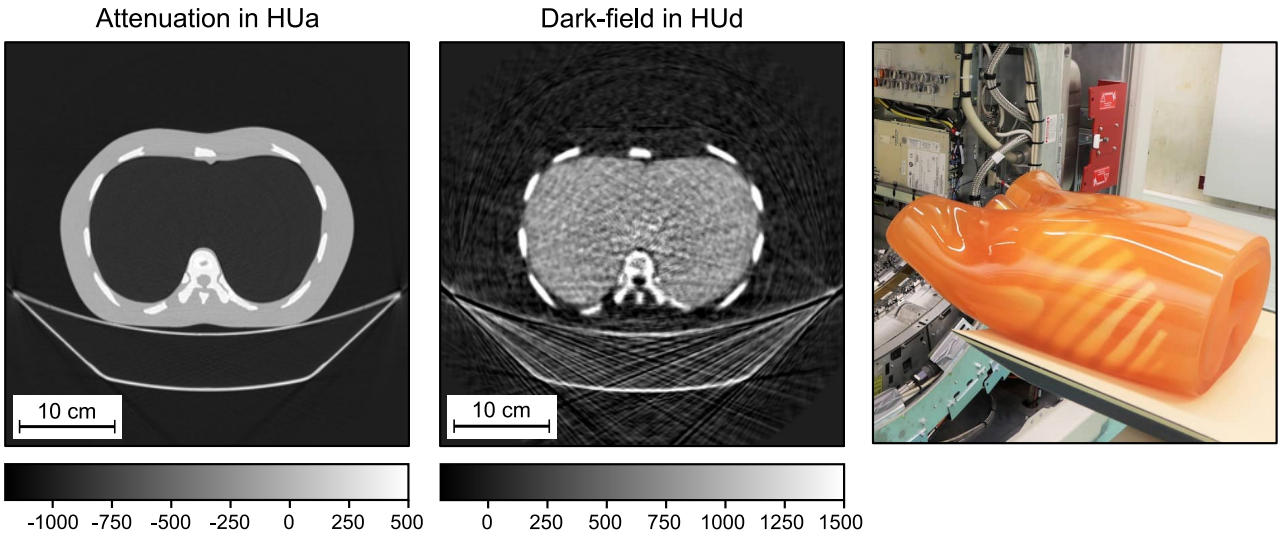

Figure 7.27: Dark-field CT results of Lungman phantom with neoprene insert. The photo on the right shows the Lungman phantom on the couch of the dark-field CT system. The CT scan was acquired with 80 kVp, 550 mAs, and 1 s rotation period, i.e., a $CTDI_{vol}$ of 7.4 mGy. During the reconstruction of the dark-field channel the beam-hardening correction has been applied. An isotropic voxel-size of 0.62 mm is reconstructed, hence, the slice thickness of the reconstruction is 0.62 mm. Image adapted from [136] CC BY.

can be found in Figures 7.26 and 7.27. The latter is a scan of the Lungman phantom with a full neoprene insert which should give a homogeneous signal inside the entire area of the chest. The streak like noise pattern is also visible in the low-dose scan shown earlier in Figure 7.24, but is more blurred by the strong filtering. This pattern is the result of movement-artifacts which are difficult to avoid when sliding window signal extraction is used. Furthermore, also insufficiently optimized per-shot coefficients of the vibrations in the correction patterns can contribute to this artifact.
To improve the reconstruction results a more advanced signal extraction or reconstruction is required. Advanced image filtering as evaluated in [70] can be used to reduce formation of the streak like artifacts. Alternatively, model based iterative reconstruction as demonstrated by Teuffenbach [126] is a promising solution. Nevertheless, the currently achieved quality is a promising result for dark-field imaging at human scale. It demonstrated that the prototype system is capable to maintain its image quality for human-sized samples at reasonable dose levels.

7.12.3 Ventilated Ex-vivo Pork Lung

For a more realistic evaluation of lung imaging at the dark-field CT, an experiment with an ex-vivo porcine lung is set up. This allows to demonstrate the feasibility of dark-field imaging with real lung tissue at a large scale. Porcine lung is used because it is very similar to the humane lung [22] and has regularly been used for pre-clinical experiments at dark-field imaging systems [37], [71].
A problem with ex-vivo lungs is their elasticity which lets them collapse as soon as it is excised from the pork. For the experiment the lung must be re-inflated. This is achieved by applying positive pressure through the trachea, similar to ventilation of an intubated patient. While this works well, it is actually not fully restoring the in-vivo state of the lung tissue. Usually, the lung inflates due to negative pressure applied from the rib-cage and the diaphragm during

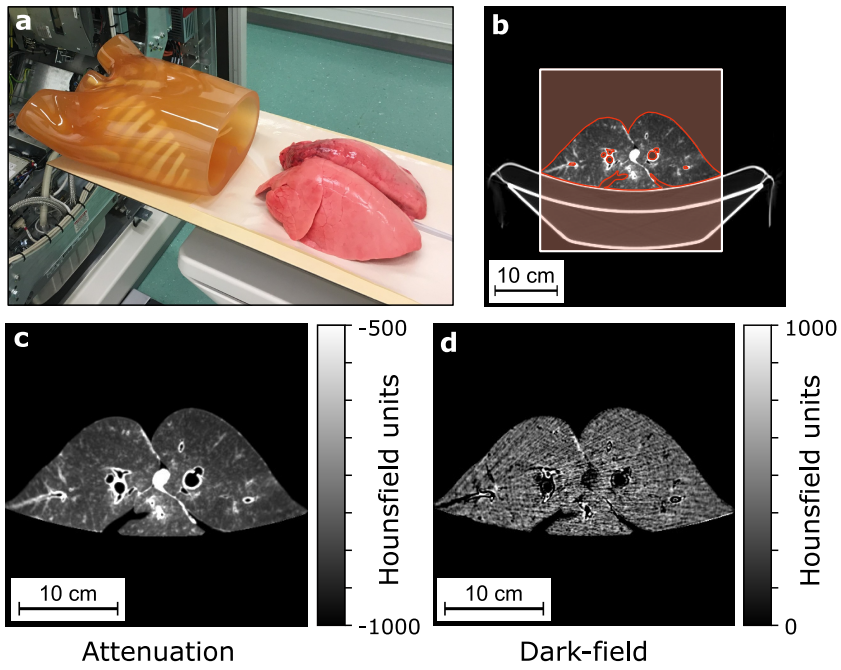

Figure 7.28: Ex-vivo lung of a pork examined with dark-field CT. **a,** Preparation of the porcine lung. The lung gets inflated by a clinical ventilator to pressures up to 30 mBar. **b,** Couch, couch cover (not shown in panel a), and sample-free area are segmented based on the attenuation reconstruction. **c and d,** Attenuation and Dark-field images after cropping and applying the segmentation. The porcine lung is inflated to a constant pressure of 15 mBar.

breathing. An experimental setup based on negative pressure, however, is significantly more complex to develop, and it is unknown if attenuation and dark-field would be any different. Hence, for this initial evaluation, a clinical ventilator is attached to the trachea and is used to inflate the porcine lung by applying a constant pressure between 5 and 40 mBar. The inflated pork lung next to the Lungman phantom is shown in Figure 7.28a.
During the dark-field CT scan the pressure is kept constant to avoid movement artifacts. The reconstruction of the attenuation channel, as shown in Figure 7.28b, is yielded and shows a slice through the center of the lung. The CT couch and the padded couch cover are visible, too. A segmentation of the lung tissue is applied, consequently, all other parts are removed in the final reconstruction images. These are shown in Figure 7.28c and d for the attenuation and dark-field channel, respectively. These initial results of a fully inflated porcine lung at 30 mBar demonstrate that a distinct dark-field signal is generated from lung tissue.
To further evaluate the dark-field signal which is generated by the porcine lung, the pressure is varied and multiple scans are measured. The segmentation is repeated for each scan and allows calculating mean attenuation and dark-field Hounsfield units for each pressure level. Furthermore, the volume of the lung in the reconstructed slice can be calculated. The results are shown in Figure 7.29 and were measured in 5 mBar steps.
The volume of the lung increases for higher pressures, which is expected within the pressure range where the lung tissue is elastic. This process can be observed in both contrast channels. In the attenuation and the dark-field images, the value of the lung tissue is highest for the 5 mBar case and reduces towards higher pressures. This is also supported by the calculated mean values for the respective contrast channels. The reason for this pressure dependent relation is the change of volume and the consequent reduction of density for higher pressures. In the attenuation channel, the mean attenuation coefficient of the reconstructed voxels decreases because of the density reduction during the expansion. Similarly, in the dark-field channel the number of pores at which the radiation can be small-angle scattered changes with tissue density, assuming that no new pores are generated. Hence, when the lung inflates, the number of alveoli per voxel gets reduced and leads to a reduction of the reconstructed dark-field signal. In the fully exhaled state of the presented measurement row, i.e., at 5 mBar, the density of pores per voxel is highest and leads to the highest mean HUd value of 490 in the experiment.

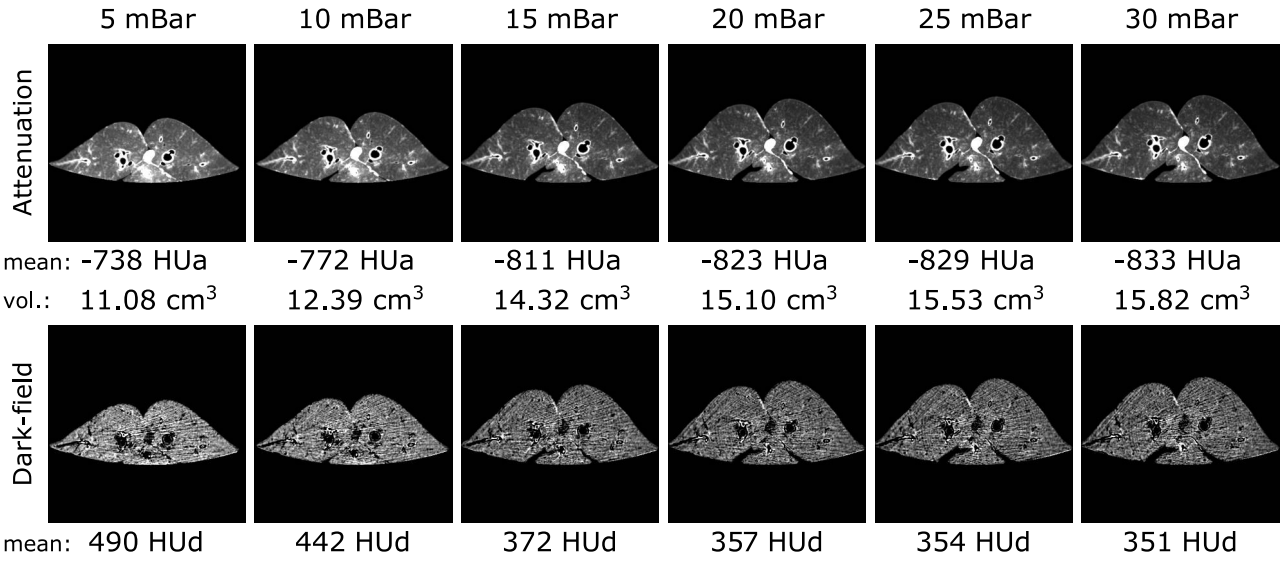

Figure 7.29: Reconstruction results of an ex-vivo porcine lung at various ventilation pressures between 5 and 30 mBar. The same gray-scales and segmentation as in Figure 7.28 has been applied to the attenuation and dark-field images. Mean HUa and HUd values, and the volume of the lung tissue shown in the slices is indicated for each evaluated pressure. Inside the lung, some bronchi of various sizes can be identified in both contrast channels. These are excluded from the evaluation.

These results can also be derived from the plots in Figure 7.30 where the pressure, mean HUa, and mean HUd values are plotted for the respective lung volume on the x-axis. The data shows that the examined lung used expands almost linearly for pressures below 20 mBar. It is assumed that above this pressure the elasticity limit of the lung tissue is approached but not yet exceeded. Additionally, it is assumed that at this pressure most of the previously collapsed bronchi and their connected porous lung tissue are inflated. Only some small areas with still collapsed alveoli remain, which can be inflated at further increasing pressures. This only slightly increases the overall volume of the lung but generates additional pores.
In the plot of the mean attenuation signal of the pork lung during the ventilation process, an almost linear decrease is found. This observation matches the expectation of density reduction due to expansion of the lung tissue. A slight overestimation of the attenuation values remains in the plotted data, which is probably caused by errors in the segmentation of the images. In the low pressure cases differentiation between lung tissue, air, and denser lung tissue is difficult and can lead to an overestimation of the HUa mean values.
The dark-field signal also decreases towards larger volumes as the density of small-angle scattering pores gets lower. Contrary to the almost linear decrease found in the attenuation channel, in the dark-field a more distinct deviation from a linear behavior becomes apparent. This can be observed for pressures exceeding 20 mBar, i.e., the volume of the examined lung is larger than about 23 cm^3, in Figure 7.30. On the one hand, this can, similarly as in the attenuation channel, be caused by better segmentation results for the inflated lung. On the other hand, the previously mentioned inflation process of collapsed alveoli, which require a high pressure to be mobilized, can lead to additional dark-field signal. This process generates new small-angle scattering pores and is only visible in the dark-field channel.
Another important observation in this experiment with an ex-vivo pork lung is the dark-field signal level of lung tissue. Until now, only neoprene has been use as a calibration and test material. This experiment reveals that the dark-field signal of the examined pork lung reaches values between 350 and 500 HUd depending on the pressure. For the “exhaled” state, i.e., at

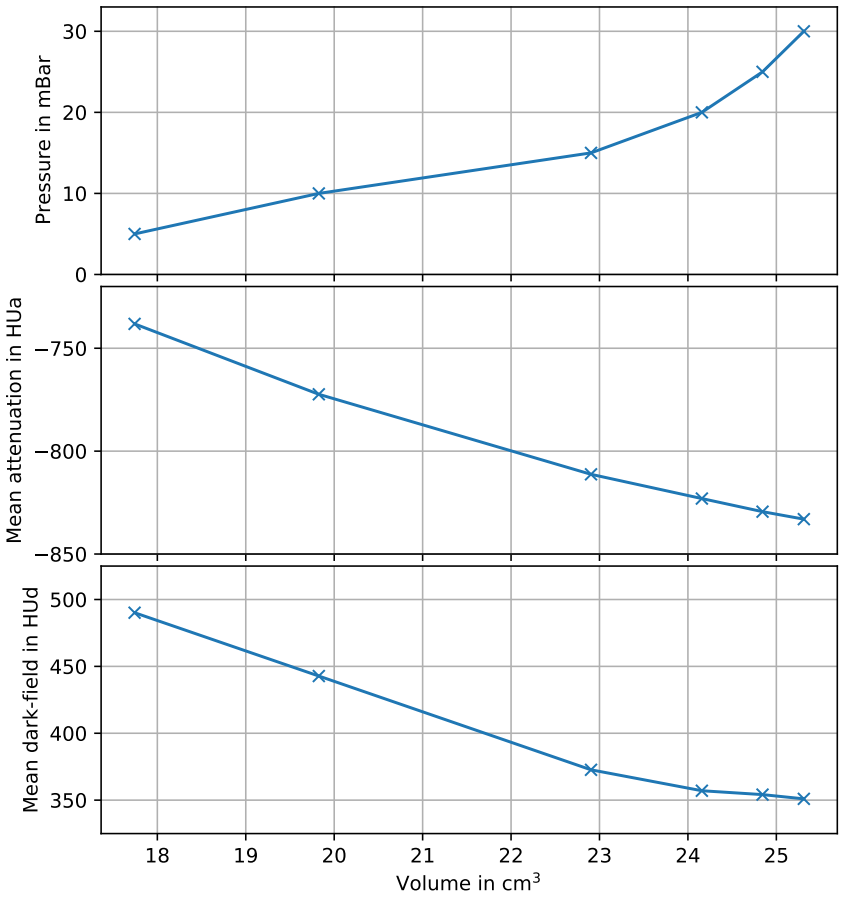

Figure 7.30: Plot of mean values from scans shown in Figure 7.29. Volume increase is coupled to applying more pressure to inflate the lung. For small volumes the relation is almost linear but deviates for large volumes. It is assumed that there the elasticity limit of the lung is approached. The attenuation and dark-field mean values decrease almost linearly with increasing volume. This matches the expectation that these signals are strongly related to density of the material or is pores. In the dark-field channel the decrease stops for pressures above 20 mBar. It is assumed that above this pressure previously collapsed parts of the lung where able to inflate.

5 mBar, the examined lung tissue generates a dark-field signal which is about half as strong as the neoprene calibration material.
These results and following conclusions must be carefully considered because they are based on an ex-vivo pork lung. The absence of a rib cage, diaphragm, and other body parts of the chest might have led to an unrealistic inhalation and inflation of the lung tissue. Additionally, no blood-filled vessels are included in this experiment. Furthermore, decay of the tissue might have changed its properties, e.g., led to trapped liquid inside the alveoli.
Differences become obvious when comparing the measured mean HUa values to expected values from conventional chest CT. In the attenuation channel, -600 to -700 HUa are expected for lung tissue in a clinical examination, but here lower values around -750 to -850 HUa are measured. This is probably caused by the absence of blood in the ex-vivo lung, which can easily lead to such a reduction of the attenuation.
To demonstrate a realistic imaging case for clinical dark-field chest CT, the Lungman phantom and the pork lung are combined. The previously examined porcine lung is placed inside the Lungman phantoms chest, replacing the neoprene inserts used in the previous section. Again, the lung is ventilated by applying positive pressure of 30 mBar to fill almost the entire space inside the chest of the phantom. Since the shape of a porcine lung is more elongated than a human lung, it was not possible to fill the entire area within the chest. This setup now models the patient size and the lung, but still misses features such as the heart and blood in the vessels of the lung tissue.
The resulting reconstructions in attenuation and dark-field contrast are presented in two different gray-scale windows in Figure 7.31. In the attenuation window 1, i.e., panel a, the bones and soft tissues around the bones are clearly visible and in window 2 the focus is on the structures

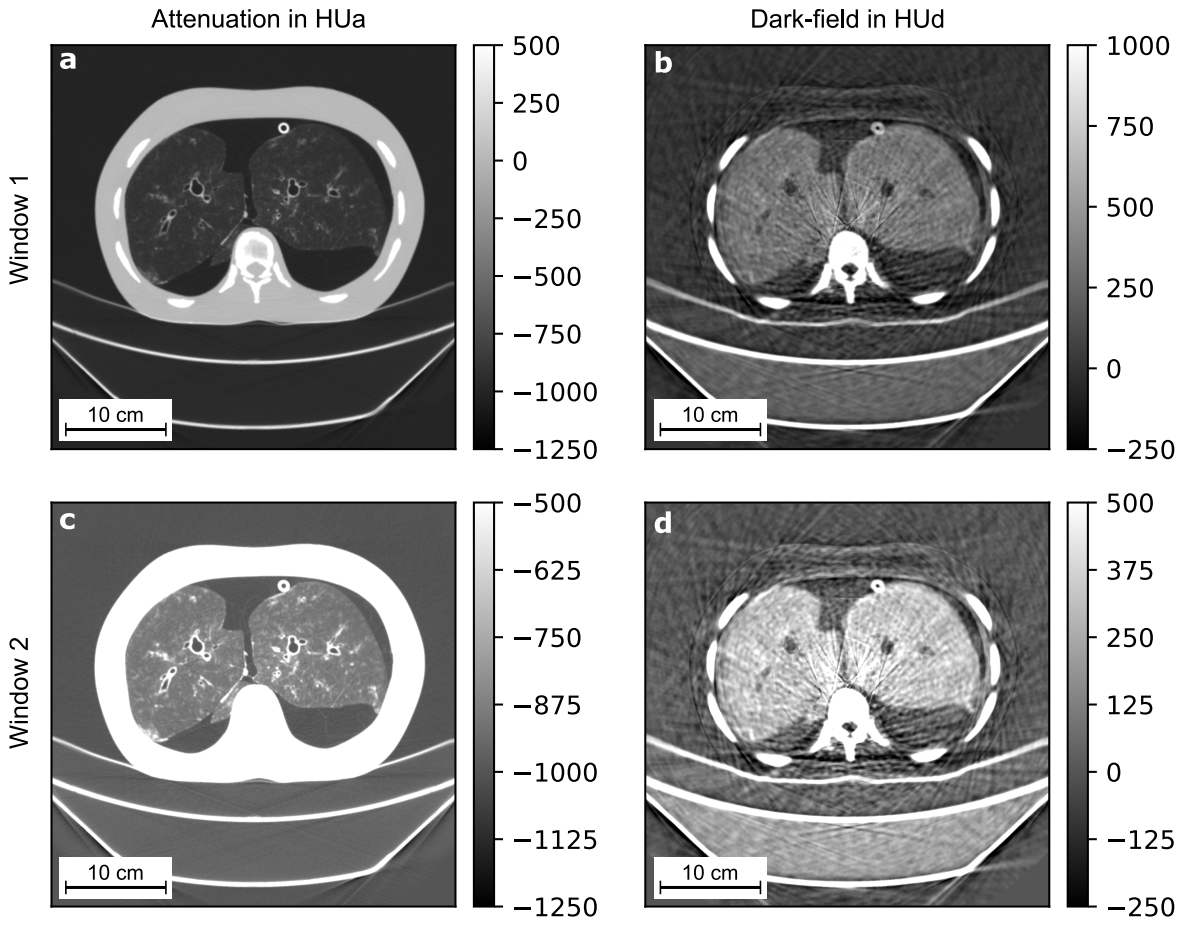

Figure 7.31: Dark-field CT results of the Lungman chest phantom with a ventilated porcine lung. Data is obtained from a single rotation at 1.5 s rotation period at 80 kVp and a $CTDI_{vol}$ of 11.1 mGy. During the reconstruction of the dark-field channel the beam-hardening correction has been applied. An isotropic voxel-size of 0.62 mm is reconstructed, hence, the slice thickness of the reconstruction is 0.62 mm. The small plastic tube for ventilation is visible above the right lung wing. **a and c,** attenuation reconstruction images in two different gray-scale windows. **b and d,** dark-field reconstruction images in two different gray-scale windows.

in the lung tissue. These two windows are similar to the bone and lung windows regularly used in clinical diagnostics, respectively. An important difference to clinical attenuation chest CT images is the absence of blood vessels, which usually dominates these images.
Figures 7.31 b and d show the dark-field reconstruction. These results demonstrate that the small-angle scattering in lung tissue can also be reconstructed when the lung is inside a human chest phantom. The bronchi are visible by absence of any dark-field signal. The tighter windowing of the gray scales in Figure 7.31d reveals that the reconstructed tissue values are around 350 HUd which matches the results from Figure 7.30.
This scan has been measured with 80 kVp, 825 mAs, and a rotation period of 1.5 s, consequently the $CTDI_{vol}$ is about 11.1 mGy. While the attenuation images are sharp and artifact free, significant noise is present in the dark-field channel. It is dominated by streak-like artifacts caused by the sliding window signal extraction. These are mostly extending along sharp edges, e.g., from the spine, between the ribs, or at the soft tissue interface. With more aggressive image filters these artifacts can be reduced at the cost of image sharpness. However, this is not applied here, as the dark-field signal from the lung tissue is sufficiently strong and allows a visual differentiation from the streak-like artifacts. Additionally to the streak like artifacts

also cupping-like behavior in the upper part of the chest soft tissue is found in the dark-field channel. This is difficult to correct with image filters alone and would require a more advanced signal extraction or processing approach.
These results demonstrate that with the dark-field CT prototype, chest examinations of lung tissue are feasible on a human scale. Certainly, a porcine lung inside the Lungman phantom is only a vast approximation of a realistic clinical chest CT of a human patient. Nevertheless, for now, it is the closest model before conducting studies with animals or human patients. The results can be used as a base to decide on further optimizations and allow assessing the expectations for a potential patient study.

8 Conclusion and Outlook

8.1 Summary of Results

Dark-field imaging with X-rays is an emerging technology in the process of being translated to clinical practice. It can offer otherwise inaccessible information on the microscopic structure of the sample, i.e., the porosity of tissue. This makes it a valuable addition to conventional attenuation-only X-ray imaging. For radiography, dark-field X-ray imaging has already reached the development stage of initial clinical studies with human patients. For dark-field CT, however, several significant technical challenges still remained.

The first part of this thesis evaluates these challenges, finds possible solutions, and selects the most feasible design for a prototype system. For this purpose, a wave-optical simulation framework is developed in Chapter 3. It allows to simulate a large range of geometries and grating properties, closely modeling many effects and limitations to obtain realistic results. Particularly important is the consideration of the system's spectral response, as a wide polychromatic X-ray spectrum is used. Furthermore, the influence of the large X-ray source spot and bent gratings is modeled.

Various approaches for compensation of shadowing-related artifacts are evaluated in Chapter 4. With currently available grating fabrication methods in mind, bent gratings are shown to be the most feasible option. Some alternative methods show promise but require further optimization to be employed for clinical dark-field CT.

The evaluation of shadowing in the grating structures also reveals two additional design related issues for a clinical dark-field CT. Both originate from the large focal spot of CT X-ray sources; Firstly, an upper bound for the aspect-ratio of absorption gratings is found, as bending and X-ray source size otherwise leads to signification shadowing. The second finding is that systems with a large X-ray source spot have a high sensitivity to grating period deviations. Since clinical CT X-ray source spots can reach a width of several millimeters, this makes tight tolerances for grating fabrication a top priority. Otherwise, even small grating period deviations in the nanometer range can lead to a massive visibility loss of the interferometer.

Based on the presented simulation framework, a comprehensive study of various Talbot-Lau interferometer designs is evaluated throughout Chapter 5. It also includes a description of the geometry of the Brilliance iCT gantry and a discussion how a three-grating interferometer can be integrated into this gantry. An inverse interferometer geometry is shown to come with several advantages. It makes the best use of the available space by positioning G_0 and G_1 in front of the patient. The comparably small size of these two gratings simplifies their fabrication process. The only large grating is then G_2, which has a rather coarse grating period, making its fabrication and implementation feasible by combining multiple smaller tiles. In the specific case of the Brilliance iCT, the inverse geometry achieves the best interferometer sensitivity, which optimizes the system for dark-field imaging.

During the evaluation several promising setup configurations are identified. Most of these candidates, however, are not feasible with current state-of-the-art grating fabrication. A common

limitation is that too fine grating periods or too high aspect-ratios are required. Besides conventional binary grating profiles also non-binary grating structures, i.e., triangular gratings, are considered in the evaluation. Finally, two promising and feasible configurations are found. Both designs have identical G_0 and G_2, and only differ in their G_1 parameters. One design is based on a triangular G_1 and the other on an absorption G_1. An in-depth analysis of the two options demonstrates that the triangular design is currently superior in performance and feasibility. Such a G_1 is comparably simple to fabricate as it is a phase-shifting grating which requires only a small aspect-ratio. Furthermore, it is found that as a phase-shifting grating it stops only a small amount of the incoming X-ray flux. This allows a better flux efficiency and achieves a 27% increase in signal-to-noise ratio compared to a design with an absorption G_1. The only drawback of using a triangular G_1 design has been missing experience; In contrast to absorption G_1 designs, triangular gratings have never before been used for any large-scale X-ray Talbot-Lau interferometer. Nevertheless, the advantages of the triangular G_1 design are found to outweigh this risk. Finally, the geometry and grating configuration for the first dark-field CT of clinical scale is selected as listed in Table 5.9.

The second part of the thesis covers the implementation and adjustment of the Talbot-Lau interferometer into the gantry of a Brilliance iCT. Furthermore, the initial characterization and data processing procedure is presented. Afterwards the first reconstruction results of human-sized test objects from the dark-field CT are shown.

In Chapter 6, the focus is on the technical details of the implementation. Illustrated by detailed CAD renderings the mounts and adjustment mechanics are discussed. Here, two new approaches of mounting a Talbot-Lau interferometer are shown. The combined G_0 and G_1 mount bends these two gratings keeping them at a precise inter-grating distance and providing stability against vibrations. The other design novelty is the thirteen-tiled bent G_2 which is focused on the X-ray source spot and allows adjustment of each individual tile. Particularly, the translation along the beam axis, i.e., the distance of the grating from the X-ray source spot, is important for the CT implementation. It allows adjusting the interferometer for a specific length, hence, a precise density of Moiré fringes on the detector.

The initial imaging results from the first implementation of the Talbot-Lau interferometer in the CT gantry are presented in Chapter 7. The first characterization results reveal the presence of vibrations, which cause the Moiré fringe pattern to oscillate. An analysis finds that there are two dominant frequencies in the interferometer which are both induced by the X-ray source. The frequencies of 175 Hz and 189 Hz are related to the anode rotation and the electromagnetic driver, respectively. It is assumed, that the anode rotation at 175 Hz leads to small displacements of the gratings and causes the change in the interferometer phase. Furthermore, since this movement is continuous during the individual exposures, the fringe pattern becomes blurred, which induces a periodic visibility drop. At 189 Hz only a flux and shadowing variation is observed which most dominantly affects the intensity channel of the interferometer. It is assumed that this is induced purely electromagnetically by displacing or distorting the X-ray focal spot.

A new data processing approach is introduced to compensate for all these variations in the interferometer state. It was found that the G_2 tiles must be modeled as individual parts of the system during the reference processing. Fortunately, with principal component analysis these tile-wise behaviors can be compressed to only a few global variation patterns. Based on these global variation patterns and the observation that these are scan-to-scan persistent, a complex sample processing pipeline is developed. It uses prior knowledge of the previously identified frequencies to correct the variations and corrects them. The sample information is derived from the measured data by sliding window signal extraction. These projections are then corrected

for beam-hardening in the dark-field channel. Otherwise, the small-angle scattering would be overestimated in the reconstruction images as beam-hardening leads to a visibility reduction. The corrected projections are then reconstructed to tomographic images in the attenuation and the dark-field modality.
To demonstrate the capabilities of this system and to characterize it, several test objects are evaluated. These tests reveal that the resolution of the dark-field CT currently cannot compete with conventional clinical CT machines. This is expected because several resolution enhancing techniques have been turned off to simplify processing of the dark-field CT data. For example, the ultra-high-resolution comb and the flying focal spot are currently not in use. The resolution in the reconstructed attenuation images is about 5.0 lp/cm, which is sufficient for now, but not comparable to the approximately 10 lp/cm in conventional CT. An even lower resolution of only 2.6 lp/cm is found for the dark-field channel because strong filters lead to further blurring of the dark-field image data. Nevertheless, since it is concluded that as the dark-field image shows sub-resolution information independent of its actual resolution, this result is sufficient.
Promising results are found for the dose levels of the developed dark-field CT prototype. It is possible to reconstruct decent image quality even at a low dose scan of only 4 mGy $\mathrm{CTDI}_{\mathrm{vol}}$. The maximum applicable $\mathrm{CTDI}_{\mathrm{vol}}$ is 11.1 mGy, hence, the full suggested dose range for chest CT can be configured. Due to the limitation to 80 kVp no higher doses can be reached in axial scans.
The dark-field CT results, presented throughout Section 7.12, also reveal that there are still artifacts in the reconstructed images. Particularly in the dark-field image, higher noise level and streak artifacts are found. These are caused by the sliding window signal extraction process, which is sensitive to sample movements within the window of consecutive projections. Furthermore, insufficient convergence of the oscillation correction coefficients can lead to these streaks. The noise is also increased, as the interferometer visibility directly affects the signal-to-noise-ratio (see (5.13)). The mean system visibility is currently only around 0.18 which is sufficient, but a higher value would certainly be preferred. Despite these artifacts, the image quality is within our expectations for a first-of-its-kind imaging system.
Since no studies with patients were possible yet, a pork lung inserted in the Lungman phantom is currently the most realistic experiment to simulate clinical chest CT. Similar experiments at other setups previously demonstrated that ex-vivo pork lungs generate a similar small-angle scattering signal as a human lung. These experiments with pork lungs allow us to verify that the system can reconstruct the dark-field signal of lung tissue inside a human thorax. Experiments with various ventilation pressures reveals a strong dependency on the breath state during the scan. The strongest signal is reconstructed for an exhaled state because then the number of small-angle scattering pores per volume is highest. These results are a convincing demonstration that the design goal of developing a dark-field CT system for clinical scale has been successful.
In summary, we demonstrate the first dark-field CT, which can scan a human thorax with a 45 cm diameter field of view in a single second. Several technical challenges are overcome and solutions are combined into one system. The performance is evaluated and a new data processing procedure is introduced. This processing compensates for vibration induced oscillations in the measured image data and achieves a high sensitivity in both image channels. This now puts dark-field CT just one step away from clinical studies with patients.

8.2 Future Work

The latest imaging and characterization results discussed in this thesis reveal several fields where optimization is possible. For example, there are some issues which can be solved by upgrading the gratings. With latest grating fabrication methods now larger G_2 tiles can be realized which will significantly reduce the number of required tiles. This simplifies the adjustment during implementation and reduces the number of borders between tiles which usually provide only low visibility. Furthermore, fewer polynomial correction patterns are required to model the impact of the vibrations in the reference processing. Such an upgrade could be combined by evaluating silicon etched substrates filled with tungsten, as demonstrated by Pinzek et al. [96]. While larger tiles had not been available when the initial G_2 design was developed, such an upgrade was considered during in the design process. Therefore, only minor modifications of the G_2 adjustment modules are required.
Another upgrade would be switching to finer grating periods to improve the interferometer sensitivity to small-angle scattering. The simulation results in Figure 5.20 suggest that in a triangular G_1 design the periods can be freely down-scaled as long as the G_1 period is larger than 1.85 µm. However, it must be considered that finer grating periods also lead to higher aspect-ratios for G_0 which becomes harder to fabricated and exhibits more acceptance induced shadowing. Hence, such a step must be well considered and probably requires a horizontal grating layout instead of a vertical one (as defined in Figure 5.13). Another important aspect which must be considered is the increasing sensitivity to vibrations when smaller grating periods are used. With finer gratings displacements have a larger impact on the interferometer. This, however, is currently not seen as the major restriction, as the primary oscillation amplitude is only about 1.5π of the interferometer phase.
The development of the prototype system focuses on the 80 kVp spectrum as this is advantageous for absorption grating performance. Unfortunately, as has been shown in Section 7.11, the X-ray flux at 80 kVp is limited. This can become a problem when fast rotation speeds are required, e.g., for helical scans, or larger objects should be examined. An optimization towards higher kVp settings might be an option to solve this issue. A brief evaluation of such an upgrade towards 120 kVp in Section 5.6.7 shows promising results. It would require an adapted G_1, either implemented as an absorption grating or an optimized triangular phase-grating.
In the dark-field CT prototype the reference detector and the flying focal spot have been removed or deactivated. While the latter simplifies the data processing at the cost of spatial resolution, the former makes the data processing more complex. Developing a compatible reference detector will be beneficial and can reduce the complexity of the sample data processing. Re-activating the flying focal spot is also an interesting project for future work. It requires extending the data processing to consider multiple focal spots, and might also require individual oscillation correction patterns for each spot. This effort will come with two advantages; the reconstruction resolution can be improved and a better phase-sampling within the sliding windows can be achieved. The latter aspect has recently been evaluated by Pleier [98] and is very promising, but has not yet been utilized.
The most dominant artifacts in the reconstructed dark-field images are streaks caused by movement artifacts from the sliding window signal extraction. Using smaller windows of fewer consecutive projections can only reduce this issue, but cannot fully compensate it. Unfortunately, smaller windows come with the problem of waning statistics and worse phase-sampling which can lead to new artifacts. Intermediate solutions are advanced image filters to suppress characteristic streak artifacts caused by movement artifacts [70]. Alternatively, a more advanced data processing such as the intensity based statistical iterative reconstruction (IBSIR) [125],

[127], [126] must be applied. It omits any intermediate signal extraction step and directly reconstructs the attenuation and dark-field images from the measured data. Certainly, vibration effects still have to be compensated, but the absence of any sliding window related artifacts is a significant advantage. Such an advanced processing can also be combined with the introduction of the flying focal spot, as this enhances the phase-sampling. A challenge for such an implementation is the simultaneous compensation of the system vibrations and keeping the reconstruction time to a reasonable duration. It is assumed that IBSIR can profit massively from the current sliding-window-based reconstructions as a start image. The rewards for such an implementation are expected to be higher spatial resolution, reduced noise, and removal of sliding window related streak artifacts.
Another important addition to the dark-field CT system's processing pipeline will be a more elaborate beam-hardening correction. While currently no beam-hardening correction is applied in the attenuation channel, this should be implemented, e.g., based on a water calibration measurement or a simulation. Furthermore, also the benefits of a beam-hardening correction for bones should be investigated. These corrections are standard in clinical CT and should be fully compatible with the dark-field CT imaging chain.
Parallel to the suggested technical optimizations more realistic imaging cases should be considered. The latest experiments are based on ex-vivo pork lunges in a Lungman phantom and come with several uncertainties. The vessels are with blood and since the lung tissue was not fixated it had already started to degrade. Furthermore, it is not clear if the dark-field signal of an ex-vivo ventilated lung is comparable to a normal lung. Hence, ventilated ex-vivo lung tissue experiments cannot replace first clinical studies with human patients. These are important to clarify which signal levels can be expected from a healthy human lung. Moreover, the feature size of dark-field signal loss in lung disease cases is an important information. It will allow to prioritize the optimization for, e.g., more spatial resolution, higher sensitivity, or better noise suppression. Dark-field CT patient studies on COPD and other lung disease can follow to evaluate the diagnostic value of the added dark-field modality.
For future application of dark-field CT – beyond a prototype system – it is important to demonstrate compatibility to other conventional CT gantries. As this thesis shows, an upgrade-like implementation of a Talbot-Lau interferometer is feasible. It is expected that future implementations can also be based on other CT gantry models. Consequently, a combination of dark-field CT with other emerging novelties, such as photon-counting and spectral CT should be considered. These technologies use new detectors, X-ray sources, or modified acquisition methods and should in general be compatible with dark-field imaging. Such systems can then profit form the added dark-field contrast, which otherwise remains inaccessible, even for these novel CT technologies. Furthermore, it is expected that particularly with spectral CT better image quality in the dark-field channel can be achieved.

Bibliography

[1] "Adult Routine Chest CT Protocols Version 2.1". URL: https://www.aapm.org/pubs/CTProtocols/ (visited on 10/31/2022) (Cited on pages 165, 166).

[2] Jens Als-Nielsen and Des McMorrow. "Elements of Modern X-ray Physics". John Wiley and Sons, Inc., 2011. ISBN: 9781119998365. DOI: 10.1002/9781119998365 (Cited on pages 5, 8, 9, 12).

[3] Jana Andrejewski. "Human-sized X-ray Dark-field Imaging". TUM, 2021. URL: http://d-nb.info/125091695X/34 (Cited on page 81).

[4] Fulvia Arfelli et al. "A Gaussian Extension for Diffraction Enhanced Imaging". In: *Scientific Reports* 8 (2018), p. 362. DOI: 10.1038/s41598-017-18367-x (Cited on page 2).

[5] David Attwood and Anne Sakdinawat. "X-Rays and Extreme Ultraviolet Radiation". Cambridge: Cambridge University Press, 2016. ISBN: 978-1-107-47762-9. DOI: 10.1017/CBO9781107477629 (Cited on page 8).

[6] Shivaji Bachche et al. "Laboratory-based X-ray phase-imaging scanner using Talbot-Lau interferometer for non-destructive testing". In: *Scientific Reports* 7 (1 2017), p. 6711. DOI: 10.1038/s41598-017-07032-y (Cited on page 75).

[7] M. Bech et al. "Quantitative x-ray dark-field computed tomography". In: *Physics in Medicine and Biology* 55 (18 2010), pp. 5529–5539. DOI: 10.1088/0031-9155/55/18/017 (Cited on pages i, iii, 14).

[8] Martin Bech. "X-Ray Imaging with a Grating Interferometer: Phase Contrast and Dark-Field Imaging Using a Grating Interferometer". Saarbrücken: LAP Lampert Academic Publishing, 2010. ISBN: 978-3-8383-8254-8 (Cited on pages 10, 24–26, 30).

[9] Martin Bech et al. "Hard X-ray phase-contrast imaging with the Compact Light Source based on inverse Compton X-rays". In: *Journal of Synchrotron Radiation* 16 (2009), pp. 43–47. DOI: 10.1107/S090904950803464X (Cited on page 5).

[10] Rolf Behling. "Modern Diagnostic X-Ray Sources: Technology, Manufacturing, Reliability". 2021. ISBN: 9781003095408. DOI: 10.1201/9781003095408 (Cited on pages 7, 84, 86, 145, 150).

[11] Rolf Behling. "Performance and Pitfalls of Diagnostic X-ray Sources: An Overview". In: *Medical Physics* 43 (6.47 2016), pp. 3903–3903. DOI: 10.1118/1.4958291 (Cited on page 84).

[12] Sebastien Berujon et al. "X-ray phase microscopy using the speckle tracking technique". In: *Applied Physics Letters* 102 (2013), p. 154105. DOI: 10.1063/1.4802729 (Cited on page 14).

[13] Lorenz Birnbacher et al. "Experimental Realisation of High-sensitivity Laboratory X-ray Grating-based Phase-contrast Computed Tomography". In: *Scientific Reports* 6 (2016), p. 24022. DOI: 10.1038/srep24022 (Cited on pages 2, 74, 81).

[14] Lorenz Birnbacher et al. "Tilted grating phase-contrast computed tomography using statistical iterative reconstruction". In: *Scientific Reports* 8 (1 2018). DOI: 10.1038/s41598-018-25075-7 (Cited on pages 15, 94).

[15] John M. Boone and J. Anthony Seibert. "An Accurate Method for Computer-Generating Tungsten Anode x-Ray Spectra from 30 to 140 kV". In: *Medical Physics* 24 (1997), pp. 1661–1670. DOI: 10.1118/1.597953 (Cited on page 37).

[16] Margarita Braunagel et al. "Qualitative and Quantitative Imaging Evaluation of Renal Cell Carcinoma Subtypes with Grating-based X-ray Phase-contrast CT". In: *Scientific Reports* 7 (2017), p. 45400. DOI: 10.1038/srep45400 (Cited on page 2).

[17] Thorsten M. Buzug. "Computed Tomography: From Photon Statistics to Modern Cone-Beam CT". Berlin: Springer, 2008. 521 pp. ISBN: 978-3-540-39408-2 (Cited on page 31).

[18] Sébastien Bérujon et al. "Two-Dimensional X-Ray Beam Phase Sensing". In: *Physical Review Letters* 108 (2012), p. 158102. DOI: 10.1103/PhysRevLett.108.158102 (Cited on page 14).

[19] C.T. Chantler et al. "X-Ray Form Factor, Attenuation and Scattering Tables (version 2.1)". Gaithersburg, MD.: National Institute of Standards and Technology, 2005. URL: http://physics.nist.gov/ffast (Cited on page 9).

[20] Peter Cloetens et al. "Hard x-ray phase imaging using simple propagation of a coherent synchrotron radiation beam". In: *Journal of Physics D: Applied Physics* 32 (1999), A145–A151. DOI: 10.1088/0022-3727/32/10A/330 (Cited on page 22).

[21] Peter Cloetens et al. "Phase objects in synchrotron radiation hard x-ray imaging". In: *Journal of Physics D: Applied Physics* 29 (1996), pp. 133–146. DOI: 10.1088/0022-3727/29/1/023 (Cited on page 14).

[22] Fabio De Marco et al. "Contrast-to-noise ratios and thickness-normalized, ventilation-dependent signal levels in dark-field and conventional in vivo thorax radiographs of two pigs". In: *PLOS ONE* 14 (6 2019), e0217858. DOI: 10.1371/JOURNAL.PONE.0217858 (Cited on page 171).

[23] Fabio De Marco et al. "X-Ray Dark-Field Signal Reduction Due to Hardening of the Visibility Spectrum". Preprint. 2020. DOI: 10.48550/ARXIV.2011.03542 (Cited on pages 30, 160).

[24] D. Devitt. "Design World Magazine". In: *Radial Air Bearings Help CT Scanners See into Your Heart.* (2009), pp. 62–64. URL: https://www.designworldonline.com/radial-air-bearings-help-ct-scanners-see-into-your-heart/ (Cited on page 149).

[25] "DIN EN 60336:2006-09, Medical electrical equipment X-ray tube assemblies for medical diagnosis". DOI: 10.31030/9722435 (Cited on pages 84, 85).

[26] Jonas Dittmann et al. "Optimization Based Evaluation of Grating Interferometric Phase Stepping Series and Analysis of Mechanical Setup Instabilities". In: *Journal of Imaging* 4 (6 2018), p. 77. DOI: 10.3390/jimaging4060077 (Cited on pages 112, 140).

[27] Tilman Donath et al. "Inverse geometry for grating-based x-ray phase-contrast imaging". In: *Journal of Applied Physics* 106 (5 2009). DOI: 10.1063/1.3208052 (Cited on pages 23, 80, 89, 91).

[28] Elena Eggl et al. "The Munich Compact Light Source: initial performance measures". In: *Journal of Synchrotron Radiation* 23 (2016), pp. 1137–1142. DOI: 10.1107/S1600577516009675X (Cited on page 5).

[29] P. Emma et al. "First lasing and operation of an ångstrom-wavelength free-electron laser". In: *Nature Photonics* 4 (2010), pp. 641–647. DOI: 10.1038/nphoton.2010.176 (Cited on page 5).

[30] Marco Endrizzi et al. "Hard X-ray dark-field imaging with incoherent sample illumination". In: *Applied Physics Letters* 104 (2014), p. 024106. DOI: 10.1063/1.4861855 (Cited on page 21).

[31] "Engineering ToolBox". Thermal Expansion - Linear Expansion Coefficients. 2003. URL: https://www.engineeringtoolbox.com/linear-expansion-coefficients-d_95.html (visited on 10/31/2022) (Cited on page 59).

[32] Alexander A. Fingerle et al. "Simulated Cystic Renal Lesions: Quantitative X-ray Phase-Contrast CT—An in Vitro Phantom Study". In: *Radiology* 272 (2014), pp. 739–748. DOI: 10.1148/radiol.14130876 (Cited on page 2).

[33] T. G. Flohr et al. "Novel ultrahigh resolution data acquisition and image reconstruction for multi-detector row CT". In: *Medical Physics* 34 (2007), pp. 1712–1723. DOI: 10.1118/1.2722872 (Cited on page 82).

[34] Manuela Frank et al. "Dark-Field Chest X-ray Imaging for the Assessment of COVID-19-Pneumonia". Preprint. 2022. DOI: 10.21203/rs.3.rs-1427370/v1 (Cited on page 3).

[35] Florian T. Gassert et al. "Dark-Field Chest Radiography of Combined Pulmonary Fibrosis and Emphysema". In: *Radiology: Cardiothoracic Imaging* 4 (1, 2022), e220085. DOI: 10.1148/ryct.220085 (Cited on page 3).

[36] J. Graetz et al. "Review and Experimental Verification of X-Ray Dark-Field Signal Interpretations with Respect to Quantitative Isotropic and Anisotropic Dark-Field Computed Tomography". In: *Physics in Medicine & Biology* 65 (2020), p. 235017. DOI: 10.1088/1361-6560/abb7c6 (Cited on page 160).

[37] Lukas B. Gromann et al. "In-vivo X-ray Dark-Field Chest Radiography of a Pig". In: *Scientific Reports* 7 (1 2017), p. 4807. DOI: 10.1038/s41598-017-05101-w (Cited on pages 3, 75, 80, 171).

[38] T. E. Gureyev et al. "Dark-Field Signal Extraction in Propagation-Based Phase-Contrast Imaging". In: *Physics in Medicine & Biology* 65 (7, 2020), p. 215029. DOI: 10.1088/1361-6560/abac9d (Cited on page 2).

[39] Alex Gustschin et al. "High-resolution and sensitivity bi-directional x-ray phase contrast imaging using 2D Talbot array illuminators". In: *Optica* 8 (2021), p. 1588. DOI: 10.1364/OPTICA.441004 (Cited on pages 15, 47, 94).

[40] Nikolai Gustschin et al. "Dark-Field Imaging on a Clinical CT System: Performance and Potential Based on First Results". In: *7th International Conference on Image Formation in X-Ray Computed Tomography*. Seventh International Conference on Image Formation in X-Ray Computed Tomography (ICIFXCT 2022). Baltimore, United States: SPIE, 2022, p. 82. DOI: 10.1117/12.2646988 (Cited on page 168).

[41] Nikolai Gustschin et al. "Quality and Parameter Control of X-ray Absorption Gratings by Angular X-ray Transmission". In: *Optics Express* 27 (27, 2019), p. 15943. DOI: 10.1364/oe.27.015943 (Cited on pages 47, 54, 57, 145, 146).

[42] Jakob Haeusele. "Statistical Signal Processing and Reconstruction Algorithms for a Clinical Darkfield CT Prototype". Master Thesis. TUM, 2020 (Cited on page 159).

[43] Jakob Haeusele et al. "Advanced Phase-Retrieval for Stepping-Free X-Ray Dark-Field Computed Tomography". In preparation. (Cited on page 159).

[44] Jakob Haeusele et al. "Dark-Field Imaging on a Clinical CT System: Sample Data Processing and Reconstruction". In: *7th International Conference on Image Formation in X-Ray Computed Tomography*. Seventh International Conference on Image Formation in X-Ray Computed Tomography (ICIFXCT 2022). Baltimore, United States: SPIE, 2022, p. 27. DOI: 10.1117/12.2646440 (Cited on page 159).

[45] Dieter Hahn. "Statistical Iterative Reconstruction for X-ray Phase-Contrast Computed Tomography". PhD Thesis. TUM, 2014. URL: http://d-nb.info/1052995500/34 (Cited on page 27).

[46] Charles R. Harris et al. "Array programming with NumPy". In: *Nature* 585 (2020), pp. 357–362. DOI: 10.1038/s41586-020-2649-2 (Cited on page 26).

[47] Hiroto Hatabu and Bruno Madore. "Dark-Field Chest Radiography in the Detection of Emphysema". In: *Radiology* (2022), p. 212910. DOI: 10.1148/radiol.212910 (Cited on page 77).

[48] Eugene Hecht. "Optics". 2017. ISBN: 978-1-292-09696-4 (Cited on page 13).

[49] Katharina Hellbach et al. "In Vivo Dark-Field Radiography for Early Diagnosis and Staging of Pulmonary Emphysema". In: *Investigative Radiology* 50 (7 2015). DOI: 10.1097/RLI.0000000000000147 (Cited on pages 2, 3, 79).

[50] Katharina Hellbach et al. "X-Ray Dark-field Imaging to Depict Acute Lung Inflammation in Mice". In: *Scientific Reports* 8 (1, 2018), p. 2096. DOI: 10.1038/s41598-018-20193-8 (Cited on pages 2, 79, 93).

[51] Katharina Hellbach et al. "X-ray dark-field radiography facilitates the diagnosis of pulmonary fibrosis in a mouse model". In: *Scientific Reports* 7 (23, 2017), p. 340. DOI: 10.1038/s41598-017-00475-3 (Cited on pages 2, 3, 76, 79).

[52] Andrew M. Hernandez and John M. Boone. "Tungsten anode spectral model using interpolating cubic splines: Unfiltered x-ray spectra from 20 kV to 640 kV: Unfiltered Monte Carlo-based tungsten anode spectral model". In: *Medical Physics* 41 (2014), p. 042101. DOI: 10.1118/1.4866216 (Cited on pages 7, 86).

[53] Julia Herzen et al. "3D Grating-Based X-ray Phase-Contrast Computed Tomography for High-Resolution Quantitative Assessment of Cartilage: An Experimental Feasibility Study with 3T MRI, 7T MRI and Biomechanical Correlation". In: *PLOS ONE* 14 (14, 2019), e0212106. DOI: 10.1371/journal.pone.0212106 (Cited on page 2).

[54] Holger Hetterich et al. "Phase-Contrast CT: Qualitative and Quantitative Evaluation of Atherosclerotic Carotid Artery Plaque". In: *Radiology* 271 (2014), pp. 870–878. DOI: 10.1148/radiol.14131554 (Cited on page 2).

[55] Florian Horn et al. "Implementation of a Talbot-Lau interferometer in a clinical-like c-arm setup: A feasibility study". In: *Scientific Reports* 8 (1 2018). DOI: 10.1038/s41598-018-19482-z (Cited on pages 3, 150).

[56] Jiang Hsieh. "Adaptive Streak Artifact Reduction in Computed Tomography Resulting from Excessive X-Ray Photon Noise". In: *Medical Physics* 25 (1998), pp. 2139–2147. DOI: 10.1118/1.598410 (Cited on page 164).

[57] Jiang Hsieh. "Computed Tomography: Principles, Design, Artifacts, and Recent Advances". Third edition. Bellingham, Washington, USA: SPIE, 2015. 639 pp. ISBN: 978-1-62841-825-5. DOI: https://doi.org/10.1117/3.2197756 (Cited on page 160).

[58] Zhirong Huang and Ronald D. Ruth. "Laser-Electron Storage Ring". In: *Physical Review Letters* 80 (1998), pp. 976–979. DOI: 10.1103/PhysRevLett.80.976 (Cited on page 5).

[59] "IEC 61223-2-6:2006, Constancy Tests – Imaging Performance of Computed Tomography X-ray Equipment". DOI: https://dx.doi.org/10.31030/1444180 (Cited on pages 88, 165, 166).

[60] Xu Ji et al. "Studies of signal estimation bias in grating-based x-ray multicontrast imaging". In: *Medical Physics* 44 (6 2017), pp. 2453–2465. DOI: 10.1002/mp.12235 (Cited on page 164).

[61] Christoph Jud et al. "Trabecular bone anisotropy imaging with a compact laser-undulator synchrotron x-ray source". In: *Scientific Reports* 7 (2017), p. 14477. DOI: 10.1038/s41598-017-14830-x (Cited on page 76).

[62] M. Kachelriess et al. "Flying focal spot (FFS) in cone-beam CT". In: *IEEE Transactions on Nuclear Science* 53 (2006), pp. 1238–1247. DOI: 10.1109/TNS.2006.874076 (Cited on pages 84, 163).

[63] Steffen Ketelhut and Ludwig Büermann. "Catalogue of unfiltered x-ray spectra from tungsten-, molybdenum-, and rhodium-anode-based x-ray tubes with generating voltages from 10kV to 50kV in steps of 1kV". 2020. DOI: 10.7795/720.20201118 (Cited on page 7).

[64] Steffen Ketelhut et al. "Catalog of x-ray spectra of Mo-, Rh-, and W-anode-based x-ray tubes from 10 to 50 kV". In: *Physics in Medicine & Biology* 66 (2021), p. 115013. DOI: 10.1088/1361-6560/abfbb2 (Cited on page 7).

[65] O. Klein and Y. Nishina. "Über die Streuung von Strahlung durch freie Elektronen nach der neuen relativistischen Quantendynamik von Dirac". In: *Zeitschrift für Physik* 52 (1929), pp. 853–868. DOI: 10.1007/BF01366453 (Cited on page 12).

[66] F. J. Koch et al. "Note: Gratings on low absorbing substrates for x-ray phase contrast imaging". In: *Review of Scientific Instruments* 86 (12 2015), p. 126114. DOI: 10.1063/1.4939055 (Cited on pages 33, 36, 50).

[67] Thomas Koehler et al. "Slit-Scanning Differential x-Ray Phase-Contrast Mammography: Proof-of-concept Experimental Studies: Slit-scanning Differential x-Ray Phase-Contrast Mammography". In: *Medical Physics* 42 (27, 2015), pp. 1959–1965. DOI: 10.1118/1.4914420 (Cited on page 3).

[68] C. Kottler et al. "Grating interferometer based scanning setup for hard x-ray phase contrast imaging". In: *Review of Scientific Instruments* 78 (4 2007). DOI: 10.1063/1.2723064 (Cited on page 14).

[69] D. Krämer et al. "New developments for the investigation of hard X-rays emitted by peeling adhesive tapes". In: *Review of Scientific Instruments* 84 (2013), p. 055104. DOI: 10.1063/1.4803155 (Cited on page 5).

[70] Tom Kumschier. "Advanced Processing Algorithms for X-ray Dark-Field CT Reconstruction". Master Thesis. TUM, 2021 (Cited on pages 171, 180).

[71] Veronika Ludwig et al. "Exploration of different x-ray Talbot-Lau setups for dark-field lung imaging examined in a porcine lung". In: *Physics in Medicine and Biology* 64 (6 2019). DOI: 10.1088/1361-6560/ab051c (Cited on pages 79–81, 171).

[72] Susanna K. Lynch et al. "Interpretation of dark-field contrast and particle-size selectivity in grating interferometers". In: *Applied Optics* 50 (22 2011), pp. 4310–4319. DOI: 10.1364/AO.50.004310 (Cited on pages 79, 80, 160).

[73] A. Malecki et al. "Quantitative Wave-Optical Numerical Analysis of the Dark-Field Signal in Grating-Based X-ray Interferometry". In: *EPL (Europhysics Letters)* 99 (1, 2012), p. 48001. DOI: 10.1209/0295-5075/99/48001 (Cited on page 37).

[74] Korbinian Mechlem et al. "A Theoretical Framework for Comparing Noise Characteristics of Spectral, Differential Phase-Contrast and Spectral Differential Phase-Contrast x-Ray Imaging". In: *Physics in Medicine & Biology* 65 (1, 2020), p. 065010. DOI: 10.1088/1361-6560/ab7106 (Cited on page 37).

[75] Felix G. Meinel et al. "Improved Diagnosis of Pulmonary Emphysema Using In Vivo Dark-Field Radiography:" in: *Investigative Radiology* 49 (2014), pp. 653–658. DOI: 10.1097/RLI.0000000000000067 (Cited on pages 2, 3).

[76] Felix G. Meinel et al. "Lung tumors on multimodal radiographs derived from grating-based X-ray imaging–a feasibility study". In: *Physica medica: PM: an international journal devoted to the applications of physics to medicine and biology: official journal of the Italian Association of Biomedical Physics (AIFB)* 30 (2014), pp. 352–357. DOI: 10.1016/j.ejmp.2013.11.001 (Cited on pages 3, 79).

[77] Pascal Meyer et al. "X-ray gratings for grating-based x-ray DPCI fabricated using the deep x-ray lithography process: state of the art". July 2017 (Cited on pages 2, 33, 34).

[78] Peter Modregger et al. "Small angle x-ray scattering with edge-illumination". In: *Scientific Reports* 6 (2016), p. 30940. DOI: 10.1038/srep30940 (Cited on page 21).

[79] Jürgen Mohr et al. "High Aspect Ratio Gratings for X-ray Phase Contrast Imaging". In: *AIP Conference Proceedings* 1466 (31, 2012), pp. 41–50. DOI: 10.1063/1.4742267 (Cited on pages 14, 33).

[80] Atsushi Momose. "Recent Advances in X-ray Phase Imaging". In: *Japanese Journal of Applied Physics* 44 (2005), pp. 6355–6367. DOI: 10.1143/JJAP.44.6355 (Cited on page 14).

[81] Atsushi Momose. "X-Ray Phase Imaging Reaching Clinical Uses". In: *Physica Medica* 79 (2020), pp. 93–102. DOI: 10.1016/j.ejmp.2020.11.003 (Cited on page 14).

[82] Kaye S. Morgan et al. "X-ray phase imaging with a paper analyzer". In: *Applied Physics Letters* 100 (2012), p. 124102. DOI: 10.1063/1.3694918 (Cited on page 14).

[83] "Multipurpose Chest Phantom N1 "LUNGMAN", KYOTO KAGAKU". URL: https://www.kyotokagaku.com/en/products_data/ph-1_01/ (visited on 10/31/2022) (Cited on page 169).

[84] "NOMEX Dosimeter, PTW". URL: https://www.ptwdosimetry.com/en/products/nomex-dosemeter/ (visited on 09/28/2022) (Cited on page 165).

[85] Susan Notohamiprodjo et al. "Qualitative and Quantitative Evaluation of Structural Myocardial Alterations by Grating-Based Phase-Contrast Computed Tomography". In: *Investigative Radiology* 53 (2018), pp. 26–34. DOI: 10.1097/RLI.0000000000000408 (Cited on page 2).

[86] Alessandro Olivo and Robert Speller. "A coded-aperture technique allowing x-ray phase contrast imaging with conventional sources". In: *Applied Physics Letters* 91 (2007), p. 074106. DOI: 10.1063/1.2772193 (Cited on page 21).

[87] Alessandro Olivo et al. "Noninterferometric phase-contrast images obtained with incoherent x-ray sources". In: *Applied Optics* 50 (2011), p. 1765. DOI: 10.1364/AO.50.001765 (Cited on page 21).

[88] David Paganin. "Coherent X-Ray Optics". Oxford University Press, 2006. ISBN: 978-0-19-856728-8. DOI: 10.1093/acprof:oso/9780198567288.001.0001 (Cited on pages 9, 14, 18, 23, 38, 39, 110).

[89] Georg Pelzer et al. "A Beam Hardening and Dispersion Correction for X-Ray Dark-Field Radiography". In: *Medical Physics* 43 (6Part1 2016), pp. 2774–2779. DOI: 10.1118/1.4948671 (Cited on page 161).

[90] Franz Pfeiffer et al. "Grating-based X-ray phase contrast for biomedical imaging applications". In: *Zeitschrift für Medizinische Physik* 23 (3 2013), pp. 176–185. DOI: 10.1016/j.zemedi.2013.02.002 (Cited on page 14).

[91] Franz Pfeiffer et al. "Hard-X-ray dark-field imaging using a grating interferometer". In: *Nature Materials* 7 (2 2008), pp. 134–137. DOI: 10.1038/nmat2096 (Cited on pages 2, 26, 77, 112).

[92] Franz Pfeiffer et al. "Hard X-ray Phase Tomography with Low-Brilliance Sources". In: *Physical Review Letters* 98 (8, 2007), p. 108105. DOI: 10.1103/PhysRevLett.98.108105 (Cited on page 2).

[93] Franz Pfeiffer et al. "High-sensitivity phase-contrast tomography of rat brain in phosphate buffered saline". In: *Journal of Physics: Conference Series* 186 (1 2009), p. 012046. DOI: 10.1088/1742-6596/186/1/012046 (Cited on page 14).

[94] Franz Pfeiffer et al. "Phase retrieval and differential phase-contrast imaging with low-brilliance X-ray sources". In: *Nature Physics* 2 (4 2006), pp. 258–261. DOI: 10.1038/nphys265 (Cited on pages i, iii, 2, 14, 20).

[95] Franz Pfeiffer et al. "Tomographic reconstruction of three-dimensional objects from hard X-ray differential phase contrast projection images". In: *Nuclear Instruments and Methods in Physics Research Section A: Accelerators, Spectrometers, Detectors and Associated Equipment* 580 (2 2007), pp. 925–928. DOI: 10.1016/j.nima.2007.06.104 (Cited on page 2).

[96] Simon Pinzek et al. "Fabrication of X-ray Absorption Gratings by Centrifugal Deposition of Bimodal Tungsten Particles in High Aspect Ratio Silicon Templates". In: *Scientific Reports* 12 (2022), p. 5405. DOI: 10.1038/s41598-022-08222-z (Cited on pages 36, 49, 119, 180).

[97] Simon Pinzek et al. "Fabrication of X-Ray Absorption Gratings via Deep X-Ray Lithography Using a Conventional X-Ray Tube". In: *Journal of Micro/Nanopatterning, Materials, and Metrology* 20 (4, 2021). DOI: 10.1117/1.JMM.20.4.043801 (Cited on pages 35, 48, 94).

[98] Amanda Pleier. "Characterization and Processing for a Clinical Prototype Grating-Based Computed Tomography System". Master Thesis. TUM, 2019 (Cited on page 180).

[99] Ervin B. Podgorsak. "Radiation Physics for Medical Physicists". Berlin, Heidelberg: Springer Berlin Heidelberg, 2010. ISBN: 978-3-642-00874-0. DOI: 10.1007/978-3-642-00875-7 (Cited on pages 11, 12).

[100] Vincent Revol et al. "X-ray interferometer with bent gratings: Towards larger fields of view". In: *Nuclear Instruments and Methods in Physics Research, Section A: Accelerators, Spectrometers, Detectors and Associated Equipment* 648 (2011). DOI: 10.1016/j.nima.2010.11.040 (Cited on pages 58, 79, 146).

[101] Elena Reznikova et al. "Soft X-ray Lithography of High Aspect Ratio SU8 Submicron Structures". In: *Microsystem Technologies* 14 (9, 2008), pp. 1683–1688. DOI: 10.1007/s00542-007-0507-x (Cited on page 33).

[102] Jens Rieger et al. "Designing the phase grating for Talbot-Lau phase-contrast imaging systems: a simulation and experiment study". In: *Optics Express* 24 (12 2016), p. 13357. DOI: 10.1364/oe.24.013357 (Cited on pages 14, 99, 105).

[103] André Ritter et al. "Simulation Framework for Coherent and Incoherent X-ray Imaging and Its Application in Talbot-Lau Dark-Field Imaging". In: *Optics Express* 22 (22, 2014), p. 23276. DOI: 10.1364/oe.22.023276 (Cited on page 37).

[104] F. Salvat et al. "Penelope: a code system for Monte Carlo simulation of electron and photon transport." Illy-les-Moulineaux, France: OECD/NEA Data Bank, 2006 (Cited on pages 7, 37).

[105] Kai Scherer. "Grating-Based X-Ray Phase-Contrast Mammography". Springer International Publishing AG, 2018. ISBN: 978-3-319-81908-2 (Cited on page 76).

[106] Kai Scherer et al. "X-ray Dark-field Radiography - In-Vivo Diagnosis of Lung Cancer in Mice". In: *Scientific Reports* 7 (1 2017), p. 402. DOI: 10.1038/s41598-017-00489-x (Cited on pages 2, 79, 93).

[107] Simone Schleede et al. "Emphysema diagnosis using X-ray dark-field imaging at a laser-driven compact synchrotron light source". In: *Proceedings of the National Academy of Sciences of the United States of America* 109 (44 2012), pp. 17880–17885. DOI: 10.1073/pnas.1206684109 (Cited on pages i, iii, 2, 79).

[108] Clemens Schmid et al. "Dark-Field Imaging on a Clinical CT System: Modelling of Interferometer Vibrations". In: *7th International Conference on Image Formation in X-Ray Computed Tomography*. Seventh International Conference on Image Formation in X-Ray Computed Tomography (ICIFXCT 2022). Baltimore, United States: SPIE, 2022, p. 66. DOI: 10.1117/12.2646676 (Cited on page 139).

[109] Clemens Schmid et al. "Modeling vibrations of a tiled Talbot-Lau interferometer on a clinical CT". In: *IEEE Transactions on Medical Imaging* (2022). DOI: 10.1109/TMI.2022.3217662 (Cited on pages 139–142, 149, 150).

[110] Tom Schoonjans et al. "The xraylib library for X-ray–matter interactions. Recent developments". In: *Spectrochimica Acta Part B: Atomic Spectroscopy* 66 (2011), pp. 776–784. DOI: 10.1016/j.sab.2011.09.011 (Cited on pages 9, 11–14, 37).

[111] Tobias J. Schröter et al. "Large field-of-view tiled grating structures for X-ray phase-contrast imaging". In: *Review of Scientific Instruments* 88 (1 2017), p. 015104. DOI: 10.1063/1.4973632 (Cited on pages 51, 75, 76).

[112] Tobias J. Schröter et al. "Large-Area Full Field x-Ray Differential Phase-Contrast Imaging Using 2D Tiled Gratings". In: *Journal of Physics D: Applied Physics* 50 (7, 2017), p. 225401. DOI: 10.1088/1361-6463/aa6e85 (Cited on pages 58, 75).

[113] Tobias J. Schröter et al. "Large Area Gratings by X-Ray LIGA Dynamic Exposure for x-Ray Phase-Contrast Imaging". In: *Journal of Micro/Nanolithography, MEMS, and MOEMS* 16 (12, 2017), p. 013501. DOI: 10.1117/1.JMM.16.1.013501 (Cited on page 33).

[114] Markus Schüttler et al. "Height Control for Small Periodic Structures Using X-Ray Radiography". In: *Measurement Science and Technology* 27 (1, 2016), p. 025015. DOI: 10.1088/0957-0233/27/2/025015 (Cited on page 47).

[115] Zhitian Shi et al. "Laboratory X-ray interferometry imaging with a fan-shaped source grating". In: *Optics Letters* 46 (15 2021), pp. 3693–3696. DOI: 10.1364/OL.426867 (Cited on pages 36, 47).

[116] Zhitian Shi et al. "Towards the fabrication of high-aspect-ratio silicon gratings by deep reactive ion etching". In: *Micromachines* 11 (9 2020). DOI: 10.3390/MI11090864 (Cited on page 36).

[117] A. Snigirev et al. "On the possibilities of x-ray phase contrast microimaging by coherent high-energy synchrotron radiation". In: *Review of Scientific Instruments* 66 (1995), pp. 5486–5492. DOI: 10.1063/1.1146073 (Cited on page 14).

[118] M Strobl. "General solution for quantitative dark-field contrast imaging with grating interferometers". In: *Scientific Reports* 4 (28, 2014), p. 7243. DOI: 10.1038/srep07243 (Cited on pages 79, 80).

[119] Junji Tanaka et al. "Cadaveric and in Vivo Human Joint Imaging Based on Differential Phase Contrast by X-ray Talbot-Lau Interferometry". In: *Zeitschrift für Medizinische Physik* 23 (2013), pp. 222–227. DOI: 10.1016/j.zemedi.2012.11.004 (Cited on page 3).

[120] Arne Tapfer. "Small Animal X-ray Phase-Contrast Imaging". PhD Thesis. TUM, 2013. URL: http://d-nb.info/104227701X/34 (Cited on page 81).

[121] Arne Tapfer et al. "Development of a prototype gantry system for preclinical x-ray phase-contrast computed tomography". In: *Medical Physics* 38 (11 2011), pp. 5910–5915. DOI: 10.1118/1.3644844 (Cited on pages 2, 77).

[122] Arne Tapfer et al. "Experimental results from a preclinical X-ray phase-contrast CT scanner". In: *Proceedings of the National Academy of Sciences* 109 (39 2012), pp. 15691–15696. DOI: 10.1073/pnas.1207503109 (Cited on pages 2, 3).

[123] Kirsten Taphorn et al. "Direct Differentiation of Pathological Changes in the Human Lung Parenchyma with Grating-Based Spectral X-ray Dark-Field Radiography". In: *IEEE Transactions on Medical Imaging* 40 (1, 2021), pp. 1568–1578. DOI: 10.1109/TMI.2021.3061253 (Cited on pages 37, 39).

[124] Kirsten Taphorn et al. "Grating-Based Spectral X-ray Dark-Field Imaging for Correlation with Structural Size Measures". In: *Scientific Reports* 10 (2020), p. 13195. DOI: 10.1038/s41598-020-70011-3 (Cited on pages 32, 169).

[125] Maximilian von Teuffenbach. "Iterative reconstruction algorithms for phase-contrast computed tomography". Master Thesis. TUM, 2015 (Cited on pages 2, 180).

[126] Maximilian von Teuffenbach. "Statistical signal processing and reconstruction algorithms for grating-based X-ray imaging and computed tomography". PhD Thesis. TUM, 2020. URL: http://d-nb.info/1228536015/34 (Cited on pages 171, 181).

[127] Maximilian von Teuffenbach et al. "Grating-based phase-contrast and dark-field computed tomography: a single-shot method". In: *Scientific Reports* 7 (1 2017), p. 7476. DOI: 10.1038/s41598-017-06729-4 (Cited on pages 77, 137, 138, 155, 181).

[128] "The Nobel Prize in Physiology or Medicine 1979". URL: https://www.nobelprize.org/prizes/medicine/1979/summary/ (visited on 04/12/2022) (Cited on page 1).

[129] T. Thuering and M. Stampanoni. "Performance and optimization of X-ray grating interferometry". In: *Philosophical Transactions of the Royal Society A: Mathematical, Physical and Engineering Sciences* 372 (2010 2014), pp. 20130027–20130027. DOI: 10.1098/rsta.2013.0027 (Cited on pages 105, 106).

[130] "Tissue Substitutes in Radiation Dosimetry and Measurement". Bethesda, Md., U.S.A: International Commission on Radiation Units and Measurements, 1989. 189 pp. ISBN: 978-0-913394-38-0 (Cited on pages 115–119).

[131] Henrik Turbell. "Cone-Beam Reconstruction Using Filtered Backprojection". PhD thesis. Linköping: Linköping University, 2001. 177 pp. URL: http://urn.kb.se/resolve?urn=urn:nbn:se:liu:diva-54325 (Cited on page 31).

[132] Stephan Umkehrer et al. "Optimization of in vivo murine X-ray dark-field computed tomography". In: *Review of Scientific Instruments* 90 (2019), p. 103103. DOI: 10.1063/1.5115436 (Cited on pages 3, 49, 58, 77, 79, 93).

[133] Udo van Stevendaal et al. "Reconstruction Method Incorporating the Object-Position Dependence of Visibility Loss in Dark-Field Imaging". In: *SPIE 2013* (6, 2013), 86680Z. DOI: 10.1117/12.2006711 (Cited on pages 31, 77).

[134] Guido Van Rossum and Fred L. Drake. "Python 3 Reference Manual". Scotts Valley, CA: CreateSpace, 2009. ISBN: 1-4414-1269-7 (Cited on page 26).

[135] A. Velroyen et al. "Grating-based X-ray Dark-field Computed Tomography of Living Mice". In: *EBioMedicine* 2 (10 2015), pp. 1500–1506. DOI: 10.1016/j.ebiom.2015.08.014 (Cited on pages 3, 31, 32, 77, 79, 80, 93).

[136] Manuel Viermetz et al. "Dark-Field Computed Tomography Reaches the Human Scale". In: *Proceedings of the National Academy of Sciences* 119 (22, 2022), e2118799119. DOI: 10.1073/pnas.2118799119 (Cited on pages 31, 33, 37, 81, 137–140, 143, 145, 157, 159, 166, 168, 170, 171).

[137] Manuel Viermetz et al. "Dark-Field Imaging on a Clinical CT System: Realization of Talbot-Lau Interferometry in a Gantry". In: *7th International Conference on Image Formation in X-Ray Computed Tomography*. Seventh International Conference on Image Formation in X-Ray Computed Tomography (ICIFXCT 2022). Baltimore, United States: SPIE, 2022, p. 26. DOI: 10.1117/12.2646439 (Cited on page 146).

[138] Manuel Viermetz et al. "High Resolution Laboratory Grating-Based X-ray Phase-Contrast CT". In: *Scientific Reports* 8 (2018), p. 15884. DOI: 10.1038/s41598-018-33997-5 (Cited on page 2).

[139] Manuel Viermetz et al. "Initial Characterization of Dark-field CT on a Clinical Gantry". In: *IEEE Transactions on Medical Imaging* (2022). DOI: 10.1109/TMI.2022.3222839 (Cited on pages 144, 146–152, 160–163, 165, 167, 168).

[140] Manuel Viermetz et al. "Technical Design Considerations of a Human-Scale Talbot-Lau Interferometer for Dark-Field CT". In: *IEEE Transactions on Medical Imaging* (2022). DOI: 10.1109/TMI.2022.3207579 (Cited on pages 34, 37, 46, 48, 49, 81, 85, 91, 92, 94, 108, 112, 113, 122, 123).

[141] Hongchang Wang et al. "X-ray phase contrast tomography by tracking near field speckle". In: *Scientific Reports* 5 (2015), p. 8762. DOI: 10.1038/srep08762 (Cited on page 14).

[142] Jia Wang and Dominik Fleischmann. "Improving Spatial Resolution at CT: Development, Benefits, and Pitfalls". In: *Radiology* 289 (1, 2018), pp. 261–262. DOI: 10.1148/radiol.2018181156 (Cited on page 163).

[143] Thomas Weber et al. "Noise in x-ray grating-based phase-contrast imaging". In: *Medical Physics* 38 (7 2011), pp. 4133–4140. DOI: 10.1118/1.3592935 (Cited on page 107).

[144] Timm Weitkamp et al. "Tomography with grating interferometers at low-brilliance sources". In: ed. by Ulrich Bonse. Aug. 2006, 63180S. DOI: 10.1117/12.683851 (Cited on pages 18, 20).

[145] Harold H. Wen et al. "Single-shot x-ray differential phase-contrast and diffraction imaging using two-dimensional transmission gratings". In: *Optics Letters* 35 (2010), p. 1932. DOI: 10.1364/ol.35.001932 (Cited on page 15).

[146] Konstantin Willer et al. "X-ray dark-field chest imaging for detection and quantification of emphysema in patients with chronic obstructive pulmonary disease: a diagnostic accuracy study". In: *The Lancet Digital Health* 3 (2021), e733–e744. DOI: 10.1016/S2589-7500(21)00146-1 (Cited on pages 3, 75, 76, 79–81).

[147] Konstantin Willer et al. "X-ray dark-field imaging of the human lung—A feasibility study on a deceased body". In: *PLOS ONE* 13 (9 2018). Ed. by Anna Nolan, e0204565. DOI: 10.1371/journal.pone.0204565 (Cited on page 3).

[148] Marian Willner et al. "Quantitative Breast Tissue Characterization Using Grating-Based X-Ray Phase-Contrast Imaging". In: *Physics in Medicine and Biology* 59 (7, 2014), pp. 1557–1571. DOI: 10.1088/0031-9155/59/7/1557 (Cited on page 2).

[149] Marian Willner et al. "Quantitative Three-Dimensional Imaging of Lipid, Protein, and Water Contents via X-Ray Phase-Contrast Tomography". In: *PLOS ONE* 11 (22, 2016). Ed. by Antonio Gonzalez-Bulnes. DOI: 10.1371/journal.pone.0151889. eprint: 27003308 (Cited on page 2).

[150] Z. Wu et al. "Prototype system of noninterferometric phase-contrast computed tomography utilizing medical imaging components". In: *Journal of Applied Physics* 129 (7 2021). DOI: 10.1063/5.0031392 (Cited on pages 3, 21, 58, 78, 81, 111, 138).

[151] Jinqiu Xu et al. "Intensity-Based Iterative Reconstruction for Helical Grating Interferometry Breast CT with Static Grating Configuration". In: *Optics Express* 30 (11, 2022), p. 13847. DOI: 10.1364/OE.455967 (Cited on pages 137, 138, 155).

[152] Andre Yaroshenko et al. "Improved In vivo Assessment of Pulmonary Fibrosis in Mice using X-Ray Dark-Field Radiography." In: *Scientific reports* 5 (2015), p. 17492. DOI: 10.1038/srep17492 (Cited on pages i, iii, 3, 79, 93).

[153] Andre Yaroshenko et al. "Non-binary phase gratings for x-ray imaging with a compact Talbot interferometer". In: *Optics Express, Vol. 22, Issue 1, pp. 547-556* 22 (1 2014), pp. 547–556. DOI: 10.1364/OE.22.000547 (Cited on pages 21, 102, 122).

[154] Andre Yaroshenko et al. "Pulmonary Emphysema Diagnosis with a Preclinical Small-Animal X-ray Dark-Field Scatter-Contrast Scanner". In: *Radiology* 269 (2013), pp. 427–433. DOI: 10.1148/radiol.13122413 (Cited on pages 2, 3, 79, 93).

[155] Wataru Yashiro et al. "Effect of Beam Hardening on a Visibility-Contrast Image Obtained by X-ray Grating Interferometry". In: *Optics Express* 23 (7, 2015), pp. 23462–23471. DOI: 10.1364/OE.23.023462 (Cited on pages 160, 161).

[156] Wataru Yashiro et al. "On the origin of visibility contrast in x-ray Talbot interferometry". In: *Optics Express* 18 (2, 2010), p. 16890. DOI: 10.1364/OE.18.016890 (Cited on pages 79, 80).

[157] Guibin Zan et al. "High-Resolution Multicontrast Tomography with an X-ray Microarray Anode–Structured Target Source". In: *Proceedings of the National Academy of Sciences* 118 (22, 2021), e2103126118. DOI: 10.1073/pnas.2103126118 (Cited on page 63).

[158] I. Zanette et al. "Quantitative phase and absorption tomography with an X-ray grating interferometer and synchrotron radiation". In: *Physica Status Solidi (A) Applications and Materials Science* 208 (11 2011), pp. 2526–2532. DOI: 10.1002/pssa.201184276 (Cited on pages 2, 138, 157, 164).

[159] Marie-Christine Zdora. "State of the Art of X-ray Speckle-Based Phase-Contrast and Dark-Field Imaging". In: *Journal of Imaging* 4 (25, 2018), p. 60. DOI: 10.3390/jimaging4050060 (Cited on pages 2, 14).

[160] T. Zhou et al. "Comparison of Two X-Ray Phase-Contrast Imaging Methods with a Microfocus Source". In: *Optics Express* 21 (16, 2013), p. 30183. DOI: 10.1364/OE.21.030183 (Cited on page 63).

Publications and Scientific Presentations

Publications as First Author

Viermetz, M., Birnbacher, L., Willner, M., Achterhold, K., Pfeiffer, F., & Herzen, J. (2018). "High resolution laboratory grating-based X-ray phase-contrast CT." *Scientific Reports*, 8(1), 15884. https://doi.org/10.1038/s41598-018-33997-5

Viermetz, M., Gustschin, N., Schmid, C., Haeusele, J., von Teuffenbach, M., Meyer, P., Bergner, F., Lasser, T., Proksa, R., Koehler, T., & Pfeiffer, F. (2022). "Dark-field computed tomography reaches the human scale." *Proceedings of the National Academy of Sciences*, 119(8), e2118799119. https://doi.org/10.1073/pnas.2118799119

Viermetz, M., Gustschin, N., Schmid, C., Haeusele, J., Noël, P., Proksa, R., Loescher, S., Koehler, T., & Pfeiffer, F. (2022). "Technical design considerations of a human-scale Talbot-Lau interferometer for dark-field CT." *IEEE Transactions on Medical Imaging*. https://doi.org/10.1109/TMI.2022.3207579

Viermetz, M., Gustschin, N., Schmid, C., Haeusele, J., Koehler, T., & Pfeiffer, F. (2022). "Initial Characterization of Dark-field CT on a clinical gantry." *IEEE Transactions on Medical Imaging*. https://doi.org/10.1109/TMI.2022.3222839

Publications as Co-author

Koch, F. J., Schröter, T. J., Kunka, D., Meyer, P., Meiser, J., Faisal, A., Khalil, M. I., Birnbacher, L., **Viermetz, M.**, Walter, M., Schulz, J., Pfeiffer, F., & Mohr, J. (2015). "Note: Gratings on low absorbing substrates for x-ray phase contrast imaging." *Review of Scientific Instruments*, 86(12), 126114. https://doi.org/10.1063/1.4939055

Willner, M., **Viermetz, M.**, Marschner, M., Scherer, K., Braun, C., Fingerle, A., Noël, P., Rummeny, E., Pfeiffer, F., & Herzen, J. (2016). "Quantitative three-dimensional imaging of lipid, protein, and water contents via x-ray phase-contrast tomography." *PLoS ONE*, 11(3), e0151889. https://doi.org/10.1371/journal.pone.0151889

Teuffenbach, M. von, Koehler, T., Fehringer, A., **Viermetz, M.**, Brendel, B., Herzen, J., Proksa, R., Rummeny, E. J., Pfeiffer, F., & Noël, P. B. (2017). "Grating-based phase-contrast and dark-field computed tomography: A single-shot method." *Scientific Reports*, 7(1), 7476. https://doi.org/10.1038/s41598-017-06729-4

Braunagel, M., Birnbacher, L., Willner, M., Marschner, M., De Marco, F., **Viermetz, M.**, Notohamiprodjo, S., Hellbach, K., Auweter, S., Link, V., Woischke, C., Reiser, M. F., Pfeiffer, F., Notohamiprodjo, M., & Herzen, J. (2017). "Qualitative and Quantitative Imaging Evaluation of Renal Cell Carcinoma Subtypes with Grating-based X-ray Phase-contrast CT." *Scientific Reports*, 7(1), 45400. https://doi.org/10.1038/srep45400

Birnbacher, L., **Viermetz, M.**, Noichl, W., Allner, S., Fehringer, A., Marschner, M., Von Teuffenbach, M., Willner, M., Achterhold, K., Noël, P. B., Koehler, T., Herzen, J., & Pfeiffer, F. (2018). "Tilted grating phase-contrast computed tomography using statistical iterative reconstruction." Scientific Reports, 8(1). https://doi.org/10.1038/s41598-018-25075-7

Notohamiprodjo, S., Webber, N., Birnbacher, L., Willner, M., **Viermetz, M.**, Herzen, J., Marschner, M., Mayr, D., Bartsch, H., Saam, T., Auweter, S., Pfeiffer, F., Reiser, M. F., & Hetterich, H. (2018). "Qualitative and Quantitative Evaluation of Structural Myocardial Alterations by Grating-Based Phase-Contrast Computed Tomography." *Investigative Radiology*, 53(1), 26–34. https://doi.org/10.1097/RLI.0000000000000408

Gustschin, N., Gustschin, A., Meyer, P., **Viermetz, M.**, Riederer, P., Herzen, J., Mohr, J., & Pfeiffer, F. (2019). "Quality and parameter control of X-ray absorption gratings by angular X-ray transmission." *Optics Express*, 27(11), 15943. https://doi.org/10.1364/oe.27.015943

Herzen, J., Karampinos, D. C., Foehr, P., Birnbacher, L., **Viermetz, M.**, Burgkart, R., Baum, T., Lohoefer, F., Wildgruber, M., Schilling, F., Willner, M., Marschner, M., Noël, P. B., Rummeny, E. J., Pfeiffer, F., & Jungmann, P. M. (2019). "3D grating-based X-ray phase-contrast computed tomography for high-resolution quantitative assessment of cartilage: An experimental feasibility study with 3T MRI, 7T MRI and biomechanical correlation." *PLOS ONE*, 14(2), e0212106. https://doi.org/10.1371/journal.pone.0212106

Gustschin, A., Neuwirth, T., Backs, A., **Viermetz, M.**, Gustschin, N., Schulz, M., & Pfeiffer, F. (2020). "Comparison of Thermal Neutron and Hard X-ray Dark-Field Tomography." *Journal of Imaging*, 7(1), 1. https://doi.org/10.3390/jimaging7010001

Mechlem, K., Sellerer, T., **Viermetz, M.**, Herzen, J., & Pfeiffer, F. (2020). "A theoretical framework for comparing noise characteristics of spectral, differential phase-contrast and spectral differential phase-contrast x-ray imaging." *Physics in Medicine & Biology*, 65(6), 065010. https://doi.org/10.1088/1361-6560/ab7106

Pinzek, S., Beckenbach, T., **Viermetz, M.**, Meyer, P., Gustschin, A., Andrejewski, J., Gustschin, N., Herzen, J., Schulz, J., & Pfeiffer, F. (2021). "Fabrication of x-ray absorption gratings via deep x-ray lithography using a conventional x-ray tube." *Journal of Micro/Nanopatterning, Materials, and Metrology*, 20(04). https://doi.org/10.1117/1.JMM.20.4.043801

Taphorn, K., Mechlem, K., Sellerer, T., De Marco, F., **Viermetz, M.**, Pfeiffer, F., Pfeiffer, D., & Herzen, J. (2021). "Direct Differentiation of Pathological Changes in the Human Lung Parenchyma with Grating-Based Spectral X-ray Dark-Field Radiography." *IEEE Transactions on Medical Imaging*, 40(6), 1568–1578. https://doi.org/10.1109/TMI.2021.3061253

Pinzek, S., Gustschin, A., Gustschin, N., **Viermetz, M.**, & Pfeiffer, F. (2022). "Fabrication of X-ray absorption gratings by centrifugal deposition of bimodal tungsten particles in high aspect ratio silicon templates." *Scientific Reports*, 12(1), 5405. https://doi.org/10.1038/s41598-022-08222-z

Schmid, C., **Viermetz, M.**, Gustschin, N., Noichl, W., Haeusele, J., Lasser, T., Koehler, T., & Pfeiffer, F. (2022). "Modeling vibrations of a tiled Talbot-Lau interferometer on a clinical CT system." *IEEE Transactions on Medical Imaging*. https://doi.org/10.1109/TMI.2022.3217662

Frank, M., Gassert, F., Urban, T., Willer, K., Noichl, W., Schick, R., Schultheiß, M., **Viermetz, M.**, Gleich, B., De Marco, F., Herzen, J., Koehler, T., Engel, K. J., Renger, B., Gassert, F., Sauter, A., Fingerle, A., Haller, B., Makowski, M., Pfeiffer, D., & Pfeiffer, F. (2022). "Dark-field Chest X-ray Imaging for the Assessment of COVID-19-Pneumonia." *Communications Medicine*, 2, 147. https://doi.org/10.1038/s43856-022-00215-3

Conference Proceedings

Viermetz, M., Birnbacher, L., Fehringer, A., Willner, M., Noël, P. B., Pfeiffer, F., & Herzen, J. (2017). "High resolution laboratory grating-based x-ray phase-contrast CT." *Proc. SPIE 10132, Medical Imaging 2017: Physics of Medical Imaging*. https://doi.org/10.1117/12.2255657

Viermetz, M., Gustschin, N., Schmid, C., Haeusele, J., Proksa, R., Koehler, T., & Pfeiffer, F. (2022). "Dark-field imaging on a clinical CT system: Realization of Talbot-Lau interferometry in a gantry." *Proc. SPIE 12304, 7th International Conference on Image Formation in X-Ray Computed Tomography*. https://doi.org/10.1117/12.2646439

Conference Proceedings as Co-Author

Gustschin, N., **Viermetz, M.**, Schmid, C., Haeusele, J., Bergner F., Lasser T., Koehler, T., & Pfeiffer, F. (2022). "Dark-field imaging on a clinical CT system: performance and potential based on first results." *Proc. SPIE 12304, 7th International Conference on Image Formation in X-Ray Computed Tomography*. https://doi.org/10.1117/12.2646988

Schmid, C., **Viermetz, M.**, Gustschin, N., Haeusele, J., Lasser T., Koehler, T., & Pfeiffer, F. (2022). "Dark-field imaging on a clinical CT system: modelling of interferometer vibrations." *Proc. SPIE 12304, 7th International Conference on Image Formation in X-Ray Computed Tomography*. https://doi.org/10.1117/12.2646676

Haeusele, J., Schmid, C., **Viermetz, M.**, Gustschin, N., Lasser T., Bergner F., Koehler, T., & Pfeiffer, F. (2022). "Dark-field imaging on a clinical CT system: sample data processing and reconstruction." *Proc. SPIE 12304, 7th International Conference on Image Formation in X-Ray Computed Tomography*. https://doi.org/10.1117/12.2646440

De Marco, F., Marschner M., Birnbacher L., **Viermetz, M.**, Noël, P. B., & Pfeiffer, F. (2017). "Improving image quality in laboratory x-ray phase-contrast imaging." *Proc. SPIE 10132, Medical Imaging 2017: Physics of Medical Imaging*. https://doi.org/10.1117/12.2255537

Oral Presentations

Tissue decomposition using grating-based phase-contrast computed tomography (PC-CT). *DPG-Frühjahrstagung, Wuppertal, Germany, March 2015.*

Dark-Field Imaging on a Clinical CT System: Realization of Talbot-Lau Interferometry in a Gantry. *7th International Conference on Image Formation in X-Ray Computed Tomography, Baltimore, USA, June 2022.*

Poster Presentations

High resolution laboratory grating-based x-ray phase-contrast CT. *International Symposium on Biomedical Applications of X-ray Phase-Contrast Imaging (IMXP), Garmisch-Partenkirchen, Germany, January 2016.*

High resolution laboratory grating-based x-ray phase-contrast CT. *4th International Conference on Image Formation in X-Ray Computed Tomography, Bamberg, Germany, July 2016.*

High resolution laboratory grating-based x-ray phase-contrast CT. *SPIE Medical Imaging, Orlando, USA, February 2017.*

Acknowledgments

Throughout the entire period of this doctoral thesis, I have experienced great support, guidance and assistance from many different people. I would like to thank:

Franz Pfeiffer for giving me the opportunity to conduct my research at the Chair of Biomedical Physics. Thank you for giving me the opportunity to work on this very exciting project, for sharing your vast experience in the field of X-ray imaging, and for your helpful guidance.

Niko Gustschin, Clemens Schmid, Jakob Haeusele, and Maximilian Teuffenbach for their reliable support in the variety of topics involved in this prototype development. We had countless insightful discussions in a positive and productive working atmosphere and worked together very well as a team. This allowed us to solve the variety of complex problems, learn a lot, and keep momentum in the massive project to really advance dark-field imaging a significant step towards clinical practice. Working with you in the "dark-field CT team" has been a great time, thank you!

Thomas Koehler for your tireless and patient commitment, your encouragement and your very valuable advice in numerous discussions. I see your extraordinary dedication to the project as a key feature which made our development a success. Thank you for sharing your extensive knowledge on the whole bandwidth of CT and dark-field related topics with me.

Roland Proksa, Frank Bergner, Stefan Löscher, Sven Prevrhal, Ami Altman, and Slomo Gotman for your strong commitment to build such a scanner, and for giving me the opportunity to be part of this very exciting development. Thank you for your support with the technical design, the reconstruction, and configuration of the system to do dark-field CT scans.

Pascal Meyer, Joachim Schulz, Tomas Beckenbach, Martin Börner, and Jürgen Mohr for providing us with the superb micro-structured gratings on which the dark-field CT relies. In particular I would like to thank Pascal Meyer for his dedication and endless efforts.

Bernhard Gleich for his commitment to the project and help to provide the infrastructure for the dark-field CT prototype. Thank you for your valuable advice on all electronics related issues.

Wolfgang Hefele for his support whenever we encountered technical problems with the iCT system.

Alen Begic for his help from the workshop fabricating all the custom-made mounts for the dark-field CT.

The IT-Team around Martin, Wolfgang, and Clemens for keeping the software and computing infrastructure running smoothly. You have saved us a tremendous amount of time with your work!

Nelly de Leiris and Klaus Achterhold for their help with managing the administrative work and keeping everybody safe.

Julia Herzen, Tobias Lasser, and Peter Noël for their guidance, mentoring, insightful discussions, and for correcting my paper drafts.

Marian Willner and Lorenz Birnbacher for their outstanding supervision during my time as a bachelor and master student. It was great fun and a pleasure working together with you on the high-sensitivity and high-resolution phase-contrast projects.

Amanda Pleier, Tom Kumschier, Philipp Riederer, and Julius Gassert for their contributions to the dark-field CT project as working or master students.

My office colleagues at the IMETUM/MSB/MIBE and in the Physics department. You have made an important contribution to the fact that I thoroughly enjoyed my time at the Chair of Biomedical Physics. Special thanks go to my direct office mates Lisa, Kirsten, Manuela, Theresa, Simone, Clemens, Jakob, Niko, Alex, Thorsten, Simon, Florian, Konstantin, Johannes, Fabio, Daniel, and Lorenz. Thank you for the friendly and positive atmosphere, for the good company, all the refreshing coffee breaks, and the great discussions on X-rays and beyond. You have made an important contribution to the fact that I thoroughly enjoyed my time at the Chair of Biomedical Physics.

Last but not least, I would like to thank my parents Marlies and Michael and my brother Fabian, who have always supported and motivated me. And finally and most importantly Anna: Thank you for listening, patience, motivation, and enduring ups and downs.